The C-Band All Sky Survey (C-BASS): Observing diffuse Galactic emission at 5 GHz

A thesis submitted to The University of Manchester for the degree of
Doctor of Philosophy
in the Faculty of Engineering and Physical Sciences

2014

Melis Omer Irfan
School of Physics and Astronomy

Contents

List of Figures

List of Tables

Abstract

ABSTRACT OF THESIS submitted by Melis Omer Irfan for the Degree of Doctor of Philosophy and entitled The C-Band All Sky Survey (C-BASS): Observing diffuse Galactic emission at 5 GHz. June 2014. The University of Manchester.

Measurements of the diffuse Galactic emission are used for both the interpretation of sensitive cosmic microwave background data and the understanding of our Galaxy. I examine the diffuse Galactic emission at a central frequency of 4.76 GHz using data from the C-Band All-Sky Survey (C-BASS). The technical work presented here focuses on microphonic oscillation mitigation, receiver noise measurements and radio frequency interference detection. Northern C-BASS is a continuous comparison radiometer with a system temperature of 40 K, a knee frequency of 0.10 mHz in polarisation and a noise level of 2 mK $\sqrt{\text{s}}$. A calibration scheme was devised, using astronomical calibrators, to convert the data to Kelvin and correct for atmospheric opacity. This scheme is stable to 1 % over several months and accurate to better than 5 %. A major systematic in the C-BASS data is ground emission. In this work the ground emission is modelled and subtracted from the data resulting in a reduction of ground spillover by a factor of 8 in intensity and 7 in Stokes Q and U. The ground emission remaining in the maps is roughly 4 %, 5 % and 14 % of the sky signal in intensity, Stokes Q and Stokes U, respectively. A first scientific analysis of C-BASS Northern intensity data was made to investigate the contributions of free-free and synchrotron emission within the Galactic plane. The synchrotron spectral index was determined to be -2.63 ± 0.07 between 0.408 and 4.76 GHz and -2.71 ± 0.14 between 1.420 and 4.76 GHz and the ratio of free-free to synchrotron emission at 4.76 GHz was found to be 53$\pm$ 8 % to 47$\pm$ 8 %. Bringing in higher frequency data allowed for the detection of anomalous microwave emission associated with W43, W44 and W47 at a level of 4.9σ, 6.0σ and 3.4σ, respectively and demonstrated the need for C-BASS data to constrain the spectral form of AME within certain regions.

Declaration

I declare that no portion of the work referred to in the thesis has been submitted in support of an application for another degree or qualification of this or any other university or other institute of learning.

Copyright Statement

Dedication

To my father. For your poet’s soul and sense of wonder.

Acknowledgements

Above all else I would like to thank my family: my mother, my father and my sister for their unwavering support, devotion, humour and unique ability to make anything unpleasant in this world pale into insignificance with their love and optimism. My sister, Melodi, you are my confidant and the most glorious person I will ever know.

I would like to thank my supervisor, Clive Dickinson for his guidance and knowledge, Paddy Leahy for always giving me his time and attention and Rod Davies for his unsurpassed wisdom. I have been fortunate enough to work with the members of the C-BASS collaboration. At Oxford University, I would like to thank Angela Taylor, Mike Jones, Jamie Leech and Luke Jew who made me feel so welcome whenever I visited. Charles Copley, Oliver King, Matthew Stephenson, Justin Jonas and Tim Pearson who have all dedicated their time and expertise. I would especially like to thank Stephen Muchovej, without whom the last three and half years would have been so much harder and far less rewarding.

During my time at Manchester I have had the absolute pleasure of working with many excellent people. I would like to specifically mention Matias Vidal for his ability to find beauty and understanding in everything, Stefania Maccalli who is just completely lovely, Melanie Gendre for her support and humour, Peter Schemmel for his wit, Mareike Haberichter for making me laugh and making sure my work was up to standard (!). Also, Chris Wallis and David Cuadrado-Calle for both being so cheerful and positive that it lifts everyone around them, Mike Peel, Anna Bonaldi, Bob Watson and Joe Zuntz for their unlimited kindness and generosity with regards to their time and Mark Purver, Indy Leclercq, Cristobal Espinoza and Sotoris Sanidas for their reasonable and chilled out approaches to life. I have nothing but love for you all. Lastly, I want to thank the beautiful and vibrant city of Manchester, which has shared all my PhD experiences with me.

This thesis was typeset with LaTeX.

The Author

Melis Irfan did her undergraduate in Experimental Physics at the University of York, where she graduated in 2010 with a First Class masters. Her masters dissertation was on ‘Hot methane spectral lines for exoplanet and brown dwarf atmospheres’.

Supporting Publications

The C-Band All-Sky Survey (C-BASS): design and implementation of the northern receiver

King, O.G.; Jones, Michael E.; Blackhurst, E.J.; Copley, C.; Davis, R.J.; Dickinson, C.; Holler, C.M.; Irfan, M.O.; John, J.J.; Leahy, J.P.; Leech, J.; Muchovej, S.J.C.; Pearson, T.J.; Stevenson, M.A.; Taylor, Angela C. MNRAS (March 01, 2014), Vol. 438 p. 2426-2439

Separation of Diffuse Galactic Emission at 5 GHz using C-BASS

Irfan, M.O.; Dickinson, C.; Copley, C.; Davis, R.J.; Jones, Michael E.; King, O.G.; Leahy, J.P.; Leech, J.; Muchovej, S.J.C.; Pearson, T.J.; Stevenson, M.A.; Taylor, Angela C.; Zuntz, J. In Prep.

Several C-BASS papers, including the project description (Jones et al.), commissioning paper (Muchovej et al.), as well as an early analysis of the North Celestial Pole (Stevenson et al.) are forthcoming. I will be a co-author on these due to my contribution to commissioning, pipeline development, data analysis, and scientific interpretation of C-BASS data, which is presented in this thesis.

Chapter 1

Introduction

It is less than fifty years since the groundbreaking first detection of the radiation left over from the Big Bang (Penzias & Wilson 1965): the cosmic microwave background (CMB). Yet during this time four satellite missions have been launched, *RELIKT-1*, *COBE*, *WMAP* and *Planck* and the first measurement of the CMB temperature anisotropies has been made (Wright et al. 1992). These anisotropies have revealed many cosmological parameters including values for the curvature of space, the age of the Universe and the density of dark matter. What makes the CMB data such a rich source of information is the fact that the CMB anisotropies allow us to probe back to *before* the beginning of the electromagnetically visible Universe. Between cosmologists and the CMB, however, are the CMB foregrounds: diffuse and point source emissions that can only be disentangled from the primordial information using information obtained from experiments such as C-BASS.

1.1 The early Universe

The early Universe ($t \sim 3$ mins) was roughly 10 billion K and was entirely ionised so photons and baryons, in the form of atomic nuclei, were coupled together whilst electrons roamed free. At this point the Universe was opaque as the photons, although able to propagate within the baryonic plasma, were not free to traverse the Universe.

The baryons and dark matter would be gravitationally attracted towards each other and their coupled photons would be compelled to follow. However, the collision of matter would produce an opposing outward pressure experienced by both the baryons and the photons. The actions of these two rival forces on the Universe's primordial constituents led to acoustic oscillations, which can be seen in the CMB anisotropies.

As the Universe aged it cooled to around 3,000 K, which is no longer sufficiently high to support electron ionisation. The baryons captured their electrons to form hydrogen and helium atoms thus leaving the photons decoupled and free to propagate. This stage is known as 'recombination' and occurred when the Universe was around 380,000 years old. Recombination occurred at the last scattering surface (LSS); the last surface before decoupling, where photon and baryon scattering still occurred. These baryons carried the imprint of the acoustic oscillations through to the formation of galaxies that can be seen to cluster on scales of around 150 Mpc (Eisenstein et al. 2005). These mass oscillations are known as baryon acoustic oscillations (BAOs) and the 150 Mpc distance is the sound horizon at the time of recombination.

At this point it is worthwhile to abandon the concept of time elapsed or distance travelled for the cosmologically preferred measurement of redshift (z). Redshift is a specific result of the Doppler effect; it is an increase/decrease in the observed wavelength/ frequency. Redshift occurs when an observed source is moving away from its observer's rest frame with a velocity:

$$z = \frac{\lambda_{\text{observed}}}{\lambda_{\text{emitted}}} - 1. \tag{1.1}$$

So taking the Earth as $z = 0$, i.e any radiation emitted from Earth will undergo no notable wavelength/frequency change according to an observer on Earth, the last scattering surface (LSS) is at $z = 1091.3$ (Komatsu et al. 2011).

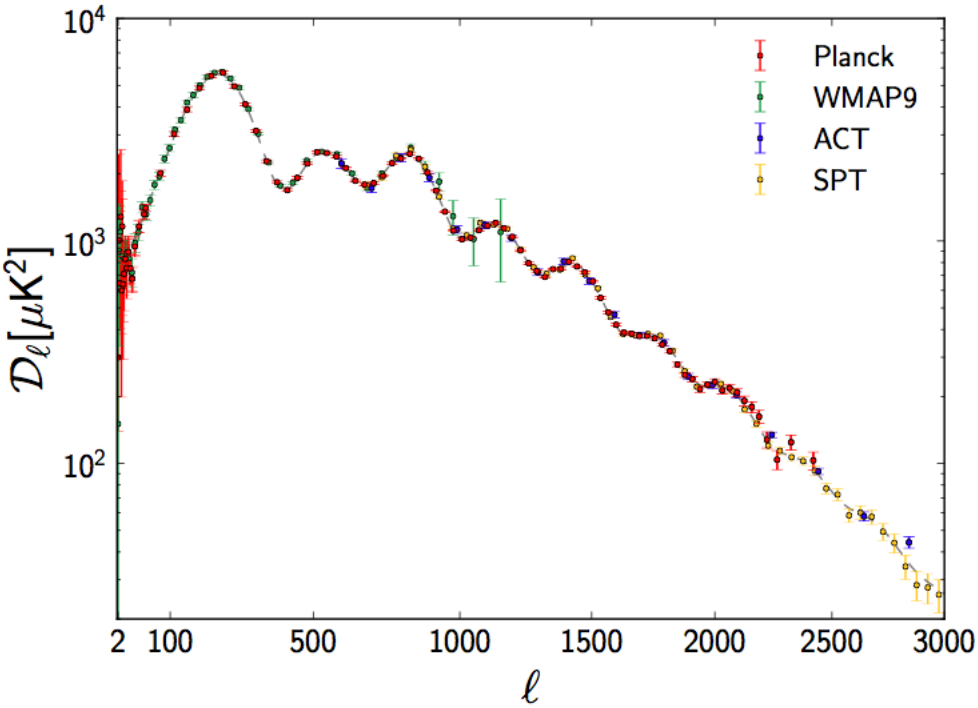

Figure 1.1: The CMB temperature angular power spectrum, with empirical data points obtained through two satellites (*WMAP* 9-year data and *Planck*) and two ground-based experiments (SPT and ACT). The black dotted line represents the best fit to the ΛCDM cosmological model. Image taken from Planck Collaboration et al. (2013c).

1.2 CMB experiments

The CMB is one of the main cosmological probes available to astrophysicists. Throughout this introduction empirical data taken from various CMB experiments will be shown. Table 1.2 introduces these CMB experiments alongside their main parameters.

1.3 The Angular Power Spectrum

The acoustic oscillations can be seen as peaks in the CMB angular power spectrum representing small temperature differences, over degree scales, known as CMB anisotropies. Figure 1.1 displays the CMB angular power spectrum, which is the power fluctuations

Name	ν	**Type**	**Lifetime**	**Reference**
ACBAR	150, 220, 280, 350 GHz	Ground	2002 – 2009	Runyan et al. (2003)
ACT	148, 218, 277 GHz	Ground	2007 – present	Hincks et al. (2010)
BICEP	100, 150 GHz	Ground	2005 – present	Keating et al. (2003)
BOOMERanG	90, 150, 240, 400 GHz	Balloon	1997– 2003	Lange et al. (2001)
CAPMAP	40, 90 GHz	Ground	2003 – 2005	Barkats et al. (2005)
CBI	26 – 36 GHz in 10 bands	Ground	1999 – 2008	Padin et al. (2002)
COBE-DIRBE	1.25, 2.2, 3.5, 4.9, 12, 25, 60, 100, 140, 240 μm	Satellite	1989 – 1992	Mather (1982)
DASI	26 – 36 GHz in 10 bands	Ground	1999 – 2003	Halverson et al. (2002)
EBEX	150, 250 and 410 GHz	Balloon	2010 – present	Reichborn-Kjennerud et al. (2010)
LSPE	95, 145 and 245 GHz	Balloon	2012 – present	The LSPE collaboration et al. (2012)
MAXIPOL	140, 420 GHz	Balloon	2002 – 2003	Richards et al. (2002)
Planck	30, 44, 70, 100, 143, 217, 353, 545, 857 GHz	Satellite	2009 – 2013	Planck Collaboration et al. (2013b)
POLARBEAR	150 and 220 GHz	Ground	2012 – present	Kermish et al. (2012)
QUaD	100, 150 GHz	Ground	2004 – 2008	Bowden et al. (2004)
QUIET	43, 95 GHz	Ground	2008 – 2012	QUIET Collaboration et al. (2011)
SPT	100, 150, 230 GHz	Ground	2010 – present	Ruhl et al. (2004)
VSA	26 – 36 GHz	Ground	2000 – 2008	Dickinson et al. (2004)
WMAP	23, 33, 41, 61, 94 GHz	Satellite	2001 – 2012	Bennett et al. (2013)

Table 1.1: Various CMB experiments and their parameters.

over angular scales. Here, the temperature anisotropies across the sky are expressed using spherical harmonics. The multipoles are constructed as follows:

$$\frac{\Delta T}{\mu K}(\theta, \phi) = \sum_{\ell=1}^{\infty} \sum_{m=-\ell}^{\ell} a_{\ell,m} \; Y_{\ell,m}(\theta, \phi), \tag{1.2}$$

where ℓ and m represent the anisotropy angular wavenumber. ℓ, which represents the angular scale on the sky, determines the multipole produced. The relation between ℓ and angular scale is as follows:

$$\ell \approx \frac{180}{\theta^{\circ}}. \tag{1.3}$$

The monopole, a_{00}, is the CMB mean temperature 2.72548 ± 0.00057 K (Fixsen 2009). The largest anisotropy, the dipole (a_{1-1}, a_{10} and a_{11}) has a magnitude of 3.372 mK and is due to an overall Doppler shift of the CMB photons caused by the motion of Earth as viewed from the CMB rest frame. The first peak visible in Figure 1.1 is the first acoustic peak at $\ell \sim 200$ ($\sim 0.9°$ angular scale) with the subsequent peaks showing the 2$^{\mathrm{nd}}$, 3$^{\mathrm{rd}}$ etc. harmonics.

The multipole complex amplitudes are expressed as $a_{\ell,m}$ and their normalised spherical harmonics are represented by $Y_{\ell,m}$. The CMB anisotropies are believed to be Gaussian in nature and so their angular power spectrum can be described by the variances of the multipole amplitudes (Tegmark 1995):

$$\frac{C_{\ell}}{\mu K^2} = \frac{1}{2l+1} \sum_{m=-\ell}^{\ell} |a_{\ell,m}|^2. \tag{1.4}$$

As m can take any value between $-\ell$ and ℓ there are $(2\ell+1)$ values of $a_{\ell,m}$ for each ℓ. It is actually more common to see the mean square fluctuations of C_{ℓ} plotted, as in Figure 1.1 :

$$D_{\ell} = \text{mean square fluctuations at } \ell = \frac{\ell\,(\ell+1)\,C_{\ell}}{2\,\pi}. \tag{1.5}$$

It is clear that an entirely homogenous and isotropic Universe would not lead to the formation of the large-scale structures (e.g galaxy clusters) that are in evidence. The CMB temperature anisotropies are indicative of some form of initial perturbations. The question as to what seeded these initial perturbations is a hotly debated topic which currently revolves around a selection of theories under the term ‘inflation’.

1.4 Inflation

The inflationary period is a purely theoretical framework designed to explain how structure was formed in the Universe. There are many different models of inflation, however, all inflation theories must agree on the production of near Gaussian, near scale-invariant CMB anisotropies whilst simultaneously explaining the formation of structure in the Universe.

Inflation describes a period of rapid expansion undertaken by the Universe between the age of 10^{-35} s and 10^{-32} s in which it expanded by a factor of $\sim 10^{26}$. Inflation is one of the few circumstances where a theory rooted in both General Relativity and Quantum Mechanics produces a measurable observable (Martin, Vennin & Peter 2012). The 'smoking gun' for inflation is primordial gravitational waves. Primordial gravitational waves, a phenomenon predicted by General Relativity, would be produced and magnified within the inflationary period. Detecting primordial gravitational waves is the Holy Grail of current CMB cosmology (Baumann et al. 2009).

1.5 CMB polarisation

Mathematical analysis, including the effect of Thomson scattering (Silk 1967), of the inhomogeneities within the CMB were being conducted as early as the sixties. However, it was not until 2002 that the first CMB polarisation detection was made (Kovac et al. 2002), confirming such scattering and measuring its effect.

Thomson scattering of the CMB resulting in polarisation could only have occurred after the decoupling of baryons from photons and before the end of recombination. CMB radiation would scatter off of the primordial free electrons and if two waves of incident radiation were perpendicular and at different temperatures the resultant scattered wave would be linearly polarised. These particular initial conditions are known as a quadrupole anisotropy and are shown in Figure 1.2.

There are three different scenarios which could cause the temperature anisotropies

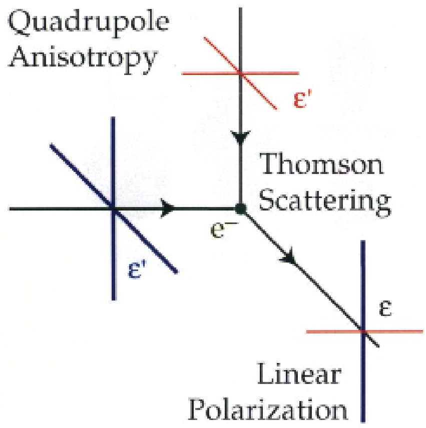

Figure 1.2: Pictorial representation of the CMB quadrupole resulting in linear polarisation (Hu & Dodelson 2002).

required for the quadrupole: scalar perturbations, vector perturbations and tensor perturbations. All three of these perturbations can trace the roots of their existence to the pre-inflation Universe. Scalar perturbations describe density fluctuations in the primordial plasma. Pre-existing temperature anisotropies within the fabric of space result in hot and cold plasma regions, as the hotter regions have higher energy there is a net particle flow which results in denser and colder regions. Vector perturbations result from plasma fluid vortices but are considered negligible in the wake of inflation, due to damping (Kaplan 2003). Lastly, there are tensor perturbations which are caused by gravitational waves and cosmic strings. These perturbations are magnified by inflation and can stretch and/or compress space, thus red and/or blue shifting the CMB photons which eventually traverse said space, which alters their energy/temperature.

The CMB polarisations, first observed by DASI (Kovac et al. 2002), and then by its successors, are perpendicular or parallel with respect to the pre-scattering propagation direction and are known as 'E-mode' polarisations. Intensity and linear polarisations can be determined via combinations of the left and right circular polarisations (E_L and E_R) and are described by a set of parameters known as Stokes parameters: I, Q, U and

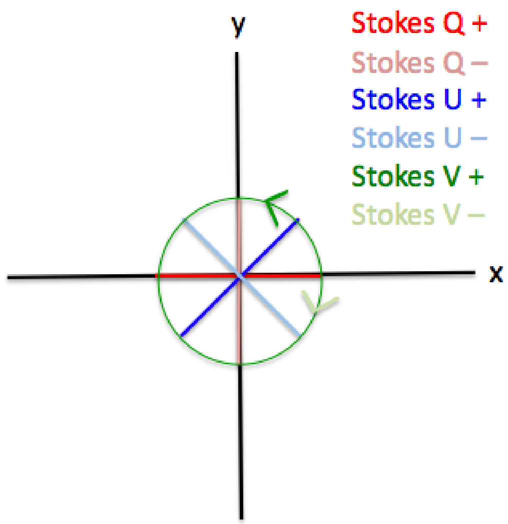

Figure 1.3: The Stokes polarisation parameters in Cartesian co-ordinates.

V defined as

$$\begin{aligned} \mathrm{I} &= E_R^2 + E_L^2, \\ \mathrm{Q} &= 2\ E_R\ E_L \cos\delta_{RL}, \\ \mathrm{U} &= 2\ E_R\ E_L \sin\delta_{RL}, \\ \mathrm{V} &= E_R^2 - E_L^2, \end{aligned} \tag{1.6}$$

where δ_{RL} is the phase difference between the right and left circular polarisations, I is the total intensity parameter, Q and U represent linear polarisations and V is circular polarisation. The polarisation parameter orientations are shown in Figure 1.3. E-modes are caused by scalar perturbations while tensor perturbations are predicted to result in a different variety of polarisation known as 'B-modes'. Both E and B-mode polarisations can be formed from Stokes Q and U measurements of the CMB.

Figure 1.4 shows the polarisation pattern of both E and B-modes, it can be seen that E-mode polarisations are all aligned perpendicular or parallel to the perturbation wave vector while B-modes are aligned at 45°.

When considering the polarisation of the CMB it is worthwhile to introduce the idea of cross-correlation power spectra. TT, TE, EE and BB each refer to a cross-

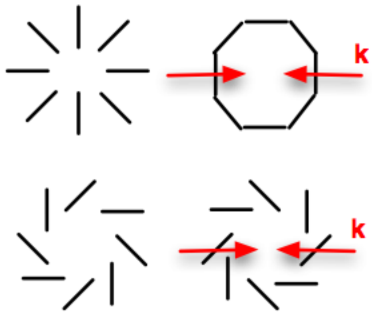

Figure 1.4: **Upper row:** Negative E-mode polarisation pattern on the left, positive E-mode on the right. **Lower row:** Negative B-mode polarisation pattern on the left, positive B-mode on the right. The red arrows represent the perturbation wave vector at that point (Bartlett 2006).

correlation angular power spectrum:

$$C_{TT,\ell} = \frac{1}{2\,\ell+1} \sum_{m} \langle a^{*}_{T,\ell m}\, a_{T,\ell m} \rangle, \tag{1.7}$$

$$C_{TE,\ell} = \frac{1}{2\,\ell+1} \sum_{m} \langle a^{*}_{T,\ell m}\, a_{E,\ell m} \rangle, \tag{1.8}$$

$$C_{EE,\ell} = \frac{1}{2\,\ell+1} \sum_{m} \langle a^{*}_{E,\ell m}\, a_{E,\ell m} \rangle, \tag{1.9}$$

$$C_{BB,\ell} = \frac{1}{2\,\ell+1} \sum_{m} \langle a^{*}_{B,\ell m}\, a_{B,\ell m} \rangle. \tag{1.10}$$

The cross correlation between temperature and B-mode polarisation ($C_{TB,\ell}$) and E and B-mode polarisation ($C_{EB,\ell}$) amount to zero because of the opposing parity between B-modes and E-modes/temperature (Zaldarriaga & Seljak 1997). The TT power spectra is already shown in Figure 1.1, while Figure 1.5 shows the EE and BB power spectra. As B-modes have yet to be detected the observed upper limits on their detection are shown. The lower panel of Figure 1.5 shows the predicted BB power spectrum, which is made from primordial gravitational waves and E-modes gravitationally lensed to appear as B-modes. Given the contamination from lensed E-modes it is clear that the best chance of primordial wave detection is at angular scales of a degree or higher. A

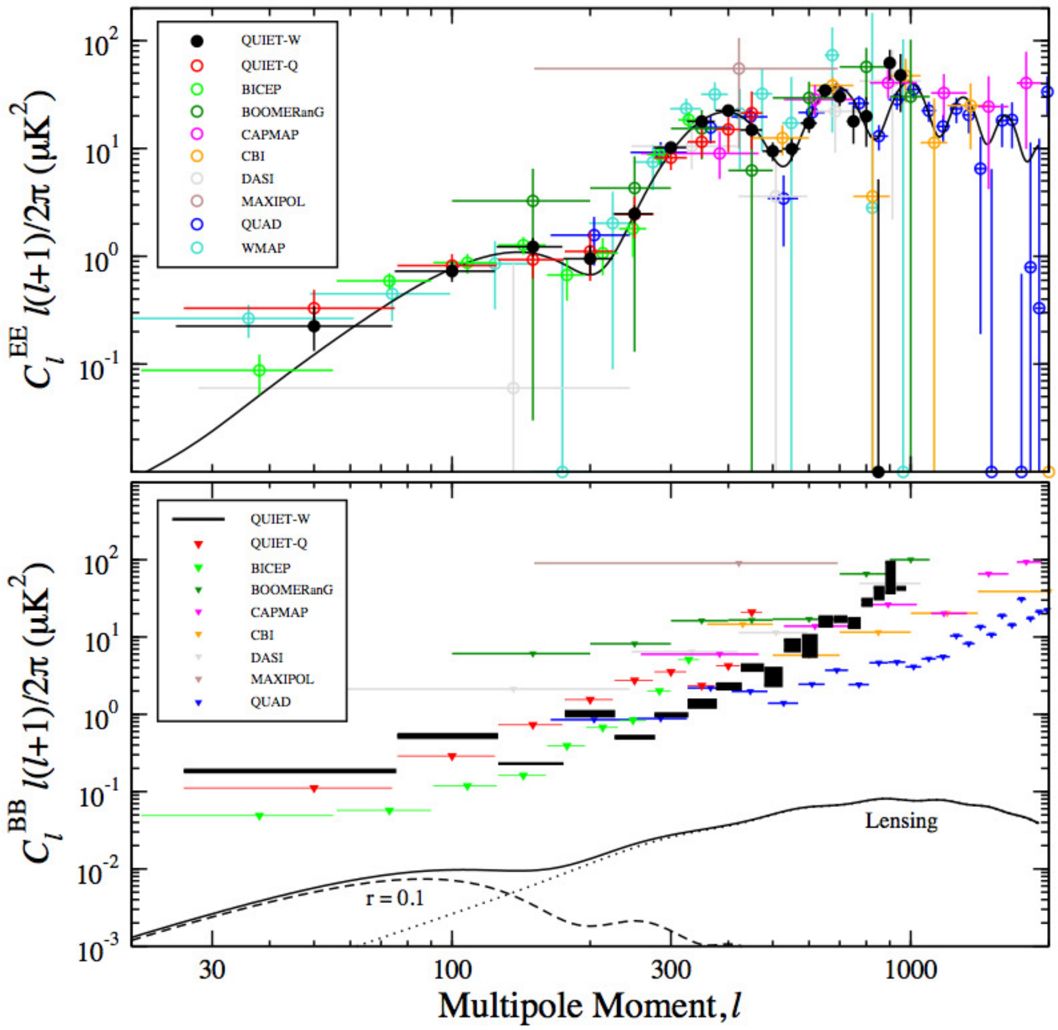

Figure 1.5: The empirical EE and BB power spectra (data points from various experiments listed in legend) alongside the ΛCDM predicted spectra (black line). The predicted BB curve is made from primordial gravitational waves and lensed E-modes which are dominant at high multipoles (QUIET Collaboration et al. 2012).

successful detection will require the accurate removal of foregrounds at large angular scales and the C-BASS maps, at FWHM $\sim 1°$, will provide the necessary large scale, 5 GHz foreground information.

B-modes were caused by tensor perturbations in the CMB which in turn result from one, or a combination of all three possible mechanisms: primordial gravitational waves from the inflationary period, perturbations within cosmic string networks and E-mode lensing by large scale structures.

Primordial gravitational waves are thought to have arisen from vacuum fluctuations during the inflationary period. These gravitational waves would expand and compress the very fabric of space, hence the wavelength of the CMB radiation. The detection of primordial gravitational waves would therefore provide the *first* piece of direct evidence of the inflationary period. Measurement of B-modes would tell cosmologists about the energy scale of the inflationary period and therefore, rule out some of the less plausible ideas from the plethora of inflationary models.

The B-mode detection level is quantified by the tensor to scalar ratio (r):

$$r(k) = \frac{P_T(k)}{P_{\mathfrak{R}}(k)}, \tag{1.11}$$

where P_T and $P_{\mathfrak{R}}$ are the tensor and scalar power spectrum of the primordial perturbations at wavenumber k respectively. Observational data can set upper limits on the tensor contributions (Figure 1.5). Within the last few days before the submission of this thesis the BICEP team announced a 5.9σ detection of B-modes from gravitational waves at $r \approx 0.20$. This groundbreaking discovery is currently being investigating, with regards to the polarised foreground subtraction and lensed E-mode contamination by the rest of the cosmological community (BICEP2 Collaboration et al. 2014).

1.6 CMB foregrounds

Up to this point, only the pure CMB signal has been considered but any measurement of the CMB, temperature or polarisation, will contain 'foreground' emissions. Here, the term foreground simply refers to any electromagnetic radiation that is present between the observer and the CMB.

Figure 1.6 shows the CMB TT angular power spectrum with and without the foreground contributions over-plotted onto SPT and *WMAP* data. It highlights how a failure to take the CMB foregrounds into account results in mis-calculation of the CMB

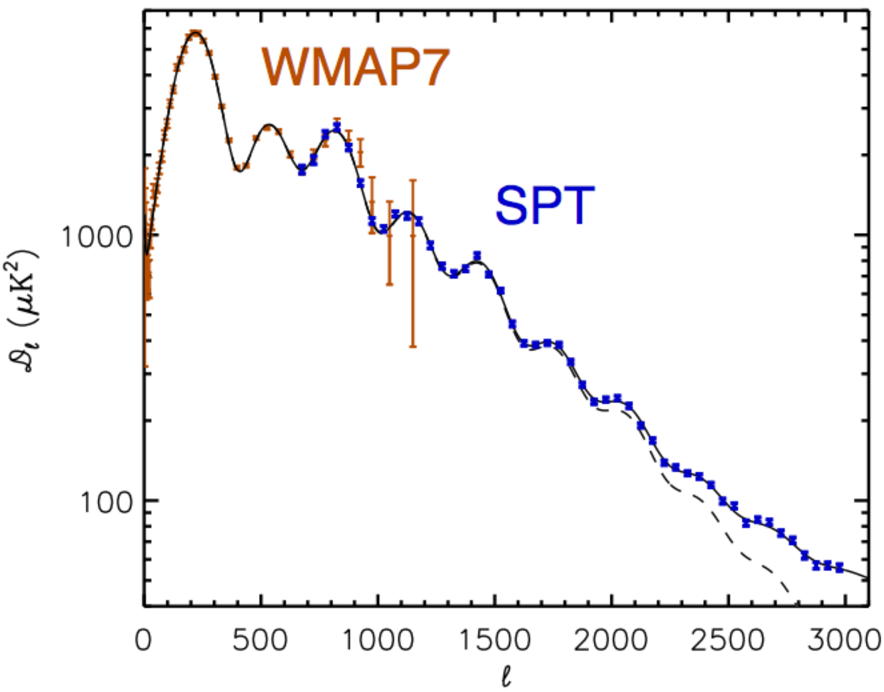

Figure 1.6: The TT power spectrum with *WMAP* and SPT data alongside the ΛCDM predictions. The ΛCDM model for pure CMB is indicated with a black dashed line while the model which takes into account CMB + foregrounds is shown with a solid black line (Story et al. 2013).

anisotropy power spectrum on small angular scales. For the 150 GHz SPT data plotted in Figure 1.6 the greatest foreground contribution at angular scales $\lesssim 10'$ is the extra-Galactic point sources. C-BASS will measure foregrounds at low ℓs and so will instead probe large-scale foregrounds, such as synchrotron emission. Figure 1.7 illustrates the effect of polarised foregrounds with regards to B-mode detection on the full sky. The figure shows the TT (black points and line), TE (red points and line), EE (green points and line) and predicted BB (blue dotted line), assuming $r = 0.3$, power spectra. The polarised foreground contribution (synchrotron and thermal dust emission) to the full sky BB power spectrum is shown with a straight blue dashed line and can be seen to surpass the B-mode detection level. Understanding and being able to separate polarised foreground emission from the CMB anisotropies is clearly an important aspect

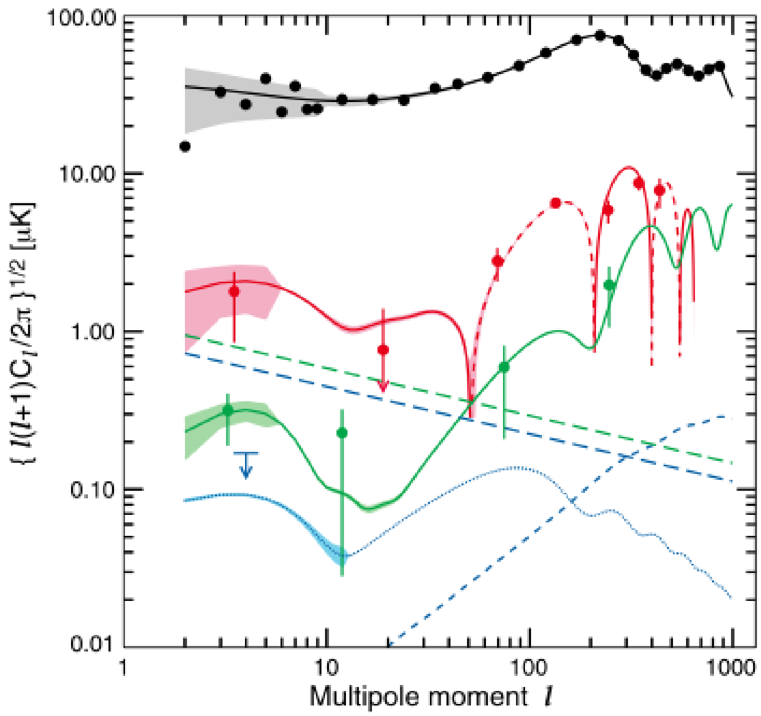

Figure 1.7: The TT (black points and line), TE (red points and line), EE (green points and line) and predicted BB (blue dotted line), assuming $r = 0.3$, power spectra. The filled circles represent measured data while the solid lines are the best fit lines. The blue dashed line indicates the lensed E-mode signal and the straight blue/green dashed line shows the polarised synchrotron plus thermal dust foregrounds for the BB/EE spectrum (Page et al. 2007).

of B-mode detection.

CMB foregrounds are either from Galactic or extra-Galactic sources and can be described as either diffuse or point like; their removal is pivotal to the accurate measurement of the CMB. CMB foregrounds can be differentiated from one another through their differing spectral and spatial dependancies. Figure 1.8 shows model spectra for the different diffuse foreground emissions.

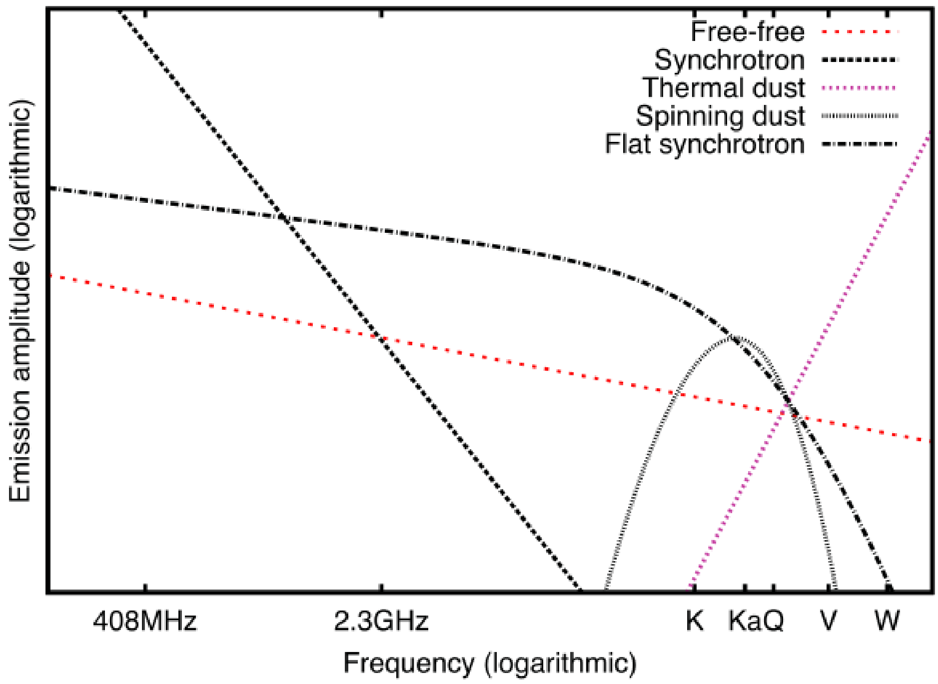

Figure 1.8: Model spectra for the various foreground emissions. Image from Peel et al. (2012).

1.6.1 Ancillary Data

An overview of a selection of full-sky CMB foreground data, which are either used directly in this thesis or referred to in Section 1.7 is given in Table 1.2. The columns detail the observatories where the work was carried out, the central frequency of operation, the full width half maximum (FWHM) instrument resolution, the uncertainties associated with their calibration scheme, the r.m.s noise level in intensity, inclusion of polarisation data and the project paper reference.

The Haslam et al. (1982) data are available in two forms, the original unfiltered map or a destriped and point source removed map. This thesis uses the unfiltered map as the C-BASS map has also yet to have point sources removed. Therefore, the stripes in the Haslam et al. (1982) data caused by correlated $1/f$ noise, either due to receiver systematics or the weather, remain within the maps. Each survey has its own zero-level that comes from the cumulative temperature contributions of the CMB, extragalactic

Observatory	**ν (GHz)**	**FWHM (′)**	**Calib. (%)**	**σ_I(mK)**	**Pol.**	**Reference**
Effelsberg, Parkes, Jodrell	0.408	51	10	700	✗	Haslam et al. (1982)
Effelsberg, Parkes	1.420	35	5	140	✗	Reich & Reich (1986)
WMAP	22.5	49	0.2	1.429	✓	Bennett et al. (2013)
	33	40	0.2	1.466	✓	
	41	31	0.2	2.188	✓	
	61	21	0.2	3.131	✓	
	94	13	0.2	6.544	✓	
Planck LFI	28.4	32.7	1	0.143	✓	Planck Collaboration et al. (2013b)
	44.1	27.9	1	0.164	✓	
	70.4	13.0	1	0.134	✓	
Planck HFI	100	9.4	2	0.017	✓	
	143	7.0	2	0.008	✓	
	217	4.7	2	0.007	✓	
	353	4.4	2	0.006	✓	
	545	3.8	10	0.005	✓	
	857	3.7	10	0.002	✓	

Table 1.2: A selection of existing full-sky foregrounds ancillary data shown alongside their survey parameters.

sources, atmospheric noise, ground radiation and the receiver system temperature. In the case of the Haslam et al. (1982) data, the $1/f$ noise causes the zero-level to vary significantly in a manner which is correlated with the scanning strategy. Haslam et al. (1982) state that the baseline uncertainties, which result in roughly vertical stripes throughout the map, are around 3 K. The Reich & Reich (1986) data, at 1.420 GHz also have a zero-level uncertainty but at a lower magnitude of 0.5 K.

The Jonas, Baart & Nicolson (1998) HartROA data at 2.3 GHz, although not full-sky ($-88^\circ < \delta < +13^\circ$), are of use for the Galactic plane work detailed in Chapter 6. This intensity map is of $20'$ FWHM and has a 5 % calibration uncertainty and a thermal noise level of 25 mK. The equivalent 2.3 GHz polarised intensity survey was conducted using the Parkes telescope and used to investigate the loops of synchrotron emission associated with supernovae activity (Carretti et al. 2013).

It is worth mentioning that in addition to the completed and available full-sky data detailed in Table 1.2 there are two other 5 GHz surveys, one of which is incomplete, the other only has partial sky coverage. The Sino-German Galactic plane survey has mapped the $10^\circ < l < 230^\circ, |b| < 5^\circ$ region of the plane in both intensity and polarisation at a central frequency of 4.8 GHz. The Urumqi 25 m telescope, which has a resolution of $9\overset{'}{.}5$ was used to produce maps in Stokes I with a thermal noise level of 1.4 mK and in Stokes Q and U with thermal noise levels of 0.5 mK. The calibration in both intensity and polarisation is good to less than 5 %.

The Galactic Emission Mapping (GEM) project is ongoing and operating at 0.408, 1.465, 2.3 and 5.0 GHz at several locations as the receiver is mobile. Several hundred observing hours have already taken place at 0.408, 1.465, 2.3 and 5.0 GHz in Colombia and California and the final all-sky maps will have a FWHM resolution of $\sim 10^\circ$ (Tello et al. 2013).

1.7 Diffuse Galactic Emissions

1.7.1 Synchrotron emission

Synchrotron emission dominates the diffuse Galactic emission at frequencies up to a few GHz (Lawson et al. 1987). The relativistic particles responsible for synchrotron emission have two possible sources: supernova remnants (SNR) and cosmic rays. In the SNR case, relativistic electrons get deflected around the magnetic field lines within the remnant and suffer energy loss in the form of synchrotron radiation. In the cosmic ray case a similar process occurs except, the relativistic electrons are deflected around the magnetic field lines of the interstellar medium.

The synchrotron temperature spectral index varies spatially across the sky, Reich & Reich (1988) document a spectral index range of -3.0 to -2.3 across the sky between 0.408 and 1.420 GHz. The spectral shape is seen to steepen the further the measurements are from the Galactic plane (Dunkley et al. 2009). This is due to the energy loss suffered by the synchrotron electrons as they propagate through the Galaxy. One of the strongest areas of synchrotron emission is the North Polar Spur, which is a region of hot electron winds from nascent stars and SNRs. Figure 1.9 shows the spatial variation of the synchrotron spectral index for the 0.408 to 23 GHz frequency range alongside the *WMAP* map of main Galactic features.

The synchrotron emission intensity depends on the power law energy distribution of the relativistic electrons:

$$N(E) \propto E^{-\delta}, \tag{1.12}$$

therefore the synchrotron intensity spectrum also takes a power law form:

$$T(\nu) = T(\nu_0)\left(\frac{\nu}{\nu_0}\right)^{\beta_S}, \tag{1.13}$$

where

$$\beta_S = -\frac{\delta + 3}{2}. \tag{1.14}$$

A typical value for δ is between 2.3 and 3 (Abdo et al. 2009).

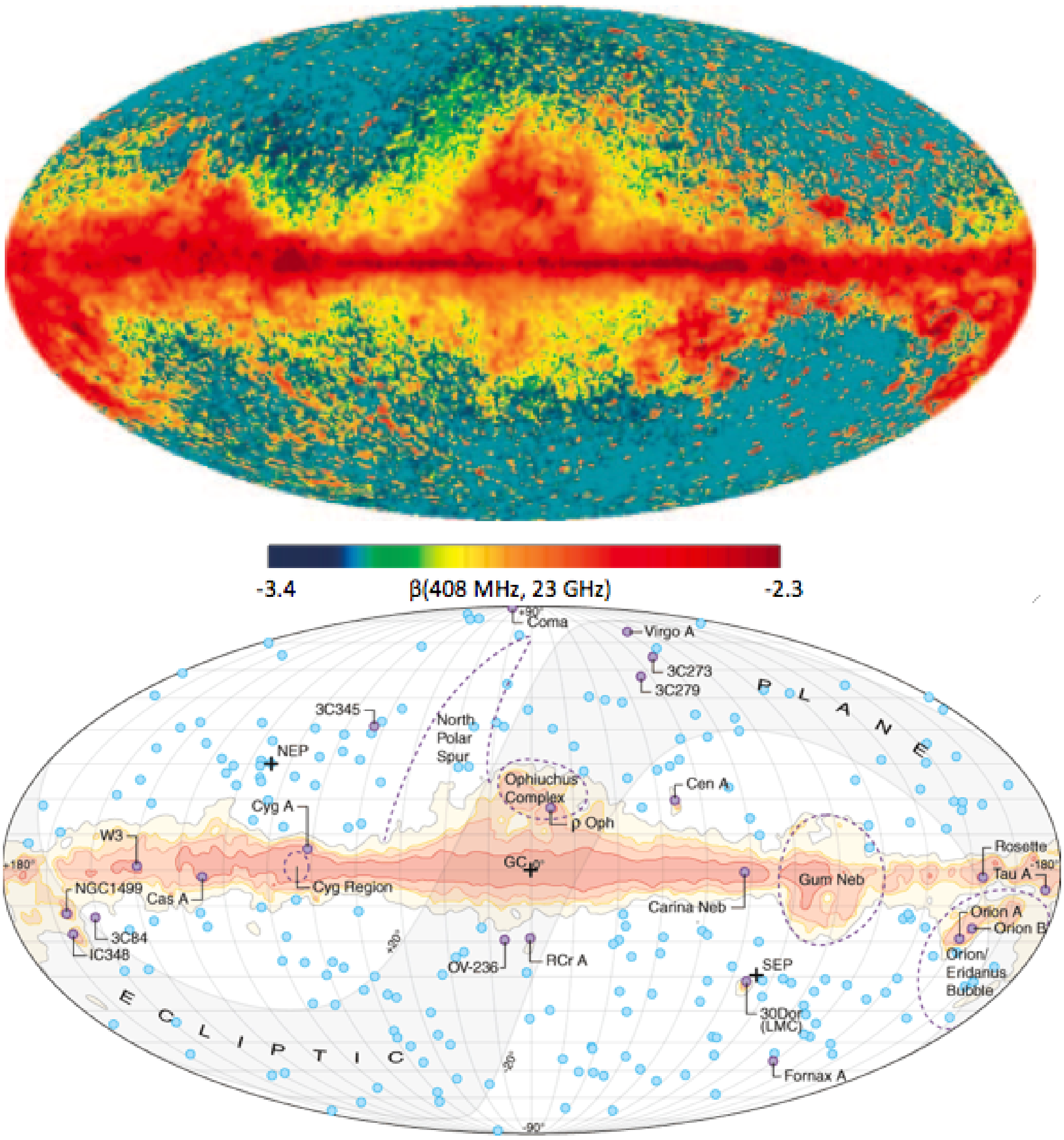

Figure 1.9: **Top:** The variation of the synchrotron spectral index across the sky as seen between 0.408 and 23 GHz (Bennett et al. 2003b). **Bottom:** The main features within the Galaxy (Bennett et al. 2003a).

Synchrotron emission is also polarised, up to around 75 %, although in reality only around 40 % polarisation is measured. This depolarisation occurs because the emission is measured and integrated over several lines of sight. Depolarisation is a frequency independent effect unlike Faraday rotation. Faraday rotation is the rotation of an electromagnetic wave's polarisation angle as the wave propagates through the magnetic field of a plasma.

$$\chi = \frac{\mathrm{RM}}{\mathrm{m}^{-2}}\left(\frac{\lambda}{\mathrm{m}}\right)^2 + \chi_0 \tag{1.15}$$

and

$$\frac{\mathrm{RM}}{\mathrm{m}^{-2}} = \frac{q_e^3(8\pi^2)^{-1}\epsilon_0^{-1}m^{-2}c^{-3}}{\mathrm{T}^{-1}}\int_{\mathrm{obs}}^{\mathrm{source}} \frac{n_e}{\mathrm{m}^{-3}}\frac{B}{\mathrm{T}}\frac{dr}{\mathrm{m}}, \tag{1.16}$$

where χ represents the measured polarisation angle, χ_0 is the intrinsic, unrotated, polarisation angle, λ is the wavelength, q_e, m and n_e are the electron charge, mass and thermal density,ϵ_0 is the permittivity of free space, c is the speed of light, B is the magnetic field, as measured along the line of sight, and r represents the distance between the observer and the source (Haverkorn, Katgert & de Bruyn 2004).

Synchrotron emission is not well modelled over a large range of frequencies by a power law with a single spectral index. This can be seen in Figure 1.10 (de Oliveira-Costa et al. 2008) which shows the eleven empirical data points available for the $(l, b) = (11.^\circ3, 89.^\circ6)$ point in Galactic longitude (l) and latitude (b). These points cannot be satisfactorily fit by a power law scaling of the Haslam et al. (1982) all-sky map which, at 0.408 GHz, is a predominantly synchrotron dominated map at high/low galactic latitudes.

The best fit to the data within Figure 1.9 is the PCA fit which contains frequency dependent parameters. This reenforces the theory that if the power law model is accurate then the synchrotron data is best fit within two distinct spectral index regimes, a flat/hard regime ($\beta \sim -2.5$) at ~ 22 MHz which eventually steepens/softens ($\beta \sim -3.0$) at frequencies over 23 GHz (Kogut 2012). Between 0.408 GHz and 3.8 GHz an index of ~ -2.7 is expected within the Galactic plane whereas between 1.42 and 7.5 GHz the spectrum appears to steepen to ~ -3.0 (Platania et al. 1998). This prediction is

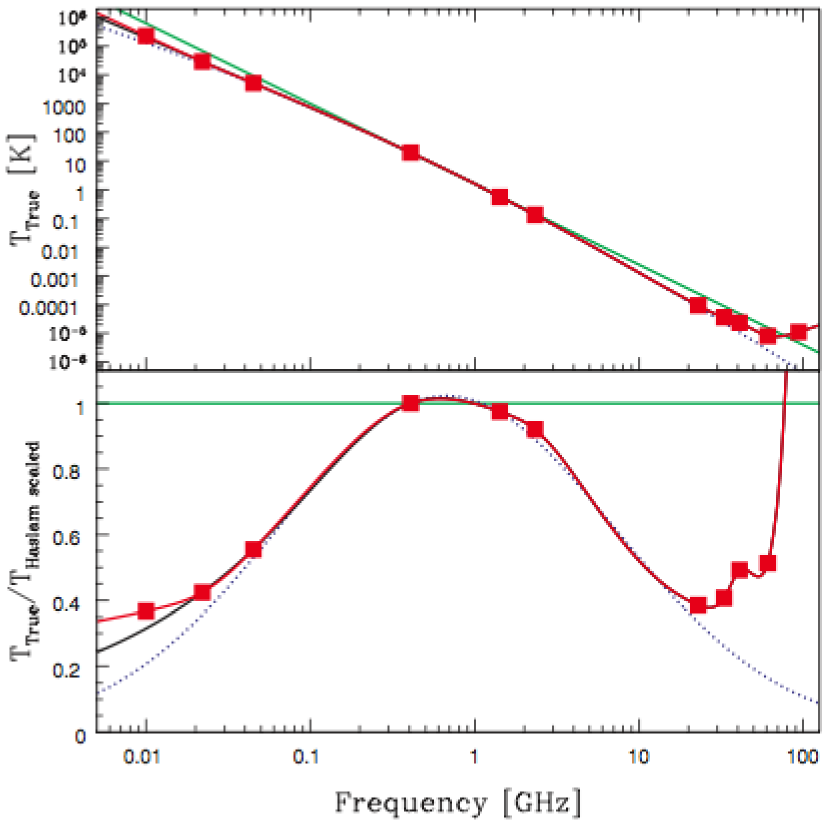

Figure 1.10: An SED for the point $(l, b) = (11^\circ.3, 89^\circ.6)$. Red squares represent empirical measurements, while the solid green line represents the Haslam et al. (1982) measurement for that point, scaled to the correct frequencies, assuming a power law with a spectral index of −2.8. The solid black line is a cubic spline fit, the dotted blue line is a quadratic polynomial fit and the red solid line is a principal component analysis (PCA) fit. The data and curves in the bottom panel have all been divided by the green curve to highlight the differences between the models and the data (de Oliveira-Costa et al. 2008).

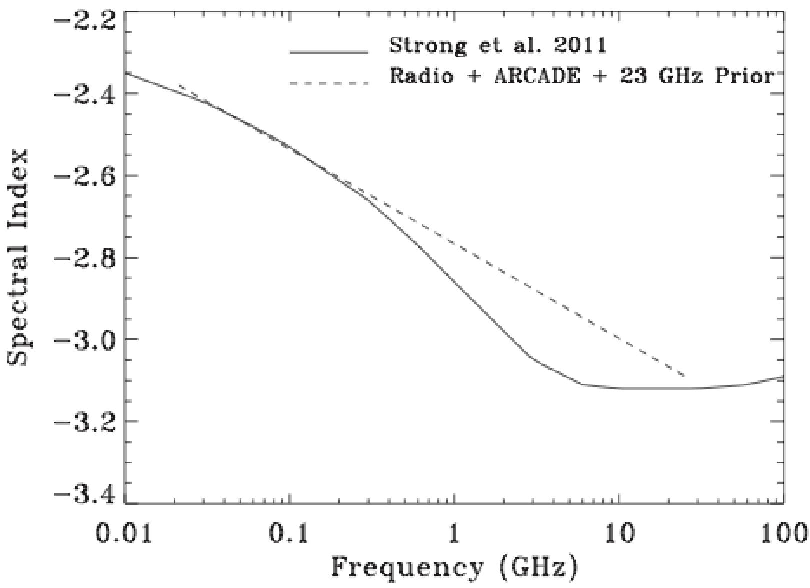

Figure 1.11: The synchrotron spectral index as a function of frequency as predicted by a radio data model (dashed line) and a radio + cosmic ray data model (solid line) (Kogut 2012).

corroborated by the 0.038/0.178 GHz measurements of Lawson et al. (1987) where $-2.6 < \beta < -2.3$ and the 0.408/22.5 GHz measurements of Bennett et al. (2003b) where $-3.1 < \beta < -3.0$.

Identifying the turn-over frequency between the flat and the steep synchrotron regimes is a task which would benefit from C-BASS data. Figure 1.11 shows the synchrotron spectral index as a function of frequency between 0.01 and 100 GHz as presented by Strong, Orlando & Jaffe (2011) and Kogut (2012). The Strong, Orlando & Jaffe (2011) model uses radio emission, cosmic ray data and the GALPROP magnetic field intensity code while the Kogut (2012) model just uses radio emission data. The cosmic ray model predicts a turn-over frequency of around few GHz yet this is not seen within the radio emission data. However, there is currently a complete absence of all-sky surveys within the 3 to 10 GHz range; this is a void C-BASS will fill.

Flat spectral index synchrotron emission is a leading contender for the astrophysical explanation of the enigmatic Galactic haze. The Galactic haze is an excess of

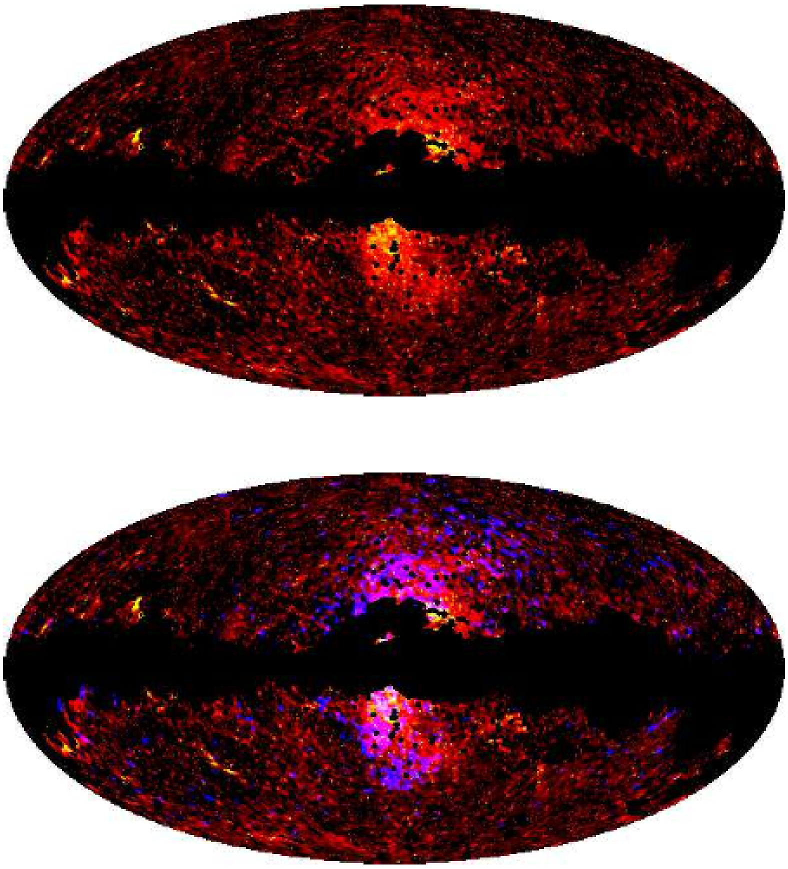

Figure 1.12: **Top:** The haze as seen by *Planck* at 30 GHz (red data) and 44 GHz (yellow data). **Bottom:** The above map but with the gamma ray counterpart overlaid (Planck Collaboration et al. 2012).

foreground emission sharing a morphological centre with the Galaxy and extending spherically by $\sim 30°$ (Finkbeiner 2004; Pietrobon et al. 2012). The haze emission has a spectral index of ~ -2.5 which accommodates the theories of hard synchrotron emission. The detection of the haze gamma ray counterpart, inverse Compton scattered stellar and CMB photons off of haze electrons, is responsible for the popularity of the hard synchrotron model (Dobler et al. 2010). Figure 1.12 shows the haze as seen by *Planck* at 30 and 44 GHz with the *Fermi* gamma ray data overlaid; all other foregrounds have been removed using ancillary data as emission templates (Planck Collaboration et al. 2012).

If the haze is synchrotron in nature then it should be detectable not only in intensity but also in polarisation. However, no such detection has been made in polarisation. It is argued that the quality of radio data collected so far is still too noisy to allow for such a detection (Dobler 2012). The C-BASS maps will cover the haze region in polarised intensity at a frequency over which flat synchrotron radiation dominates and is brighter than the instrument noise. This will provide one of the best chances to date to measure haze polarisation at an intensity strong enough to surpass the noise floor of the instrument.

1.7.2 Free-Free emission

Free-free, or Bremsstrahlung, emission results from electron-ion collisions within the hydrogen plasma of the Warm Ionised Medium (WIM). Free-free emission is unpolarised and characterised by a spectral index of $\beta \approx -2.1$. This spectral index steepens slightly at higher frequencies (to $\beta \approx -2.15$) because of the Gaunt factor ($g_{\rm ff}$):

$$T_{\rm ff} = T_e \, (1 - e^{-\tau_{\rm ff}}), \tag{1.17}$$

where

$$\tau_{\rm ff} = 3.014 \times 10^{-2} \left(\frac{T_e}{\rm K}\right)^{-1.5} \left(\frac{\nu}{\rm GHz}\right)^{-2} \left(\frac{EM}{\rm pc\ cm^{-6}}\right) g_{\rm ff} \tag{1.18}$$

and

$$g_{\rm ff} \approx \ln\left(e^{5.960-(\sqrt{3}/\pi)\ln\left(Z_i \nu_9 T_4^{3/2}\right)} + e\right), \tag{1.19}$$

and

$$\frac{EM}{\rm pc\ cm^{-6}} = \int \left(\frac{n_e}{\rm cm^{-3}}\right)^2 \frac{dl}{\rm pc}, \tag{1.20}$$

where the ion charge (Z_i) is 1, ν_9 is the frequency in GHz; T_4 is the temperature in 10,000 K; e is the natural logarithm base; n_e is the electron density and dl is the integral alongside the line of sight. The Gaunt factor is required to take into account the quantum mechanical contributions of the electrons involved in Bremmsstrahlung. A typical value for the electron temperature (T_e) is 7,000 K (Draine 2011).

The warm ($\sim 10^4$ K) hydrogen plasma, which makes up around 90 % of the WIM and is responsible for free-free emission is also responsible for the Hα 656.281 nm spectral line. This optical signal is emitted when a hydrogen ion and an electron recombine and the once free electron makes the transition from $n = 3$ to $n = 2$.

The Hα emission intensity ($I_{H\alpha}$) is dependent on the Lyman continuum optical depth. The brightness temperature (T_b) measured for a source at temperature T is related to the opacity (τ) of the medium as follows:

$$T_b = T(1 - e^{-\tau}). \tag{1.21}$$

If the medium is optically thick, $\tau \gg 1$ then $T_b = T$, however if the medium is optically thin, $\tau \ll 1$, then $T_b = \tau\ T$ (Rohlfs & Wilson 2004). The WIM is generally believed to be optically thick to Lyman alpha transitions because the competing processes of recombination and ionisation mean that the Lyman alpha photons are not free to propagate. Within an optically thick medium the Hα emission intensity is given as:

$$\frac{I_\alpha}{\text{ergs cm}^{-2}\text{ s}^{-1}\text{ sr}^{-1}} = 9.41 \times 10^{-8}\ T_4^{-1.017}\ 10^{(-0.029/T_4)} \left(\frac{EM}{\text{cm}^{-6}\text{ pc}}\right). \tag{1.22}$$

The Hα free-free template used in this thesis comes from Dickinson, Davies & Davis (2003) and therefore, their formulation for the free-free brightness temperature shall be used. Instead of using the theoretical opacity value (Oster 1961), Dickinson, Davies & Davis (2003) chose to use an approximation (Altenhoff et al. 1960) and make corrections for the discrepancies between the two opacities at higher frequencies by using a correction factor a, which is the ratio between the two opacities:

$$\frac{T_b}{\text{K}} = 8.235 \times 10^{-2}\, a \left(\frac{T_e}{\text{K}}\right)^{-0.35} \left(\frac{\nu}{\text{GHz}}\right)^{-2.1} (1 + 0.08)\ \frac{EM}{\text{cm}^{-6}\text{ pc}}, \tag{1.23}$$

where

$$a = 0.366 \left(\frac{\nu}{\text{GHz}}\right)^{0.1} \left(\frac{T_e}{\text{K}}\right)^{-0.15} \times \left[\ln\left(4.995 \times 10^{-2} \left(\frac{\nu}{\text{GHz}}\right)^{-1}\right) + 1.5 \ln\left(\frac{T_e}{\text{K}}\right)\right]. \tag{1.24}$$

This approach was first taken by Mezger & Henderson (1967) who note that between 0.001 and 100 GHz, for electron temperatures between 3,000 K and 15,000 K, the a

values range from 0.75 to 1. The (1 + 0.08) factor is present to take account of the Helium atoms within the WIM which become single ionised.

As both the free-free and Hα emission depend on the emission measure of their medium the two intensities can be related:

$$\frac{T_b^{\mathrm{ff}}}{I_\alpha} = 8.396 \times 10^3 \; a \left(\frac{\nu}{\mathrm{GHz}}\right)^{-2.1} \; T_4^{0.667} \; 10^{(0.029/T_4)} \; (1 + 0.08). \tag{1.25}$$

Dickinson, Davies & Davis (2003) use the Wisconsin Hα Mapper (WHAM) and the Southern Hα Sky Survey Atlas (SHASSA) data to produce their Hα free-free template. WHAM is a Fabry-Perot spectrometer (Reynolds et al. 1998) with a resolution of $\sim 1^\circ$ which mapped Hα at declinations $\delta \geq +30^\circ$, while SHASSA operated at $\delta \leq +15^\circ$ with a $0\overset{'}{.}8$ resolution (Gaustad et al. 2001).

Optical Hα emission, however is absorbed by dust and so I_α must be corrected. This absorption will increase within the Galactic plane and Dickinson, Davies & Davis (2003) note that at $|b| < 5^\circ$ this correction becomes unreliable. Dickinson, Davies & Davis (2003) find the Hα absorption (A(Hα)) can be expressed as:

$$\frac{A(\mathrm{H}\alpha)}{\mathrm{mag}} = (0.0462 \pm 0.0035)\frac{D}{\mathrm{MJy\ sr^{-1}}}, \tag{1.26}$$

where D is the 100 μm dust map from Finkbeiner, Davis & Schlegel (1999). To form the absorption formula, Dickinson, Davies & Davis (2003) assume an extinction slope across wavelength of 3.1 and reddening values (see Appendix A.1) for the dust map from Schlegel, Finkbeiner & Davis (1998). The Hα absorption is proportional to the fraction of dust within the measurement line of sight (f_d), which Dickinson, Davies & Davis (2003) calculate as 0.33. The corrected Hα intensity can then be calculated as:

$$0.0462\left(\frac{D}{\mathrm{MJy\ sr^{-1}}}\right) = 2.5 \; \log_{10}\left(\frac{I_\alpha}{I_\alpha^{corr}}\right), \tag{1.27}$$

which gives

$$\frac{I_\alpha^{corr}}{\mathrm{ergs\ cm^{-2}\ s^{-1}\ sr^{-1}}} = \left(\frac{I_\alpha}{\mathrm{ergs\ cm^{-2}\ s^{-1}\ sr^{-1}}}\right) \times 10^{0.0185\left(\frac{D}{\mathrm{MJy\ sr^{-1}}}\right)f_d}. \tag{1.28}$$

Dust absorption is a prominent problem within the optical and infra-red regimes and can only be entirely overcome by switching to the radio regime.

Radio recombination lines (RRLs) can provide an absorption free alternative for tracing free-free emission within the Galactic plane. Hydrogen RRLs are spectral emission lines resulting from the recombination of electrons and hydrogen atoms within the WIM. The collisions between hydrogen atoms will keep the atoms in excited Rydberg states where electrons are within the $n > 100$ energy levels. Decays from these levels will result in emissions and radio frequencies are denoted as $Hn\alpha$ transitions when the electron decays from the $n + 1$ to the n state.

The RRL spectral line temperature is calculated as follows (Rohlfs & Wilson 2004):

$$\frac{T_L}{\mathrm{K}} = 1.92 \times 10^3 \left(\frac{T_e}{\mathrm{K}}\right)^{3/2} \left(\frac{EM}{\mathrm{cm^{-6}\ pc}}\right) \left(\frac{\Delta\nu}{\mathrm{kHz}}\right)^{-1}, \tag{1.29}$$

As with Hα emission both the RRLs and the free-free emission depend on the EM and so can be equated to each other:

$$\frac{\int T_L \left(\frac{dV}{\mathrm{km\ s^{-1}}}\right)}{T_{\mathrm{ff}}} = 6.985 \times 10^3 \frac{1}{a} \frac{1}{(1 + 0.08)} \left(\frac{T_e}{\mathrm{K}}\right)^{-1.15} \left(\frac{\nu}{\mathrm{GHz}}\right)^{1.1}. \tag{1.30}$$

where a is given in Equation 1.24 and the integral over velocity takes into account the broadening of line widths by the thermal Doppler effect. It can be seen that the accuracy of this ratio completely relies upon the accuracy of the electron temperature chosen.

1.7.3 Anomalous emission

Throughout the late nineties, measurements of emission at 14.5 and 32 GHz were being conducted around the North Celestial Pole (NCP) at the Owens Valley Radio Observatory (OVRO): the Ring5m experiment (Leitch et al. 1997). Upon analysis, it was discovered that the total emission measured had a flatter spectral index than expected, namely around -1.1 and was strongly correlated with the *IRAS* 100 μm thermal dust map of the NCP. This correlation is shown in Figure 1.13.

Leitch et al. (1997) believed the cause of this flatter index was the inclusion of an anomalous component, of which flat spectrum synchrotron radiation and flatter free-free emission were amongst the possibilities. However, the poor correlation with Hα

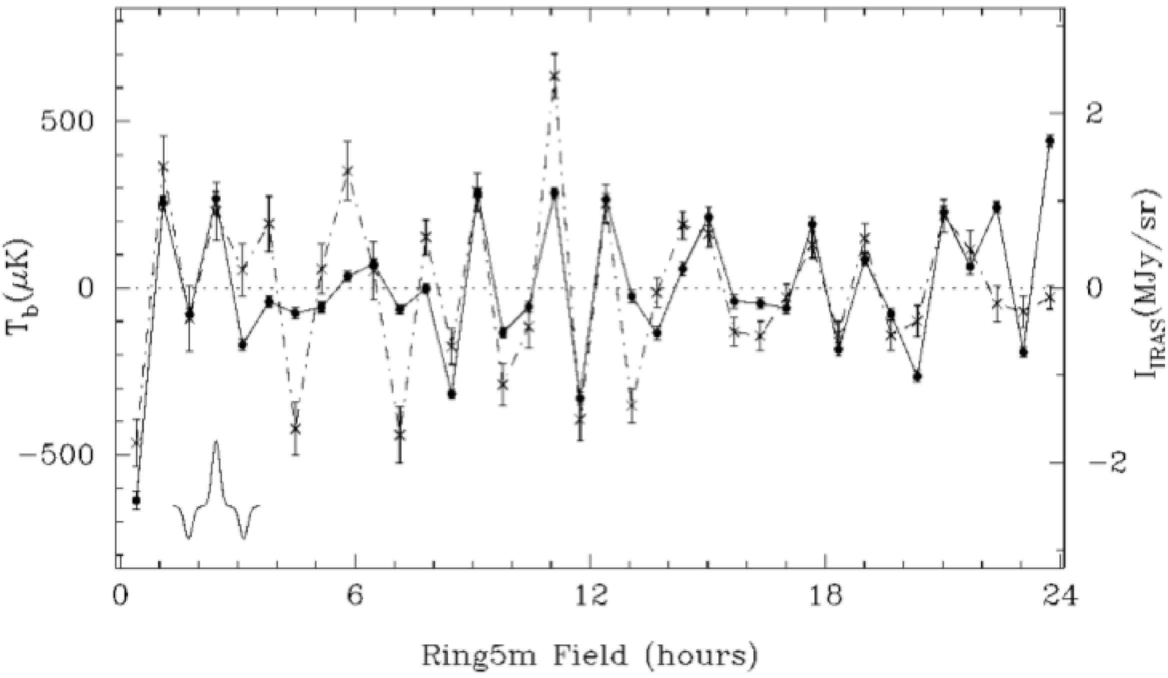

Figure 1.13: The 14.5 GHz OVRO data of the NCP (solid line) alongside the *IRAS* 100 μm NCP data (dot-dashed line) convolved to the Ring5m beam, shown bottom left. Image taken from Leitch et al. (1997).

emission meant the anomalous component would need to originate from a region of the WIM $\sim 60\times$ higher in temperature than generally seen if it were flat spectrum free-free emission. Within two years of these measurements, Draine and Lazarian had proposed two possible explanations for the mechanism behind this anomalous microwave emission (AME): spinning dust (Draine & Lazarian 1998) and magnetic dipole emission (Draine & Lazarian 1999).

Magnetic dipole emission comes from magnetic dust grains, which have had their electron spins altered by thermal fluctuations within the ISM. The strength of the emission depends on the strength of the magnetism and in their original paper, Draine and Lazarian consider para-, ferri-, ferro- and supermagnetic materials. Current studies however, favour the idea of magnetic dipole emission from ferromagnetic materials (electron spins in parallel alignment) and ferrimagnetic materials (electron spins of

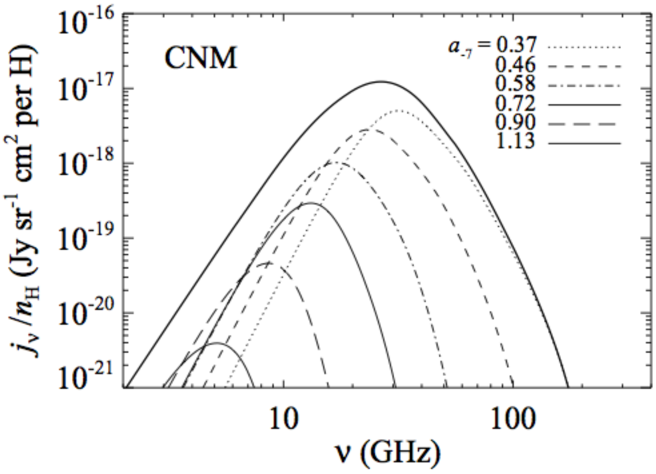

Figure 1.14: The variation of the spinning dust emissivity per H atom with grain radius (units of 10^{-7} cm) for the cold neutral medium model of spinning dust (Ali-Haïmoud, Hirata & Dickinson 2009).

two different materials in antiparallel).

In the spinning dust model, dust grains experience rapid rotation due to their electric dipole moment and the electric field of the ISM. Generally, only small dust grains, grains containing less than around a thousand atoms, spin fast enough to emit appreciably; their rotations are sustained through both ion and neutral atom collisions. In the spinning dust model emissivity per H atom can be calculated as (Ali-Haïmoud, Hirata & Dickinson 2009):

$$\frac{j_\nu\, n_H^{-1}}{\text{erg s}^{-1}\ \text{sr}^{-1}\ \text{H atom}^{-1}} = \int_{a_{min}}^{a_{max}} \left(\frac{da}{\text{cm}}\right)\left(\frac{n_H^{-1} dn_{gr}/da}{\text{sr}^{-1}\ \text{cm}^{-1}\ \text{H atom}^{-1}}\right)\omega^2\ f_a(\omega)\ 2\pi\ P, \quad (1.31)$$

where

$$P = \frac{2}{3}\left(\frac{\mu_{a\perp}^2 \omega^4 c^{-3}}{\text{erg s}^{-1}}\right), \quad (1.32)$$

and the peak frequency in Hz is $\omega/2\pi$, $\mu_{a\perp}$ is the component of the electric dipole moment perpendicular to ω in debye, $f_a(\omega)$ is the angular velocity distribution, c is the speed of light in cm s^{-1}, a is the grain radius and $n_H^{-1}\mathrm{dn_{gr}/da}$ is the number of dust grains per unit size per H atom.

AME dominates over thermal dust, free-free and synchrotron emission within the

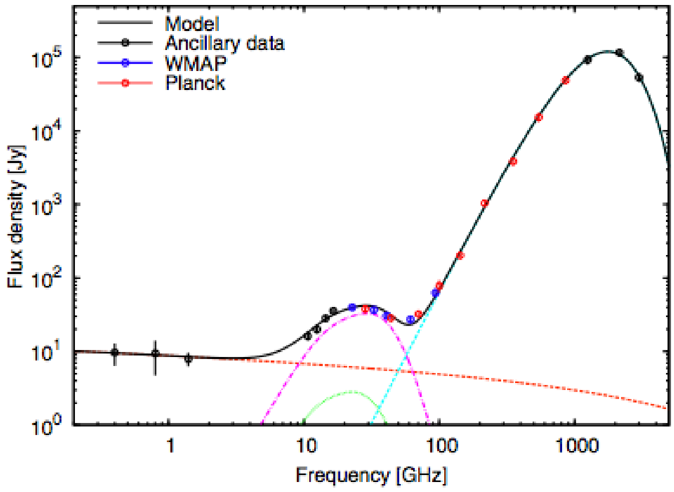

Figure 1.15: SED of AME-G160.26 – 18.62 within the Perseus molecular cloud using *Planck*, *WMAP* and ancillary data. The model fit to the data is a combination of free-free (orange dashed line), thermal dust (cyan dashed line), high density molecular spinning dust (magenta dot-dashed line) and low density atomic gas spinning dust (green dotted line) emission (Planck Collaboration et al. 2011c).

10-60 GHz frequency region and it has a peak shaped spectrum. Figure 1.14 shows the variation of peak frequency and 'bump' width with dust grain radius assuming the medium that the dust resides in is cold (≈ 100 K) and neutral (Ali-Haïmoud, Hirata & Dickinson 2009). The spinning dust model is a popular explanation for AME because of the successful modelling of the excess emission seen in the ρ Ophiuchi (Casassus et al. 2008), Perseus molecular clouds and various HII regions (Dickinson et al. 2009). In Figure 1.15, we can see the anomalous emission bump within the 10-100 GHz frequency range on data taken from the Perseus molecular cloud. The model fit is made up from a combination of the free-free emission model, the thermal dust emission model and a two component spinning dust model. The combination of all these models provides a convincing fit to the *Planck*, *WMAP*, Haslam 0.408 GHz, Dwingeloo 0.820 GHz, Reich 1.420 GHz and HartRAO 2.3 GHz data, reenforcing the idea of the spinning dust model for anomalous emission (Planck Collaboration et al. 2011c).

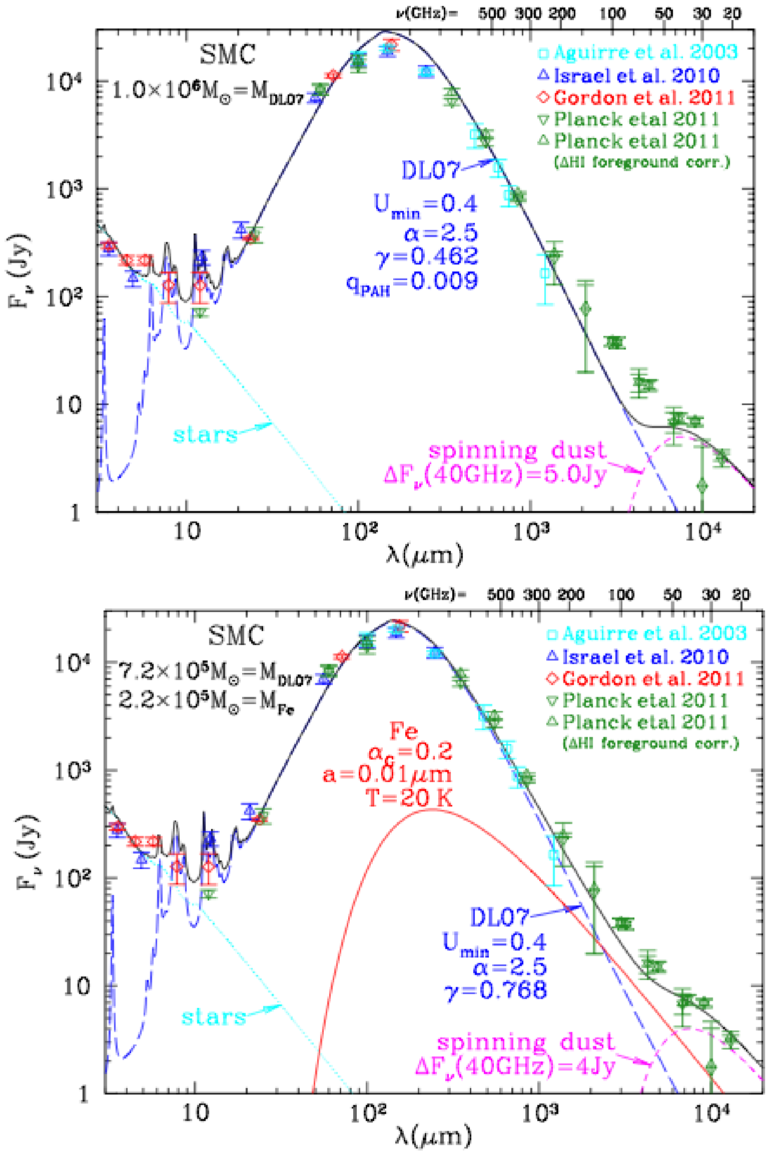

Figure 1.16: **Top:** SED of the diffuse foreground and CMB subtracted SMC region. The solid line represents the sum of the starlight, thermal dust (DL07) and spinning dust emission (Draine & Hensley 2012). **Bottom:** The same as above but with the addition of magnetic dipole emission to the solid line model.

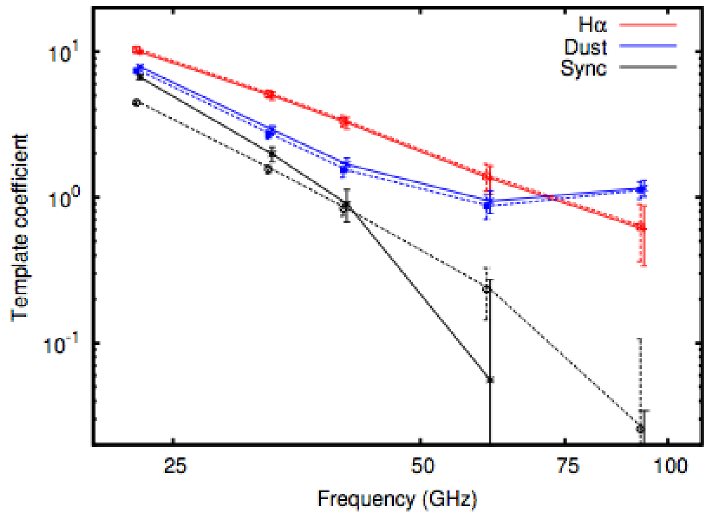

Figure 1.17: The *WMAP* 7-year template fit coefficients for roughly 50 % of the sky. The red points and lines are Hα fits, the blue points and lines are the thermal dust fits and the black points and lines are the synchrotron fits. The solid data represent the fit to the model which uses the steep synchrotron data while the dotted data represent the model which uses the flat synchrotron data (Peel et al. 2012).

Magnetic dipole emission is not generally the preferred explanation of AME as it would generate greater amounts of polarised emission than is actually measured in prominent AME regions (e.g Perseus, ρ Ophiuchus). However, recent work on the Small Magellanic Cloud (Draine & Hensley 2012) has shown that there is a predilection amongst low-metallicity dwarf Galaxies to emit more submm dust correlated emission than can be explained by the spinning dust model. Figure 1.16 shows two SEDs for the SMC after the removal of diffuse Galactic foregrounds and the CMB. The top SED presents a fit to the data which includes emission from starlight, thermal dust (DL07) and spinning dust but this fit falls short of the data at $\nu < 100$ GHz. The bottom SED presents a similar fit incorporating magnetic dipole emission from Fe nanoparticles and this improves the fit at lower frequencies.

Flat spectrum synchrotron emission was also dismissed eventually as a favoured candidate for AME using the *WMAP* 7-year data (Peel et al. 2012). Figure 1.17 shows the minimal impact of altering the synchrotron spectral index with regards to the dust correlated emission by using template fitting. Template fitting to empirical data involves combining ancillary foreground data with fit coefficients specifically chosen to minimise the chi-squared fit between the model and the empirical data. The ancillary data used in Figure 1.17 are the Haslam 0.408 GHz data and the HartRAO 2.3 GHz data for the steep and flat synchrotron models respectively, Hα data as a free-free tracer and *IRAS* and *COBE* infra-red measurements for the thermal dust model. The introduction of 5 GHz C-BASS data as an additional flat synchrotron spectral model would help to constrain these findings.

AME has been measured to be very weakly polarised at a maximum of 4 % at 10 GHz within the Perseus region and a maximum of 1 % within diffuse Galactic emission at 30 GHz (López-Caraballo & Génova-Santos 2013). A maximum polarisation fraction of 2 % between 20 and 40 GHz has also been made within ρ Ophiuchi (Dickinson, Peel & Vidal 2011). The number of AME polarisation measurements are so sparse that they can all be represented by Figure 1.18. From this figure, it can be seen that the AME fractional polarisation upper limits associated with specific regions appear to be consistently higher than those from diffuse Galactic emission. This, however, is not indicative of an actual difference between diffuse and compact AME polarisation because of the differing signal-to-noise levels associated with various experiments and measurement techniques. Hoang, Lazarian & Martin (2013) compute the theoretical polarised fraction for spinning dust electric dipole emission and find their models to show a 1.6 % polarisation fraction at $\approx$ 3 GHz and a less than 0.9 % polarisation fraction for $\nu > 20$ GHz.

AME is believed to be negligible at frequencies under 10 GHz although there is no sufficient data yet to validate the claim. One example of a region which would benefit from C-BASS data is the ρ Ophiuchi West molecular cloud. Figure 1.19 shows an SED of AME-G353.05+16.90, which is within this region that appears to show the presence of AME at $\nu > 3$ GHz. This detection, however, is poorly constrained owing to the lack of 1 – 10 GHz observations.

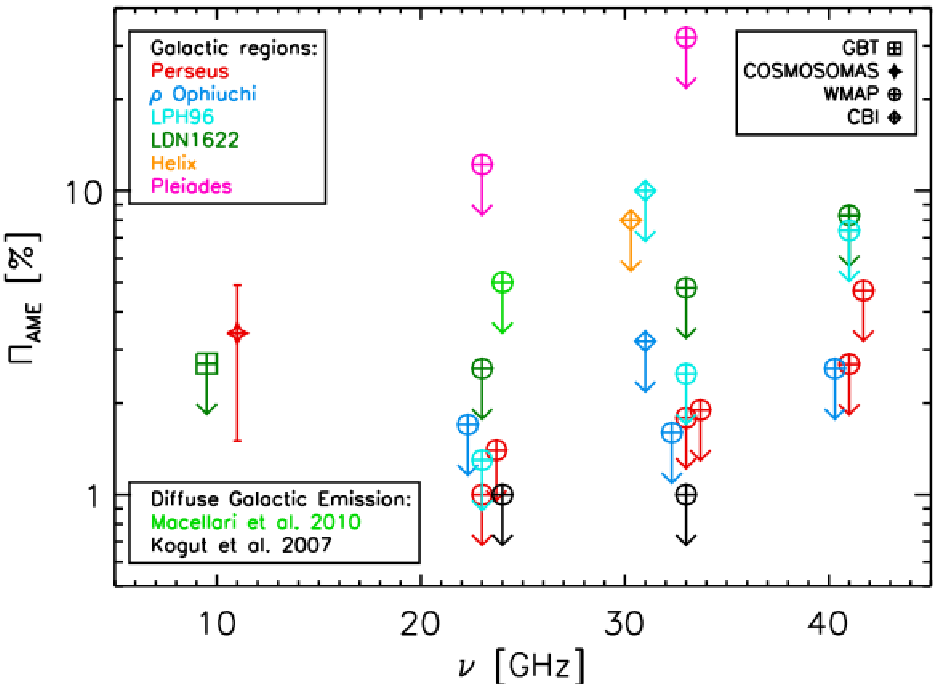

Figure 1.18: The fractional polarisation upper limits of AME as measured by various experiments (López-Caraballo & Génova-Santos 2013).

1.7.4 Thermal Dust emission

Thermal dust emission is emitted by vibrating dust grains heated to 10 – 30 K by interstellar radiation (Draine 2011). The main constituents of the dust are silicates, carbonaceous particles and polycyclic aromatic hydrocarbons (PAHs). This dust can be found not only within the Galactic plane but also, at far higher latitudes and its emission dominates the CMB foreground at frequencies over 100 GHz. As of such, diffuse thermal emission cannot be detected by C-BASS. For large-scale polarised Galactic structures thermal dust and synchrotron emission are correlated, however the components differ on measured polarisation angles and small-scale structures (Planck Collaboration et al. 2014).

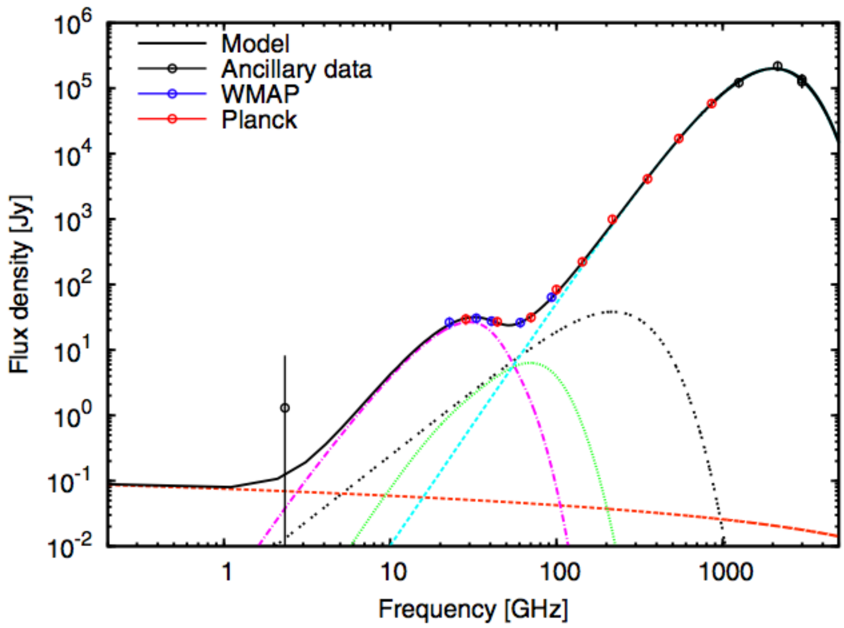

Figure 1.19: SED of AME-G353.05+16.90 within the ρ Ophiuchi West molecular cloud using *Planck*, *WMAP* and ancillary data points. The model fit to the data points is a combination of free-free (orange dashed line), thermal dust (cyan dashed line), high density molecular spinning dust (magenta dot-dashed line) and low density atomic gas spinning dust (green dotted line) emission (Planck Collaboration et al. 2011c).

1.8 Point Sources

So far all the foregrounds discussed are diffuse in nature, in other words, they emanate from a region as opposed to a specific source. Extragalactic point sources of radio wavelength emission include quasars, radio galaxies and active galactic nuclei (AGN), including blazars.

Point sources contribute to radio surveys in two ways, the brightest sources are easily visible within survey maps whilst the fainter sources contribute to an effect known as 'confusion noise'. Confusion noise (σ_c) is a background noise within the beam size caused by the clustering together of many unresolvable faint sources. This effect is dependent on both the normalised beam response and the differential source distribution

(Rohlfs & Wilson 2004):

$$\sigma_c^2 = \int f^2(\theta, \phi)\, d\theta\, d\phi \int_{S_{\min}}^{S_{\max}} S^2 \frac{dN}{dS}\, dS, \tag{1.33}$$

where for a Gaussian beam with an effective beam area of A_e:

$$\int f^2(\theta, \phi)\, d\theta\, d\phi = \frac{\lambda^2}{2\, Ae}. \tag{1.34}$$

N is the source count which is dependent on frequency (ν) and flux density (S). The differential source distribution requires empirical values for its integral and so an approximation for confusion noise at cm wavelengths (Stanimirovic et al. 2002) is used in this 5 GHz analysis:

$$\sigma_c \left(\frac{\text{mJy}}{\text{beam}}\right) = 0.2 \left(\frac{\nu}{\text{GHz}}\right)^{-0.7} \left(\frac{\theta}{\text{arcmin}}\right)^2. \tag{1.35}$$

For the C-BASS central frequency of 5 GHz and FWHM (θ) of 45′ the confusion noise limit is 131.3 mJy per beam or 0.88 mK. The C-BASS measurements will therefore be confusion noise limited in intensity but not in polarisation as the average polarisation fraction is $\sim$ 3.5 % (Battye et al. 2011).

The confusion noise of a survey is an astrophysical sensitivity limit, however the removal of bright sources can be accomplished using radio source catalogues. Table 1.3 presents several available radio source catalogues alongside their central frequencies, instrument FWHM, region coverage and lower detection limit (3σ). Figure 1.20 shows the point sources present in the GB6 (Gregory et al. 1996) and PMN (Tasker et al. 1994) 4.85 GHz catalogues with sources greater than the C-BASS confusion noise flux limit. The sources have been convolved with a Gaussian beam of 45′. The brightest few of these sources will need to be deconvolved out of the final maps to remove the contamination from their sidelobes.

1.9 Thesis layout

This thesis details the work carried out by the author towards the actualisation of the C-BASS project. The work ranges from technical to data reduction and processing, all

ν (GHz)	FWHM ($'$)	Dec $^\circ$	$>$ (mJy)	Reference
1.4	0.75	$\delta > -40$	2.5	Condon et al. (1998)
4.85	10.5	$0 < \delta < 75$	18	Gregory et al. (1996)
4.85	5.0	$-88 < \delta < 10$	30	Tasker et al. (1994)
8.4	0.003	$0^\circ < \delta < 75^\circ$	30	Myers et al. (2003)
20.0	2.4	$\delta < 0$	40	Murphy et al. (2010)
28.4	5.5	Full Sky	461	Planck Collaboration et al. (2013b)
44.1	27.10	Full Sky	825	Planck Collaboration et al. (2013b)
70.4	13.30	Full Sky	566	Planck Collaboration et al. (2013b)
100.0	9.65	Full Sky	266	Planck Collaboration et al. (2013b)
143.0	7.25	Full Sky	169	Planck Collaboration et al. (2013b)
217.0	4.99	Full Sky	149	Planck Collaboration et al. (2013b)
353.0	4.82	Full Sky	289	Planck Collaboration et al. (2013b)
545.0	4.68	Full Sky	457	Planck Collaboration et al. (2013b)
857.0	4.33	Full Sky	658	Planck Collaboration et al. (2013b)

Table 1.3: A selection of radio source catalogues shown alongside their survey central frequency, resolution, declination, detection limit and reference.

the way through to the scientific analysis of the preliminary data. Chapter 2 describes the C-BASS project goals and requirements and describes the Northern and Southern optics, the receivers, the backends and outlines the current status of the project. In Chapter 3 the Northern cryostat components are described in detail alongside both the Northern and Southern commissioning work. The main features of this commissioning work are the microphonics mitigation, radio frequency interference detection, Hot/Cold load tests and receiver balancing. Chapter 4 deals with the steps of the data reduction pipeline, from the digital backend through to map-making, while Chapter 5 describes the removal of ground spillover signal from the maps using ground emission templates. Scientific analysis of preliminary intensity data is shown in Chapter 6 where free-free and synchrotron emission are separated within the Galactic plane and AME

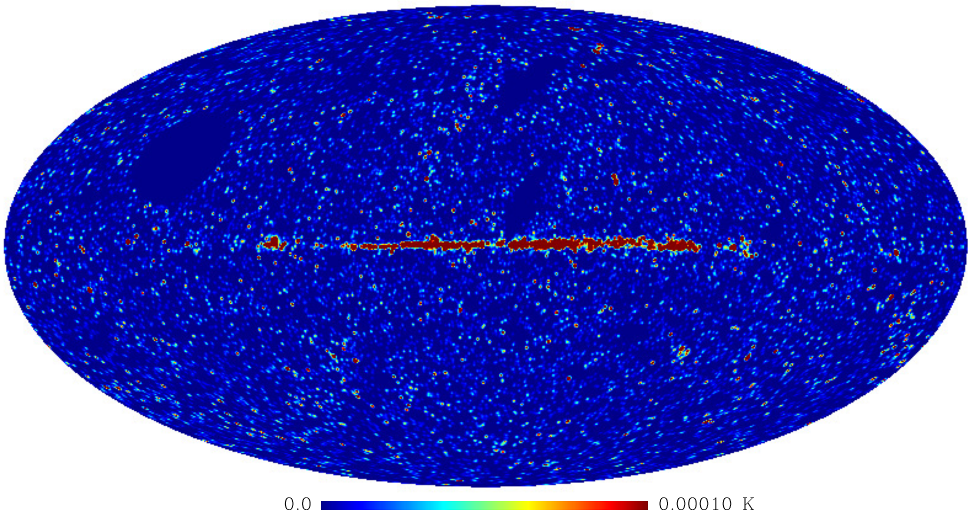

Figure 1.20: The point sources in the GB6 and PMN point source catalogues with flux densities greater than the C-BASS confusion noise limit. The sources have been convolved with a Gaussian beam of the same FWHM as the C-BASS beam (45′).

at higher frequencies is constrained using C-BASS data. Lastly, Chapter 7 concludes.

Chapter 2

C-BASS

C-BASS, the C-Band All Sky Survey, is a foregrounds project currently mapping Galactic intensity and linear polarisation at a frequency of 5 GHz (King et al. 2010). C-BASS consists of two correlation receivers: Northern C-BASS resides at the Owens Valley Radio Observatory (OVRO) in California, USA whilst Southern C-BASS is in South Africa.

The radiometer designs for both telescopes are fairly similar, notable differences include the handling of manmade radio frequency interference (RFI) and the dishes. Northern C-BASS uses notch filters, which reduce the bandwidth from 1 GHz to 489 MHz, while the Southern has a digital backend. Northern C-BASS has a 6.1 m Gregorian dish while Southern C-BASS has a 7.6 m Cassegrain. Northern C-BASS achieved first light in 2009 and entered its final survey mode in November 2012. Southern C-BASS achieved first light in August 2013. The final maps will be at a Full Width Half Maximum (FWHM) resolution of $43\overset{\prime}{.}8$ and a nominal average sensitivity of 0.1 mK per beam in polarisation.

Table 2.1 presents several of the main observational parameters for both Northern and Southern C-BASS.

	Northern	**Southern**
Latitude	$37\overset{\circ}{.}2$	$-30\overset{\circ}{.}7$
Antenna type	Gregorian	Cassegrain
Diameter	6.1 m	7.6 m
FWHM	$0\overset{\circ}{.}73$	$0\overset{\circ}{.}73$
Main Beam Efficiency	80.0%	80.0%
Full Beam Efficiency	91.9%	91.3%
Intensity central frequency	4.76 GHz	–
Intensity Bandwidth	489 MHz	–
Total System Temperature	40 K	–

Table 2.1: Northern and Southern C-BASS observational parameters. Blank parameters have yet to be measured.

2.1 Project Goals and Products

C-BASS is, above anything else, a CMB foregrounds project and therefore has the primary aim of producing an all-sky polarisation map of synchrotron emission to assist in the measurement of primordial B-modes. However, with the data in hand, there are opportunities to consider and pursue several other interesting avenues of Galactic science:

- Probing the Galactic magnetic field using synchrotron radiation which, at 5 GHz, is weakly affected by Faraday rotation.
- Producing a spectral index map for synchrotron emission.
- Investigating the possible spectral curvature of synchrotron emission.
- The intensity data can be used to constrain the spectral behaviour of AME within specific regions, e.g. Perseus, ρ Ophiuchus etc.

- The various free-free templates (e.g radio recombination lines, maximum entropy models e.t.c) can be tested.

The products of the C-BASS survey will be $\mathrm{N_{side}} = 256$ HEALPix maps in Stokes I, Q and U. The HEALPix (Hierarchical, Equal Area and iso-Latitude Pixelisation) software package presents survey data onto a spherical region, which has been split up into $12 \times \mathrm{N_{side}}^2$ pixels of equal area (Górski et al. 2005). The $\mathrm{N_{side}}$ values allowed are 2^n, where n can be any positive integer. The HEALPix $\mathrm{N_{side}} = 256$ pixels have a linear size of 13$'$.7, which is appropriate for oversampling the C-BASS beam size of 43$'$.8 (three pixels per beam). Northern C-BASS has a bandwidth ($\Delta\nu$) of 489 MHz and a system temperature ($\mathrm{T_{sys}}$) of $\approx$ 40 K:

$$\mathrm{T_{sys}} = \mathrm{T_{sky}} + \mathrm{T_{rx}}, \tag{2.1}$$

where $\mathrm{T_{sky}}$ is the 5 GHz sky temperature and $\mathrm{T_{rx}}$ is the receiver temperature. The Northern C-BASS system temperature will be further discussed in Section 3.6. Survey sensitivity can be determined from the system temperature using the radiometer equation:

$$\sigma\ (\mathrm{K}) = \frac{\mathrm{F\ T_{sys}}}{\sqrt{\Delta\nu\ \tau}}, \tag{2.2}$$

where τ is the integration time per pixel and F is the sensitivity constant, which depends on the receiver type. C-BASS continuously observes the sky however it combines the sky intensity signal with a constant load signal thus forfeiting a factor of $\sqrt{2}$ in intensity sensitivity (assuming the load and sky temperatures are equal). This factor is recaptured as the C-BASS receivers have two 'arms' of identical analogue components (receiver channels) each with identical reference loads, meaning $F = 1$ in Equation 2.2 for C-BASS intensity. For the polarisation measurements, the signal is not shared between sky and load because the two signals are separated and the load signal is discarded before Stokes Q and U detection; $F = \frac{1}{\sqrt{2}}$ for C-BASS polarisation.

2.2 Frequency and Sensitivity Requirements

The motivation behind the 5 GHz central frequency choice was twofold. First, 5 GHz bridges the frequency gap between the highest frequency all-sky, high resolution ground based survey at 1.420 GHz and the lowest all-sky satellite based survey at 22.5 GHz. Ideally, we would observe as close to the lower end of this gap as possible to ensure the strongest possible synchrotron signal. Figure 1.8 shows the spectrum for synchrotron emission; it can be seen that the relationship between frequency and synchrotron emission amplitude is a negative power law.

In reality, however, Faraday rotation prevents the accurate measurement of low frequency polarisation and provides the second motivation for the 5 GHz central frequency choice. Faraday rotation results in a decrease in polarised intensity (depolarisation). Figure 2.1 shows the all-sky polarised intensity maps at 1.4 and 22.5 GHz. The 1.4 GHz map is clearly seen to be suffering from the effects of depolarisation, especially within the Galactic plane. The squared dependency between measured polarisation angle and wavelength indicates that the depolarisation experienced by the 1.4 GHz map will be $\sim \frac{1}{12^{\mathrm{th}}}$ of the effect at 5 GHz. The areas worst affected by depolarisation fall within the Galactic plane. In fact, this area has already been examined at 5 GHz by the Urumqi 25 m telescope for the Sino-German λ6 cm polarisation survey (Gao et al. 2010). This survey was conducted with a FWHM of $9\farcm5$ and an average polarised intensity sensitivity of 0.6 mK. The Sino-German survey detected two extended Faraday screens, regions which result in Faraday rotation due to their thermal electrons and magnetic fields, within the Perseus arm (Galactic longitude $\sim 140°$). Notwithstanding these specific regions, it is fair to assume that the 5 GHz sky is relatively free from the effects of Faraday rotation.

The sensitivity requirement of the survey is governed by the objective to measure the polarised intensity signal at a signal-to-noise $> 5\sigma$ for 90 % of the sky pixels. Dr. Oliver King, a collaboration member, used the 22.5 GHz and 1.4 GHz polarised intensity maps to calculate the mode polarisation synchrotron spectral index for this

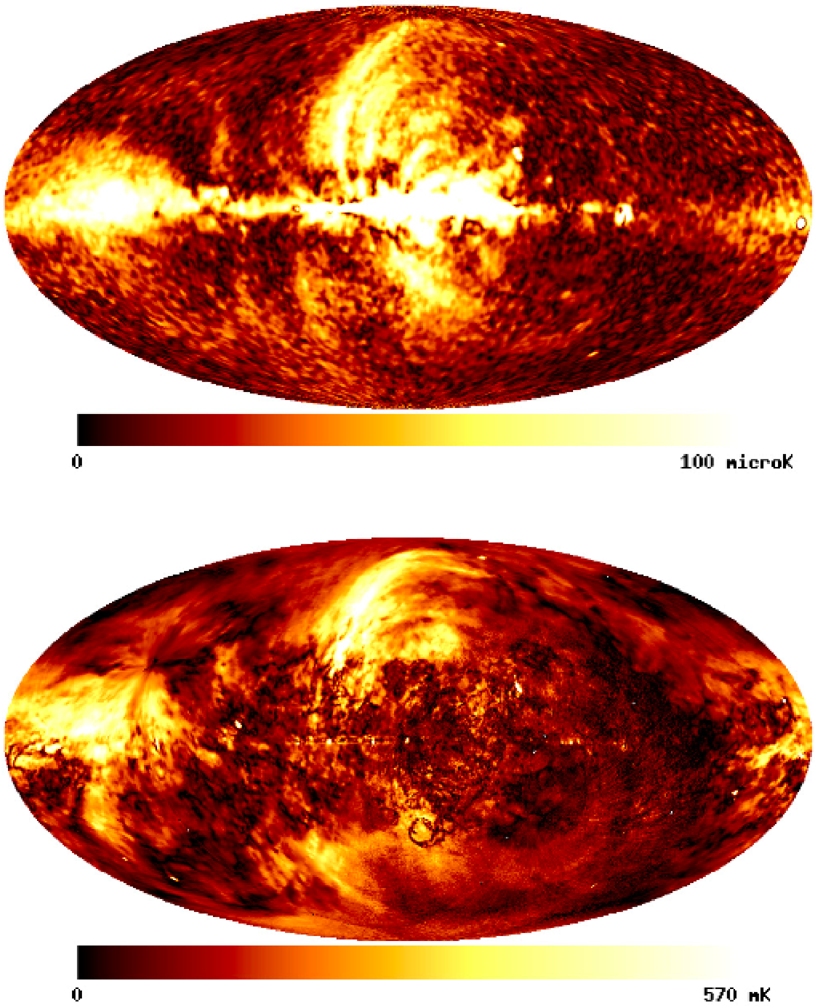

Figure 2.1: **Top:** The 22.5 GHz polarised intensity map. **Bottom:** The 1.4 GHz polarised intensity map. Image from Sun et al. (2008).

frequency range. He then used this value to scale down the 22.5 GHz polarised map to 5 GHz and predicted that 90 % of the polarised intensity pixels would have an antenna temperature > 0.59 mK, thus dictating the need for the 0.1 mK per beam sensitivity.

2.3 Northern scanning strategy

Northern C-BASS observes 24 hours a day; the post-processing software locates and flags data contaminated by the Sun and Moon, using solar and lunar ephemerides.

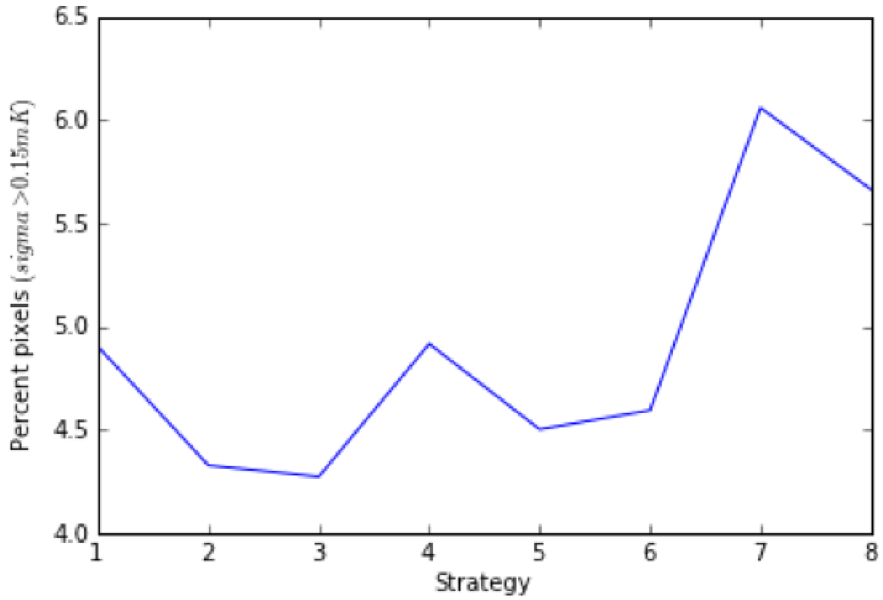

Figure 2.2: The percentage of pixels with an r.m.s noise greater than 0.15 mK for each scanning strategy. Figure courtesy of Dr. Joe Zuntz.

The telescope scans in azimuth and spends two-thirds of its time at elevation 37° and one-third at 47°. We avoid scanning in elevation in order to minimise the effects of the ground spillover (see Chapter 5) and atmospheric 1/*f* noise which is caused by fluctuations in the distribution of atmospheric water vapour. Scanning simulations constructed by collaboration member Dr. Joe Zuntz revealed that the split between the North Celestial Pole (NCP) elevation (37°) scans and NCP + 10° elevations scans provided the optimum sky coverage. Figure 2.2 shows the percentage of pixels with an r.m.s thermal noise greater than 0.15 mK for each of the eight scanning strategies detailed in Table 2.2. It can be seen that splitting the survey time between elevation 37° and 47° provides better coverage over a larger range of pixels.

Strategy	**Northern Elevations (°)**
1	37
2	37 - 47
3	37 - 37 - 47
4	37 - 57
5	37 - 57 - 57
6	37 - 47 - 57
7	37 - 52
8	37 - 37 - 52

Table 2.2: The eight survey strategies tested by collaboration member Dr. Joe Zuntz using scanning simulations.

Northern C-BASS scans in azimuth at 5 different scanning speeds: $3^{\circ}\!.8$, $3^{\circ}\!.9$, $4^{\circ}\!.0$, $4^{\circ}\!.1$ and $4^{\circ}\!.2$/sec. The minimum scan speed is set by the requirement to complete a full 360° scan on a time scale shorter than that of the low noise amplifier gain variations. The five different scan speeds are a relatively recent addition to the scanning strategy (early 2013) and have been introduced because of the 1.2 Hz mircrophonics; a hardware feature of the Northern receiver, which will be discussed in greater detail in Section 3.4. The varying scan speeds were introduced to decouple the Galactic plane signal from the 1.2 Hz signal in Fourier space thus simplifying the task of modelling and removing the 1.2 Hz signal.

The observations are divided between survey schedules, where the telescope circles in azimuth between the two elevations and calibrator schedules, tracking Cassiopeia A, Taurus A, and Cygnus A to collect data for use in survey calibration. The survey schedules last an hour and a half each with a SkyDip performed every 30 minutes (see section 4.5.2) while the calibrator schedules are up to 15 minutes long. Two survey schedules are followed by a calibrator schedule and this pattern is repeated continuously.

2.4 Antenna and Brightness temperature

Radio astronomy uses different concepts to distinguish between various types of temperature: these are antenna, brightness, main beam and full beam. Antenna temperature (T_A) is defined as the temperature the receiver measures when the dish is presented with an object of a certain brightness temperature and power pattern ($P_n(\theta, \phi)$):

$$T_A = \frac{1}{\Omega_A} \int \int_{\text{source}} P_n(\theta, \phi) T_s(\theta, \phi) \, d\Omega. \tag{2.3}$$

The relationship between antenna temperature and source temperature (T_S) is dependent on the relationship between the beam solid angle (Ω_A) and the source solid angle (Ω_S):

$$\mathrm{T_A} = \begin{cases} \frac{\Omega_s}{\Omega_A} T_S \text{ if } \Omega_S < \Omega_A. \\ T_S \text{ if } \Omega_S > \Omega_A. \end{cases} \tag{2.4}$$

It can be seen that when the solid angle of the source is greater than the solid angle of the antenna, as in the case of diffuse emission, the source temperature is equal to the antenna temperature. However, with point sources ($\Omega_S < \Omega_A$) it is necessary to consider the source solid angle. For a Gaussian source with FWHM θ_s the FWHM observed (θ_o) through a main beam of FWHM θ_{mb} is

$$\theta_o^2 = \theta_s^2 + \theta_{mb}^2, \tag{2.5}$$

so when $\theta_{mb} \gg \theta_s$ it is actually the main beam which is required for consideration.

Figure 2.3 shows the power response of a typical antenna as a function of position ($P_n(\theta, \phi)$), both the full antenna pattern and the main beam are illustrated. For C-BASS, the main beam power is defined as the fraction of total radiated power within the first null ($1\overset{\circ}{.}5$ from the beam centre) and is given as 0.8 (Holler et al. 2013). The main beam temperature when looking at a source where source size $\ll$ beam size is related to the antenna temperature through the main beam efficiency (η_B):

$$T_{MB} = \frac{T_A}{\eta_B}. \tag{2.6}$$

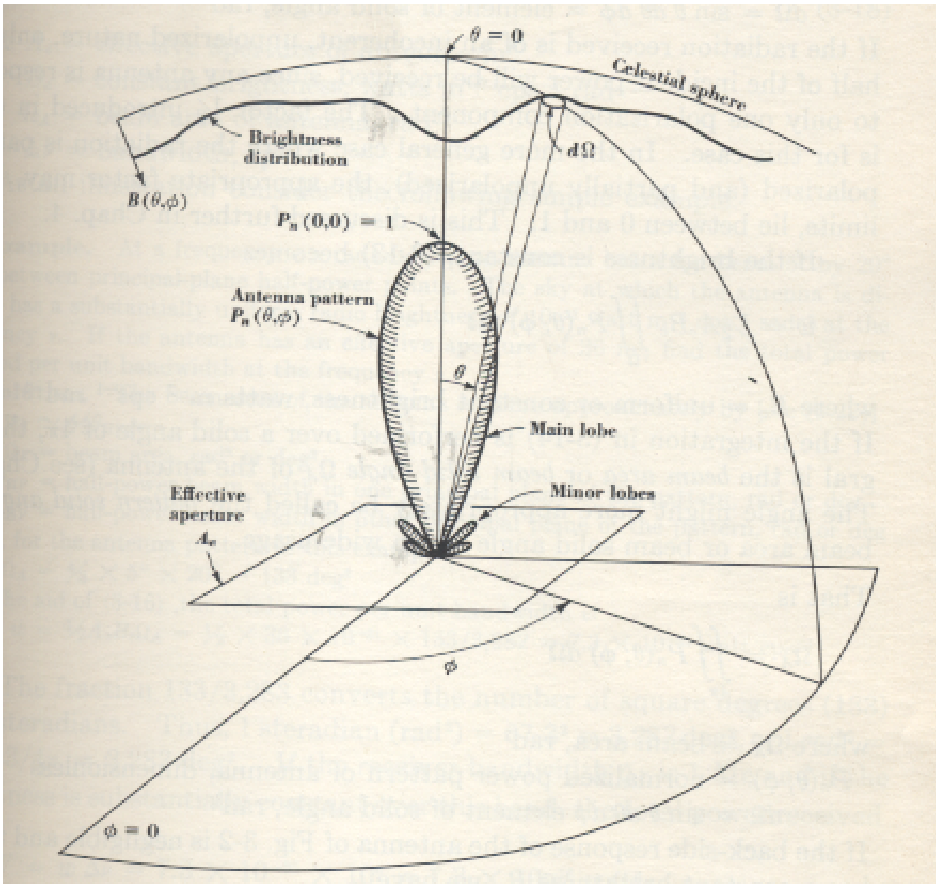

Figure 2.3: The power response of a typical antenna observing a source of brightness distribution $B(\theta, \phi)$. Image from (Kraus 1966).

The main beam efficiency is defined as the ratio between the main beam solid angle (Ω_B) and the beam solid angle:

$$\eta_B = \frac{\Omega_B}{\Omega_A}. \tag{2.7}$$

The C-BASS maps themselves are in Kelvin antenna temperature and the full beam power for C-BASS, defined as the fraction of total power within 5° of the beam centre, is 0.919. Therefore, before making any comparisons with ancillary data sets, the C-BASS maps need to be divided by the full beam efficiency factor to express them in terms of full beam temperature.

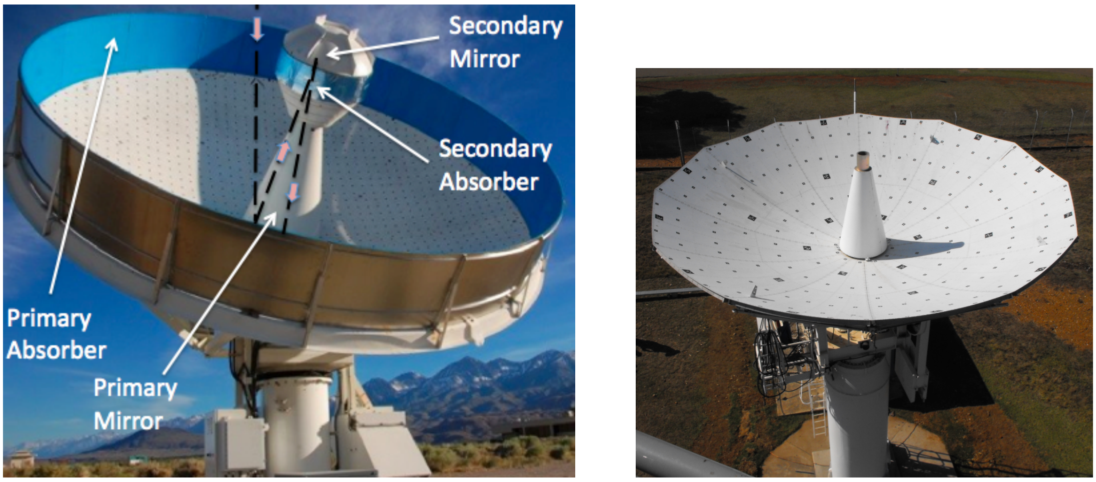

Figure 2.4: **Left:** The Northern C-BASS antenna. **Right:** The incomplete Southern C-BASS antenna, the secondary optics and feed horn had yet to be installed.

2.5 The Northern and Southern Antennas

Both of the C-BASS antennas were originally designed for different projects and then donated to C-BASS. As of such the Northern and Southern antennas are different in design - the Northern antenna is Gregorian, the Southern, Cassegrain. The different shapes of the primary mirrors called for two different approaches when dealing with ground spillover. The Northern system requires the use of absorbing baffles around the primary and secondary mirrors to minimise the effect of ground spillover, while the Southern system will be under-illuminated (Holler et al. 2013). The feed horns were designed and constructed by Thomas Keating Ltd. and, when used alongside each system's optics, provide identical beam FWHMs for both antennas. Figure 2.5 shows both the Northern and Southern dishes, the Northern dish is complete with its absorbing baffles attached. However, at the time of photographing the Southern dish had only the receiver attached and not the secondary optics or the dielectric foam support.

2.6 The Northern and Southern Receivers

The C-BASS receivers combine elements from ‘continuous comparison’ radiometer and correlation polarimeter designs to produce a unique hybrid receiver capable of detecting Stokes I, Q, U and V whilst simultaneously monitoring a reference load. The receivers can be considered as an amalgam of a radiometer and polarimeter. In the case of Northern C-BASS the radiometer and polarimeter are two distinct components whereas in Southern C-BASS the polarimetry is carried out by an integrated circuit board known as a Field-Programmable Gate Array (FPGA) board.

Figures 2.5 and 2.6 show diagrams for the Northern and Southern receivers. The receiver designs will be discussed in more detail in Chapter 3, however the diagrams are included here to illustrate that both receivers share the continuous comparison radiometer design of reference loads and 180° hybrids. The *Planck* LFI instrument shares this continuous comparison design (Davis et al. 2009) but differs from the C-BASS receiver as it only measures one linear polarisation per receiver orientation. Northern C-BASS, on the other hand, through the inclusion of additional 90° hybrids can measure both Stokes Q and U simultaneously in a similar manner to the QUIET receiver (Buder 2010). Southern C-BASS achieves the same simultaneous measurement of Stokes Q and U but uses the FPGA to achieve this instead of analogue components.

2.6.1 The Radiometers

The radiometers are ‘continuous comparison’, meaning they simultaneously observe both the sky and a constant resistive load. This is achieved through the use of a 180° hybrid, a four port device which takes the load signal (L) and the sky signal (S) and yields the following:

$$\text{Output Voltage 1} = \frac{\text{S} + \text{L}}{\sqrt{2}}, \tag{2.8}$$

$$\text{Output Voltage 2} = \frac{\text{S} - \text{L}}{\sqrt{2}}, \tag{2.9}$$

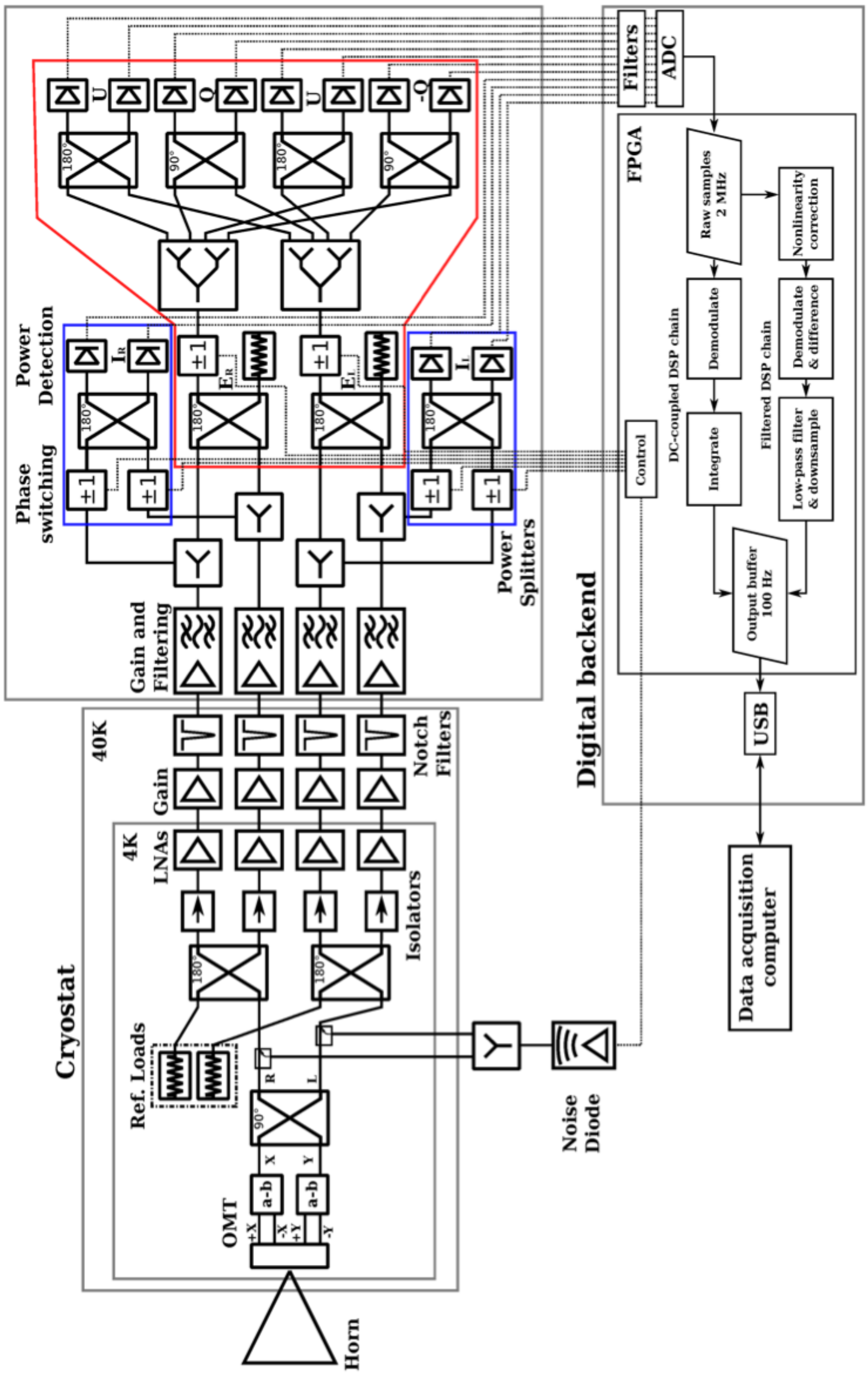

Figure 2.5: Schematic of the Northern receiver. Image from (King et al. 2014).

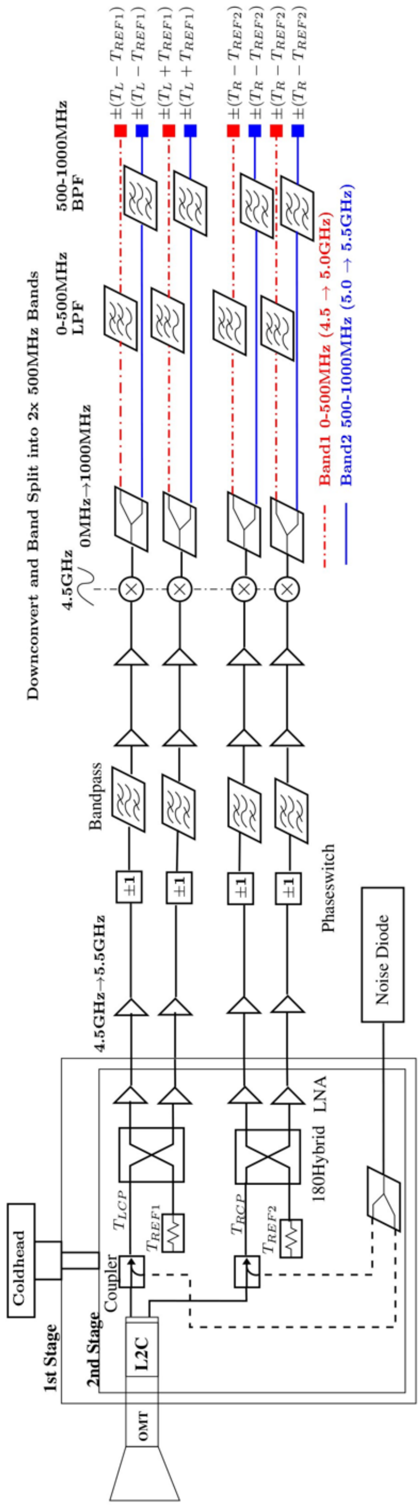

Figure 2.6: Schematic of the Southern Receiver. Image courtesy of collaboration member Dr. Charles Copley.

and as

$$\text{Power} = |\text{Voltage}|^2, \tag{2.10}$$

then

$$\text{Output Power 1} = \text{Output Power 2} = \frac{\text{S}^2 + \text{L}^2}{2}. \tag{2.11}$$

This is, in fact, a simplification of the signal propagation through the hybrids, as the sky and load signals are complex. The cancellation of the (2SL/2) component due to the 180° phase difference between S and L, however allows this simplification to hold true. The purpose of the load signal is to suppress $1/f$ noise and reduce receiver instabilities, which would otherwise be indistinguishable from variations on the sky. Instabilities within the receiver are made up of gain drifts and non-Gaussian amplifier noise and they posses a $1/f$ power spectrum. The frequency at which the $1/f$ noise reaches the white noise level is called the knee frequency (ν_k). The power spectral density of the instrumental noise is characterised as:

$$P_{noise}(\nu) \sim \sigma^2 \left[1 + \left(\frac{\nu}{\nu_k} \right)^{\alpha} \right], \tag{2.12}$$

where σ is the white noise level and α is the slope steepness for the $1/f$ region of the spectrum (Meinhold et al. 2009).

The C-BASS detector diodes measure a combination of sky, load, and amplifier noise (N) signals amplified by the LNA gain (G):

$$\text{Power detected} \propto \text{G (S + N} - \text{L)}. \tag{2.13}$$

Any change in measured power will either be due to a change in sky temperature (ΔT) or a change in gain drift (ΔG). If a gain variation is misconstrued as a change in sky temperature, so for the case $\Delta G \neq 0$, then (Rohlfs & Wilson 2004):

$$\Delta P = (S - L)(G + \Delta G) = (S - L + \Delta T)\, G, \tag{2.14}$$

therefore

$$\Delta T = \left(\frac{\Delta G}{G} \right) (S - L)\,. \tag{2.15}$$

If the constant load signal perfectly matches the average temperature of the sky, in other words if the receiver is balanced, then the effect of gain drifts are completely negated and only variations in S will be detected.

2.6.2 The Polarimeters

Both the Northern and Southern polarimeters are correlation polarimeters: they use the correlation of the right (E_R) and left (E_R) circular polarisations of the sky signal to detect Stokes Q and U:

$$Q = \langle E_L E_R^* \rangle + \langle E_R E_L^* \rangle, \tag{2.16}$$

$$iU = \langle E_R E_L^* \rangle - \langle E_L E_R^* \rangle, \tag{2.17}$$

where * denotes the complex conjugate and $\langle\rangle$ denotes the time-averaged signal (Kraus 1966).

The Northern C-BASS polarimeter acquires the products $E_L E_R^*$ and $E_L^* E_R$ through differencing the two power outputs of a 180° hybrid (Σ and Δ), rather than by direct signal multiplication:

$$\Sigma \propto (E_L + E_R^*)^2 \propto E_L^2 + E_R^{*2} + 2E_L E_R^*, \tag{2.18}$$

$$\Delta \propto (E_L - E_R^*)^2 \propto E_L^2 + E_R^{*2} - 2E_L E_R^*, \tag{2.19}$$

$$\Sigma - \Delta \propto E_L E_R^*. \tag{2.20}$$

Phase switching enables the complex conjugate of the sky signals to be measured and the use of 90° hybrids, which impose a 90° phase shift between their two outputs, ensures that the combinations required for the formation of Stokes Q and U are detected.

Southern C-BASS, however, uses an FPGA board to directly cross- and autocorrelate E_L and E_R to form Stokes Q and U. The advantage of correlation polarimeters is that they enable both Stokes Q and U to be measured simultaneously, thus minimising the effect of gain drifts.

2.6.3 The Northern Backend

Southern C-BASS converts its analogue signals to digital before carrying out polarimetry using an FPGA, whereas the Northern system conducts polarimetry by using analogue components. The Northern system has a digital backend which, also using an FPGA, is responsible for controlling the phase switching used in the cryostat. The Northern data are anti-alias filtered below 1 MHz to allow for Nyquist sampling of the data.

In the Northern backend, the analogue-to-digital converter (ADC) samples the analogue data at two million samples per second, these data are then subject to two different processing paths: filtered and unfiltered. Both the non-filtered and the filtered data are demodulated to a higher frequency carrier signal to enable filtering at lower frequency levels.

The filtered data are filtered for 60 Hz power line interference and corrected for detector diode non-linearity. The Northern backend uses a global positioning satellite (GPS) clock to accurately match the telescope pointing information to the time ordered data. However, this GPS signal contains 60 Hz interference from the mains power transmission lines. Fortunately the backend has its own internal 50 MHz clock and so it was possible to iterate between both clocks to produce a reliable time frame unaffected by 60 Hz interference. The Northern detector diodes display non-linear behaviour when in certain power regimes, this behaviour was characterised in the lab before cryostat assembly and so the effects of non-linearity can be corrected for in the data processing.

The non-filtered data contain neither of these corrections and therefore are not used for map making. They are, however, recorded for the purposes of receiver monitoring as they preserve two important receiver diagnostics, which are otherwise lost in the combination of signals required to form the filtered data channels. The diagnostics are the 'r-factor', which shows the factor that the reference load temperature must be multiplied by to give the sky temperature (Mennella et al. 2003) and the 'α-values' (for

Stokes I, Q and U) which show the leakage between both independent measurements of Stokes I, Q and U taken by the two receiver arms. As our reference loads are set equal to the sky temperature and our receiver is balanced to prevent leakage between the two arms both the α- and r-values should have a magnitude of 1.

2.7 Current Status

During the three and half year duration of this thesis the Northern and Southern receivers have undergone significant technical upgrades; Table 2.3 gives a summary of these improvements. The Northern survey completed commissioning and officially entered survey mode in late 2012. This thesis leaves the Northern survey almost in completion with regard to data collection: the survey will end in Summer 2014 with the Southern survey just beginning. Southern commissioning is currently taking place out at HartRAO, South Africa.

Date	Northern System	Southern System
Sep 2010	Identification of onsite, in-band RFI.	
Nov 2010	Re-glueing of foam cone.	
Dec 2010	Identification of 60 Hz interference.	
Jan 2011	$\sim$ 100 K system temperature.	
Feb 2011	Layer of water found over secondary mirror.	
March 2011		Machining Cryostat.
April 2011	Attachment of new foam cone and carbon fibre secondary mirror.	
May 2011	Installation of notch filters for RFI, external gain box built and oscillations seen in LNAs.	Building Jodrell low noise amplifiers (LNAs).
July 2011	Cracks found in LNAs, all four sent back to Jodrell.	Cryostat cabling competed.
Aug 2011		Cold plate configuration designed.
Oct 2011	Filters put in digital backend, fixed Jodrell LNAs installed, backend FPGA goes out of time with the GPS.	Temperature sensors tested.
Nov 2011	New FPGA code fixes timing.	Vacuum leaks in Cryostat fixed.
Dec 2011		Foam cone made, compresor shipped.
Jan 2012		Receiver testing.
March 2012	Bias card installed to control LNA biases, change cable path lengths into polarimeter to ensure α =1.	Reference load made with improved design (decoupled from cold stage).
Apr 2012	LNA oscillations return.	
May 2012	New reference loads installed.	
June 2012	Slope compensators re-soldered.	Post-amps installed.
July 2012	Decision to buy LNAs from an external company.	
Aug 2012	1.2 Hz oscillations increase in amplitude.	
Sep 2012	New LNAs installed.	

Continued on next page

Table 2.3 – continued from previous page

Date	**Northern System**	**Southern System**
Oct 2012	Gain box redesigned.	
Jan 2013	New cold head installed.	
Feb 2013	Bracket made to hold stainless steel cables exiting the cryostat	Cryostat shipped to S.A
March 2013		OMT mechanically decoupled from cold plate for better alignment with horn.
Apr 2013	Replaced azimuth drive gears.	
May 2013		Commissioning begins.
Aug 2013		Horn re-machined.
Oct 2013		Compressor replaced.
Nov 2013		Waterproofing of secondary mirror.
Jan 2014		In-band RFI identification.

Table 2.3: Timeline of significant Northern and Southern technical upgrades.

Chapter 3

Commissioning C-BASS

In order to cover the full-sky C-BASS has both a Northern and a Southern telescope. Northern C-BASS observes the declination range $-15^\circ < \delta < +90^\circ$, while Southern C-BASS observes $-90^\circ < \delta < +65^\circ$ so the two surveys will overlap.

Although the author of this thesis had no part in designing or building any of the Northern or Southern radiometer components, the *in situ* testing and subsequent receiver alterations described in the following sections were carried out by the author whilst onsite at OVRO and HartRAO.

The Northern cryostat was designed and assembled at Oxford University as part of the Ph.D thesis by Dr. O. G. King (King 2009). The Southern, which was based on a similar design was assembled as part of the Ph.D thesis by Dr. C. J. Copley (Copley 2013). Contributions to the Southern cryostat were made by Dr. S. J. Melhuish in the form of cryogenic wiring and Mr E. Blackhurst in the form of low noise amplifier work, both from the University of Manchester. The Northern system design and assembly was funded by Professor M. E Jones, University of Oxford, the Southern receiver by the King Abdulaziz City for Science and Technology (KACST). All subsequent funding was provided by Caltech, HartRAO, the University of Manchester and Oxford University.

3.1 The Northern Cryostat

The Northern receiver was the first to enter the commissioning phase, during late 2009 and was commissioned onsite at OVRO. Northern C-BASS contains a continuous comparison radiometer, a pseudo-correlation polarimeter and a digital backend. The radiometer components are distributed between a cryostat and an external gain box. Figure 3.1 shows both the outer body of the cryostat during receiver testing at OVRO and a photo of inside the cryostat showing the two internal stages. The first components to receive the incident sky signal, after the receiver feed horn, are housed within the cryostat. The cryostat is mechanically cooled through Helium pumping and has two tiers encased within an aluminium heat shield, which differ in temperature. The second stage holds the low noise amplifiers (LNAs) and is at ∼ 4 K.

The sky signal measured by Northern C-BASS is split into linear polarisations by an ortho-mode transducer (OMT) which forms orthogonal linear polarisation voltages from the circular waveguide. The C-BASS OMTs (both Northern and Southern) are based on a design by Bock (1999) but modified by the Oxford team to work at 4 K and at C-band frequencies(Grimes et al. 2007). The OMT consists of four probes at right angles to each other within an aluminium waveguide. The linear polarisation voltages are then converted to right and left circular polarisations by a linear to circular converter (L2C). These two polarisations propagate through two identical receiver channels and are eventually combined outside the cryostat. Figure 3.2 is a circuit diagram of one of these receiver channels within the cryostat. The components shown in Figure 3.2, e.g. the noise diode, isolators, LNAs and notch filters will now be discussed.

3.1.1 The Noise Diode

After the sky signal exits the L2C it is coupled with the noise diode signal. The noise diode is housed in a room temperature box outside the cryostat and when fired it injects a signal of constant I and Q into the sky signal. The reason the signal does not appear in the linear polarisation U is that $U = 2\ E_R E_L \sin \delta_{RL}$ and δ_{RL} is 0 for the noise diode

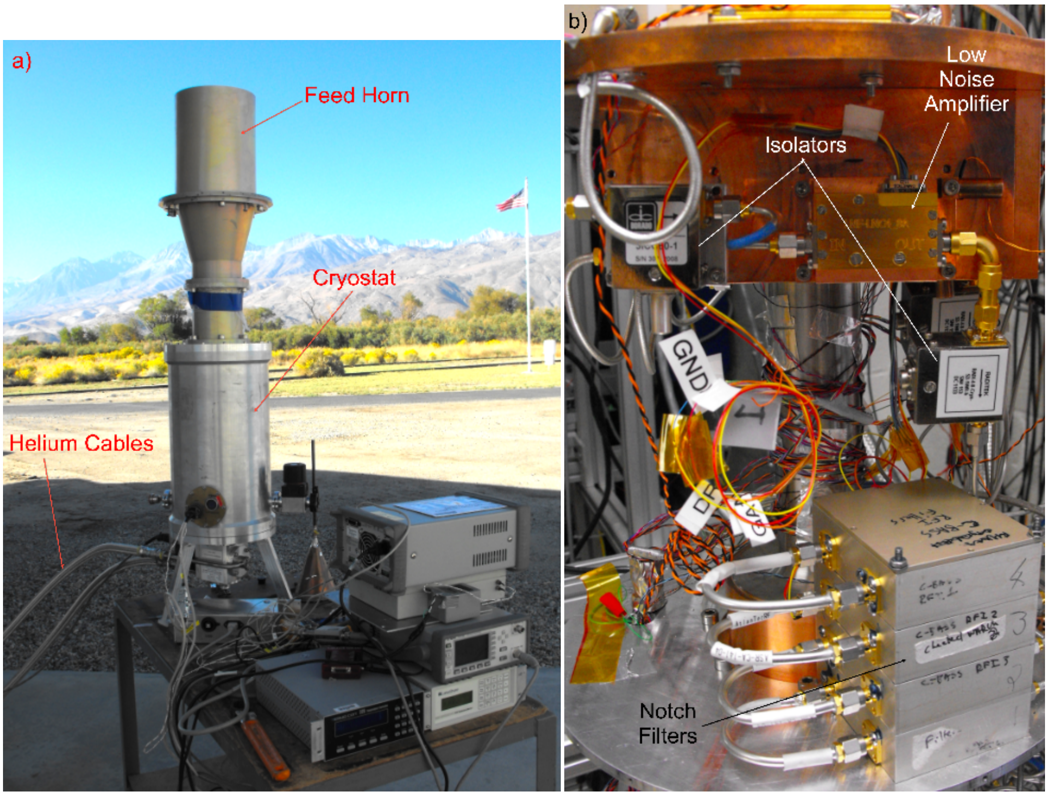

Figure 3.1: **a)** The Northern cryostat and feed horn undergoing testing separately to the rest of the telescope at OVRO. **b)** Inside the Northern cryostat, with the heat shield removed. Visible components are the LNAs (low noise amplifiers), isolators attached to the lower side of the second stage and the notch filter stack.

signal. The noise diode is fired roughly every four minutes and is used to monitor the gain, which can in turn be used to obtain an absolute flux scale using astronomical sources. As the noise diode signal is injected into the sky signal immediately after the L2C it is included as part of the sky signal throughout the following descriptions of the components.

3.1.2 Isolators

Isolators are directional devices that only allow for the transmission of signal from their input port to their output port and not vice-versa. After the sky signal is combined with

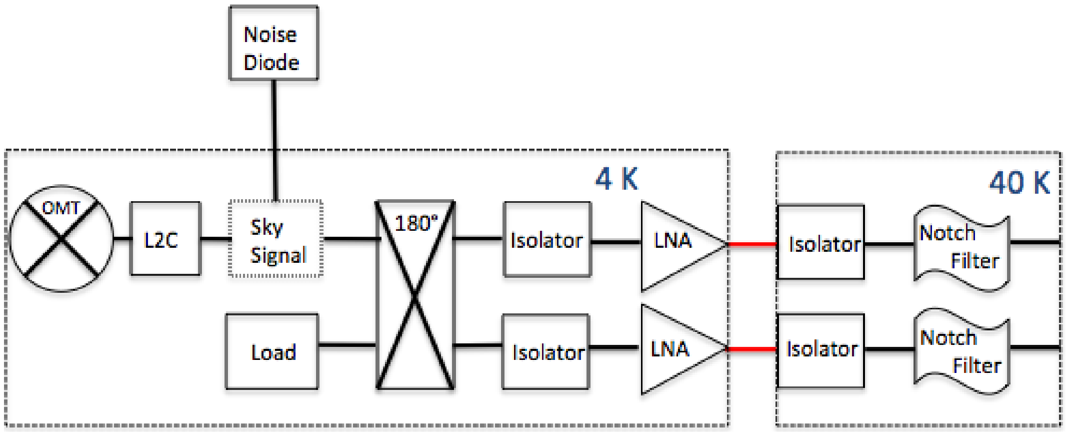

Figure 3.2: One of the two identical receiver channels which exist inside the Northern cryostat. The two red connection lines represent stainless steel cables, all other connections are copper coaxial cables.

the load signal it is amplified by the LNAs. If the LNAs were attached directly to the output of the 180° hybrid, via coaxial cables, the impedance mismatch between the two components would result in signal reflection and the formation of standing waves between the LNAs and hybrids. These standing waves would add further system noise *before* the first stage of amplification. In a simplified receiver setup, where each component posses its own gain (G) and noise temperature (T), the total receiver noise temperature (T_{rx}) is given by the Friis formula (Rohlfs & Wilson 2004):

$$T_{rx} = T_1 + \frac{T_2}{G_2} + \frac{T_3}{G_1 G_2} + ... + \frac{T_n}{G_1 G_2 ... G_{n-1}}. \tag{3.1}$$

From Equation 3.1 it can be seen that the system noise before the first amplifier (T_1) is the biggest contributor to the total receiver noise. Therefore standing waves forming in front of the LNAs would have been detrimental to the receiver sensitivity. To avoid this, an isolator was included to curtail the signal reflection.

Isolators are also present at the output of the LNAs to prevent standing waves which, when at the LNA output, result in amplifier oscillations. The output isolators are mounted on the ≈ 40 K stage while the LNAs are on the ≈ 4 K stage; stainless steel cables were chosen to connect the two because of their low thermal conductivity.

The insertion loss of a component is the log of the ratio between the transmitted output power and the reflected power. Equation 3.1 shows the importance of minimising instrumental noise before the LNAs, hence the use of the more expensive 0.1 dB insertion loss isolators as input isolators while 0.4 dB insertion loss isolators were used on the LNA outputs. The insertion losses quoted are for the 4 – 77 K temperature range.

3.1.3 Low Noise Amplifiers

The LNAs originally supplied for use inside the Northern cryostat were C-band amplifiers made by Jodrell Bank Centre for Astrophysics (JBO LNAs) and designed for and used in the e-MERLIN project. These amplifiers had noise temperatures of 10 – 12 K when cooled to 4 K. During the design of the Northern receiver it was thought that this noise temperature would allow for a system temperature (T_{sys}) of $\sim$ 20 K. However, during commissioning, the Northern bandwidth was reduced from 1 GHz to 500 MHz after including the of notch filters (see section 3.1.4) and the optics (baffles, dish, mirror, foam cone and horn) were found to contribute $\approx$ 10 K more to the sky temperature than initially estimated.

Lowering the receiver noise temperature would regain the receiver sensitivity after the decreased bandwidth and increased optical noise. What is more, the JBO LNAs were sometimes found to display instabilities in the form of oscillations. Table 2.3 shows the occasions where the JBO LNAs were noted to be oscillating. Subsequently, these were replaced by commercially built LNAs from Low Noise Factory (LNF) for their low noise temperature and stability whilst at cryogenic temperatures[1]. Figure 3.3 shows a measured noise temperature of $<$ 4 K and gain of $\sim$ 36 dB for one of the eight LNF LNAs when operating at 8 K and within the C-BASS bandwidth of 4.5 to 5.5 GHz.

[1] http://www.lownoisefactory.com/

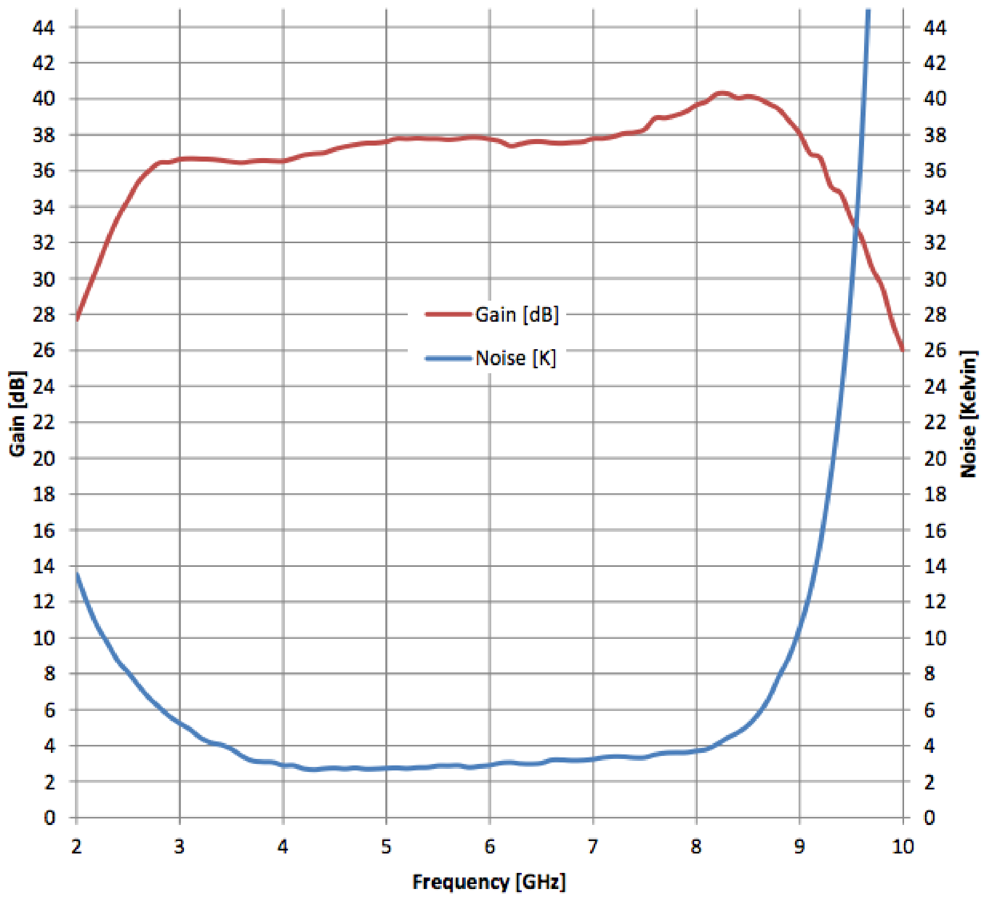

Figure 3.3: Gain and noise temperature over the C-band operational range for one of the eight LNF LNAs purchased. The noise temperature is < 4 K within the C-BASS bandwidth of 4.5 – 5.5 GHz. Image from Low Noise Factory.

3.1.4 Notch Filters

The final components within the cryostat are the notch filters. The notch filters result in a 520 MHz reduction in the 1 GHz C-BASS passband, however they are necessary in the presence of permanent radio frequency interference (RFI). Transient RFI, for instance aeroplanes, are removed in data processing as opposed to through hardware modifications.

Figure 3.4 shows an azimuthal sweep of the area surrounding the Northern receiver, generated using a radio horn and waveguide connected to a spectrum analyser. Two

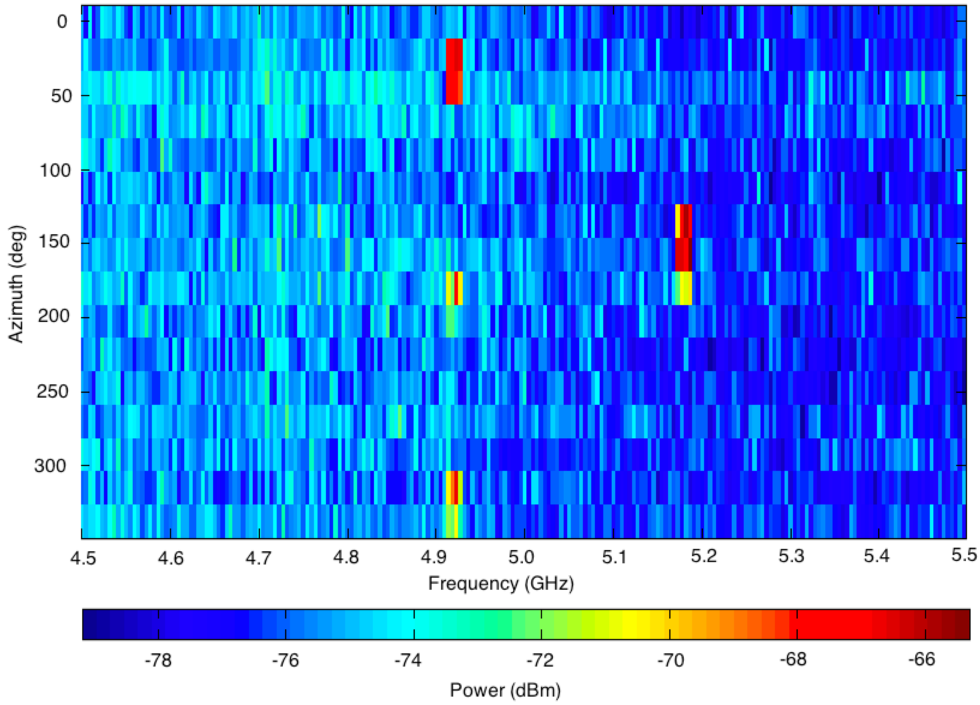

Figure 3.4: An azimuthal sweep of the Northern receiver site made using a radio horn and spectrum analyser. Power, measured in dBM (decibel power ratio compared to 1 mW) is plotted as a function of azimuth and frequency. Two sources of permanent RFI can be seen at ~ 4.9 and ~ 5.2 GHz.

sources of in-band permanent RFI can be seen in Figure 3.4, one near 5.2 GHz and the other around 4.9 GHz. To remove these RFI signals from our survey data Dr. Charles Copley built four different notch filters, each with stop bands centred around 4.79, 4.92, 5.18 and 5.24 GHz respectively. The combined effect of these four notch filters is the creation of two distinct notches centred at ~ 4.95 and ~ 5.2 GHz, which remove the appearance of permanent RFI from the survey scans. Figure 3.5 shows the impact of the notch filters on each of the four channels out of the cryostat. It should be noted that Figure 3.5 does not show the actual Northern C-BASS passband as the signal has yet to pass through the 4.5 – 5.5 GHz bandpass filters which sit outside the cryostat.

Figure 3.6 shows the intensity azimuth-elevation maps made by Northern C-BASS before and after the installation of the notch filters. The sources of RFI which can be

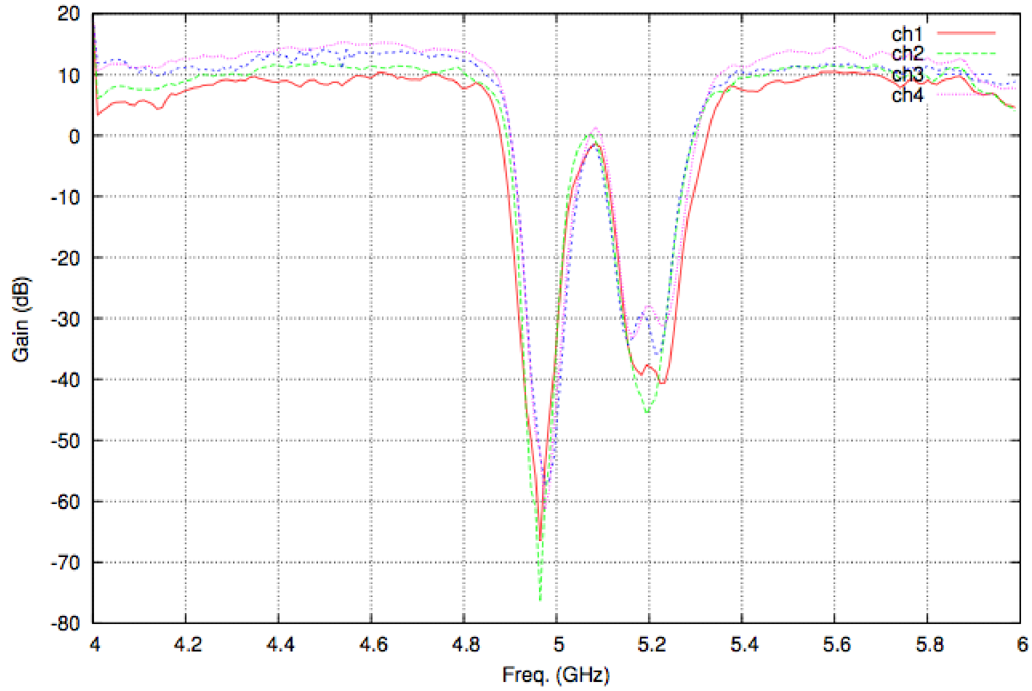

Figure 3.5: The effect of the notch filters on the C-BASS passband as seen at the exit of the cryostat, before the 4.5 – 5.5 GHz bandpass filters.

seen centred at $\sim$ 160° and $\sim$ 310° in azimuth in the top map, which was made using pre-notch filtered data, are no longer present in the lower map made from notch filtered data. The maps in Figure 3.6 display several other interesting features of the Northern observation site: two mountains can been seen at $\sim$ 50° and $\sim$ 250° in azimuth, a ring of geostationary satellites is present in the pre-notch filtered map (100 – 200° in azimuth) and all of these satellites are removed by the notch filters. The moon is also present above elevation 70° in the top map and of course, the Galactic plane features in both maps. A feature can be seen at az $\sim$ 110° in both the pre- and post-notch filtered maps; this feature is a microwave link from the observatory floor to the Combined Array for Research in Millimeter-wave Astronomy (CARMA) site. This feature appears to change in intensity between the pre- and post-notch filtered maps, which were made from 2010 and 2012 data, respectively. The CARMA link is expected to change in intensity between day and night as the transmitter is powered by a solar cell, however

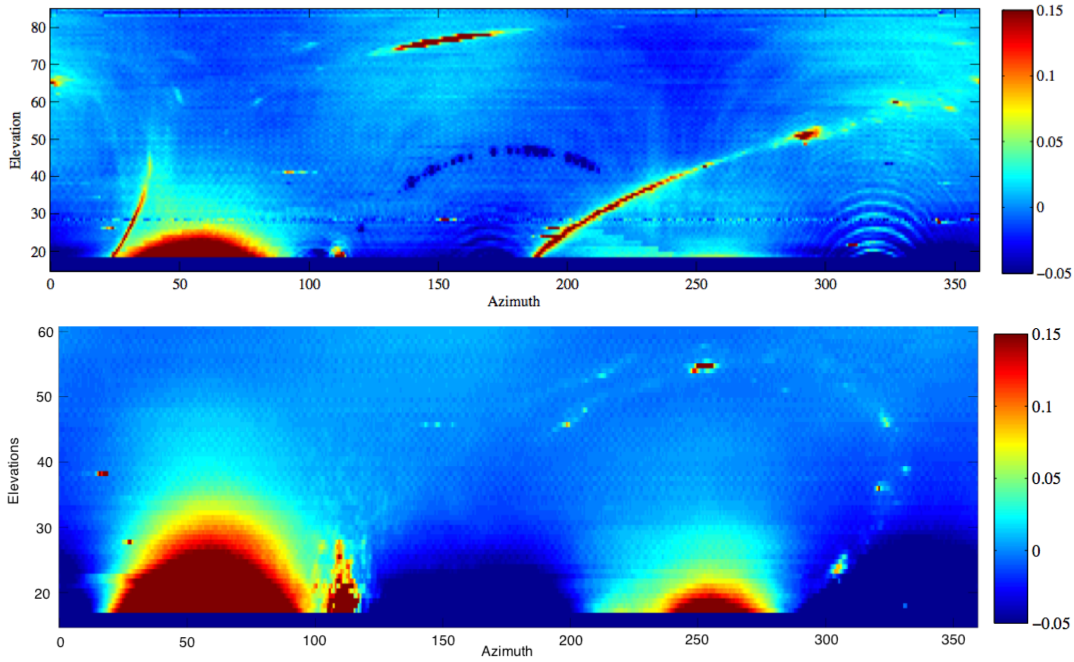

Figure 3.6: Azimuth-elevation intensity maps made by Northern C-BASS **top:** before and **bottom:** after the installation of the notch filters. The colour scale is in noise diode units. The bright features of RFI have been mitigated, except for one geostationary satellite positioned at azimuth $\sim 110°$.

the pre- and post-notch filtered map scales are not comparable. Both maps are shown in noise diode units but the receiver went through significant changes between 2010 and 2012: the noise diode temperature changed, the filtering conducted by the digital backend changed and the secondary optics were refurbished. Therefore Figure 3.6 should only be used to note the success of the notch filters.

3.2 The Gain Box

The four outputs of the cryostat are connected to the gain box via radio frequency (RF) coaxial cables. The gain box contains the collection of warm ($\sim$ 300 K) receiver components and sits just outside of the cryostat. It contains additional amplifiers (post amps) which were previously situated on the first stage of the cryostat,. However,

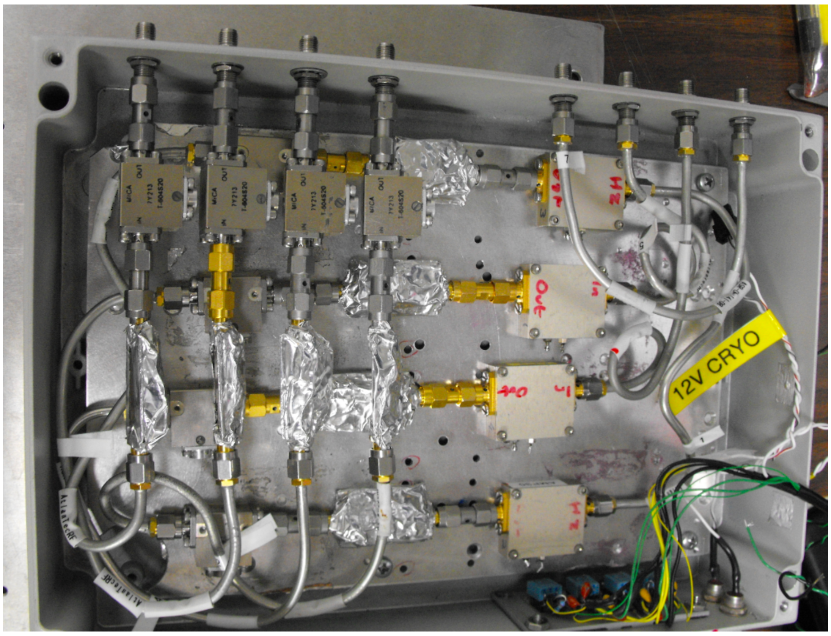

Figure 3.7: The gain box containing post amps, slope compensators and isolators. The right four ports are the gain box inputs while the left are the output ports.

when the JBO LNAs were replaced by LNF LNAs, amplifier oscillations were seen indicating feedback between the LNF LNAs and the post amps. The LNF LNAs have a gain of around 40 dB while the JBO LNAs had 30 dB and the post amps have roughly 30 dB. This extra gain of 10 dB per amplifier brought to the cryostat by the LNF LNAs was enough to cause signal reflection off of the aluminium heat shield. Therefore the post amps were moved outside of the cryostat and into the warm (≈ 300 K) component box, now the gain box which is shown in Figure 3.7.

Figure 3.8 shows the components along one channel of the gain box. From this figure it can been seen that apart from the post amps the gain box also houses the slope compensators. Slope compensators are present to mitigate the changing response of the bandpass filters over frequency. This changing response causes a sloping decrease in signal across the increasing frequency range; the slope compensators provide the opposite of this effect. The slope compensators are preceded and followed by isolators.

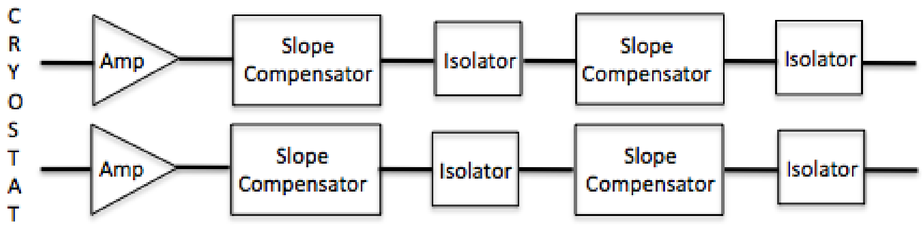

Figure 3.8: Diagram of one channel of the gain box components.

3.2.1 Bandpass filters

The bandpass filters sit on top of the gain box and define the bandwidth to be the 1 GHz range between 4.5 and 5.5 GHz. A Northern C-BASS bandpass filter consists of two separate filters: a bandpass filter to set the 4.5 to 5.5 GHz bandwidth and a lowpass filter to reject the higher frequency harmonics of the bandpass filter response. Each filter has a signal rejection of roughly $\sim$ 70 dB within their stop-band. Two Northern C-BASS filters are present in each of the four signal paths from the cryostat as one alone was not enough to exclude all the signal from the brightest satellites, which lie just outside of the C-BASS passband in frequency. As mentioned before, this bandpass is decreased by the presence of the notch filters.

The receiver noise temperatures for each signal path through the cryostat, bandpass filters and gain box were measured for the revised system (LNF LNAs and new warm component box), using Hot/Cold load testing.

3.3 Hot/Cold Load Tests

The receiver temperature is the combined noise temperature of all the receiver components. It is therefore, a constant addition in temperature to any receiver measurements made. In Section 2.1 the radiometer equation showed the effect of receiver temperature on the survey sensitivity, this means it is important to have as low a receiver temperature as possible. It is possible to directly measure receiver temperature however, the

Hot/Cold load test is too involved to be used as a frequent check. In the case of Northern C-BASS, the receiver temperature was only ever directly measured during receiver down time when technical work was taking place.

To directly measure receiver temperature, the receiver feed horn is first presented with a hot load (T_H) and then a cold load (T_C), both of known temperature and the difference between the two powers relates to the receiver temperature as follows:

$$T_{rx} = \frac{T_H - T_C\, y}{y - 1}, \tag{3.2}$$

where

$$y = 10^{\frac{P_{\mathrm{diff}}}{10}} \tag{3.3}$$

and P_{diff} is the difference in power (dBm) between the hot and cold load measurements and y is referred to as the y-factor. In the particular case of a continuous comparison radiometer like C-BASS, the hot/cold load signal becomes combined and differenced with the internal receiver cold load signal ($\mathrm{T_L}$) within the 180° hybrid. This alters the above relation as follows:

$$T_{rx} = \frac{\frac{T_H+T_L}{2} - \frac{(T_C+T_L)\,y}{2}}{y - 1}. \tag{3.4}$$

For the Hot/Cold results detailed in Table 3.1, the cold load was the sky and was assumed to be 6±1 K at 5 GHz, 2.75 K from the CMB and a few K for the atmospheric contribution. The hot load was a slab of ECCOSORB®, a microwave absorber assumed to be a blackbody at the ambient temperature of 298 K. This is a similar method to the Hot/Cold load tests carried out by Bersanelli et al. (1994) to find their radiometer gain. The cold load temperature during this Hot/Cold load test was 4.2 K. The system under investigation was not the full receiver, only the revised cryostat (featuring LNF LNAs) and the gain box, i.e. the optics and any ground spillover are not included in the receiver noise temperature. Before conducting the Hot/Cold load tests, it was known roughly what to expect given the receiver component specifications. Therefore the Hot/Cold load tests are a good way of checking for broken cables, water accumulation or any other fault which could raise the noise temperature above the expected value.

Component	Cumulative noise temp (K)
Horn1	0
Horn2	0
OMT	2
Cable	2
L2C	2
Cable	2
Noise Coupler	2
Cable	2
Hybrid	2
Cable	2
Isolator	3.5
Connector	3.5
LNA	7.5
Stainless Steel Cable	7.5
Isolator	9
Notch Filter	9
Cable	9
Connector	9
Post Amp	9.5
Connector	9.5
Slope Compensator	9.5
Connector	9.5
Isolator	11
Connector	11
Slope Compensator	11
Connector	11
Isolator	12.5

Figure 3.9: Estimated cumulative noise temperatures of the Northern cryostat and external gain box components.

Table 3.1 shows the noise temperatures resulting from the Hot/Cold load testing for the following components: cryostat, cable, gain box, bandpass filter, 27 dB amplifier, bandpass filter, cable and finally, the power-meter. For Northern C-BASS the estimated noise temperatures are summarised in Figure 3.9 and the expected receiver noise temperature can be seen to be roughly between 12 and 14 K. Table 3.1 confirms this expected receiver temperature for each of the four paths out of the cryostat. The path containing LNA 2 has a slightly higher receiver temperature than the other three paths; this may be due to a cable with slightly higher losses or simply an inaccurate measurement.

LNA	Hot Load power (dBm)	Cold Load power (dBm)	y	T_{rx} (K)
1	−18.7	−28.2	9.18	12.75
2	−18.9	−27.5	8.57	14.19
3	−14.8	−24.6	9.73	11.62
4	−14.8	−24.5	9.64	11.80

Table 3.1: The Hot/Cold load test power measurements and receiver temperatures for each of the four paths through the cryostat.

The Hot/Cold load testing is only as reliable as the stability of the reference loads. For instance, the sky is not a constant cold load at 6 K because of cloud coverage and the hot load temperature is based on the assumption that ECCOSORB® is a perfect blackbody. Therefore, the slightly higher receiver noise temperature seen along the LNA 2 path is still within the margin of error for this basic diagnostic.

This Hot/Cold test was conducted using the two reference temperatures of 6 K and 298 K. An additional Hot/Cold load test on the receiver has since been carried out using a different 'cold load', namely a radio transparent container of liquid nitrogen boiling at 77 K. The 77 – 298 K test was consistent, within the few K uncertainties, with the 6 – 298 K test, giving a combined Northern cryostat and external gain box temperature of 12 – 14 K.

3.4 1.2 Hz oscillations

The C-BASS signal should ideally be made up of Gaussian thermal noise, $1/f$ noise and astrophysical signal, however the Northern data are subject to 1.2 Hz and harmonic oscillations. These oscillations stem from the cold head which cools the cryostat at a frequency of 1.2 Hz; the harmonics are at integer multiplies, e.g 2.4, 3.6 Hz e.t.c. The cold head oscillations are thought to be microphonic in nature and not thermal white noise. The power spectrum in Figure 3.10 distinctly shows the 1.2 Hz and first seven harmonics oscillations within a typical sample of Northern C-BASS time ordered data.

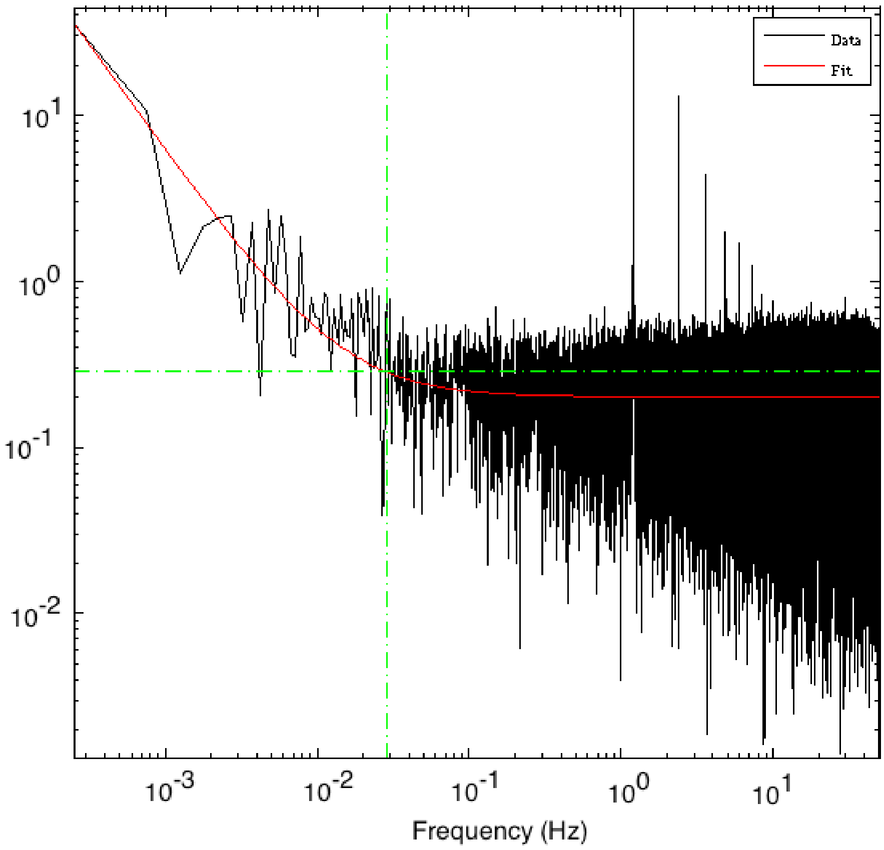

Figure 3.10: Power spectrum for a typical few minutes of Northern C-BASS data when the telescope is scanning over a region of sky that does not contain any astronomical features. The green crosshairs highlight the frequency at which the white noise and $1/f$ parts of the spectrum meet (the knee frequency).

The 1.2 Hz oscillations and harmonics are either 'stable' meaning that the oscillation magnitude remains constant over large periods of time, or 'unstable' in which case the magnitude changes over periods of less than a minute. When stable the oscillations are at a constant magnitude of $\sim$ 40 mK in intensity and $\sim$ 10 mK in polarisation. Stable oscillations are removed during post-processing of the data, this will described in greater detail in Section 4.2.

The 1.2 Hz oscillations and harmonics underwent two periods of great instability: between August and October 2012 and between February and June 2013. An

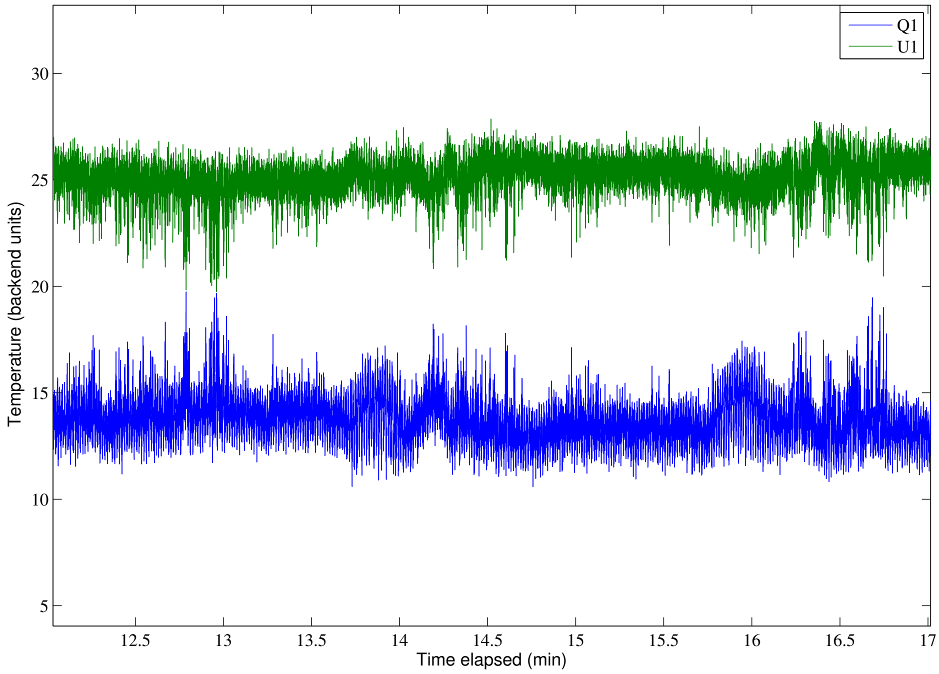

Figure 3.11: The Q and U channel of the first receiver channel displaying unstable 1.2 Hz and harmonics. The oscillation magnitudes can clearly be seen to vary over short ($\ll$ min) time scales for all the data channels.

example of this behaviour can be seen in Figure 3.11., which shows time ordered data for the Stokes Q and U measurements taken with the first receiver channel from February 2013. Oscillations of unstable magnitude cannot be completely removed post-processing and so these instabilities had to be fixed in the hardware. The unstable oscillation magnitudes seen in Figure 3.11 were caused by loose cable connections and cracked cables within the cryostat. Considerable care was therefore taken when re-assembling the cryostat after the LNF LNAs installation to retighten all the connectors and re-solder any broken wires within the cryostat. This mitigation of microphonics ensured stable 1.2 Hz and harmonics for November to December 2012. However a cold head refurbishment at the beginning of January 2013 required re-opening of the cryostat and after this the instabilities in the oscillation magnitudes returned. Miti-

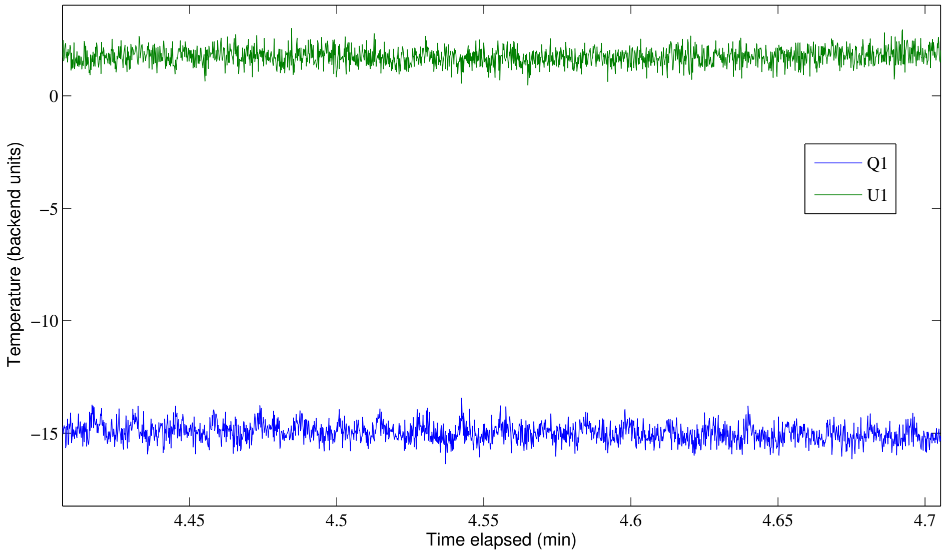

Figure 3.12: The Stokes Q and U channels from the first receiver channel displaying stable 1.2 Hz and harmonics.

gating actions were taken in July 2013 (by Professor Mike Jones and Mr Alexander Pollak) in a similar manner and after this the oscillations returned to having a stable presence in the data. Figure 3.12 shows an example of stable oscillations within the Stokes Q and U time ordered data taken from November 2013. The exact mechanism through which the 1.2 Hz oscillations propagate through to the data is still unknown.

3.5 The Southern Cryostat

Southern commissioning began in early 2013, the Southern receiver was first taken to the Hartebeesthoek Radio Astronomy Observatory (HartRAO), South Africa for commissioning at a manned site before being taken out to the Karoo. Southern C-BASS also contains a continuous comparison radiometer but, unlike the Northern system, possesses a digital correlation polarimeter. The Southern cryostat is setup in the same way as the Northern (see Figure 3.2) except in respect of two points: the noise diode in the Southern system is housed within the 4 K stage of the cryostat and notch filters

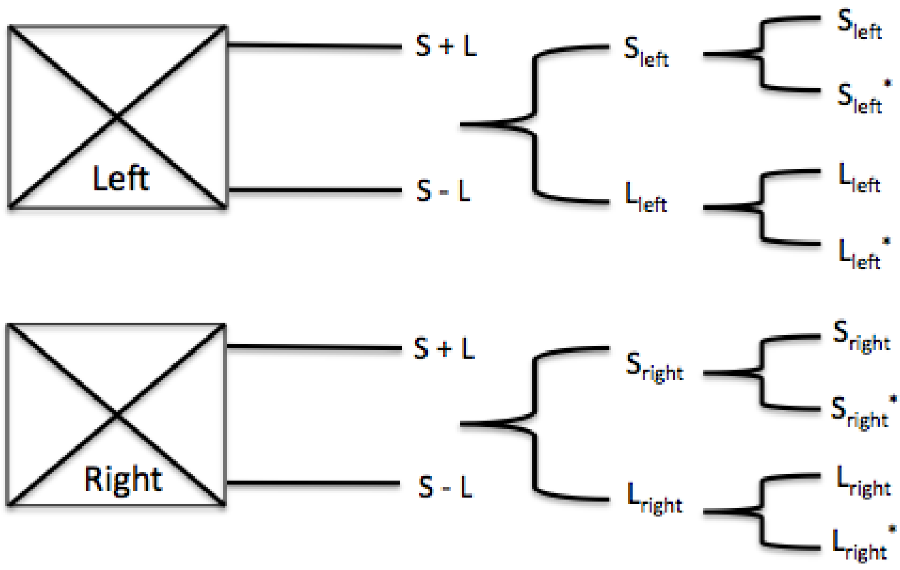

Figure 3.13: A schematic of the signals stored by the Southern digital polarimeter where S denotes the sky signal and L denotes the load signal. The asterisk indicates the 180° phase shift of a signal.

are not required. The digital polarimeter is programmed to store 64 channels of information from each of the two 500 MHz passbands, giving a total of 128 channels. The choice of 64 comes from the 8×8 correlations of the phase shifted left and right receiver channel sky and load signals shown in Figure 3.13.

3.5.1 The Horn

Both the Northern and Southern receiver horns are made up of three sections, the sections are sequential i.e. section three cannot be attached without sections one and two being in place first. During Southern commissioning the passband was measured at ambient temperature using a spectrum analyser and found to display spikes in power at the low frequency end of the band. Figure 3.14 shows three measurements of the passband; first with only section one on, then section one and two and lastly with section one, two and three on. The power spikes can be seen when section two is

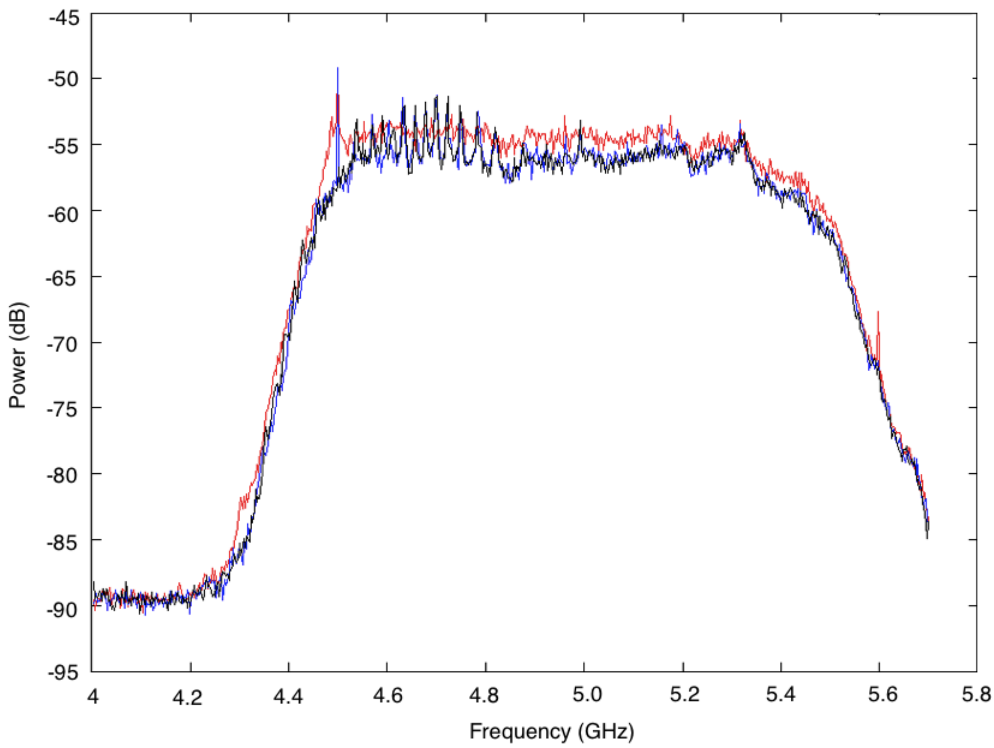

Figure 3.14: The Southern passband measured with only the first section of the horn present (red), then the first and second (blue), then the first, second and third (black). Spikes in power can be seen at the low frequency end whenever the second horn section is included in the measurement.

attached but not when only the first section of the horn is in place.

This implied that standing waves were forming between the second and first horn section, possibly caused by inaccurate machining of the second section. To test for this we used aluminium tape first on the inside of the first section where the first and second section meet and then on the inside of the second section where the first and second section meet. Figure 3.15 shows the results of this taping alongside the passband of all three horn sections. Taping up the second section removes the power spikes confirming the speculation that there was a problem with the machining of the second stage. The second horn was returned to Oxford University for re-machining. The passband shown in Figure 3.16 shows the passband measured with the new, complete horn i.e. all three

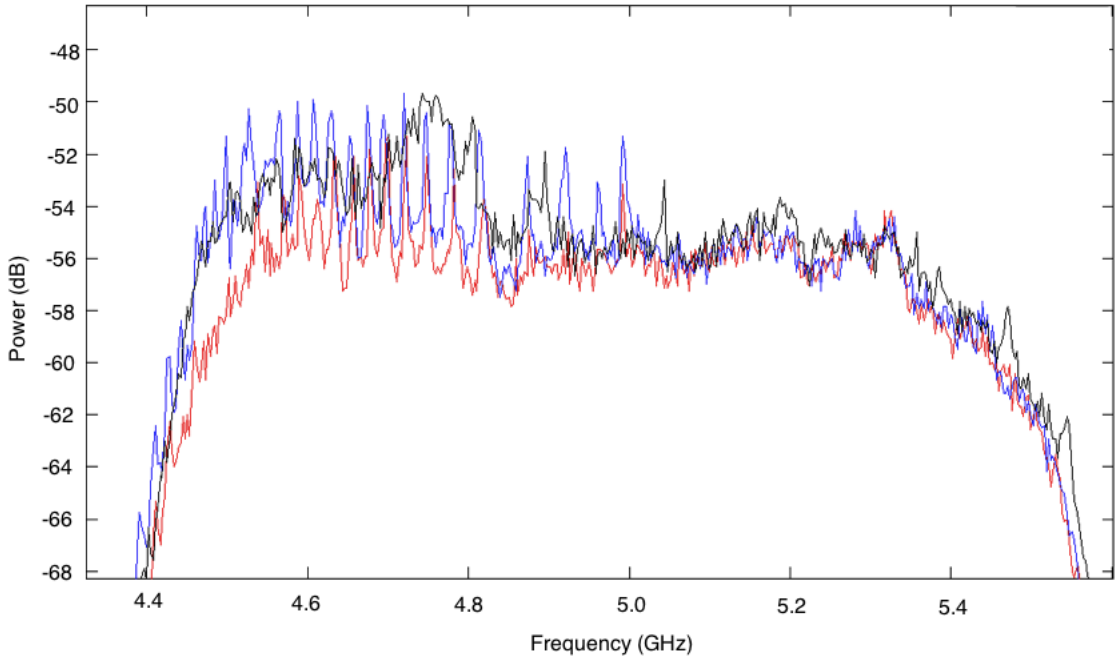

Figure 3.15: The Southern passband measured with all three horn sections present (red), then with aluminium tape at the first/second section boundary within the first section (blue), then with aluminium tape around the first/second section boundary within the second section (black). The low end power spikes are no longer seen when the second section is taped.

sections present using the newly machined second section. No power spikes intrinsic to the horn are visible, however an RFI incident can clearly be seen at 4.5 GHz.

3.5.2 The Noise Diode

The Southern noise diodes differ from the Northern in that they are phase controlled, meaning that they can be changed from featuring entirely in Stokes Q to featuring entirely in Stokes U. Figure 3.17 shows the noise diode injection undergoing a 360° phase shift, the peak-to-peak height of the sinusoid produced is double the magnitude of the noise diode amplitude. In the Northern system the noise diode signal is preset in both Stokes I and Q but not in Stokes U, so when calibrating the data onto a

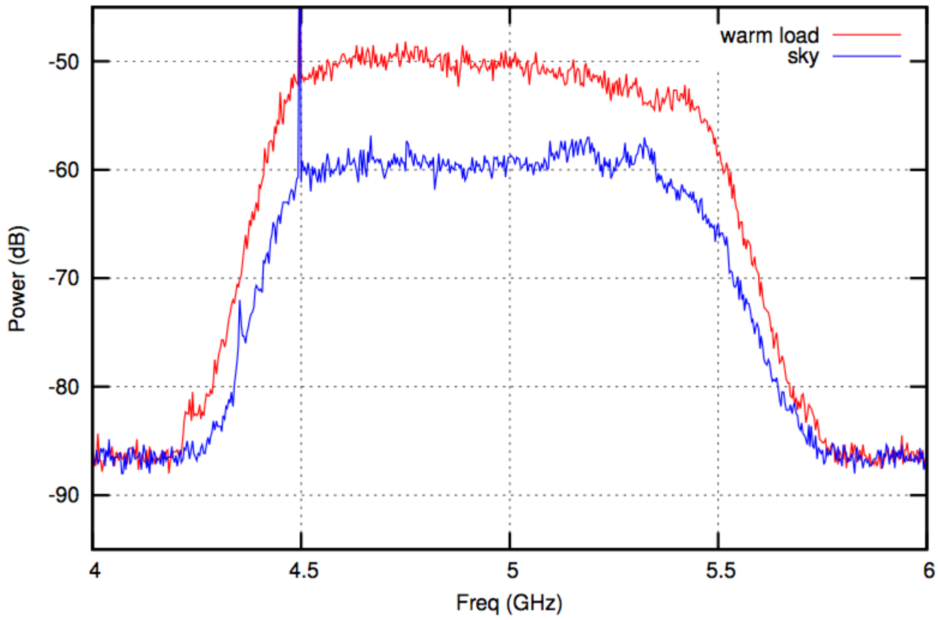

Figure 3.16: Passband measurement using the re-machined second section of the horn in place with the first and third section. The low end power spikes no longer feature; the spike at 4.5 GHz is RFI.

scale where the noise diode is equal to one unit the data reduction pipeline assumes that the calibration factor needed for Stokes U is the same as that needed for Stokes Q. Although a reasonable approximation, this does however assume that the different Stokes Q and U detector diodes behave identically. The Southern system will not need to make this assumption as the noise diode calibration can take place in all three of the linear Stokes parameters, I, Q and U.

3.5.3 Hot/Cold load tests

The Southern receiver temperature was measured using the Hot/Cold load method; the cold load was the sky and the hot load was a slab of ECCOSORB® at ambient temperature. For this test the ‘receiver’ was the cryostat, the external gain rack, 6 m long RF cables and the RFI filtering electronics. The cable length requirement was set by the distance between the telescope dish and the electronics compartment. The Southern

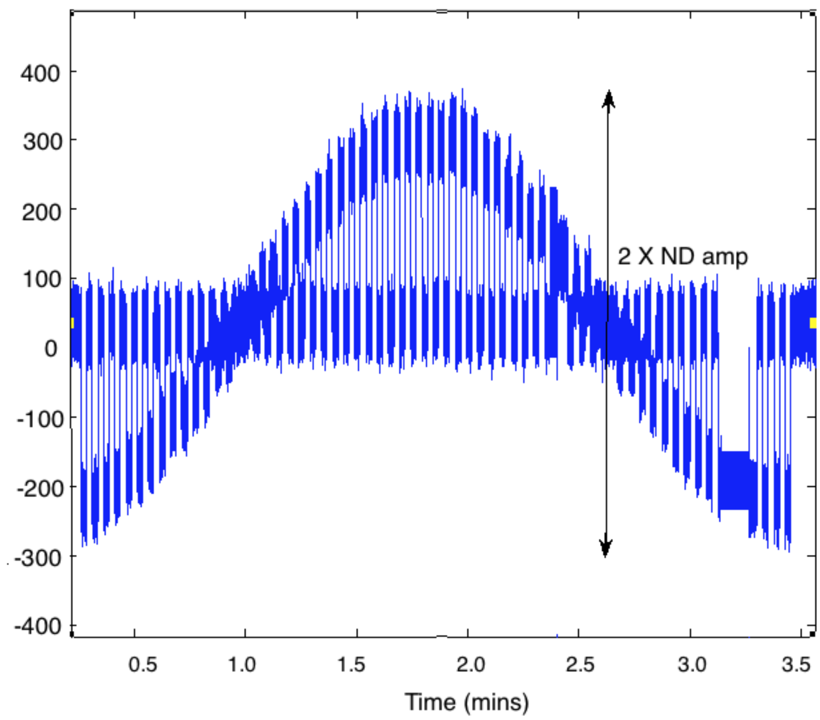

Figure 3.17: One of the Southern Stokes Q channels during a 360° noise diode phase shift.

cryostat contains the same pre-LNA components as the Northern one so the same 8 K noise temperature, which was expected for the Northern cryostat was expected for the Southern cryostat. The external gain rack, cables and filtering electronics had yet to be measured for their noise temperature and so the Hot/Cold load test would provide the first estimate of their combined temperature. Table 3.2 shows the results of the Southern Hot/Cold load test. From Table 3.2 it can be seen that the noise temperature between the four channels of the Southern receiver are consistent with each other.

3.5.4 Receiver Balancing

As previously discussed in Section 2.6.1, both the Northern and Southern radiometers simultaneously observe the sky and an internal reference load set to the temperature of the 5 GHz sky, as observed through the optics. To determine the optimum load tem-

Amp	Hot Load power (dBm)	Cold Load power (dBm)	Y	T_{rx} (K)
1	−14.67	−22.53	7.86	19.7
2	−14.02	−21.50	7.48	22.9
3	−13.20	−20.96	7.76	20.5
4	−10.80	−18.67	7.87	19.6

Table 3.2: The Hot/Cold load test power measurements and receiver temperatures for each of the four paths through the Southern cryostat.

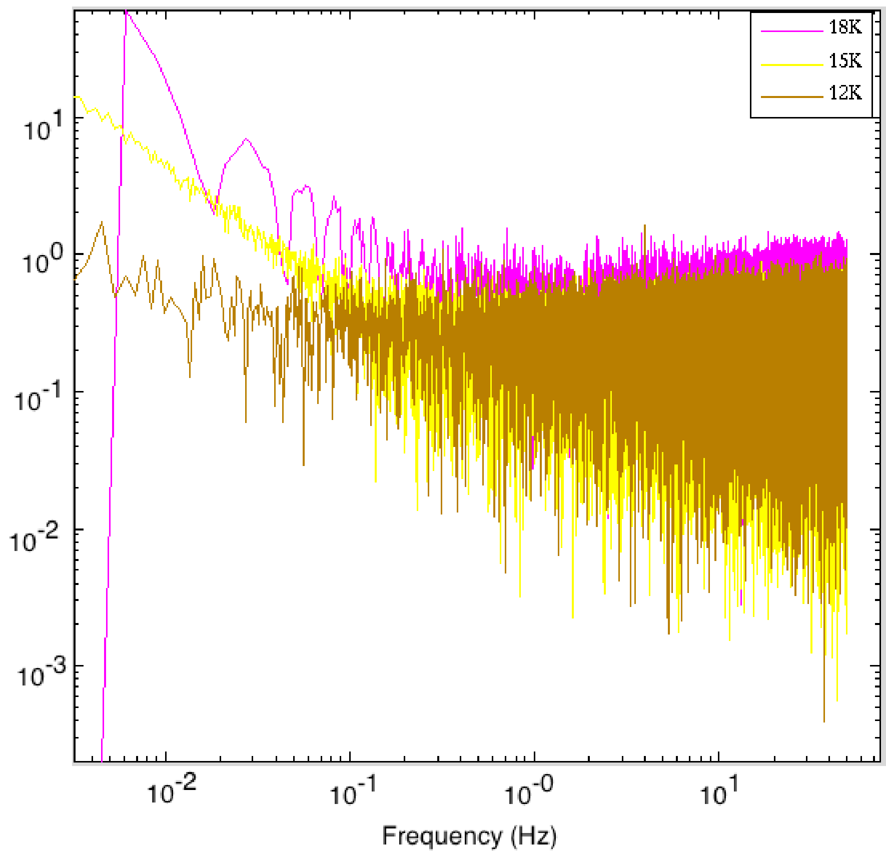

Figure 3.18: Power spectra of three half hour SCP observations which used reference load temperatures of 12, 15 and 18 K.

perature for the Southern system, the telescope was set to observe the South Celestial Pole (SCP) region for an hour an a half and during that time the reference load temperature spent half an hour at 12, 15 and 18 K. The lowest The SCP region was chosen so that the large Galactic plane signal could be avoided and mainly blank sky could be observed. Figure 3.18 shows the three power spectra formed from the Southern blank sky observations at 12, 15 and 18 K. The lowest knee frequency, $\sim$ 10 mHz, is achieved using the lowest reference load temperature of 12 K.

This reference load temperature will increase when the Southern receiver is placed on the telescope and the full optics are secured in place. This is known from experience with Northern receiver which uses a reference load set at 24 K, i.e $\sim$ 19 K contributions from the optics: the baffles, the dish, the mirror, the foam cone and both feed horns.

3.6 System Temperature and Noise Level

The Northern r.m.s. noise level in K $\sqrt{s}$ can be calculated from the power spectrum of time ordered data by fitting Equation 2.12. Figure 3.19 shows a typical fitted power spectrum for a North Celestial Pole stare in intensity. The data have been binned in frequency intervals of 0.5 Hz and so the uncertainties on the blue data points come from the standard deviation within these bins. The green line is the best fit line to the combination of the $1/f$ noise (red line) and thermal noise (black line). The $\nu > 45$ Hz data have been excluded from the fit as they feature interference from the aliased 60 Hz power line (see Section 2.6.3).

The Stokes Q and U white noise levels for several NCP observations were determined using this power spectrum method and their values are documented in Table 3.3. The intensity values are not included as the knee frequency, the frequency at which the white noise contribution is equal to the $1/f$ noise contribution, varies significantly in intensity and effects the fitted white noise values. The $1/f$ contributions are higher in intensity because of atmospheric $1/f$ noise (see Section 2.3), while in polarisation the typical knee frequency is $\sim$ 10 mHz. The mean r.m.s. noise from the power spectrum

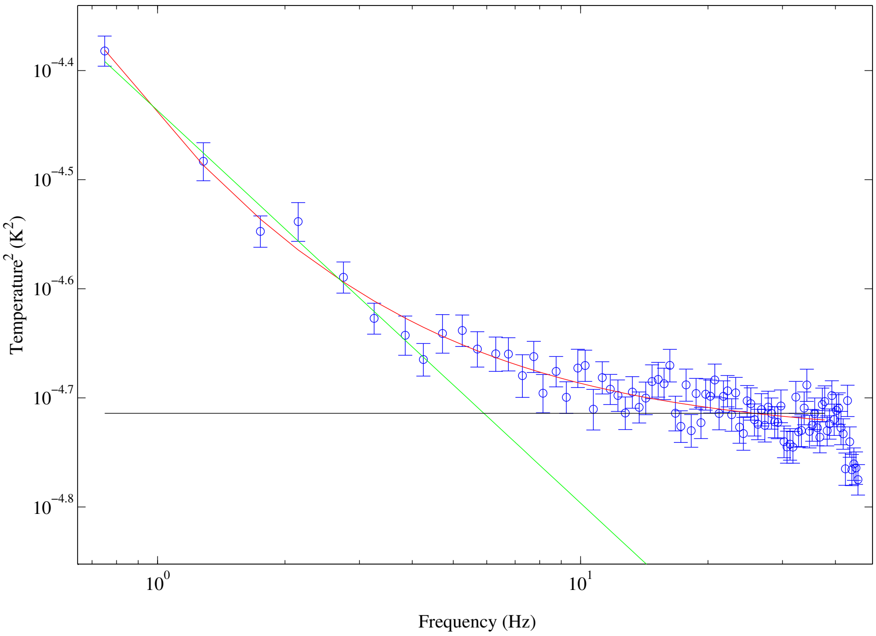

Figure 3.19: The power spectrum of time ordered intensity data taken from August 2013. The binned data points are shown in blue circles and the fit to the combination of $1/f$ (red line) and thermal noise (black line) is in green.

method is (2.03 ± 0.05) mK $\sqrt{\mathrm{s}}$ for Stokes Q and (2.06 ± 0.10) mK $\sqrt{\mathrm{s}}$ for Stokes U.

The survey noise can also be determined from the maps themselves, to achieve this the data from June to November 2013 were made into 6 one month maps. A full six month map was also made from the same data and subtracted from each of the one month maps so that the sky signal could be excluded from the analysis. The survey noise level in Kelvin can be determined by performing the following analysis on a blank patch of sky:

$$\overline{S} = \frac{\Sigma_i \, (H_i \times S_i)}{\Sigma_i \, H_i} \tag{3.5}$$

and

$$\sigma^2 = \frac{1}{N} \, \Sigma_i \, \left(H_i (S_i - \overline{S})^2 \right), \tag{3.6}$$

where S_i and H_i are the signal and hit count in a pixel i respectively, N is the total number of pixels and $\overline{S}$ is the weighted mean signal value. This analysis was performed on

Date	**Q σ (mK $\sqrt{\text{s}}$)**	**U σ (mK $\sqrt{\text{s}}$)**
26/06/13	2.09 ± 0.09	2.00 ± 0.09
09/07/13	2.01 ± 0.10	2.18 ± 0.10
08/08/13	1.99 ± 0.09	2.01 ± 0.09

Table 3.3: Stokes Q and U noise levels in units of mK $\sqrt{\text{s}}$ taken from the TOD as determined by fitting the power spectra of 'blank' data.

Month	**Q σ (mK $\sqrt{\text{s}}$)**	**U σ (mK $\sqrt{\text{s}}$)**
June	2.15 ± 0.10	2.44 ± 0.12
July	2.07 ± 0.10	1.85 ± 0.10
August	1.94 ± 0.10	1.82 ± 0.08
September	1.90 ± 0.10	1.60 ± 0.09
October	1.81 ± 0.10	1.75± 0.09
Novemeber	2.17 ± 0.10	2.01 ± 0.10

Table 3.4: The noise levels in units of mK $\sqrt{\text{s}}$ taken from the one month maps. The 'blank' patch of sky chosen was $-62^\circ < b < -60^\circ$, $60^\circ < l < 65^\circ$.

the $-62^\circ < b < -60^\circ$, $60^\circ < l < 65^\circ$ region of sky, which appeared to be blank by eye. Table 3.4 shows the monthly Stokes Q and U r.m.s. noise values as determined from the maps, the errors were calculated assuming a 5 % uncertainty for the data calibration (see Section 4.6). The means are (2.01 ± 0.15) mK $\sqrt{\text{s}}$ and (1.91 ± 0.29) mK $\sqrt{\text{s}}$ respectively.

Using the thermal noise and the radiometer equation we can also verify that the system temperature calculated from this method is consistent with the system temperature determined from adding the 24 K sky and optics contribution mentioned in the above section to the ~ 14 K receiver contribution calculated in Section 3.3. A thermal noise of 2.0 mK $\sqrt{\text{s}}$ gives a system temperature of 44 K for the Northern bandwidth of 480 MHz; this is constant with the ~ 38 K from Hot/Cold load and receiver balancing tests.

3.7 Northern Survey time

The target sensitivity for the complete survey is 0.1 mK per beam in polarisation. Calculating the total observational time needed to achieve the target sensitivity requires the observing efficiency for the Northern scanning strategy:

$$\eta = \frac{\text{total hits} \times \text{sample time}}{\text{observing time (s)}},$$

where the C-BASS sample time is 0.01 s. The observing efficiency determined from the hit counts from the September 2013 one month map is 66 %, i.e 66 % of the total time is contributing useful survey data.

The number of C-BASS beams on the sky is calculated as $\Omega_{\text{sky}}/\Omega_{\text{beam}}$, where Ω_{sky} is $4\pi \times 0.63$ for Northern C-BASS as only 63 % of the full sky is seen by the Northern receiver. Ω_{beam} is given using the standard formula, $1.133 \times \theta^2_{FWHM}$, where θ_{FWHM} is $0\overset{\circ}{.}73$ and the conversion factor between degrees squared and steradians is 1/3282.8. Taking 2.0 mK $\sqrt{\text{s}}$ as the Northern polarisation sensitivity, 0.1 mK per beam as the Northern target sensitivity and 66 % as the observation efficiency dictates a total observing time of

$$\begin{aligned} t &= \left(\frac{\Omega_{\text{sky}}}{\Omega_{\text{beam}}}\right)\left(\frac{2.0}{0.1}\right)^2\left(\frac{1}{24 \times 60 \times 60 \times 0.66}\right) \text{ days} \\ &= 299 \text{ days.} \end{aligned}$$

As of the beginning of March 2014 ten months of good quality survey data had been collected, although for two of those months the observing efficiency was slightly lower due to an inefficiency in observing calibrators, which has since been corrected. This puts the Northern receiver well on schedule to end observing in the summer of 2014.

3.8 Summary

The chapter has detailed the technical contributions to Northern and Southern commissioning by the author of this work. The components of the Northern cryostat and external gain box were explained and the problem of microphonic oscillations due to the cryostat cold head and poor quality cabling was introduced. The search for sources of permanent in-band RFI resulted in the location and removal, from the C-BASS passband, of two such sources using notch filters. Hot/Cold load testing revealed the Northern receiver temperature to be between 12 – 14 K and the Southern receiver temperature to be $\approx$ 20 K. The formation of standing waves within the Southern horn was detected and resolved through the re-machining of the horn. Southern commissioning will extend beyond the submission of this thesis and after Southern C-BASS has performed reliably in survey mode for several weeks at HartRAO it will be moved out to the Karoo.

During the Northern commissioning period technical work was completed alongside the simultaneous construction of the C-BASS data reduction software pipeline. This pipeline is a collection of all the code required to assemble and process the data acquired from the digital backend into a form suitable for scientific analysis. The data reduction pipeline will be applicable for use with both Northern and Southern data, though as it was initially tested on the Northern data several Southern specific alterations may be required. Chapter 4 will now go through the C-BASS data reduction pipeline.

Chapter 4

Northern Data Reduction

C-BASS data are processed by a selection of MATLAB, C++, IDL and Python software written by the collaboration and collectively known as the 'pipeline'. The pipeline is responsible for removing bad data, correcting for systematic effects, calibration and map making. The data fed into the pipeline comprised of a six column array of (I1+V)/2 − load1, Q1, U1, Q2, U2 and (I2-V)/2 − load2 formed from differencing the backend channels (see Figure 2.5). The Q1/U1 and Q2/U2 channels are strongly correlated as the two Q/U measurements have been through identical radiometer components and are only separated into Q1/U1 and Q2/U2 in the polarimeter. At the time of writing, the pipeline had been tested on Northern data only because there were no Southern survey observations.

The pipeline currently consists of the following stages: alpha correction, 1.2 Hz oscillation removal, radio frequency interference (RFI) removal, pointing monitoring, zenith opacity calculation, astronomical calibration and map-making. Two areas of the pipeline were significantly contributed to by the author of this thesis, namely 'atmospheric opacity' and 'astronomical calibration'. Hence a relatively detailed description, in comparison to the other steps, of these two will be given.

4.1 Alpha Correction

The Northern data contain not only the sky and load signals but also a noise diode signal, which is fired every four minutes in order to calibrate the data. The noise diode signal appears in Stokes I and Q but not in U. The main function of the alpha correction is to put the data onto a scale where a noise diode event equals unity. The alpha value itself has a magnitude and a phase component; the magnitude is interpolated over the schedule time and used to correct for gain drifts within this period. As the noise diode should not appear in U it can be used to quantify the leakage between the Q and U channels and to correct this leakage using the phase component of the alpha value, thus ensuring that the noise diode appears entirely in Q and not in U.

After the alpha correction function the data are in the form of an 8 column array; the two new columns, Q3 and U3 are the average Stokes Q and U values.

4.2 1.2 Hz Oscillation removal

The Northern system has an unfortunate quirk; the cryostat is subject to microphonic oscillations that propagate through to the intensity and polarisation data. These microphonics are at 1.2 Hz and its harmonics as the cryostat is cooled by a cryogenic pump with a 1.2 Hz periodic cycle (see Section 3.4). The solution is to remove the oscillations during post-processing. The 1.2 Hz oscillation removal code estimates a template based on the temperature variation of the cold load, which is monitored by a temperature sensor within the cryostat:

$$\delta T = A(t)\ \sin\left(B(t)t + C(t)\right), \tag{4.1}$$

where $A(t)$ is the sinusoid amplitude and $B(t)t + C(t)$ is the phase. Then the pipeline filters the TOD under 1.1 Hz within the Fourier domain, normalises the filtered TOD using the fitted sinusoid amplitude and then folds the normalised, filtered TOD with the sinusoid phase. The result is a cold load oscillation template, which is created for

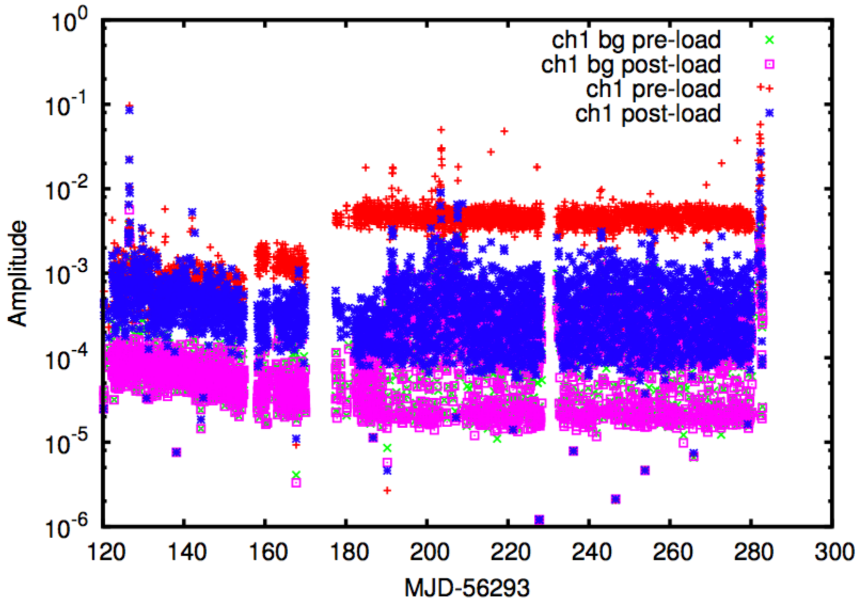

Figure 4.1: The amplitude, in Kelvin, of the cold load oscillations before (red points) and after (blue points) the application of the cold load removal code plotted alongside the signal at 1.5 Hz (purple points). If the cold load oscillation code was completely removing the 1.2 Hz signal then the blue points would be at the same level as the purple points. Image courtesy of collaboration member Dr. Mike Peel.

each two hours of TOD. These templates are subtracted from the TOD to leave data less affected by 1.2 Hz oscillations.

Figure 4.1 shows the current success of the of the 1.2 Hz oscillation removal code. The magnitude of the TOD power spectrum spike at 1.2 Hz is plotted for data with (blue stars) and without (red plus signs) the application of the 1.2 Hz removal code. The 1.5 Hz level pre- and post-correction (green crosses and purple squares respectively) is also shown to demonstrate the level at which the 1.2 Hz signal should lie after the correction. The x-axis shows days from 1st January 2013 and it can be seen that the cold load oscillations increased in magnitude during April (~ 160 on the x-axis) and again at the end of June (~ 180 on the x-axis) after a six day offline period during which the cryostat was being worked on. Also, it is clear from Figure 4.1 that although the correction is reducing the oscillation magnitude by roughly a factor of twenty in magnitude, it is not yet working optimally. If functioning optimally the correction would bring the oscillation magnitude down to the noise level.

The 1.2 Hz oscillations are one of the systematics being worked on within the C-BASS data. However, with the current 1.2 Hz code in place the corrected data are of sufficient quality to be processed by the subsequent pipeline code and used for analysis within high signal-to-noise map regions. The 1.2 Hz oscillations are visible by eye within the TOD but not within the maps as their random phases mean they do not add coherently.

4.3 RFI removal

As with most radio telescopes, C-BASS is susceptible to in-band and very bright out-of-band sources of RFI. Permanent features of RFI like local man-made transmitters and geostationary satellites are dealt with in Northern C-BASS by hardware (see Section 3.1.4). Transient sources of RFI, however, like aeroplanes, are dealt with by the pipeline. The RFI removal exploits the fact that RFI vary rapidly and possess large signals in both intensity and polarisation and uses this information to identify and remove such signals. The data are cut into short chunks and the standard deviation of these chunks is used to identify data contaminated by RFI.

Some RFI, however, varies over longer timescales. In these cases, the signal is identified as RFI using both the standard deviation of the data chunk and the fact that most RFI is circularly polarised and so the Channel 1 ((I + V)/2 - Load) and Channel 8 ((I - V)/2 - Load) signals display a different structure during a circularly polarised RFI event. An example of a circularly polarised RFI event is shown in Figure 4.2 and the different structure between Channel 1 and Channel 8 can be seen. The difference in magnitude is due to the different gains in receiver channels one and two.

RFI flagging can be seen at work in the example given in Figure 4.3. Intensity (I) and average Stokes Q and U channels (Q3 and U3) are shown alongside the flagging parameter, which goes from 0 to 1 when the data are flagged. In this example the three

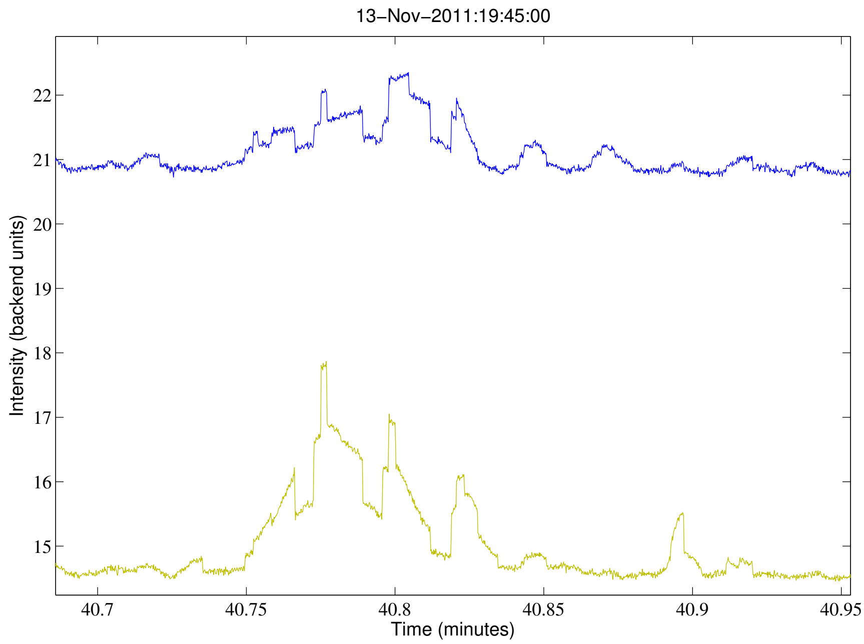

Figure 4.2: An example of a circularly polarised RFI event in Channel 1 (blue) and Channel 8 (yellow). Note the different shape of the signal in Channel 1 when compared to Channel 2.

RFI incidents seen in the Stokes I, Q and U data have been flagged.

4.4 Pointing

Northern C-BASS moves in both azimuth and elevation so it can be programmed to slew to any source on the visible sky. However, there will always be a slight discrepancy between where the telescope is physically positioned in azimuth and elevation and where its encoders record that it is positioned. This discrepancy is due to a combination of several effects, such as, the encoders may not be set to read exactly zero when azimuth and elevation are zero (encoder offsets), the azimuth and elevation telescope axes may not be perfectly perpendicular (tilt) and also, the antenna dish can deform under its own weight. The latter feature is most notable with large antennas at high elevations.

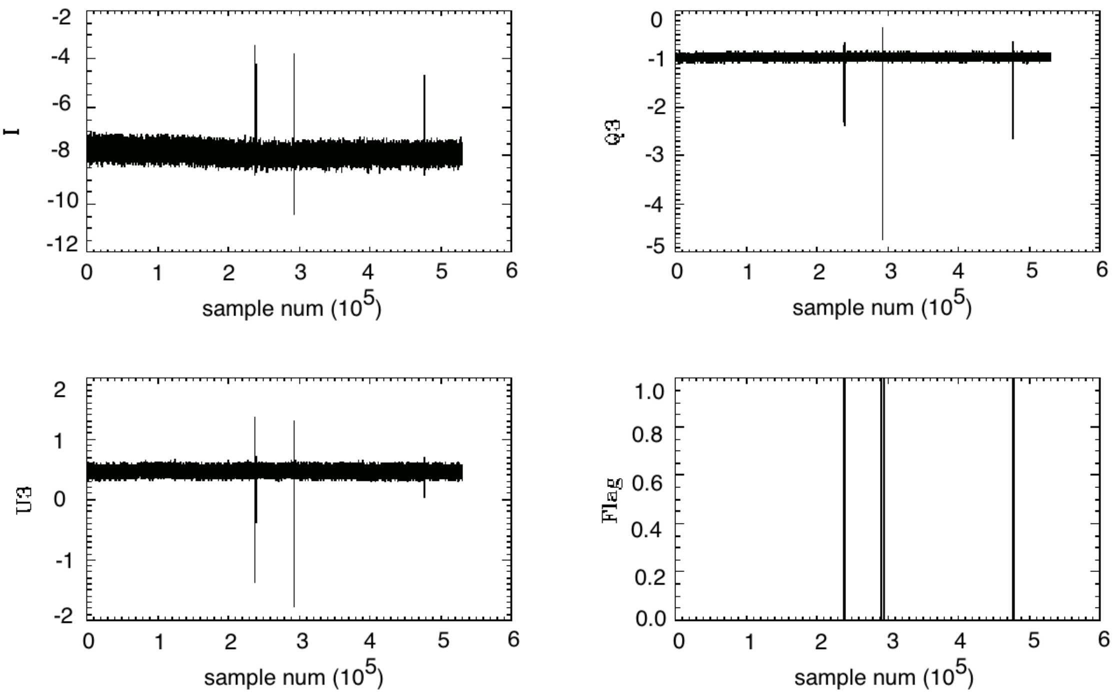

Figure 4.3: TOD data which exhibit three RFI events in Stokes I and the average Stokes Q and U. The Stokes parameters are shown in Kelvin while the flag parameter is a logic value which indicates flagged and non-flagged data. The RFI events can be seen to have been flagged.

A pointing model takes all these factors into account, calculates the difference between where the telescope is programmed to be and where it really is (the pointing offsets) and then applies a correction. The C-BASS pointing model is updated roughly every two months. It is important for the pointing uncertainties to be low as the observations will be stacked to form the complete survey and random pointing offsets will smear out the power measured thus raising the noise in each pixel. To ensure the power measured within the beam is within 3 % of the total source power, the pointing offsets should be no more than 0.1 of the beam FWHM (Rohlfs & Wilson 2004). This can be seen by considering the power response of a Gaussian beam:

$$P(\theta) = P_0 e^{\frac{-\theta^2}{2\sigma^2}}, \tag{4.2}$$

where

$$\sigma = \frac{FWHM}{2\sqrt{2\ln(2)}}, \tag{4.3}$$

therefore

$$\frac{P(\theta)}{P_0} = e^{-4\ \ln(2)(\frac{\theta}{FWHM})^2} \tag{4.4}$$

and to provide $P(\theta)/P_0 = 0.97$ the pointing offsets would have to be 0.104 FWHM. For C-BASS this means pointing offsets of no more then 4$'\!.$5. The C-BASS beam, within two degrees of the main beam peak, has been measured using the astronomical calibrator Cassiopeia A. Figure 4.4 compares this measurement with the GRASP simulated main beam. The measured main beam can be seen to be well estimated by the simulated beam while the first sidelobes show some deviation from the simulation.

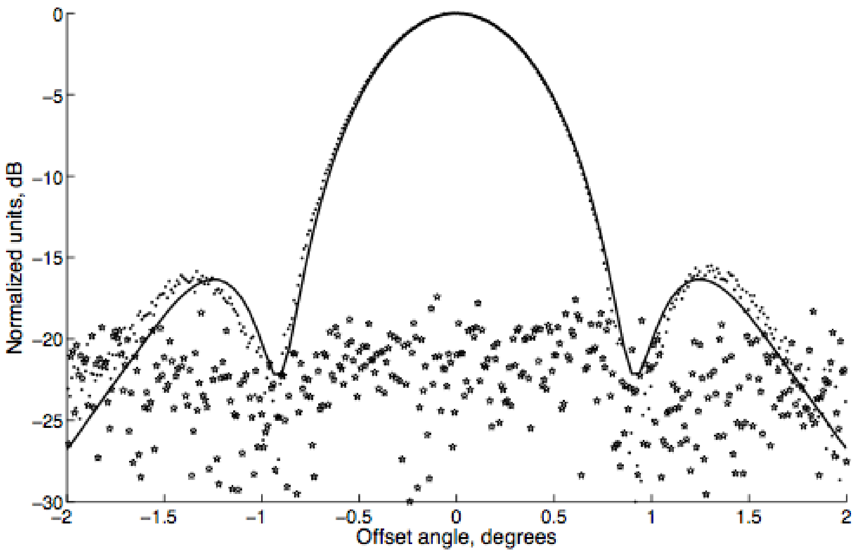

Figure 4.4: The simulated C-BASS main beam compared with observations of Cassiopeia A. Observational data for intensity are shown as points while polarised intensity data are shown as stars. The solid black line is the main beam simulated using GRASP. Image taken from Holler et al. (2013)

The pointing code within the pipeline fits 2D Gaussians to Cygnus A, Cassiopeia A, Taurus A and M42 and records the pointing offsets. The 2D Gaussian fitting routine is described in further detail in Section 4.6.1 and shows the main beam to be well estimated by a Gaussian model. The recorded values are written out daily by the automated data reduction pipeline onto an internal C-BASS website, which is monitored by a member of the collaboration assigned to the task. The total pointing offsets recorded for two weeks in March 2014 are shown in Figure 4.5 and it can be seen that pointing was good to $< 5'$. As soon as the average offset reaches $4.'5$ the pointing model is updated. The pointing models are normally stable over a period of roughly six months.

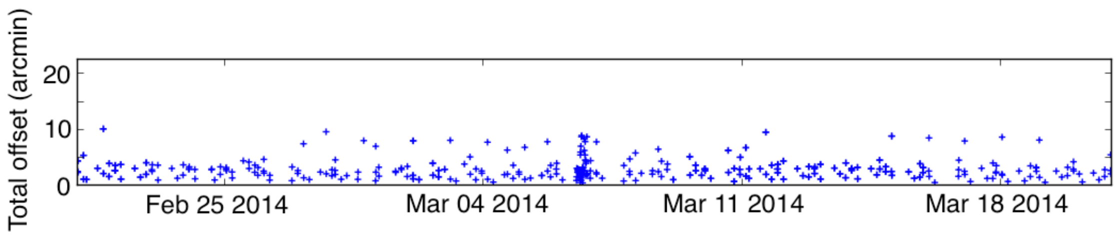

Figure 4.5: A typical pointing offset report from the automated daily pipeline showing the total pointing offsets recorded for two weeks worth of data.

4.5 Atmospheric Opacity

When observing from the ground it is necessary to consider the effect of the atmosphere on the data, namely absorption. Absorption and emission of incident electromagnetic radiation occurs because of the presence of water and oxygen molecules within the atmosphere. Atmospheric opacity (τ) describes the severity of this effect. For a source of brightness temperature $T_b(0)$, travelling through the atmosphere which is at temperature T_{atmos} the measured brightness temp $T_b(m)$ is

$$T_b(m) = T_b(0)e^{-\tau} + T_{\text{atmos}}(1 - e^{-\tau}). \tag{4.5}$$

The first term describes atmospheric absorption, which decreases the measured brightness temperature and is present in both the intensity and polarisation signals. The second term describes atmospheric emission, which increases the measured brightness temperature and is only present in intensity as the emitted photons have no preferred orientation. Pietranera et al. (2007) note the generation of polarised signals between 97 and 220 GHz at a level of μK by ice crystals in the upper atmosphere. This effect, however, is associated with higher measurement frequencies (ν > 20 GHz) and is not thought to be a problem at 5 GHz.

Atmospheric opacity is dependant on the water and oxygen absorption coefficients (Waters 1976):

$$\tau_0 = \sum_{z=122{,}200\ \mathrm{cm}}^{2{,}000{,}000\ \mathrm{cm}} \left(\frac{k_{\mathrm{H_2O}}}{\mathrm{cm}^{-1}} + \frac{k_{\mathrm{O_2}}}{\mathrm{cm}^{-1}} \right) \left(\frac{\Delta z}{\mathrm{cm}} \right), \tag{4.6}$$

where τ_0 is the zenith opacity, $k_{\mathrm{H_2O}}$ and $k_{\mathrm{O_2}}$ are the water and oxygen absorption coefficients respectively and the height (z), is measured from the location of Northern C-BASS (1.222 km above sea level) to the beginning of the stratosphere. Figure 4.6 displays the relationship between the absorption coefficients and the frequency of observation. It should be noted that the Figure 4.6 only hold true for dry weather.

Zenith opacity relates to a specific elevation opacity as follows:

$$\tau \approx \frac{\tau_0}{\sin \theta_{\mathrm{el}}}. \tag{4.7}$$

The observation elevation angle (θ_{el}) effects the magnitude of opacity because it determines the amount of atmosphere being looked through. The relation between zenith opacity and a specific elevation opacity is an approximation as it breaks down at low elevations where the atmosphere is no longer optically thin. This model and its uses will be discussed further in Section 4.5.2.

The C-BASS pipeline has two zenith opacity calculations in place, a theoretical calculation and an empirical calculation known as the ‘SkyDip’ method. The SkyDip zenith opacities are the preferred values for use, while the theoretical values are simply held in reserve in case the SkyDip data are all flagged as bad data.

4.5.1 Theoretical Opacity

It is possible to calculate a theoretical zenith opacity for the C-BASS telescopes via a model which uses measurements taken by their temperature, pressure and humidity

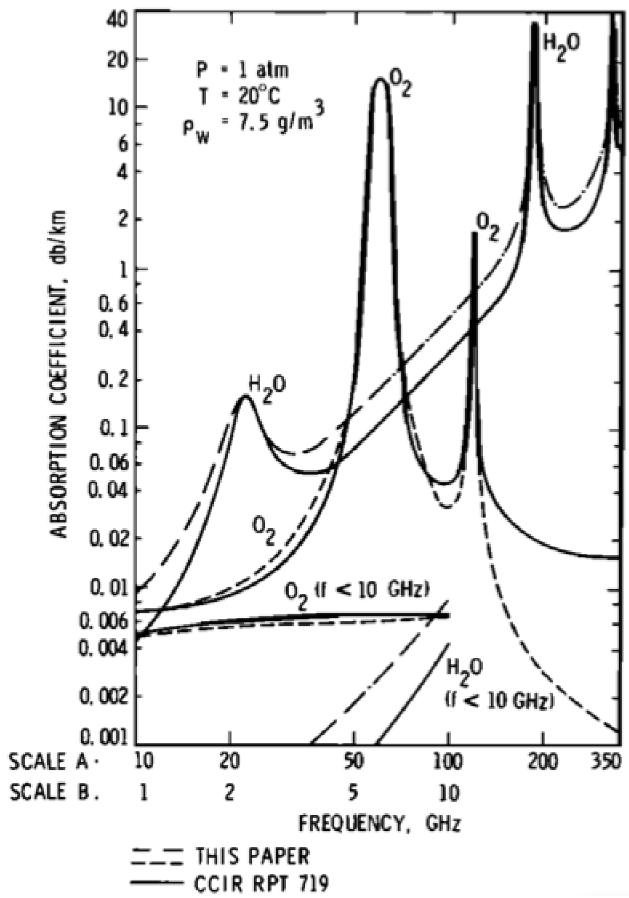

Figure 4.6: The variation of the water and oxygen absorption coefficients with frequency for a set temperature, pressure and water vapour density (Smith 1982). The two x-axis scales also allow the $\nu < 10$ GHz oxygen and water absorption coefficient dependancies on frequencies to be plotted alongside the higher frequency relations. It should be noted that the y-axis units are dB/km.

sensors. Although this method uses empirical readings, it is still termed theoretical as it relies on the following models to derive the water and oxygen absorption coefficients.

Water absorption coefficient

Atmospheric water absorption coefficients can be calculated as follows (Waters 1976):

$$\frac{k_{\mathrm{H_2O}}}{\mathrm{cm^{-1}}} = \left(\frac{\rho}{\mathrm{g\ m^{-3}}}\right)\left(\frac{\nu}{\mathrm{GHz}}\right)^2 \Delta V \left(\frac{T}{\mathrm{K}}\right)^{-3/2} \times A, \tag{4.8}$$

where

$$\Delta V = 2.96\left(\frac{P}{\text{mbar}}\frac{1}{1013}\right)\left(300\left(\frac{T}{\text{K}}\right)^{-1}\right)^{0.626}\left(1 + 0.018\left(\frac{\rho}{\text{g m}^{-3}}\right)\left(\frac{T}{\text{K}}\right)\left(\frac{P}{\text{mbar}}\right)^{-1}\right), \quad (4.9)$$

and

$$A = \left(7.18\left(\frac{T}{\text{K}}\right)^{-1} e^{-644\frac{T}{\text{K}}^{-1}} \frac{1}{(494.40190 - \left(\frac{\nu}{\text{GHz}}\right)^{2})^{2} + 4\left(\frac{\nu}{\text{GHz}}\right)^{2}\Delta V^{2}} + 2.77\times10^{-8}\right), \quad (4.10)$$

where T is the ambient temperature, P the pressure, ν the frequency and ρ is the water vapour density. The variation of temperature with altitude, referred to as the lapse rate (k_w) is taken to be a 6.5 K decrease per km up to 11 km and then the temperature remains constant through to 20 km (Sissenwine, Dubin & Wexler 1962).

The change in pressure over altitude is described by the barometric formula and uses initial pressure (at 1222 m) as the mean read-out from the telescope.

$$\frac{P}{\text{Pa}} = \begin{cases} \frac{P_0}{\text{Pa}}\left(\frac{T}{T+k_w\Delta z}\right)e^{\frac{gM}{R_d k_w}}, & \text{if } z \leq 11,000 \text{ m}, \\ \frac{P_0}{\text{Pa}}\, e^{\frac{-gM\Delta z}{R_d T}}, & \text{if } 11,000 \text{ m} < z < 20,000 \text{ m}, \end{cases} \quad (4.11)$$

where g is gravitational acceleration (9.81 m s^{-2}) and M is the molar mass of dry air (0.0290 kg mol^{-1}). R_d, the gas constant is taken as 8.314 JK^{-1}mol^{-1} and Δz, the change in height used for numerical integration, is 200 m.

Water vapour density can be calculated from the water vapour density at sea level (ρ_w) using Equation 4.12 from (Kopp & Wallace 2004), which should hold true for the 1– 20 km region of interest. For this region, the difference between height (z) and geopotential altitude (h) is considered negligible and at heights above 15 km ρ remains constant.

$$\frac{\rho}{\text{g m}^{-3}} = \left(\frac{\rho_w}{\text{g m}^{-3}}\right)e^{-0.5(\frac{2\frac{h}{\text{m}}}{3})^{\frac{5}{2}}}. \quad (4.12)$$

where the water vapour density at sea level is calculated as (Brutsaert 1975; Wagner & Pruss 1993)

$$\frac{\rho_w}{\text{g m}^{-3}} = 0.622\left(\frac{P_{wv}}{\text{mbar}}\right)\left(\frac{R_d}{\text{mbar m}^3\text{ K}^{-1}\text{ g}^{-1}}\right)^{-1}\left(\frac{T}{\text{K}}\right)^{-1}, \quad (4.13)$$

where

$$\frac{Pwv}{\text{mbar}} = \left(22.064 \times 10^4\right) e^C \tag{4.14}$$

and

$$C = 647.096 \left(\frac{T}{\text{K}}\right)^{-1} (a_1 t + a_2 t^{1.5} + a_3 t^3 + a_4 t^{3.5} + a_5 t^4 + a_6 t^{7.5}), \tag{4.15}$$

where $a_1 = -7.8595$, $a_2 = 1.8441$, $a_3 = -11.7866$, $a_4 = 22.6807$, $a_5 = -15.9619$, $a_6 = 1.8012252$ and $t = 1 - \left(\frac{T}{\text{K}}\right)/647.096$. R_d, the gas constant is taken as 8.314×10^{-2} mbar m^3 K^{-1} mol^{-1} and the molecular weight of water (18) is used to convert between moles and grams.

Water absorption coefficients can be calculated for each 200 m interval by using Equations 4.8 – 4.15. A similar method of theoretical opacity calculation was carried out by Bersanelli et al. (1995) for their measurements of the CMB at 1.47, 2.0, 3.8, 7.5, 10 and 90 GHz and they note that at low frequencies ($\nu < 3.8$ GHz) the water vapour contribution to opacity is essentially negligible.

Oxygen absorption coefficient

At 5 GHz, for dry weather, water absorption is not the dominant factor in opacity calculations; oxygen absorption is. A simple version of the oxygen absorption coefficient calculation, which does not take into account quantum transitions, was used (Frey 1999). This is because strong resonant absorptions due to the oxygen magnetic dipole moment seen at 60 and 120 GHz, will have negligible effect on our 5 GHz measurements.

$$\frac{k_{O_2}}{\text{cm}^{-1}} = 0.011 \left(\frac{\nu}{\text{GHz}}\right)^2 \left(\frac{P}{\text{mbar}} \frac{1}{1013}\right) \left(300 \left(\frac{T}{\text{K}}\right)^{-1}\right)^2 \gamma \left(\frac{1}{\left(\frac{\nu}{\text{GHz}} - 60\right)^2 + \gamma^2} + \frac{1}{\left(\frac{\nu}{\text{GHz}}\right)^2 + \gamma^2}\right), \tag{4.16}$$

where

$$\gamma = \gamma_o \left(\frac{P}{\text{mbar}} \frac{1}{1013}\right) \left(\frac{300}{T}\right)^{0.85}, \tag{4.17}$$

Hour	Theoretical opacity
00:00	0.0083 ± 0.00014
02:00	0.0090 ± 0.00016
04:00	0.0091 ± 0.00016
06:00	0.0091 ± 0.00017
08:00	0.0091 ± 0.00017
10:00	0.0091 ± 0.00017
12:00	0.0091 ± 0.00017
14:00	0.0091 ± 0.00016
16:00	0.0089 ± 0.00015
18:00	0.0087 ± 0.00013
20:00	0.0085 ± 0.00012
22:00	0.0085 ± 0.00012

Table 4.1: The theoretical opacity values taken every two hours for 9^{th} December 2013.

$$\gamma_o = \begin{cases} 0.59, & \text{if } P \geq 333 \text{ mbar} \\ 0.59\left[1 + 0.0031\left(333 - \frac{P}{\text{mbar}}\right)\right], & \text{if } 25 \text{ mbar} \geq P \geq 333 \text{ mbar} \\ 1.18, & \text{if } P \leq 25 \text{ mbar}. \end{cases} \tag{4.18}$$

Water and oxygen absorption coefficients can then be used in Equation 4.6 to find the zenith opacity. Table 4.5.1 gives an example of typical values theoretical opacity. These particular values were calculated every two hours of 9^{th} December 2013. The uncertainties were calculated assuming 5 % uncertainties for the temperature, pressure and relative humidity measurements.

4.5.2 The SkyDip Method

When a telescope performs a 'SkyDip' it slews down through the atmosphere and then up again. As atmospheric gas molecules diminish in number with increasing altitude, the aim is to measure the change in signal intensity resulting from the change in opacity. Figure 4.7 shows an example of a SkyDip as seen in the six raw data channels which come from the digital backend. The intensity channels, channel 1 (shown in blue) and 8 (shown in yellow) are the only channels which show an increase in temperature as the telescope slews through the atmosphere. The telescope detector diodes have a negative response to the antenna power, which is why the SkyDip events appear as dips. The three square waves occur when the noise diode signal is injected into the sky signal. During a SkyDip the telescope first slews to elevation = 60° so that the 20° dip in elevation can be carried out between elevation = 60° and 40°. Figure 4.8 shows an example of the change in elevation the telescope undergoes during a typical SkyDip.

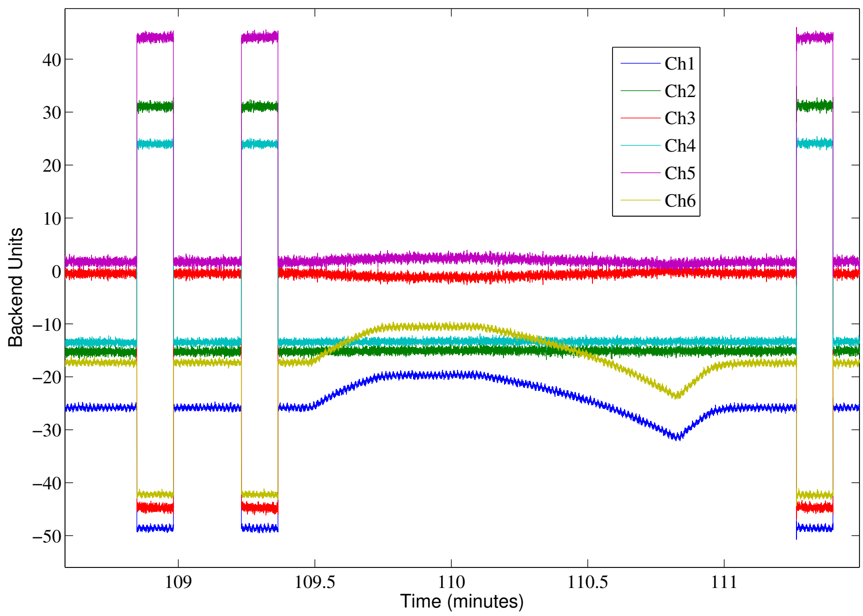

Figure 4.7: An example of a SkyDip as seen in the six raw data channels out of the digital backend. The intensity channels (shown in blue and yellow) show the increase in temperature due to a SkyDip while the polarisation channels (shown in green, light blue, red and purple) are unaffected.

Equation 4.19 outlines the basic radiometer power equation, explicitly stating the

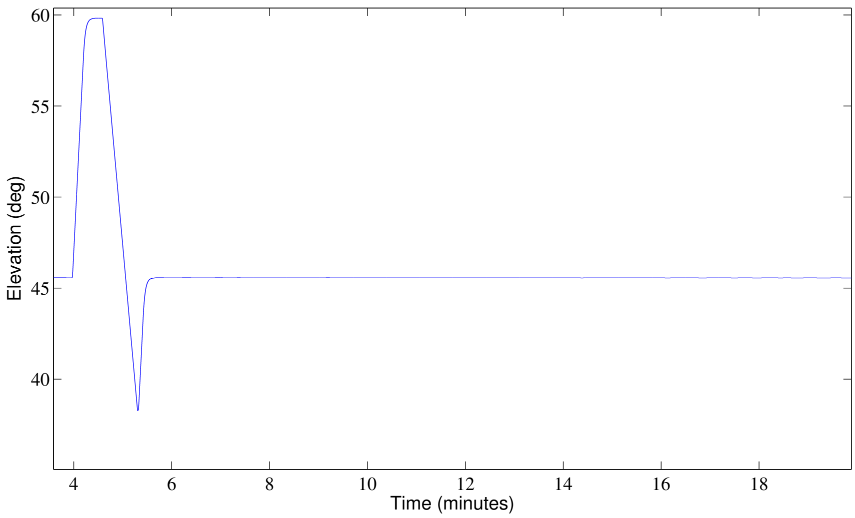

Figure 4.8: The change in elevation during a SkyDip.

contributions to receiver temperature.

$$P = k_B\ G\ \Delta\nu\ T_{\rm sys} = k_B\ G\ \Delta\nu\ (T_{rx} + T_{\rm sky}\ e^{-\tau} + T_{atmos}(1 - e^{-\tau})), \tag{4.19}$$

where $T_{\rm sky}$ is the combined extra-Galactic, Galactic and CMB contributions. For this analysis the extra-Galactic and Galactic contributions were assumed to be negligible therefore $T_{\rm sky}$ was assumed to equal $T_{\rm cmb}$. Comparison between the empirical and theoretical opacity calculations will assess the validity of this assumption. First order Taylor expansion can be used to express $e^{-\tau}$ as $1 - \tau$ so the following approximation can be made:

$$T = \tau_0 \left(T_{\rm atmos} - T_{\rm sky}\right) {\rm cosec}(\theta_{el}) + (T_{rx} + T_{\rm sky}), \tag{4.20}$$

where

$$T_{\rm atmos} = T_{\rm amb} - (0.0065 \times 778). \tag{4.21}$$

$T_{\rm atmos}$, the atmospheric temperature is calculated as the temperature 2 km above sea-level (2 – 1.22 km above the telescope). $T_{\rm amb}$ is the ambient temperature measured at the telescope and T_{rx} is the receiver noise temperature.

Zenith opacity can be determined via the gradient (m) of the linear plot between

Date	**Hour**	**Elevation Range** (°)	$\frac{\sigma m}{m}$ (%)
2010-09-01	13	12	0.57
2010-09-02	03	12	0.82
2010-09-03	09	12	0.12
2010-09-09	08	12	0.70
2010-11-02	09	20	0.02
2010-11-03	14	20	0.02
2010 -11-04	08	20	0.05
2010-11-05	12	20	0.04
2010-11-07	12	20	0.04
2010-11-08	13	20	0.05

Table 4.2: The gradient percentage error values for various surveys of difference SkyDip elevation range. The starting elevation for the SkyDip is the survey elevation of 37°.

measured temperature and cosec(elevation angle):

$$m = (T_{\mathrm{amb}} - T_{\mathrm{sky}}) \times \tau_0. \tag{4.22}$$

This method makes the assumption that the atmosphere is a uniform slab at a constant temperature, taken here to be the temperature 2 km above sea-level. This uniform slab model of the atmosphere only holds true at elevation angles over 30° as below that the atmosphere is no longer optically thin. Figure 4.9 shows a SkyDip as seen by intensity Channel 1 from a special survey schedule designed to dip the telescope far lower in elevation than the usual survey SkyDips. The linear model is plotted over the data (blue points) in red and the residuals between the data and the model are plotted on a second y-axis in green. From Figure 4.9 it can be seen that the linear relationship between temperature and cosec(θ_{el}) breaks down at low elevations. Therefore the SkyDip linear fit ignores data from above the uniform slab threshold of cosec(θ_{el}) = $2/\theta_{\mathrm{el}} < 30°$.

SkyDips occur once in every survey schedule and the first Northern C-BASS surveys featured SkyDips covering a 12° elevation range. Table 4.2 presents the gradient errors from the linear fits taken from several surveys of both 12° and 20° elevation ranges. It reveals that the lowest percentage errors on the gradient are achieved using a

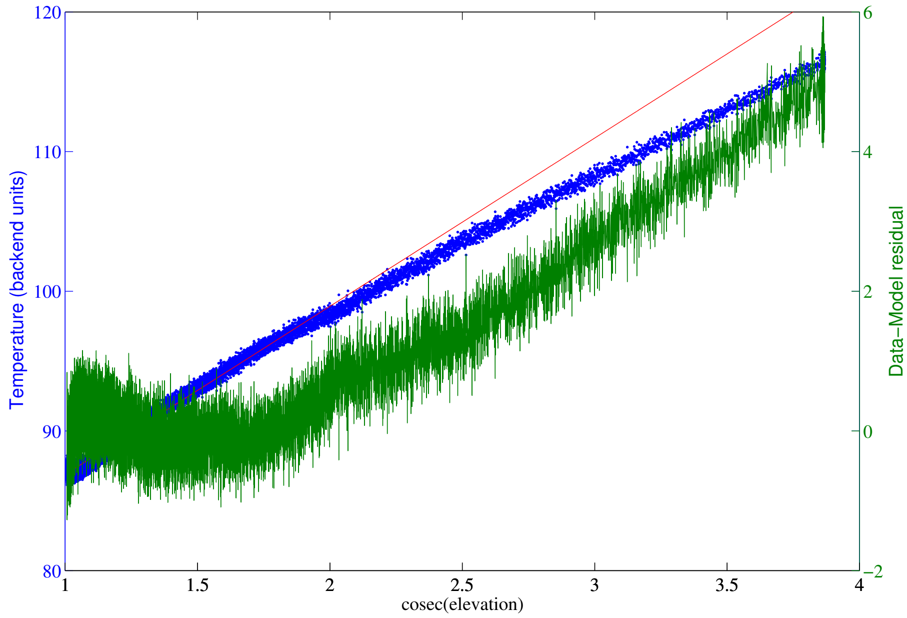

Figure 4.9: An example of the linear relationship between Temperature and cosec(elevation) during a SkyDip for elevations lower than 30°. The residuals between the data (blue points) and the linear model (red line) are plotted on the second y-axis in green to show the deterioration of the linear relationship at low elevations. The data are from intensity Channel 1.

20° range in elevation for the SkyDips. As a result, the survey schedules were altered to feature SkyDips that ranged 20° in elevation from September 2010 onwards.

4.5.3 Theoretical and SkyDip opacity comparison

The data reduction pipeline has the functionality to calculate both the theoretical and SkyDip zenith opacity as described above. Figure 4.10 shows a correlation plot between the opacities determined via the SkyDip method and those determined via the theoretical method. The SkyDip values were selected so that only values with a reduced chi-squared between 0.97 and 1.03 for the temperature against cosec(θ_{el}) fit were shown. The correlations and the errors of the correlations between two data sets

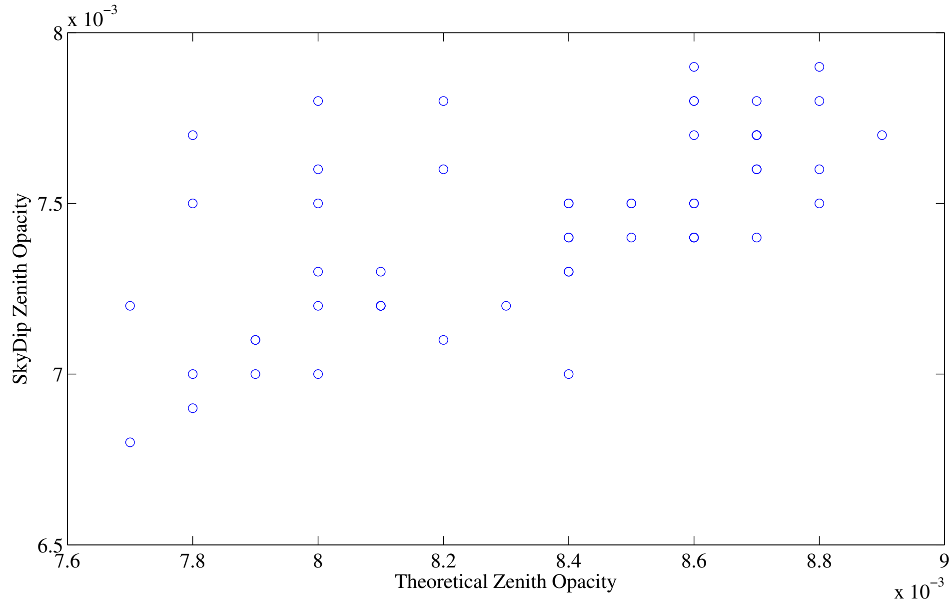

Figure 4.10: The theoretical and SkyDip zenith opacity values from November 2013 plotted against each other.

(X and Y) can be calculated using the Pearson's correlation coefficient:

$$r_{X,Y} = \frac{E[(X - \overline{X})(Y - \overline{Y})]}{\sigma_X \, \sigma_Y} \tag{4.23}$$

and

$$\sigma_r = \frac{1 - r^2}{\sqrt{n}} \tag{4.24}$$

where $\overline{X}/\overline{Y}$ is the data mean, $\sigma_{X/Y}$ is the data standard deviation, n is the number of data pairs and E indicates the expected value. The SkyDip and theoretical opacity values are fairly well correlated, with a correlation coefficient of 0.67 ± 0.09. The SkyDip values are between 5 and 10 % lower than the theoretical values. Underestimating the value of T_{sky} would overestimate the value of $(T_{\text{amb}} - T_{\text{sky}})$ and result in this discrepancy between the theoretical and empirical opacity values. Figure 4.10 also shows that for one theoretical zenith opacity value there exists several SkyDip values, this would imply that something is varying in the SkyDip measurement that is not a factor in the theoretical model. If the telescope were to the slew through the Galactic plane during a SkyDip the Galactic contributions to sky temperature would differ from the Galactic contributions off of the plane. Therefore the Galactic contribution to the sky temperature is also varying.

Antenna temperatures can be obtained from the temperature, as measured through the atmosphere (T'_A) into a temperature which has been corrected for atmospheric extinction (T_A) using the zenith opacity:

$$T_A = T'_A e^{\frac{\tau_0}{\sin(\theta_{\rm el})}}. \tag{4.25}$$

The typical zenith opacity value at 5 GHz for OVRO is seen to be ~ 0.008 which results in a maximum correction factor, at our lowest survey elevation of 37°, of 1.34 %. A 10 % uncertainty in the SkyDip zenith opacity corresponds to a 0.11 % uncertainty in the corrected antenna temperature calculated at the lowest survey elevation. As of such the Galactic and extra-Galactic contributions are considered small enough to be negligible.

The pipeline uses the opacity values as calculated by the empirical SkyDip method unless the SkyDip data have been flagged as bad, in which case a value using the theoretical method is calculated. This scenario would be quite rare because if the SkyDip data are bad then normally all the data would be bad. For example with data taken whilst it is snowing. Therefore it is reasonable to assume that all useable data have been corrected for atmospheric opacity using the SkyDip method.

4.6 Astronomical Calibration

The Northern data are calibrated using a noise diode, which in turn, is calibrated using three main astronomical calibrators: supernova remnants Cassiopeia A (Cas A) and Taurus A (Tau A) and the radio galaxy Cygnus A (Cyg A). These three sources were chosen because they are bright and point-like at 5 GHz. The first step of the data reduction pipeline, the alpha correction, calibrates all the data relative to the noise diode. All that is then needed to get the data into Kelvin is the temperature of the noise diode. The mathematical treatment used to acquire the noise diode temperature is courtesy of collaboration member Dr. Stephen Muchovej and goes as follows. The intensity (relative to the noise diode temperature) measured at a certain elevation is:

$$T(\theta_{\rm el}) = \frac{T_{\rm sky}e^{-\tau} + T_{\rm atmos}(1 - e^{-\tau}) + T_{rx} + T_{\rm spill}}{T_{ND}}, \tag{4.26}$$

where the noise diode temperature is T_{ND} and $T_{\rm spill}$ is the temperature contribution from ground spillover. If we take measurements on the sky, both with the noise diode on and off and also make a measurement of the calibrator source temperature (T'_{src}), then we can form the following 'y-factor':

$$y = \frac{T_{sky,NDon} - T_{sky,NDoff}}{T'_{src}}, \tag{4.27}$$

and we will have effectively measured:

$$y = \frac{T_{ND}}{T_{src}e^{-\tau}} = \frac{T_{ND}}{T_{src}}e^{\tau} = \frac{T_{ND}}{T_{src}}\left(1 + \frac{\tau_0}{\sin(\theta_{\rm el})}\right). \tag{4.28}$$

This can be seen by substituting a noise diode (T_{ND}) and source contribution ($T_{src}e^{-\tau}$) into Equation 4.26. Reworking Equation 4.22, which gave the slope of the linear fit between temperature and cosec(elevation) for a SkyDip, so the data are in noise diode units as opposed to Kelvin, gives:

$$m_{ND} = \frac{T_{\rm atmos} - T_{\rm Sky}}{T_{ND}} \times \tau_0 \tag{4.29}$$

and combining Equations 4.28 and 4.29 provides the following quadratic:

$$\alpha T_{ND}^2 + \beta T_{ND} + \gamma = 0, \tag{4.30}$$

with the real solution:

$$T_{ND} = \frac{-\beta + \sqrt{\beta^2 - 4\alpha\gamma}}{2\alpha}, \tag{4.31}$$

where $\alpha = \frac{m_{ND}}{T_{\rm atmos} - T_{\rm Sky}}$, $\beta = \sin\theta_{\rm el}$ and $\gamma = -y\, T_{src}\, \beta$.

My contribution to this method was the accurate measurement of the source temperature in noise diode units as measured through the atmosphere (T'_{src}) using 2D Gaussian fitting and the calculation of the calibrator antenna temperatures (T_{src}) in K based on flux density measurements from the literature.

4.6.1 2D Gaussian Fitting of Sources

C-BASS calibrator scans cross a source twice in declination (maintaining a constant right ascension) and twice in right ascension (maintaining a constant declination). This translates as movement in both azimuth and elevation in the telescope reference frame. 2D Gaussians of the following form are fit in the Az/El frame:

$$\mathrm{model} = \mathrm{A}\ \mathrm{e}^{\frac{-1}{2}\left(\frac{(\mathrm{Az}-\mathrm{Az}_0)^2}{\sigma_\mathrm{a}^2}+\frac{(\mathrm{El}-\mathrm{El}_0)^2}{\sigma_\mathrm{e}^2}\right)} + \mathrm{m_a} + \mathrm{m_e} + \mathrm{c}, \tag{4.32}$$

where A is the Gaussian amplitude, $\mathrm{Az}_0/\mathrm{El}_0$ is the centre of the Gaussian in azimuth/elevation, $\sigma_{\mathrm{a/e}}$ is the FWHM in azimuth/elevation, $\mathrm{m_{a/e}}$ is the gradient of the baseline in azimuth/elevation and c is the offset. All eight of these parameters are fit using a Levenberg-Marquardt least-squares fitting algorithm in MATLAB called '`nlinfit`'.

The C-BASS beam can be modelled as a Gaussian if the first sidelobes are ignored. Therefore data between 0.°5 and 1.°7 from the source centre were excluded from the fit. This is illustrated in Figure 4.11 where all the data are shown in cyan but only the data points circled in black are included in the fit. This method was used for Cas A and Tau A but an additional data filter had to be included for Cyg A scans.

From Figure 4.12 it can be seen that the scans through Cyg A also go through the Cygnus X region. The top figure shows this in the TOD, where Cygnus X can be seen as a lower intensity, non-compact region between two Cyg A peaks while the bottom figure shows the RA and DEC scan paths for the TOD overlaid onto the 1.420 GHz Reich & Reich (1986) data. A Cygnus X cut is therefore applied to the Cyg A scans. An example of this is shown in of Figure 4.13 where the Cygnus X data have been excluded from the fit. The fitted amplitude for the 2D Gaussian was used as $\mathrm{T_{src}}'$ in Equation 4.27.

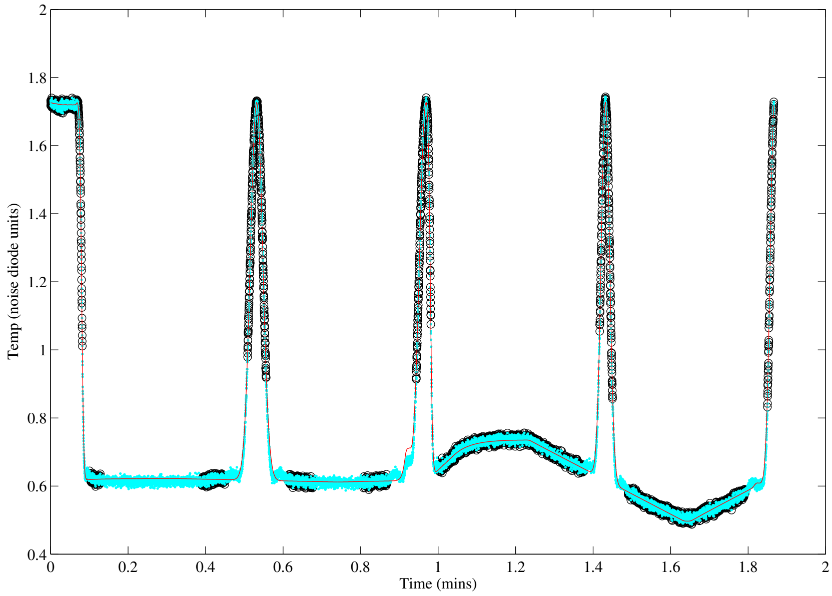

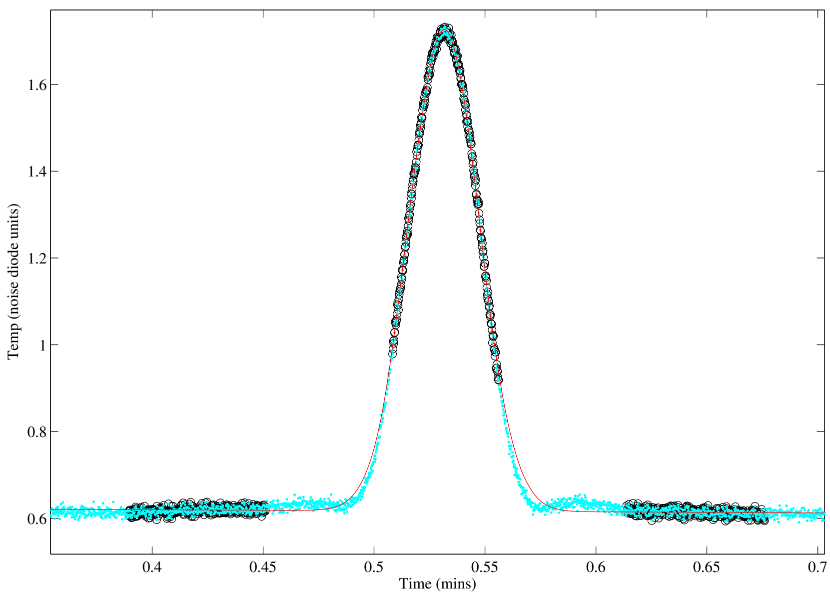

Figure 4.11: A typical 2D Gaussian fit of Cas A data. **Top:** Data points around the beam side-lobes have been missed out of the fit data as the beam is no longer strictly Gaussian within this region. The cyan points are the data, the cyan points outlined in black are the data included with the Gaussian fit and the red line represent the fit itself. **Bottom:** A magnified image of the first peak in the top figure.

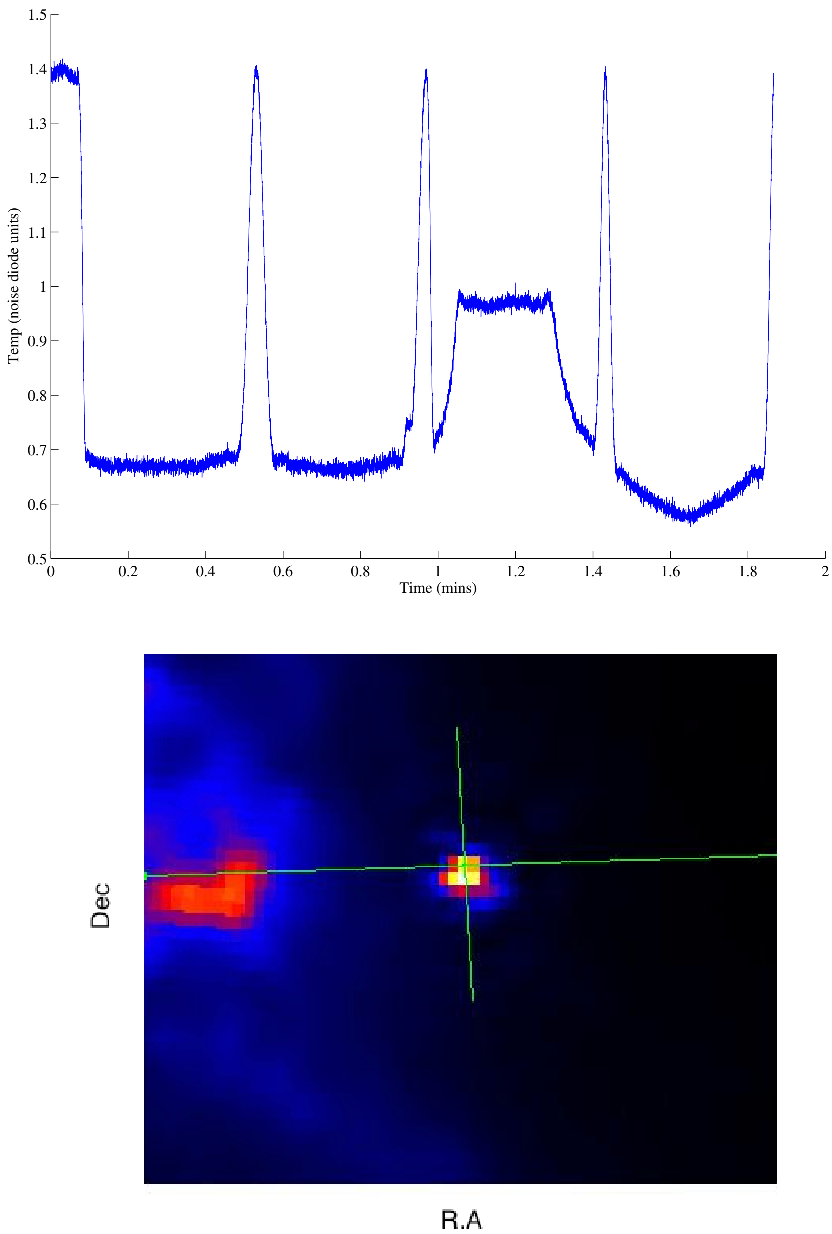

Figure 4.12: The presence of the Cygnus X region with the Cyg A scans. **Top:** A typical image of a Cyg A scan over time. The presence of the Cygnus X region can clearly be seen within the scan. **Bottom:** The 1.420 GHz Reich & Reich (1986) map showing the Cygnus region with the RA and DEC scan paths from the top figure highlighted in green

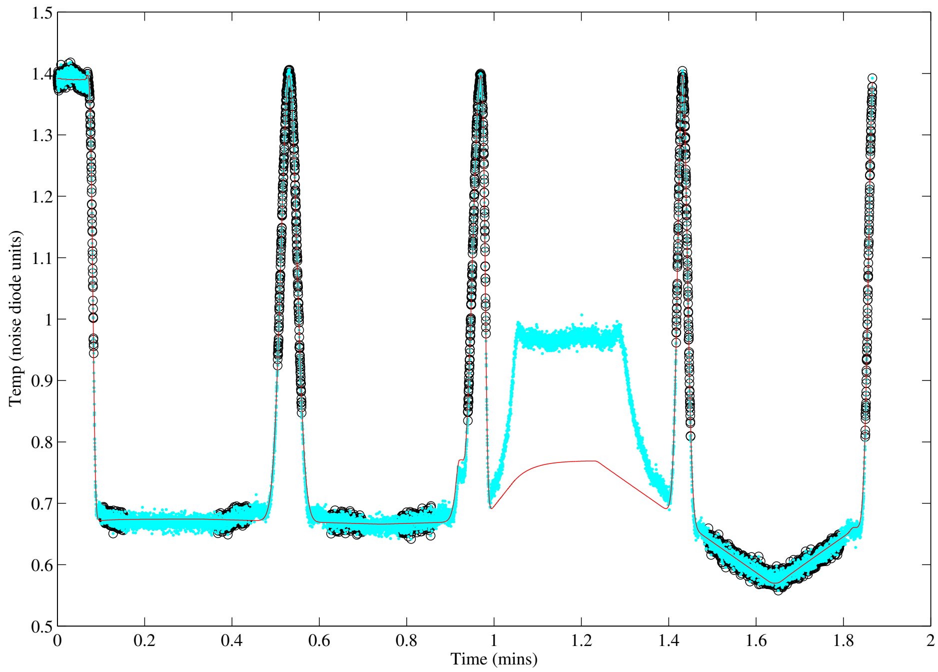

Figure 4.13: A 2D Gaussian fit of the Cyg A data after the Cygnus X region data has been excluded from the fit. The cyan points are the data, the cyan points outlined in black are the data included with the Gaussian fit and the red line represent the fit itself.

4.6.2 Astronomical calibrators

Antenna temperature is related to the flux density (Jy) of an astronomical source through the following relation (Kraus 1966):

$$\frac{T_A}{\mathrm{K}} = \left(\frac{S}{\mathrm{Jy}}\right)\left(\frac{r}{\mathrm{m}}\right)^2 \frac{\eta_A\ \pi}{2\ k_B\ 10^{26}}, \tag{4.33}$$

where S represents the flux density, the Northern aperture efficiency (η_A) is 0.55 according to the Northern bean modelling completed using the GRASP simulation software and the dish radius (r) is 3.05 m. The uncertainty of the antenna temperature is dependent on the uncertainties stated in the literature values for the flux density and the aperture efficiency:

$$\sigma_{T_A} = \sqrt{\left(\frac{\partial T_A}{\partial S}\sigma_S\right)^2 + \left(\frac{\partial T_A}{\partial \eta_A}\sigma_{\eta_A}\right)^2} \tag{4.34}$$

where σ_{η_A} is 5 % (private communication with Professor Christian Holler) and σ_S is calculated from the uncertainties of the flux density spectral forms used to calculate S.

The following spectral fit was used to acquire the Cas A flux density for the year 2000 (Weiland et al. 2011):

$$\log_{10}\left(\frac{S}{\mathrm{Jy}}\right) = 2.204 - 0.682\ \log_{10}\left(\frac{\nu}{40\ \mathrm{GHz}}\right) + 0.038\left(\log_{10}\left(\frac{\nu}{40\ \mathrm{GHz}}\right)\right)^2. \tag{4.35}$$

The secular decrease formula was measured by Hafez et al. (2008) to be:

$$\text{Percentage decrease per year} = 0.68 - 0.15\log_{10}\left(\frac{\nu}{\mathrm{GHz}}\right). \tag{4.36}$$

For Cygnus A the spectral fit used for the year 2000 was:

$$\log_{10}\left(\frac{S}{\mathrm{Jy}}\right) = 1.482 - 1.200\ \log_{10}\left(\frac{\nu}{40\ \mathrm{GHz}}\right) \tag{4.37}$$

and no notable secular decrease has been observed for Cyg A (Weiland et al. 2011) . The Tau A spectral fit was calculated for 2005 (Weiland et al. 2011):

$$\log_{10}\left(\frac{S}{\mathrm{Jy}}\right) = 2.506 - 0.302\ \log_{10}\left(\frac{\nu}{40\ \mathrm{GHz}}\right) \tag{4.38}$$

with a secular decrease of 0.17 % per year for frequencies between 0.086 and 8 GHz (Vinyaikin 2007). The frequency used in these formulae is meant to represent the central frequency of observation, which for Northern C-BASS is 4.76 GHz. However, because our measurements are not monochromatic, they cover the bandpass range of frequencies, the response of a sources's spectral index across our bandpass must also be considered. The correction factor used to account for the changing flux of a source across a bandpass is known as colour correction ($C(\alpha)$) (Zacchei et al. 2011) and for C-BASS it is calculated relative to the brightest source at 5 GHz, Cas A:

$$C(\alpha) = \frac{\int g(\nu)\ \left(\frac{\nu}{\nu_0}\right)^{\alpha_{\mathrm{source}}}}{\int g(\nu)\left(\frac{\nu}{\nu_0}\right)^{\alpha_{\mathrm{cal}}}}, \tag{4.39}$$

where $g(\nu)$ is the bandpass, ν_0 is the central frequency, ν is the frequency, α_{source} is the flux density spectral index of the source ($\alpha = \beta - 2$ where β is the temperature spectral index) and α_{source} is the flux density spectral index of Cas A. α for Cas A,

Source	4.76 GHz 2013 S (Jy)	Antenna Temperature (K)
Cassiopeia A	680 ± 4	3.96 ± 0.20
Cygnus A	390 ± 3	2.27 ± 0.11
Taurus A	584 ± 4	3.40 ± 0.17

Table 4.3: The 4.76 GHz August 2013 flux density values for the three C-BASS calibrator sources.

Cyg A and Tau A can be seen to be -0.7, -1.2, -0.3, respectively from Equations 4.35, 4.37 and 4.38. The measured Northern C-BASS bandpass provides $g(\nu)$ and the Northern central frequency (ν_0) is 4.76 GHz. The colour corrections for Cyg A and Tau A relative to Cas A are 0.9968 and 1.0033, respectively. As these correction are <1 % their contribution to the flux density calculation is not significant.

The 4.76 GHz flux densities for these three calibrators for August 2013 are shown in Table 4.3. The spectral fits are in the form $\log_{10}\left(\frac{S}{\mathrm{Jy}}\right) = a + b\ \log_{10}\left(\frac{\nu}{40\ \mathrm{GHz}}\right) + c\ \left(\log_{10}\left(\frac{\nu}{40\ \mathrm{GHz}}\right)\right)^2$. The flux density uncertainties quoted in Table 4.3 for the flux densities are the quadrature addition of the uncertainties on the a coefficients of the spectral fits, as these dominate the fit uncertainties and the secular decrease errors.

Table 4.3 also includes the antenna temperatures expected for each source which were calculated using Equation 4.33. These antenna temperatures were used as T_{src} in Equation 4.31 to find the noise diode temperature.

4.6.3 Noise Diode Stability

Using Equation 4.31 the noise diode temperatures were calculated every time the astronomical calibrators were observed. The error on T_{ND} depends on the uncertainties in the measurement of m, the gradient of the linear plots between temperature and cosec(θ_{el}), y, the measured ratio between the noise diode temperature and measured source temperature and T_{src}, the theoretical calibrator antenna temperature. It can be calculated as:

$$\sigma_{T_{nd}} = \sqrt{\left(\frac{\partial T}{\partial m}\sigma_m\right)^2 + \left(\frac{\partial T}{\partial y}\sigma_y\right)^2 + \left(\frac{\partial T}{\partial T_{src}}\sigma_{T_{src}}\right)^2}, \tag{4.40}$$

where σ_m is given by the fit uncertainties on the linear slope coefficient between the SkyDip data and cosec($\theta_{\rm el}$), $\sigma_{T_{src}}$ is given by Equation 4.34. The calculation for σ_y is as follows:

$$\sigma_y = \sqrt{\left(\frac{1}{T'_{src}}\sigma_{on}\right)^2 + \left(\frac{1}{T'_{src}}\sigma_{off}\right)^2 + \left(\frac{(T_{on} - T_{off})}{T'^{2}_{src}}\sigma_{T'_{src}}\right)^2}, \tag{4.41}$$

where $T_{on/off}$ and $\sigma_{on/off}$ are the temperature and uncertainity measured on the sky during/not during a noise diode event and the error on the source peak temperature measurement ($\sigma_{T'_{src}}$) is given by the 2D Gaussian fit error.

Noise diode data are flagged as bad using the following criteria: if the Gaussian fit error on the peak temperature is greater than 3 %, if the fitted Gaussian sigma values differ from the Northern C-BASS beam sigma by more than 20 %, or if the azimuth/elevation pointing offsets on the sky are greater than 0.°5.

Figure 4.15 shows the noise diode temperatures as determined by observations of Cas A, Tau A and Cyg A as a function of time. It is important to check that there is no correlation between noise diode and parallactic angle as this verifies that the baseline fitting carried out by the 2D Gaussian fitting code has correctly fitted the diffuse Galactic emission around the source. As parallactic angle is dependent on azimuth and elevation, any correlation between intensity and elevation caused by atmospheric opacity would also be shown as a correlation with parallactic angle.

Figure 4.14 shows the noise diode temperatures calculated from the three primary calibrators between Nov 2012 and Nov 2013 as a function of parallactic angle. It is interesting to note the two layers of noise diode temperature, most clearly visible for the first receiver channel, which indicate that the noise diode temperature changed in temperature over time. No correlation is seen between parallactic angle and noise diode temperature.

From Figure 4.15 the noise diode can be seen to be stable over a period of many days at a time. The major changes in temperature, seen at day $\sim$ 50, 150 and 230

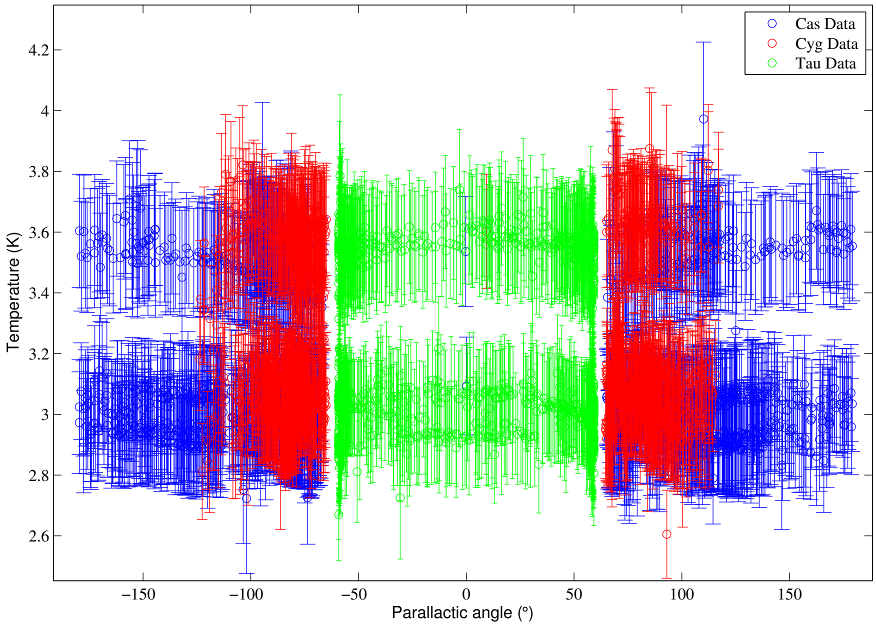

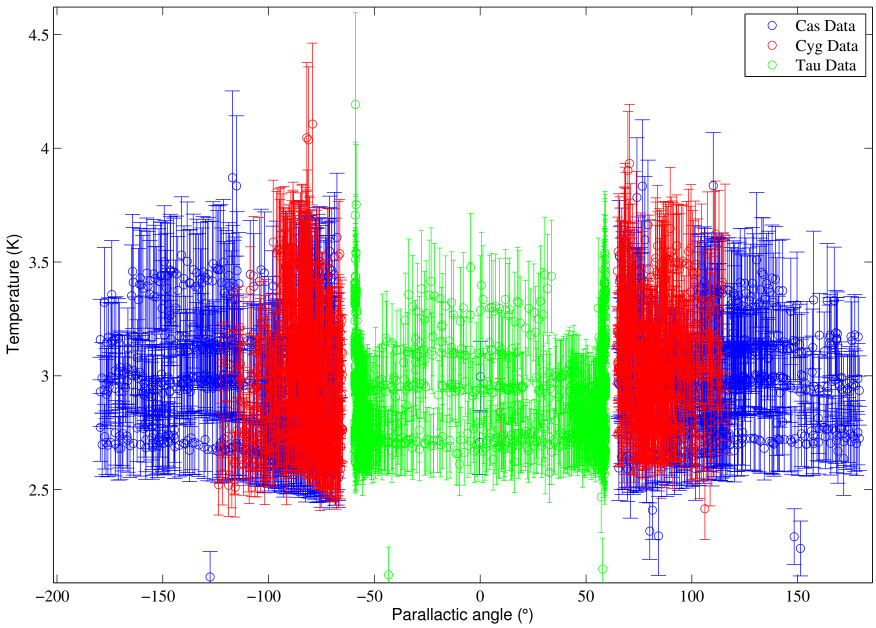

Figure 4.14: Noise diode values calculated from the three primary calibrators in **Top:** the first receiver channel over parallactic angle since Nov 2012. **Bottom:** the second receiver channel over parallactic angle since Nov 2012.

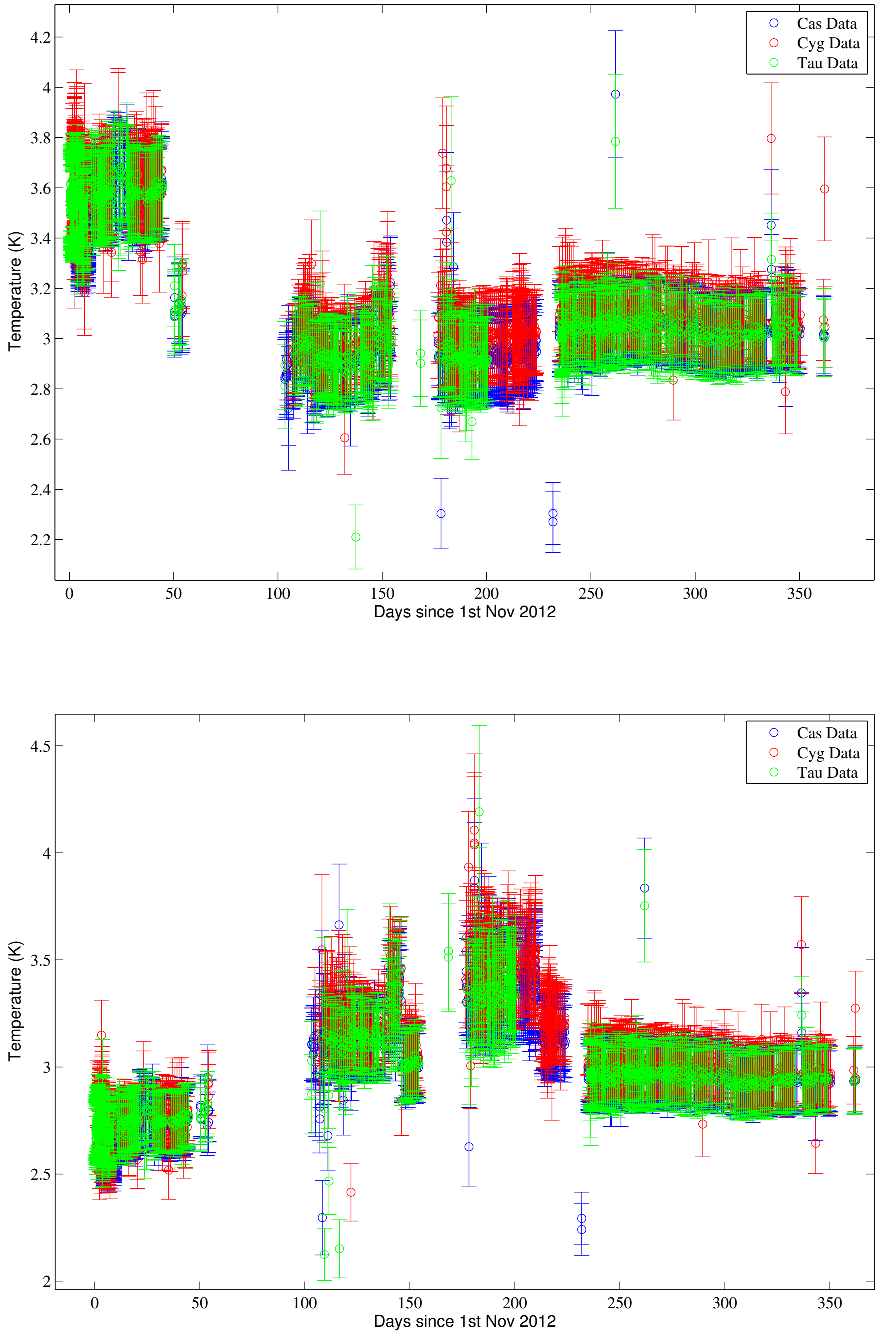

Figure 4.15: Noise diode values calculated from the three primary calibrators in **Top:** the first receiver channel over time since Nov 2012. **Bottom:** the second receiver channel over time since Nov 2012.

coincide with periods during which the telescope was offline and the hardware was being modified. Between 250 and 350 days after 1st November 2012 the noise diode values can be seen to remain stable over the hundred day time period. The average noise diode temperature is 3.09 K for the first receiver channel and 2.95 K for the second receiver channel. It can be seen in both plots in Figure 4.15 that the noise diode values determined using Cyg A are slightly higher than those determined using Cas A and Tau A. This may have something to do with the fact that the strong diffuse background emission around Cyg A, due to the Cygnus X region, is decreasing the measured Cyg A antenna temperature by raising the fitted Gaussian baseline on only one side of the peak. This would lead to a slight overestimation of the noise diode temperature. This effect, however, can be seen to be small in comparison with the noise diode uncertainties.

To calibrate the survey data, the noise diode temperatures, as calculated by all three of the primary calibrators, from 73 hours either side of the survey time, are read in from a text file and the weighted average of these values are applied to the data. These are now what we call calibrated data.

As a final test, the peak temperature of the astronomical calibrators Cas A, Cyg A and Tau A were measured for three weeks of calibrated August 2013 data. Peak temperatures were converted into flux densities using Equation 4.33. The standard deviations from the mean flux density for Cas A, Cyg A and Tau A are shown plotted over azimuth and elevation in Figure 4.16. No correlation can be seen between the flux density values and azimuth or elevation, confirming data which have been successfully corrected for atmospheric opacity and are not influenced by the observation parallactic angle.

The data in Figure 4.16 give mean flux density values of 682.7 ± 5.9 Jy, 589.3 ± 3.7 Jy and 387.8 ± 1.7 Jy for Cas A, Tau A and Cyg A respectively. Table 4.4 shows that these empirical means are in good agreement with the theoretical values given in Table 4.3 and displaying standard deviations of less than 1 %.

The noise diode temperature applied to the data have been shown to be stable to

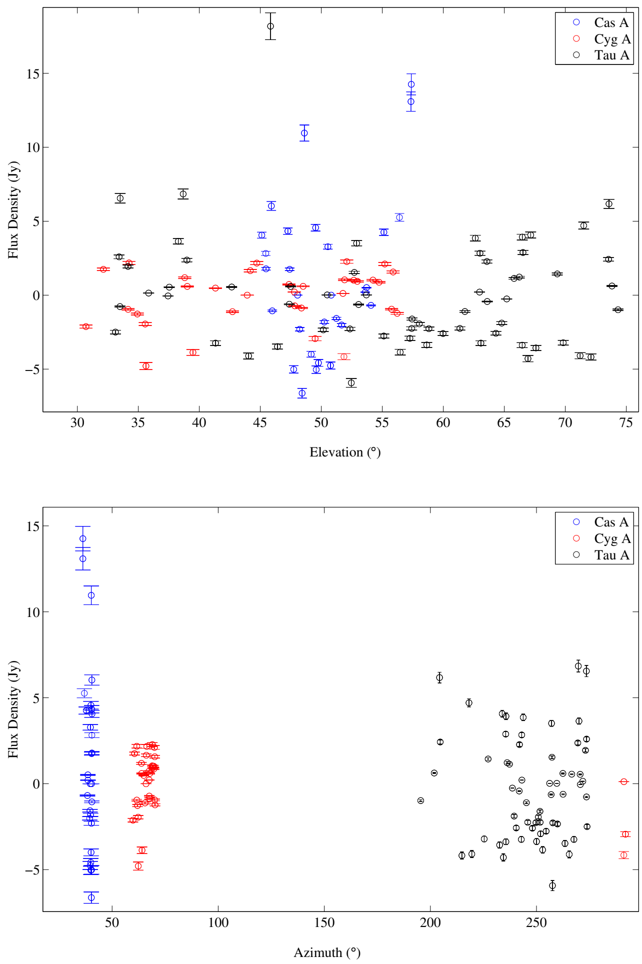

Figure 4.16: The flux densitiy variations from the mean for the main three calibrators, as calculated from calibrated August 2013 data. The standard deviations are plotted over elevation (top) and azimuth (bottom).

Source	S_{Theo} **(Jy)**	S_{Emp} **(Jy)**
Cassiopeia A	680 ± 4	682.7 ± 5.9
Cygnus A	390 ± 3	387.8 ± 1.7
Taurus A	584 ± 4	589.3 ± 3.7

Table 4.4: Comparison between the theoretical and empirical 4.76 GHz August 2013 flux density values for the three C-BASS calibrator sources.

less than 1 % and accurate to within 5 %. This is a respectable uncertainity for a low frequency ground based survey as other notable surveys such as Reich & Reich (1986), Jonas, Baart & Nicolson (1998) and Haslam et al. (1982) are known to have 5 %, 5 % and 10 % calibration uncertainties, respectively. The main source of error on the antenna temperature is the aperture efficiency, which is known to carry a 5 % uncertainty of its own. The aperture efficiency and error have been calculated using GRASP simulations, future calibration work will involve a direct and more accurate measurement of the aperture efficiency.

4.7 Map making

The final stage of the pipeline is to input an array into the map-maker containing MJD, right ascension, declination, azimuth, elevation, Stokes I, Q and U values from the first and second channels of the receiver, data flags and the day flag. The data flag is simply a logical 1 or 0 value for each of the data samples depending on whether or not they have been flagged for the presence of RFI, the Sun or the Moon. The day flag merely indicates whether or not the data has been taken during daytime. The C-BASS map maker is Descart.

4.7.1 Descart

Descart, the DEStriping CARTographer (Sutton et al. 2010), is a mapmaker which removes the $1/f$ noise by splitting the data into chunks of a user defined "baseline" length, and assuming that the low frequency $1/f$ noise is a constant offset which can be fitted for and then subtracted from these chunks. The TOD can be considered as the combination of sky and pointing information at each map pixel and time in the case of the pointing information (x_p and A_{tp}), white noise (n_t^W) and the $1/f$ noise:

$$TOD_t = A_{tp}x_p + n_t^W + F_{t\alpha}\alpha_\alpha. \tag{4.42}$$

Here the $1/f$ contribution has been represented in the TOD by a set of bias functions ($F_{t\alpha}$). Sutton et al. (2010) assume the bias function to be a constant value of amplitude α_α over the baseline length. Therefore the correlated noise can be subtracted from the TOD.

Descart runs in two stages: the first uses Python code to select the pipeline data which are acceptable for mapmaking. The flagged data are always excluded from the map making but the user can specify other cuts to make, such as, daytime only data, masking out certain regions within a co-ordinate frame or cutting out the SkyDip data.

The second stage uses Fortran code to read in a parameter input file which uses user defined values for the HEALPix N_{side}, map co-ordinate frame and the data chunk length in seconds over which to apply destriping. C-BASS maps are usually produced at HEALPix N_{side}= 256 (13.′7, in order to oversample our beam) in the Galactic co-ordinate frame using an destriping offset length of 1000 samples (10 seconds). Descart can only suppress the correlated $1/f$ noise over baseline times shorter than 1/frequency of the correlated noise, this favours the selection of short baseline lengths. However, the shorter the baseline length, the fewer TOD with different pointing information to help determine the offset value from. The Northern knee frequency in polarisation of $\sim$ 10 mHz puts an upper limit on the offset length of 100 seconds, however the intensity knee frequency can range from anywhere between 10 mHz and 1 Hz depending on the severity of the atmospheric $1/f$ noise. The optimum baseline length is still under investigation but the current value of 10 seconds is thought to be reasonable from the visual quality of the maps it produces.

The data reduction pipeline is set to run automatically on each day's worth of data so the maintenance plots showing r.m.s. noise and power spectra can be regularly monitored. The days worth of TOD are also fed into Descart to produce daily maps, the quality of which are visibly affected by RFI and bad weather so this provides a quick and efficient method of weeding out days which cannot be used in the final survey.

4.8 Summary

The data reduction pipeline is responsible for the calibration of the raw data as well as the removal of systematic noise and RFI from the astrophysical signal. The data are calibrated using an internal noise diode of constant temperature, which itself is calibrated from astronomical sources. Cas A, Cyg A and Tau A are used to measure the noise diode temperature several times a day. The noise diode is stable to 1 % over several months and the calibrated data are accurate to within 5 % of the absolute temperature scale set by Cas A, Tau A and Cyg A. This 5 % is a combination of the $\approx$1 % noise diode variations, the $<$1 % uncertainties from not applying colour corrections and the $\approx$ 5 % aperture efficiency uncertainty. The microphonic oscillations present in the data are reduced by a factor of 20 in amplitude and work to increase this factor until the oscillation magnitude is lower than the white noise level is ongoing. Transient RFI, mainly from aeroplanes are successfully removed from the data and the pointing is seen to be good to within 0.1 of the beam FWHM.

Chapter 5

Ground Spillover

The term ground spillover refers to any ground emission measured by the receiver as a result of the sidelobe response to the physical temperature of the ground. Ground spillover affects all single dish surveys and the fact that Northern C-BASS is situated within a valley surrounded by mountains means the ground emission, which spills over the secondary baffles and into the dish, is particularly strong. This is the case despite the fact that Northern C-BASS has very low far-out sidelobes of less than −70 dB (Holler et al. 2013). Figure 5.1 shows one month of intensity and polarised intensity data taken from Northern C-BASS in August 2013, presented in Galactic coordinates and on a histogram colour scale to emphasise all the data features. The C-BASS data are shown alongside the Haslam et al. (1982) 0.408 GHz intensity data and the *WMAP* 22.5 GHz polarised intensity data to highlight the ground spillover within the C-BASS maps. The ground spillover can clearly be seen obscuring the North Polar Spur region within the C-BASS intensity map and following the equatorial plane within the polarised intensity map. The C-BASS maps are shown at a resolution of $0\overset{\circ}{.}73$ and N_{side} = 256 while the Haslam et al. (1982) and *WMAP* maps are at a resolution of 1° and N_{side} = 512.

The absence of a patch of Northern data, visible at the top right hand side of the maps, $(l, b) \approx (220^\circ, 45^\circ)$, is due to solar emission flagging. Currently, the pipeline flags out observations within 15° of the sun, however, solar sidelobes still contribute a

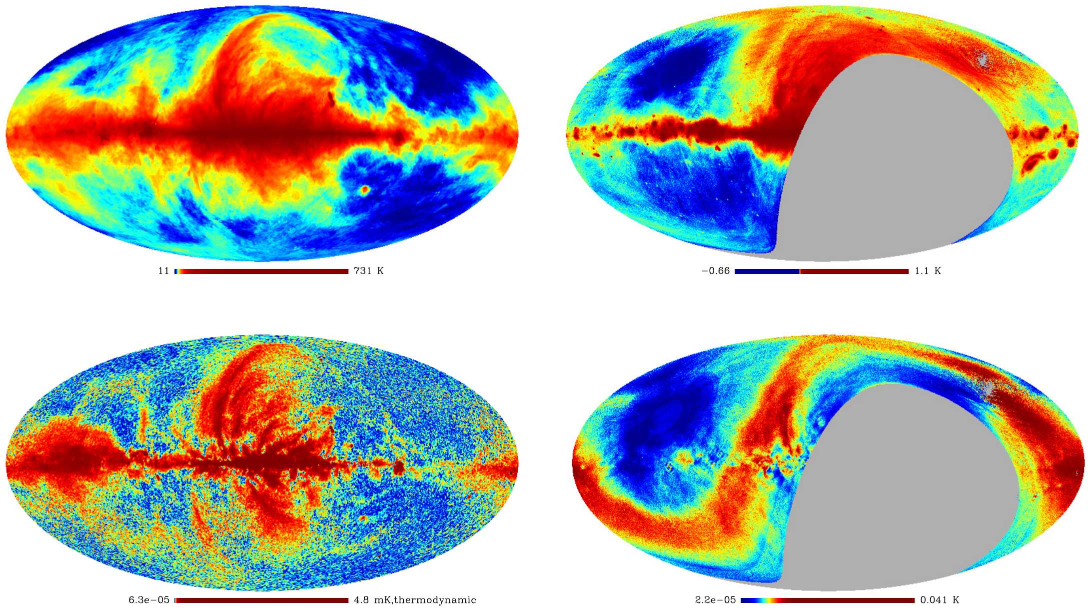

Figure 5.1: A comparison between the Northern C-BASS maps, made from one month worth of August 2013 data and destriped and the Haslam et al. (1982) and *WMAP* maps. All maps are presented in Galactic coordinates on a histogram colour scale. **Top left:** The 0.408 GHz Haslam et al. (1982) intensity map, **top right:** the C-BASS intensity map. The ground spillover is clear around the North Polar Spur. **Bottom left:** the *WMAP* K-band polarisation map, **bottom right:** the C-BASS polarised intensity map. The ground spillover signal can be seen to follow the equatorial plane.

significant portion of the total emission in that region. The Sun moves $\sim 15^{\circ}$ within a month spreading emission over the patch of sky it is in. Removing the solar side-lobe emission is a future function of the pipeline and so until this is completed solar emission will be present in the maps unless, only night-time data are used.

5.1 The Ground Templates

It is possible to model the ground spillover emission, with the intent of then subtracting it from the sky signal, by making maps in the Az-El reference frame as the ground

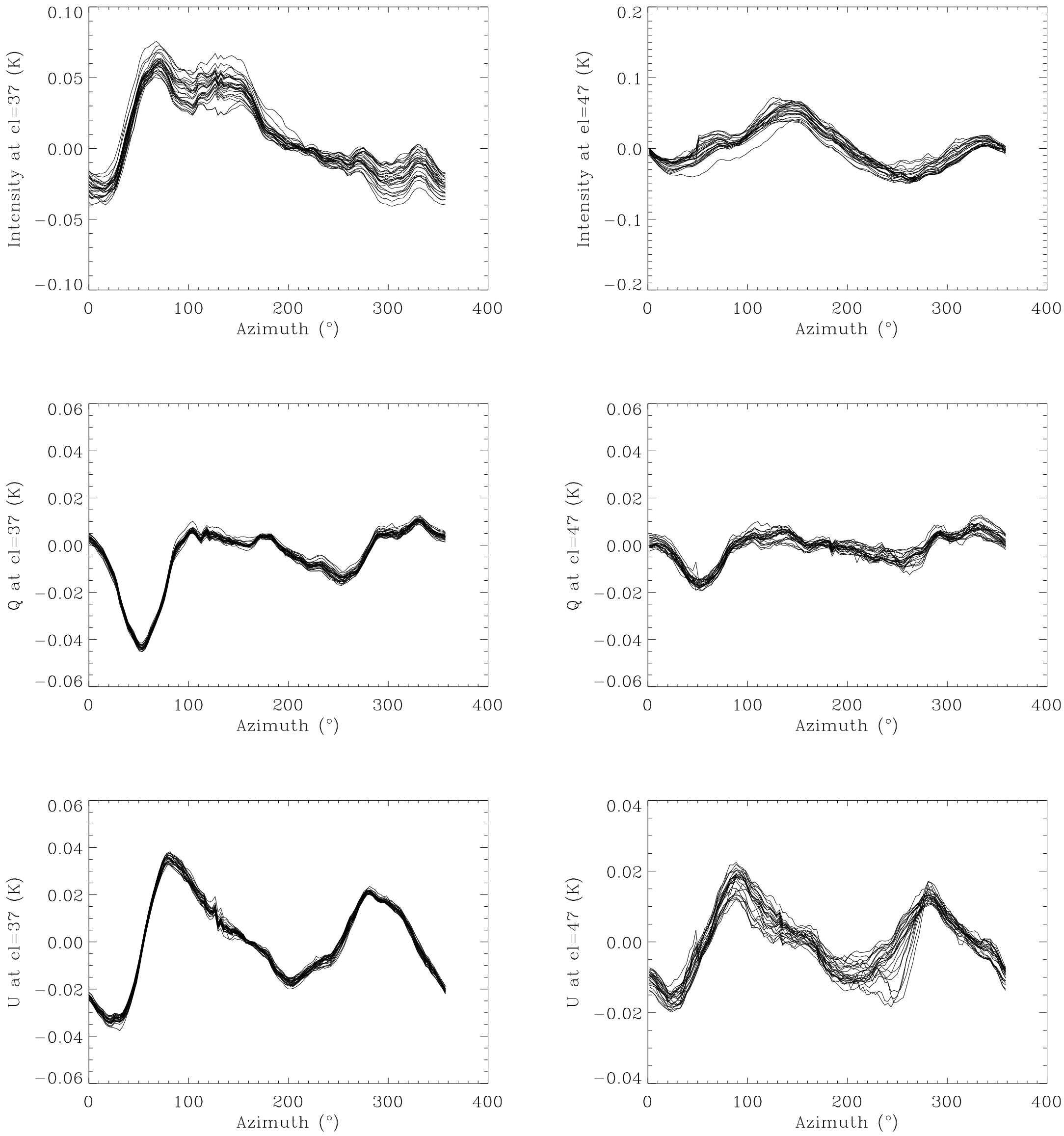

Figure 5.2: The thirty daily Stokes I, Q and U ground emission templates plotted against azimuth for both C-BASS North survey elevations. **Left:** Survey elevation = 37°, **right:** survey elevation = 47°.

signal is fixed in Az/El coordinates and so, mapmaking in this coordinate frame leaves the sky to form the varying signal. We can then use this fact to remove the sky signal by destriping. A similar method was implemented by Carretti et al. (2010) to mitigate the ground spillover emission for the S-PASS polarisation survey at 2.3 GHz.

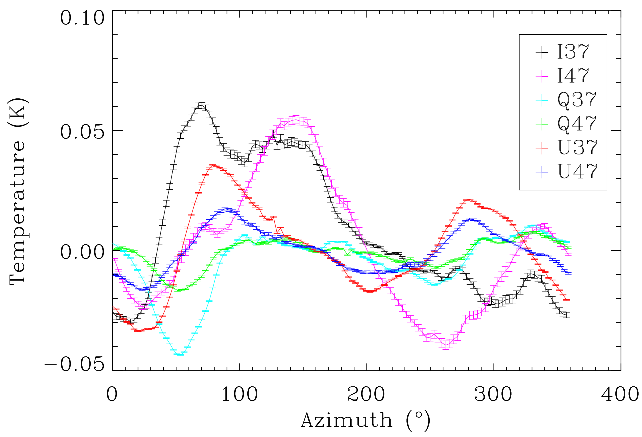

Figure 5.3: The average Stokes I, Q and U ground emission templates in Kelvin plotted against azimuth for both C-BASS North survey elevations (37° and 47°).

Thirty daily ground emission maps were formed from the month long data collected in August 2013 in Az-El coordinates. A better isolation of the ground emission was achieved by masking out the strong Galactic emission. This masking cut out a rectangular region 10° in Galactic latitude either side of the Galactic plane and a $5^\circ \times 5^\circ$ square centred on M42. The ground emission is expected to be relatively smooth whereas the Galactic signal features point source emission. Therefore, the daily ground templates were made at HEALPix $N_{\rm side} = 32$ to capture the large scale ground emission and smooth over the Galactic point sources. Figure 5.2 shows the thirty daily ground emission template for Stokes I, Q and U in Kelvin, plotted against azimuth. Each Stokes parameter has also been separated for the two Northern C-BASS scanning elevations of 37° and 47° as the ground emission magnitude will vary with elevation.

At first glance, the ground templates shown in Figure 5.2 appear to be very consistent and repeatable each day, except for some small variations. The intensity at elevation = 37° and Stokes U at elevation = 47° templates seem to show the greatest variations and these variations are around 90° and greater than 300° in azimuth. This is where the mountains can be seen in the Northern Az/El maps (see Figure 3.6). The sharp dip/increase within the Stokes Q and U ground templates at elevation = 37° is the microwave link to CARMA, which is also visible at azimuth $\sim$ 110° in the Northern Az/El maps (Figure 3.6).

Figure 5.3 shows similar plots to those in Figure 5.2 but instead of all thirty daily templates being plotted their mean shown instead. The error on the mean of each of the azimuth points is calculated from the standard deviation of the thirty daily templates, at that azimuth, divided by the square root of the number of templates.

5.1.1 Ground template stability

Variations with weather information

To try and understand the variation of the daily ground templates shown in Figure 5.2 the deviations of the individual daily templates from their mean were investigated. If the templates were found to be correlated with certain weather parameters then the ground emission could be more accurately modelled by including these additional parameters. The scale factors and offsets values required to get the daily templates to match their mean were calculated by fitting the daily templates to the following model:

$$\text{scaled profile} = (\text{mean profile} \times \text{scale factor}) - \text{offset}. \tag{5.1}$$

The templates before and after rescaling and offset removal are shown for intensity at elevation = 37° (I37) and Stokes U at elevation = 47° (U47) in Figures 5.4. These template types were chosen as they showed the largest deviations from the mean in Figure 5.2. Some improvement can be seen in the scaled templates in the form of a decrease in template scatter around the mean at azimuth $\sim$ 100° and $\sim$ 300° in I37 and azimuth $\sim$ 200° in Q47. However there is still significant scatter even after the rescaling and offset subtraction that indicates more complex variations are occurring in the ground templates. The offset and scale factors used for I37 and U47 are shown in Figure 5.5 and 5.6, respectively, alongside the daily average temperature and relative humidity values. It can be seen from both figures that the offset and scale values appear to be uncorrelated with atmospheric temperature and relative humidity.

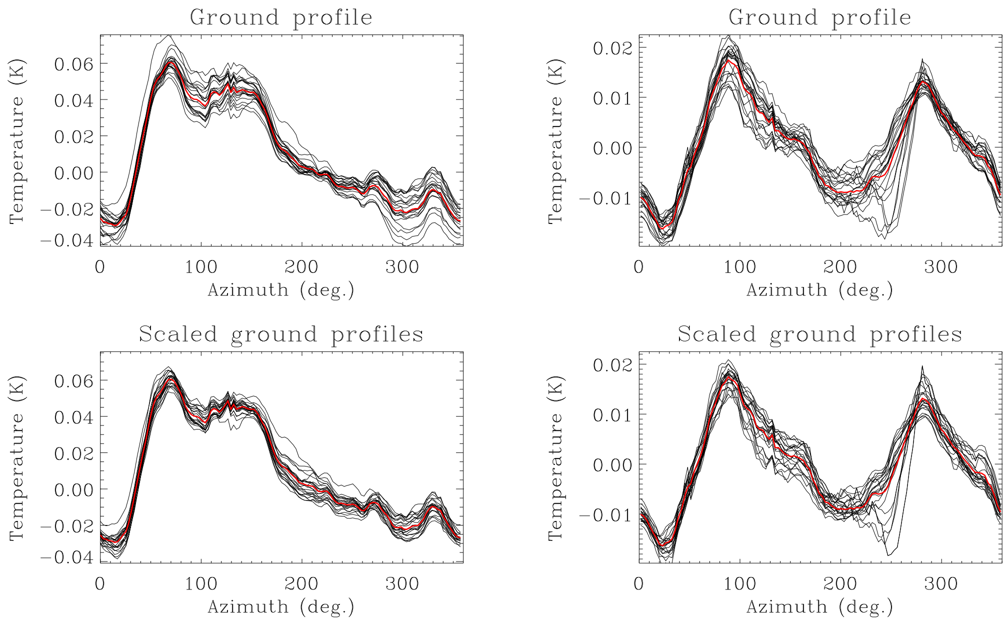

Figure 5.4: The ground templates before and after rescaling. **Top left:** The original intensity ground templates at elevation = 37° with their mean shown in red. **Bottom left:** the intensity ground templates at elevation = 37° after rescaling and the subtraction of an offset, the original templates's mean shown is red. **Top right:** The original Stokes U ground templates at elevation = 47° with their mean shown in red. **Bottom right:** the Stokes U ground templates at elevation = 47° after rescaling and the subtraction of an offset, the original templates's mean shown is red.

While the daily weather information does not appear to correlate with the full ground templates, various azimuths may show stronger correlations. To investigate this possibility a parabola of the form $A(\mathrm{az} - B)^2 + C$, where A, B and C are constants, was fit to the mountain peak seen at $50° < \mathrm{az} < 90°$ in the I37 profile (for an example see the I37 profile in Figure 5.2). The fitted peak values for each of the daily I37 profiles are shown plotted against the daily atmospheric temperature and relative humidity values in Figure 5.7. The correlation coefficients for the peak intensity and daily atmospheric temperature and relative humidity are -0.03 ± 0.19 and 0.62 ± 0.11, respectively. This result indicates that there is a correlation between relative humidity and the peak temperature between 50 and 90° in azimuth for the I37 template.

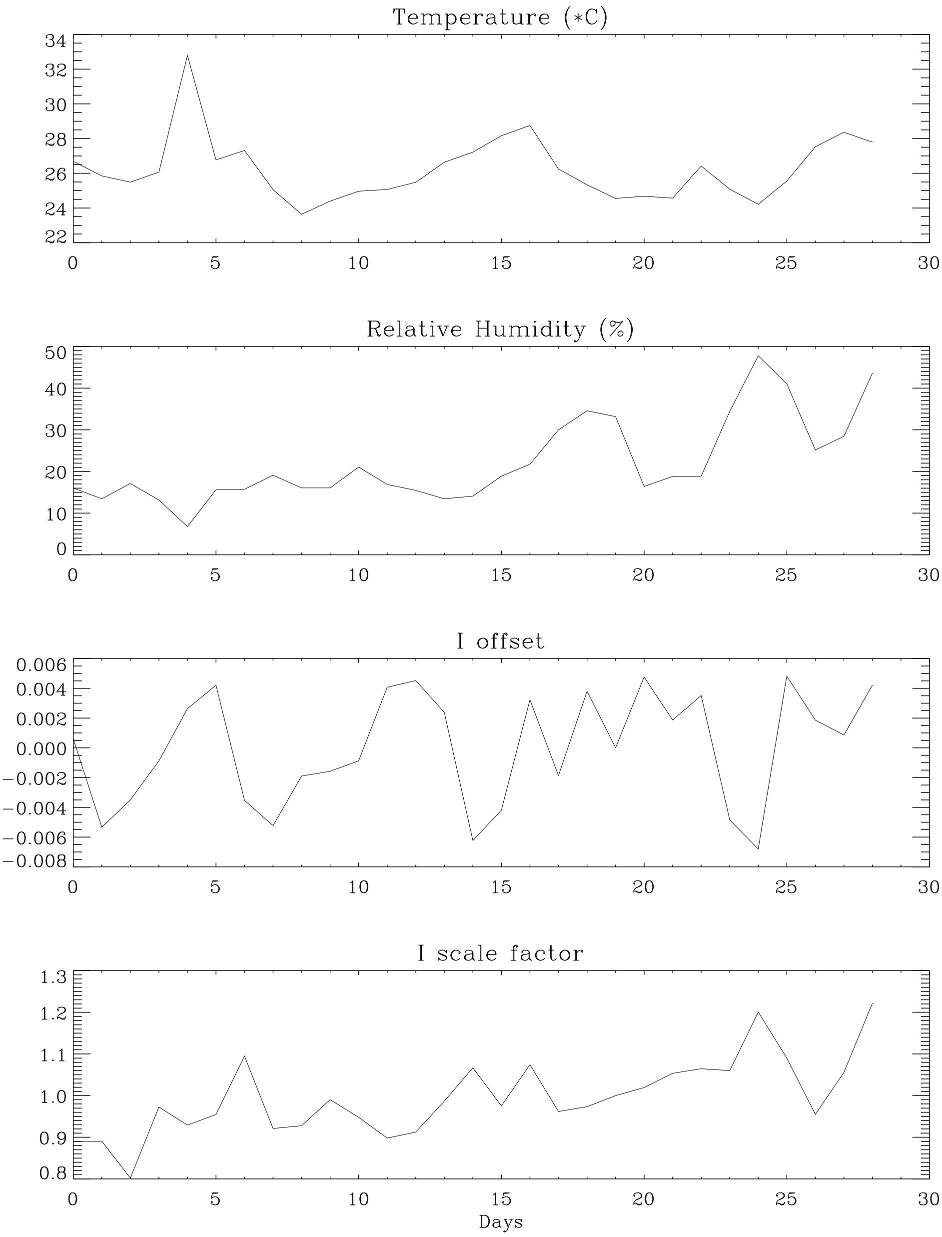

Figure 5.5: The intensity, elevation = 37° scale factors and offset values. **From top to bottom:** the average daily temperature for each of the days in August a ground template was made for, the same but for the average daily relative humidity, the fitted template offset values and the fitted template scale factors.

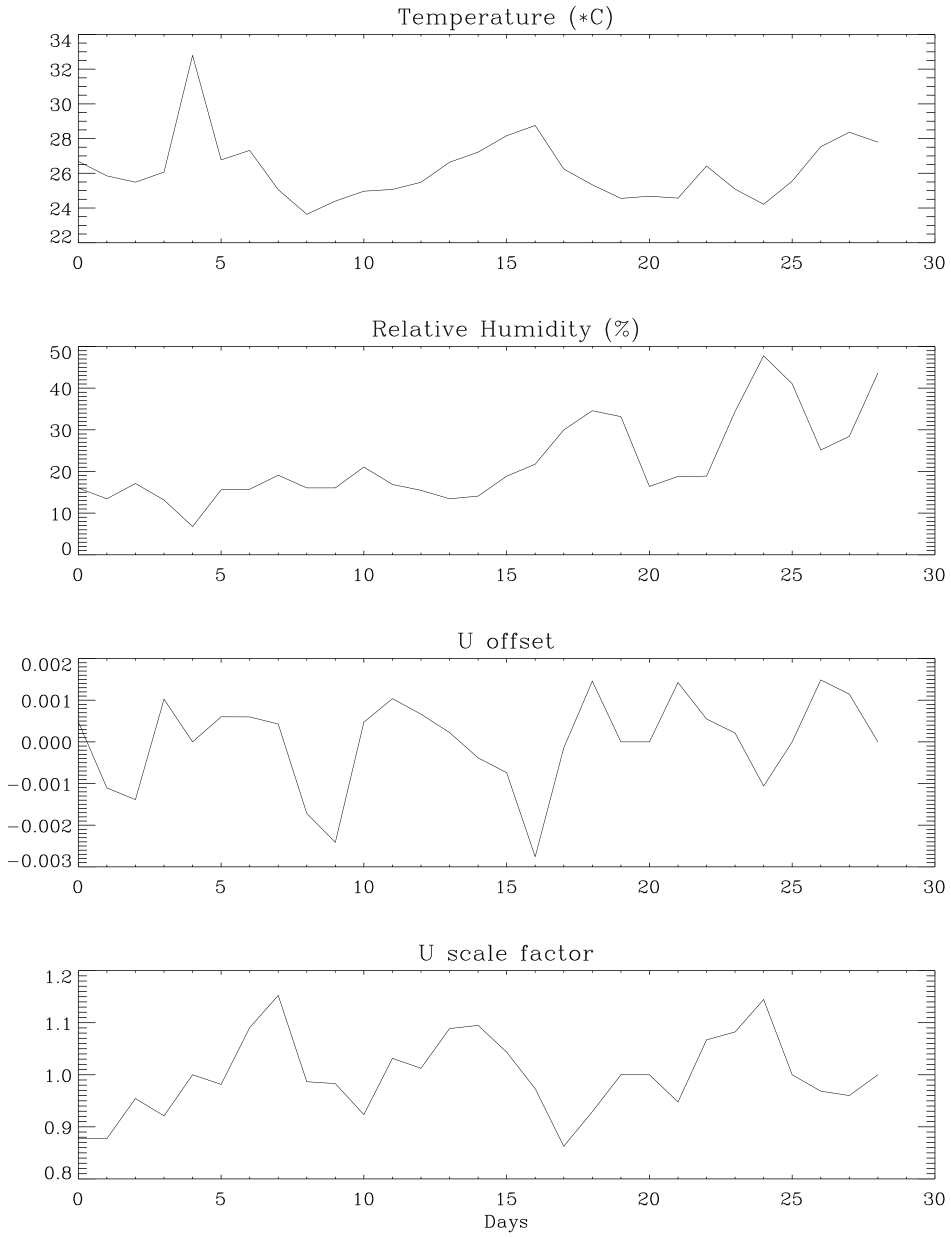

Figure 5.6: The Stokes U, elevation = 47° scale factors and offset values. **From top to bottom:** the average daily temperature for each of the days in August a ground template was made for, the same but for the average daily relative humidity, the fitted template offset values and the fitted template scale factors.

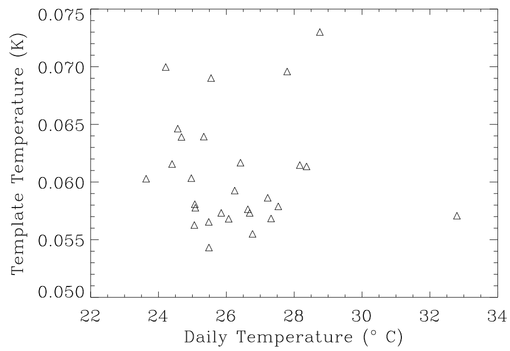

Figure 5.7: The correlation of the peak intensity at elevation = 37°, 50° < az < 90° with **left:** the average atmospheric temperature and **right:** relative humidity.

To try and use the fact that ground emission and humidity appear to correlated, at least for the emission associated with the mountain peaks, the templates were grouped together using the weather information. If ground emission profiles made during days of similar humidity are more similar in magnitude and shape then the scatter on their mean should be reduced. The daily temperatures ranged from 23 to 28°C throughout August 2013 in OVRO and the relative humidity values spanned from 6 to 48 %. The templates were grouped according to first, the daily average temperature values and then the daily average relative humidity values. The median of the standard deviation within 280° < az < 320° for each of these groupings are shown in Table 5.1. It can be seen that grouping the templates according to weather information does not appear to improve the uncertainty on the means formed. As a result of this the full data set was used to produce the monthly averaged templates.

Variations between day-time and night-time

The possibility of making day and night templates, so two ground templates per day, was also explored as the ground temperature will change between day-time and night-time because of the effects of direct sunlight and dew formation, which will affect the emission properties of the ground. The differentiation between day-time and night-time data was achieved through the use of a solar ephemeris. Day-time is defined as

Set	**σ (mK)**					
	I37	**I47**	**Q37**	**Q47**	**U37**	**U47**
Full	8.6	9.5	1.3	1.3	0.9	1.5
23 – 25°C	18.2	7.7	1.5	3.3	1.7	0.7
25 – 28°C	9.5	13.5	1.5	1.2	1.0	1.7
6 – 26 %	11.5	11.0	1.1	1.6	1.2	1.8
26 – 48 %	7.2	9.4	1.3	1.3	0.8	1.1

Table 5.1: The mean standard deviation of the ground templates within 280° < az < 320° after they have been grouped according to atmospheric temperature and humidity.

the time during which the Sun elevation is above elevation = 0°.

Figure 5.8 shows the day-time and night-time August 2013 average Stokes I, Q and U ground templates alongside the full day average ground templates. It can be seen that splitting the data into day and night subsets has very little effect on the Stokes Q and U templates formed, implying that the polarised ground signal is stable over a period of 24 hours. The same is essentially true for Stokes I at elevation = 47° but not for Stokes I at elevation = 37°. The elevation = 37° Stokes I template is clearly seen to change between day and night for the azimuth ranges of 70° – 190° and 270° – 360° by around 0.025 K. This $\sim$ 125 % increase in the ground template between day and night is unlikely to be due to variations in ground temperature. Even assuming a 20 K temperature difference between day and night ground temperature this is still only a 20/300 = 7 % variation. The CARMA link can be seen as a small kink at az $\sim$ 110° in the Stokes U elevation = 37° template. The large variations in the Stokes I elevation = 37° templates can be seen at the azimuth range that the CARMA microwave link occupies (70° – 190°) and possibly the azimuth range of the link's first sidelobe (270° – 360°). The CARMA link transmitter is powered by a solar cell therefore it is expected that any RFI caused by the link would be larger in intensity during the day. If the CARMA link is responsible for this day-time night-time variation this would also explain why the strongest variation is seen at elevation = 37°: the CARMA link is

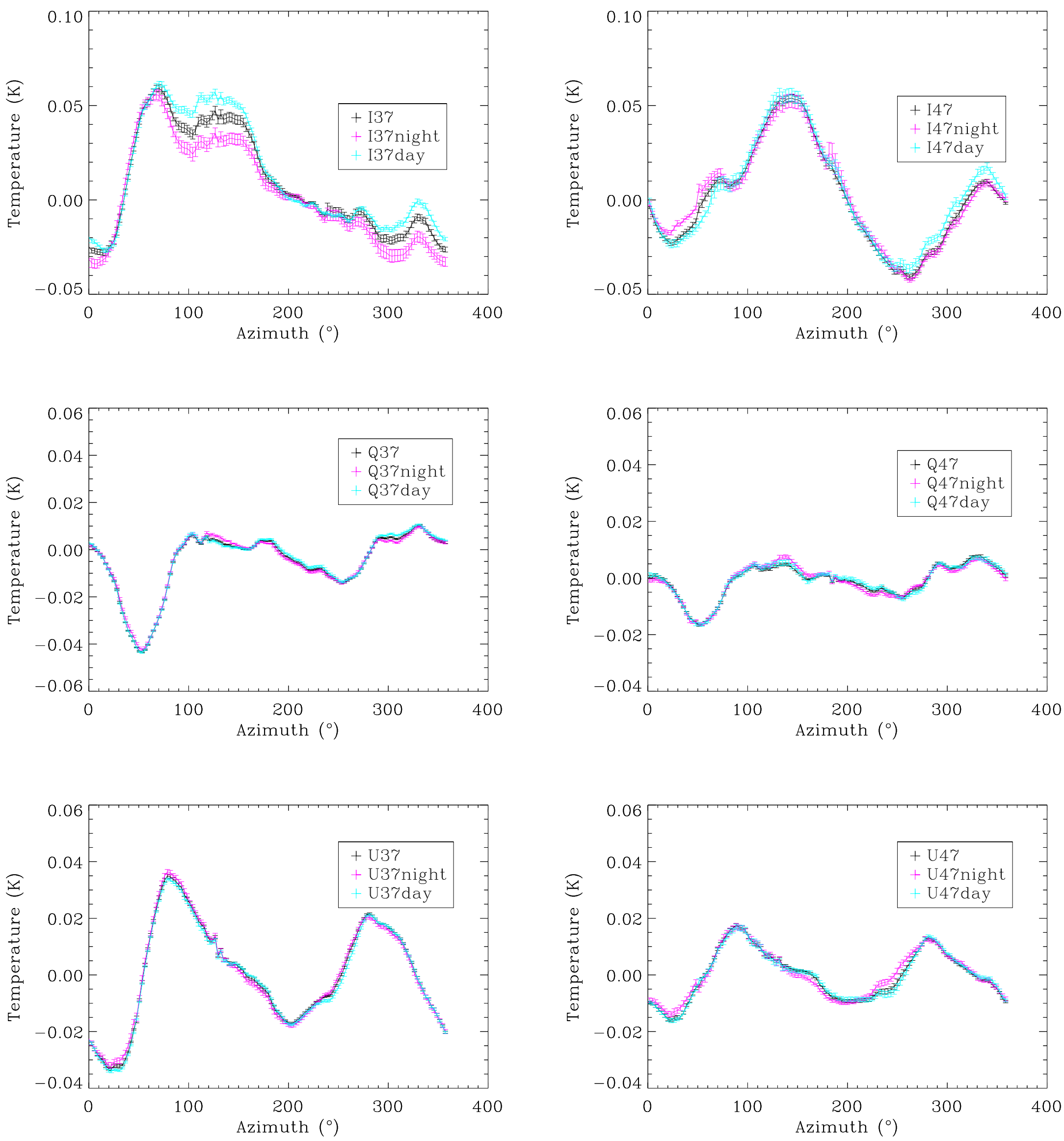

Figure 5.8: The day-time, night-time and full day average Stokes I, Q and U ground emission templates in Kelvin plotted against azimuth for both C-BASS North survey elevations (37° and 47°).

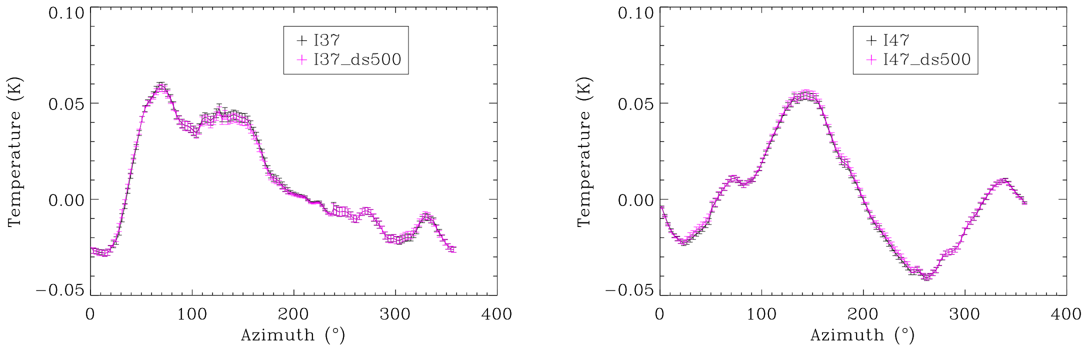

Figure 5.9: The mean Stokes I ground templates made with a destriping offset length of 500 (pink curve) and 1,000 (black curve) samples. **Left:** Elevation = 37°. **Right:** Elevation = 47°.

located on the observatory floor.

Splitting the data into the smaller chunks, however carries with it the problem of limiting the success of the destriper; several of the night-time only profiles were of such poor quality that they had to be excluded from the mean.

Variations with destriping baseline length

The ground templates were also made using a DESCART baseline length of 500 samples (5 seconds) instead of 1000 (10 seconds) to gauge the effect this would have on the averages. As discussed in Section 4.7.1, the baseline length determines the ability of the destriper to remove $1/f$ and sky signal in this case, therefore varying the baseline length may effect the quality of the ground templates produced. Figure 5.9 shows the Stokes I mean templates destriped using an offset length of 500 and 1,000 samples: the change in offset length does not appear to have altered the templates in any significant way. The same was the case for the Stokes Q and U mean templates constructed using an offset length of 500 samples.

5.1.2 Removing the ground signal

For the first attempt at ground spillover removal the destriping length was left at 1,000 samples and the full day templates were used to calculate the monthly average. The six mean ground templates for Stokes I, Q and U at elevations = 37° and 47° were saved as text files against their corresponding azimuth values. The August data were then rerun through the data reduction pipeline with the ground removal. This function interpolates the six mean ground templates onto the azimuth range, traversed by the TOD. Then it separates the data into the two survey elevations (37/47°) and subtracts the mean of all the TOD from each TOD. This leaves the data in a similar form as the ground templates, just variations around 0 K. The function then subtracts the appropriate interpolated ground templates from the mean subtracted TOD and finally returns the original baseline level by re-adding the original means. Using this two-stage pipeline the ground spillover subtracted maps shown in Figure 5.10 were made.

A comparison of Figure 5.10 with Figure 5.1 shows a vast improvement in both the intensity and polarised intensity maps after the ground spillover subtraction. In intensity, the North Polar Spur region is more clearly visible after the subtraction and in polarised intensity, the ring of emission, which followed the equatorial plane has been removed leaving visible diffuse Galactic emission. In the high latitude regions of the intensity and polarisation maps, the instrumental noise is also now visible. The dashed ellipses, present in both maps, highlight the emission from solar sidelobes. At the time of analysing this data the solar flagging code was set to flag data within a 15° radius of the Sun. These maps supported the need for a larger flagging radius of at least 30°. Figure 5.11 shows the equivalent August ground removed intensity and polarised intensity maps but this time only night-time data has been used to exclude the solar sidelobe emission from the maps. The lower map quality due to poor destriping of less data can be seen most clearly in the intensity map. Given the amount of data available for testing at this stage in the project, and the increased probability of producing unusable templates associated with the night-time only ground profiles shown in Figure 5.8

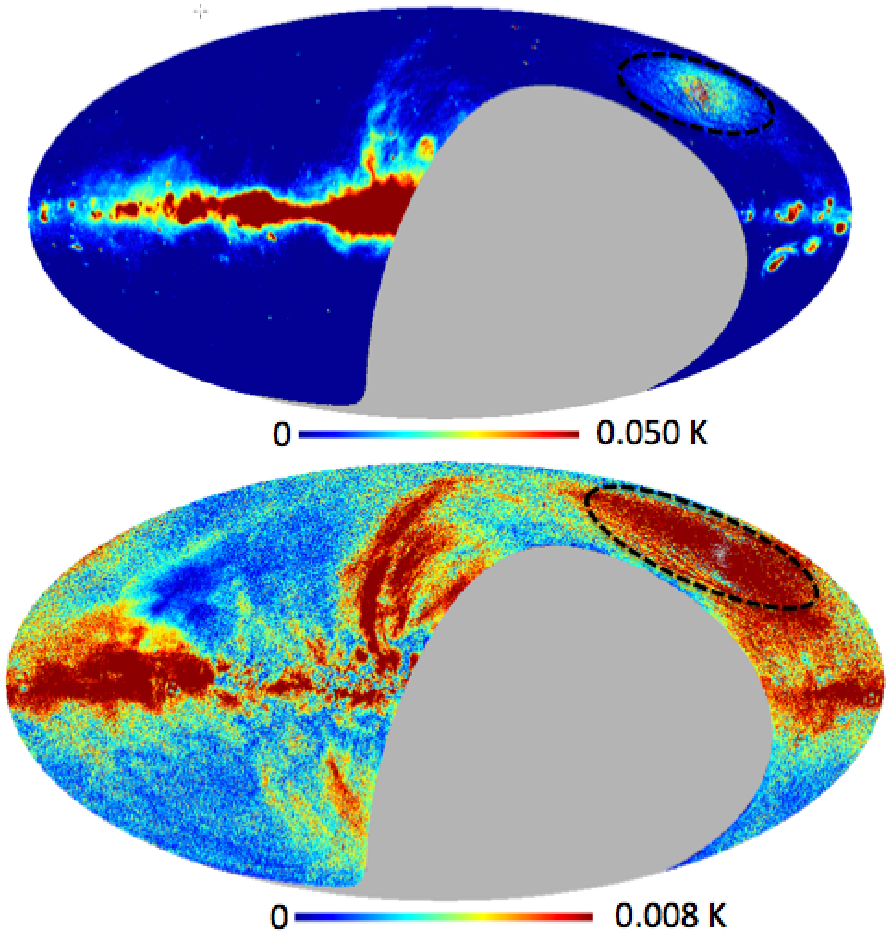

Figure 5.10: One month worth of August 2013 Northern C-BASS data after ground spillover removal has been applied. **Top:** Intensity map, **bottom:** polarised intensity map. The dashed ellipses highlight the solar sidelobe region.

the choice was made to conduct this analysis using full day (day-time + night-time) data.

Figure 5.12 shows the ground spillover emission in intensity and polarised intensity. These maps were made by subtracting the August 2013 Northern maps, made before ground spillover correction, from those made after. These residual maps are shown to provide a reference point when considering what the ground spillover signal looks like in Galactic coordinates.

As a first attempt at removing the ground spillover, these result are promising.

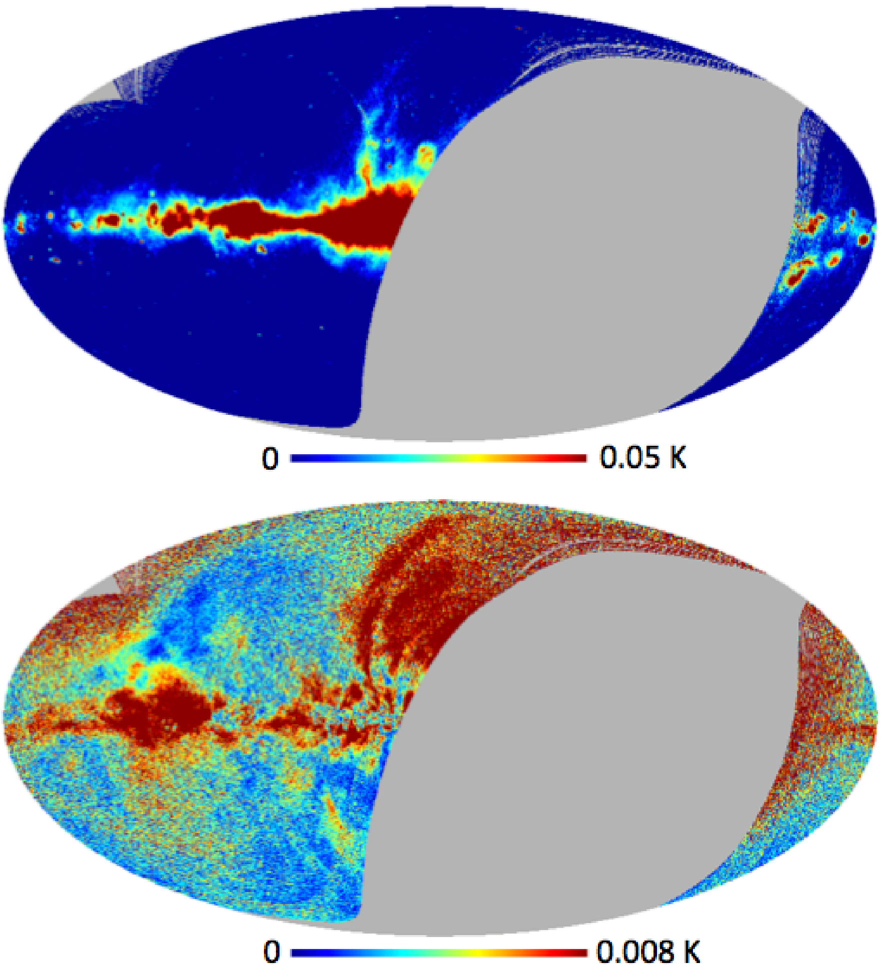

Figure 5.11: One month worth of August 2013 Northern C-BASS night-time data after ground spillover removal has been applied. **Top:** Intensity map, **bottom:** polarised intensity map.

An obvious initial question was how best to implement this ground removal function. Would one make thirty ground templates per month and then use their mean on the month's data as above or would the subtraction work better if each day had its own daily template subtracted from it? To try and answer this question, a ground-subtracted six month map was made from all the data obtained between June and November 2013 using the method in which one day's worth of data had its own daily ground template subtracted from it.

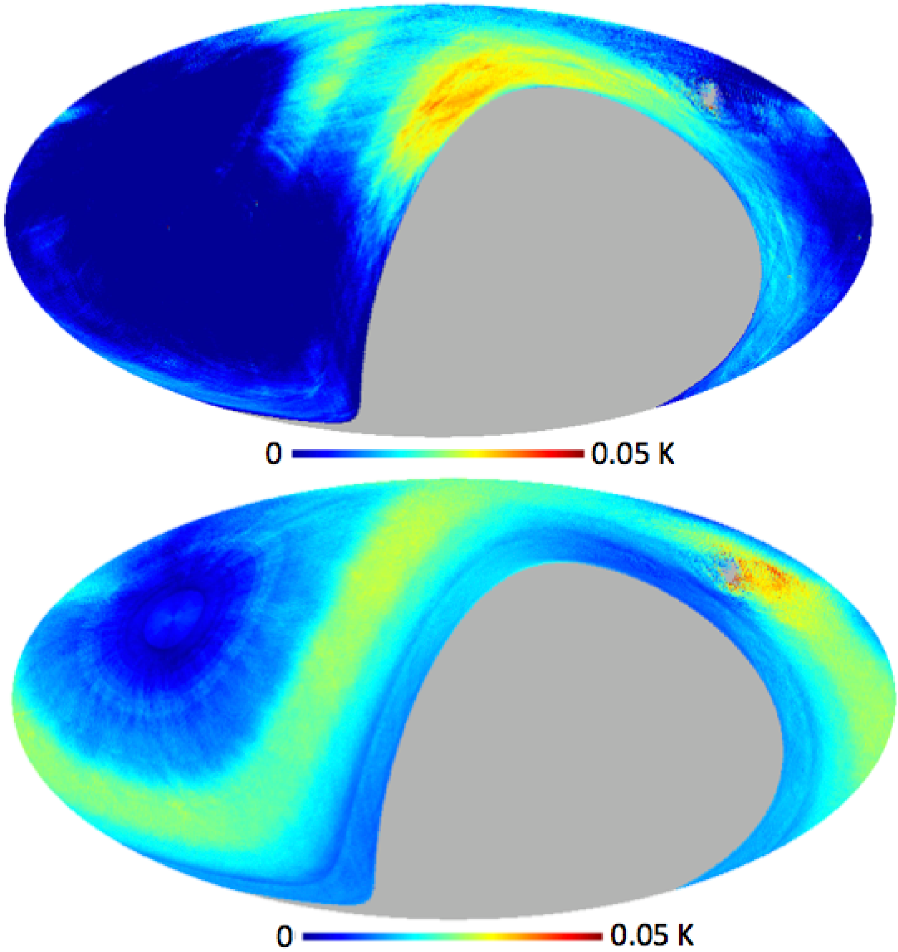

Figure 5.12: Ground spillover estimated from the residual maps between the one month worth of August 2013 Northern C-BASS data before and after ground spillover removal has been applied. **Top:** Intensity map, **bottom:** polarised intensity map.

Figure 5.13 shows the intensity and polarised intensity from August 2013 Northern C-BASS after each day has had its own daily ground template removed. The maps themselves look very comparable to the one month maps made shown in Figure 5.10, made using an average ground template. However a far more reliable test for over/under-subtraction of ground signal is through the use of jackknife tests and comparison with ancillary data.

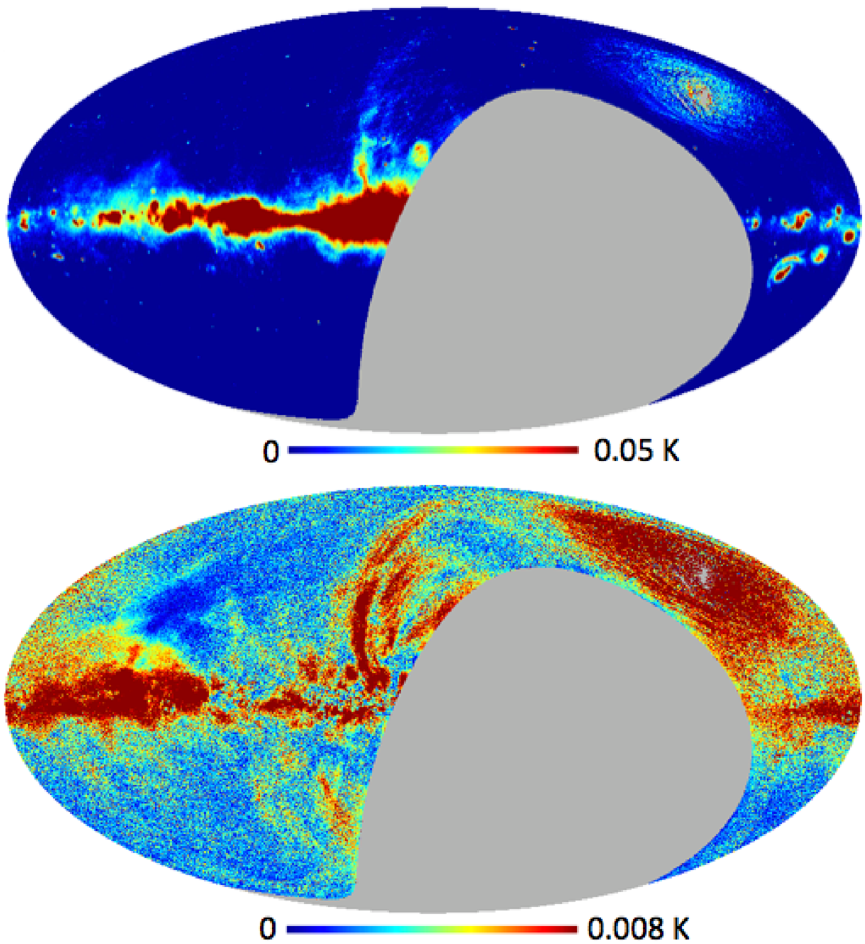

Figure 5.13: Maps for August 2013 Northern C-BASS data after daily ground templates have been removed from each days worth of data. **Top:** Intensity map, **bottom:** polarised intensity map.

5.2 Quantification of ground spillover removal methods

So far two possible variants of the ground spillover removal have been presented for the formation of ground spillover subtracted maps, the first using a monthly average, requiring 6 ground templates to be made and the second, using daily averages, requiring 6×31 templates. For simplicity, the ground spillover subtracted maps made from the monthly average ground templates will be called the Method 1 maps and the maps made from the daily average ground templates will be called the Method 2 maps.

The maps produced by these two methods are shown in Figures 5.10 and 5.13 and at first glance are very similar. Performing 'jackknife tests' can determine whether one, both or neither of the methods over/under-subtracts the ground signal. Additionally, bringing in ancillary data in the form of the 0.408 GHz Haslam et al. (1982), 1.420 GHz Reich & Reich (1986) and 22.5 GHz *WMAP* K-band maps will help to quantify the success of the ground spillover removal.

5.2.1 Jackknife tests

Jackknife tests involve subtracting various data subsets away from each other to reveal any systematic errors. If well calibrated the signal in both data sets should be the same leaving nothing apart from any differences in the systematic noise and the thermal noise. In this particular case maps would be made from the August ground spillover removed data at the two different survey elevations and various different azimuths and these maps would then be subtracted from each other. The desired residual maps would simply be white noise.

The Method 1 and 2 data were split into the following subsets: elevation = 37°, elevation = 47°, 90° $<$ azimuth $<$ 360°, 180° $<$ azimuth $<$ 90°, 270° $<$ azimuth $<$ 180° and 0° $<$ azimuth $<$ 270°. These subsets were chosen as the ground emission was known to vary with elevation and azimuth (Figure 5.2). The Stokes I, Q and U maps of the subset data were then subtracted from each other. For simplicity, the data subsection will be referred to by shorter names, the subsections and their shorthand are show in Table 5.2.

The residual maps were assessed by eye for large scale features. Figure 5.14 shows the residual maps for the Method 1 El47 − Az1 Stokes U residual and the Method 1 Az4 − El47 intensity residual to give an example as what was and was not counted as having visible large-scale residuals. The El47 − Az1 Stokes U map does not show large-scale ground structure that dominates over the noise level, however it does have

Subset	Name
el = 37°	El37
el = 47°	El47
90° < azimuth < 360°	Az1
180° < azimuth < 90°	Az2
270° < azimuth < 180°	Az3
0° < azimuth < 270°	Az4

Table 5.2: The data subsections used for the Jackknifes and their shorthand names.

residual features due to the solar sidelobe region residuals. The Az4 − El47 intensity map however, clearly displays residual ground emission. It can be seen that the signal within $|b| < 5°$ was masked out for this residual analysis. This was because the Galactic plane signal is so bright that even the pointing offsets within 0.1 of the beam FWHM or small calibrations differences will show up as beam sized (0°.73 FWHM) features.

From the jackknifes it was seen that the majority of both the Method 1 and Method 2 residual maps contained left over large-scale structure, indicating that further work is required to produce optimum ground templates. A full discussion of the future ground spillover work will be given in the summary to this Chapter. A notable difference between the Method 1 and Method 2 residual maps was the magnitude of the ground spillover signal remaining in the maps; the Method 2 maps appeared to have a lower residual level than the Method 1 maps. An example of this is given in Figure 5.15 which shows the El37 − Az1 intensity residuals for both Method 1 and Method 2. The Method 2 residual map shows less residual ground emission around the North Polar Spur.

Large-scale ground spillover level

To quantify the difference between the two methods better, the HEALPix function '`anafast`' was used to make power spectra of the residual maps. As the analysis was not being done on the full sky, the power spectra were multiplied by the fraction of sky

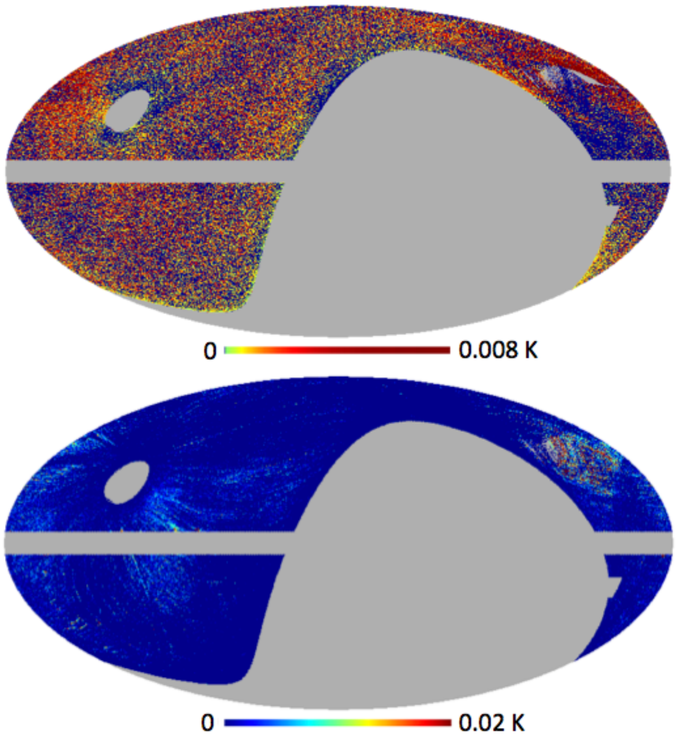

Figure 5.14: Two examples of residual ground spillover maps made using Method 1. **Top:** The El47 − Az1 Stokes U residual map showing no notably large-scale features other than those within the solar sidelobe region. **Bottom:** The Az4 − El47 intensity residual map showing large scale residual ground emission around the North Polar Spur and lower latitudes.

used, as the power spectrum variance is inversely proportional to the sky fraction.

Figure 5.16 shows power spectra for several of the residual maps in Stokes I, Q and U made using Method 1 and Method 2. The nomenclature El47El37-1 refers to the residual between the El47 and El37 maps which have been made using Method 1. The green lines on the plots represent an approximation of the 5 GHz Stokes I, Q and U signals which would be measured if no ground emission were present. The August 2013 C-BASS map with ground spillover subtracted using Method 2 was used as this approximation for the sky signal at 5 GHz. This 'ideal' signal will only roughly represent the actual 5 GHz sky because it still contains ground spillover emission.

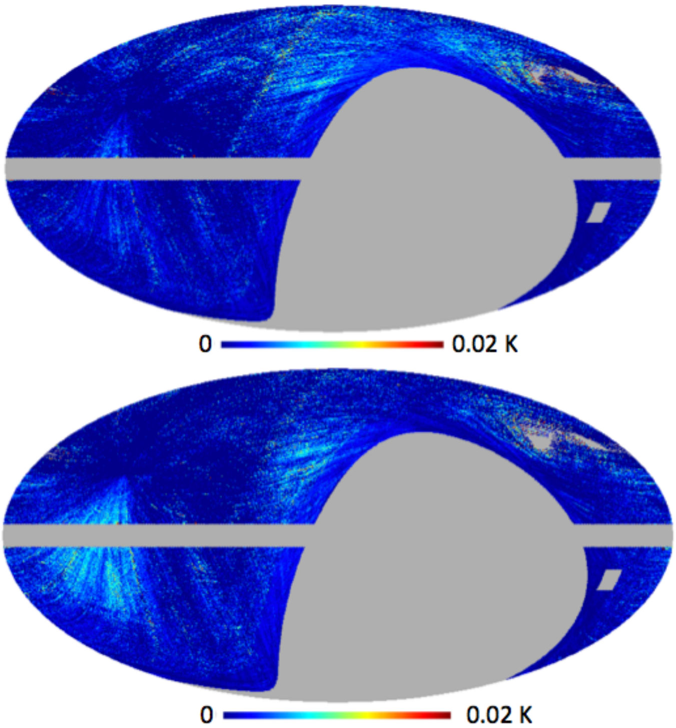

Figure 5.15: An examples of a residual ground spillover map made using Method 1 and 2. **Top:** The El37 − Az1 intensity residual map made using Method 1. **Bottom:** The El37 − Az1 intensity residual map made using Method 2.

However, as the ground subtracted maps can be seen to be dominated by sky signal, they can be used to give an estimate of the residual ground signal relative to the sky signal.

Both Method 1 and 2 power spectra show that the ground subtraction has worked well enough for the residual ground spillover to be lower than the large-scale sky signal. The Stokes I power spectra show that Method 2 is better for removing the ground spillover signal at angular scales less than 60°. In Stokes Q and U the methods perform fairly similarly over the full range of angular scales apart from the largest ($\theta \geq 40°$). Looking at the power spectra alongside the residual maps suggests that, overall Method 2 leaves less residual ground spillover in the maps than Method 1.

To assess the effect of solar sidelobe emission on the power spectra the Method 1 residual maps were reproduced for day/night-time only data. To produce day/night-

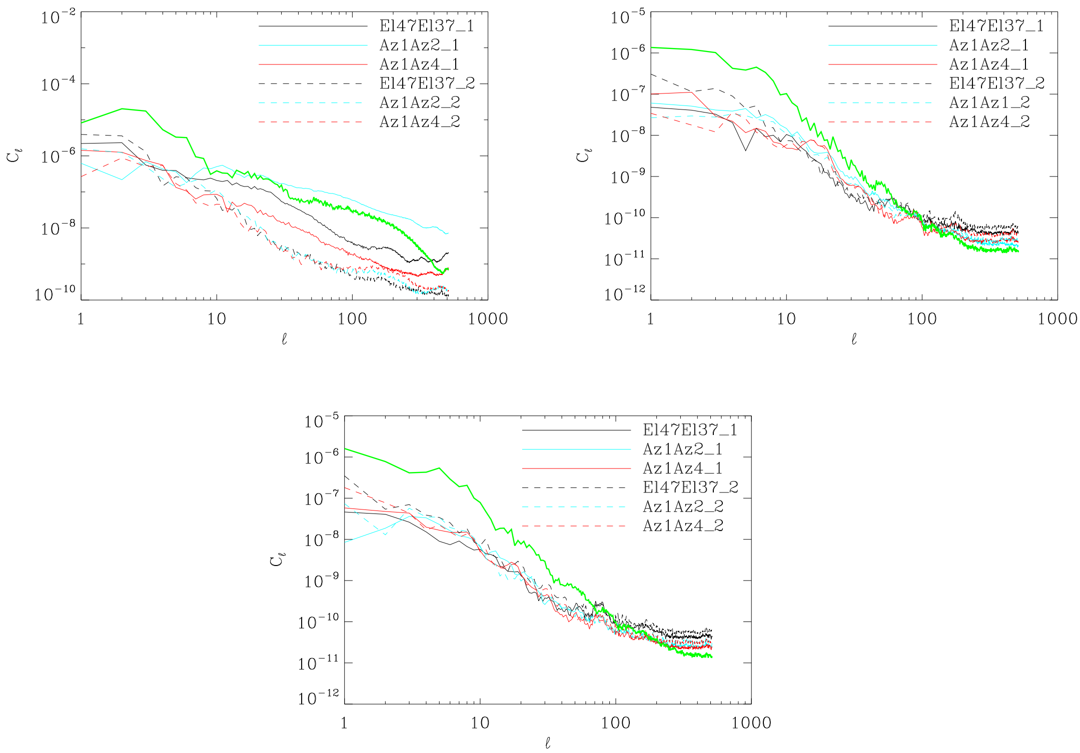

Figure 5.16: Comparison of power spectra of various residual maps made using Method 1 and Method 2. From top left clockwise: Stokes I, Stokes Q and Stokes U. The Method 2 power spectra are shown with dashed lines and the model 5 GHz sky Stokes I, Q and U signal is shown in green.

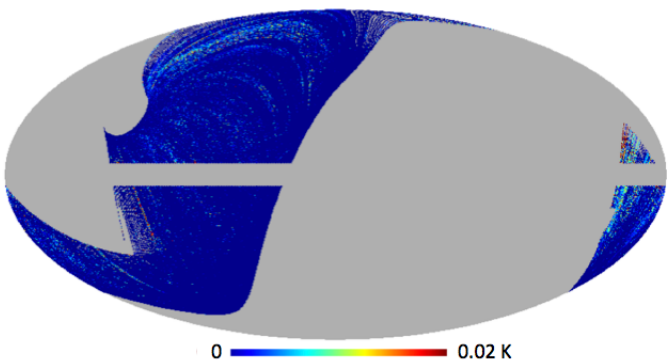

Figure 5.17: The El47 − Az1 intensity residual map made using Method 1 and night-time only data. The stripes visible across the map are caused by $1/f$ noise are present because too few data were used for the destriper to function optimally.

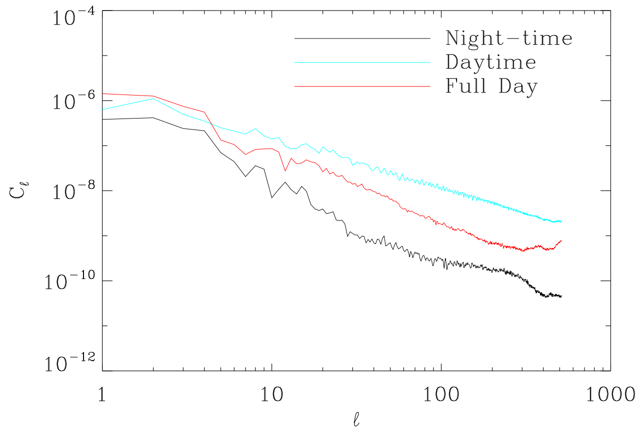

Figure 5.18: Power spectra for the full day, day-time and night-time only Intensity Method 1 Az1 − Az4 residual maps.

time ground spillover removed data, the August 2013 data were re-reduced, this time with the day/night monthly mean ground templates shown in Figure 5.8 being subtracted from the data. Figure 5.17 shows an example of a night-time Method 1 residual map in intensity made from the El47 and Az1 maps. This map shows the stripe features usually associated with $1/f$ noise which implies too few data have been provided for the map-maker to work optimally. The quality of the night/day maps produced will be of a lower standard than the full day maps, which is why at this stage of the ground spillover investigation full day data have been used.

Figure 5.18 shows the intensity power spectrum for the Az1 − Az4 residual maps made using Method 1 from night-time, day-time and full day data. The day-time power spectrum shows the highest power at small angular scales ($\ell > 50$), followed by the full day and then the night-time power spectrum. This demonstrates that the solar sidelobe emission causes a greater excess in power at smaller angular scales than the ground spillover. Comparison between the full day and night-time power spectra at large angular scales, however reveals that the solar sidelobe emission is also responsible for increasing the large scale emission by roughly a factor of three in intensity.

Having decided that Method 2 was the preferred method of ground removal, the analysis on Method 2 data was then extended to cover six months worth of data. The data was taken from June to November 2013. From Figure 5.18, it could be seen that the solar sidelobe emission only contributes significantly at around $\ell > 10$ and so the temperature variances C_ℓ for $0 < \ell < 10$ were used to quantify the level ground emission in the residual maps. A power law, normalised at $\ell = 5$, in the form of $y = A\ (\ell/5)^B$ was fit to the $3 < \ell < 15$ data, where A represents the power at $\ell = 5$ and B is the spectral index of the power law. In this way the fitted power at $\ell = 5$ could be compared for the various residual maps and the 5 GHz Sky model. The 5 GHz sky model used for this comparison was the June – November 2013 map with the ground emission removed using Method 2. Tables 5.3 shows the ratio of $\ell = 5$ powers between the Stoke I, Q and U residual maps with ground subtraction and the model 5 GHz Stokes I, Q and U maps. The residual maps were re-made, this time without the ground subtraction and the power ratios between these residual maps and the model 5 GHz maps are also shown, in parenthesis.

In Stokes I, the ground spillover subtraction reduces the large scale power by an average factor of around 60, this is a factor of roughly 8 in intensity. For Stokes Q and Stokes U the average reduction in intensity is roughly by a factor of 7. The residual ground spillover left within the ground subtracted maps is on average 0.04 of sky signal in intensity, 0.05 of the sky signal in Stokes Q and 0.14 of the sky signal in Stokes U. From Table 5.3 it can be seen that ground emission seems to be stronger in Stokes U than in Stokes Q, hence the similar reduction factor of ~ 7 but the different residual ground to sky signal fraction. Stokes Q and Stokes U are defined here in telescope reference frame as opposed to being Stokes Q and U on the sky.

5.2.2 Verification of the subtraction quality through ancillary data.

Another useful verification of the six month ground spillover subtracted (Method 2) map is its correlation with ancillary data. This verification is not as reliable as the jackknife tests as any differences between the C-BASS maps and ancillary maps can

	Stokes I					
	El37	**El47**	**Az1**	**Az2**	**Az3**	**Az4**
El37	–	0.06 (1.20)	0.03 (1.27)	0.04 (2.29)	0.04 (0.51)	0.04 (3.25)
El47	–	–	0.02 (0.74)	0.07 (1.18)	0.02 (2.45)	0.01 (3.88)
Az1	–	–	–	0.06 (1.01)	0.03 (1.99)	0.02 (4.56)
Az2	–	–	–	–	0.10 (3.51)	0.07 (3.37)
Az3	–	–	–	–	–	0.01 (3.55)
	Stokes Q					
	El37	**El47**	**Az1**	**Az2**	**Az3**	**Az4**
El37	–	0.08 (2.02)	0.03 (1.11)	0.06 (2.88)	0.04 (0.24)	0.03 (5.08)
El47	–	–	0.04 (0.10)	0.05 (3.11)	0.06(0.04)	0.01 (4.68)
Az1	–	–	–	0.05 (0.07)	0.05 (3.26)	0.02 (7.02)
Az2	–	–	–	–	0.12 (0.97)	0.07 (7.55)
Az3	–	–	–	–	–	0.05 (0.13)
	Stokes U					
	El37	**El47**	**Az1**	**Az2**	**Az3**	**Az4**
El37	–	0.08 (3.98)	0.06 (4.04)	0.13 (1.88)	0.06 (3.35)	0.05 (12.13)
El47	–	–	0.10 (1.07)	0.21 (2.58)	0.07 (3.03)	0.05 (19.50)
Az1	–	–	–	0.27 (7.33)	0.12 (7.76)	0.13 (30.16)
Az2	–	–	–	–	0.42 (1.71)	0.31 (8.66)
Az3	–	–	–	–	–	0.07 (14.8)

Table 5.3: The ratios of the C_ℓ values at $\ell = 5$ between the Method 2 ground subtracted residual intensity power spectra and the model 5 GHz power spectra for Stokes I, Q and U. The values in parenthesis show the ratios formed when using residual maps that have not had the ground emission removed.

be attributed to either map, not necessarily to the C-BASS map. Also the difference may in theory, be astrophysical in nature, as opposed to a systematic effect. However, as ground spillover subtraction is only preliminary it is reasonable to use ancillary data to look for any significant over- or under-subtractions of the ground emission.

The North Polar Spur is a prominent region in intensity and is also situated within the region worst affected by ground spillover emission. Therefore, this region shall be used to investigate the quality of the ground subtraction removal in intensity. Within polarised intensity, Loop II (the Cetus Arc) occupies the region worst affect by C-BASS polarised ground spillover emission and so Loop II shall be used to verify the polarised ground emission removal. The North Polar Spur has a well documented spectral index, Milogradov-Turin & Nikolić (1995) measured a spectral index of -2.92 ± 0.09 between 0.408 and 1.420 GHz, while Davies et al. (2006) state a spectral index of $-3.18^{+0.06}_{-0.09}$ between 0.408 and 22.5 GHz. The Cetus Arc has been noted to have a spectral index of -2.90 ± 0.28 between 0.408, 0.820 and 1.420 GHz (Borka Jovanović & Urošević 2010).

A simple and effective method to determine the spectral index of a region of diffuse emission is that of the Temperature-Temperature (T-T) plot (Turtle et al. 1962). If an emission can be described in the form of a power law then measurements of this emission taken at different frequencies (ν_1 and ν_2) will reveal a linear correlation, the gradient of which relates to the emission spectral index.

$$T(\nu_1) = \left(\frac{\nu_1}{\nu_2}\right)^{\beta} T(\nu_2) + \text{baseline}_2 - \text{baseline}_1 \left(\frac{\nu_1}{\nu_2}\right)^{\beta}. \tag{5.2}$$

A linear relationship will not be seen if more than one emission is present or if the emission cannot be described as a simple power law within the chosen frequency range. A notable advantage to the T-T plot method is the ability to decouple spectral index information from the baseline offsets. It is this which enables the comparison of different survey data.

This spectral analysis of the North Polar Spur region will use the 0.408 GHz Haslam et al. (1982) intensity, 22.5 GHz *WMAP* K-band polarised intensity and 4.76 GHz C-BASS intensity and polarisation data. The central frequency for the Northern C-BASS data is 4.76 GHz therefore, in the absence of Southern data this frequency will be used as the C-BASS frequency, as opposed to 5 GHz.

The data are all in the form of HEALPix all-sky maps and must all be smoothed to the same resolution and downgraded to the same HEALPix $\mathrm{N_{side}}$ for comparison. The maps were therefore smoothed to a resolution of 1° using a Gaussian beam with a FWHM of $\sqrt{60'^2 - \theta'^2}$ where θ is the survey FWHM. The choice of which HEALPix $\mathrm{N_{side}}$ to set all the maps to is a compromise between correlated pixels and the ability to

N_{side}	**Pixels per beam**
256	22
128	6
64	2
32	1

Table 5.4: The number of pixels per 1° FWHM beam for selection of HEALPix N_{side}

measure small angular scale structure. The solid angle covered by each pixel (Ω_p) on a HEALPix map is:

$$\Omega_p = \frac{4\pi}{12 \times N_{\mathrm{side}}^2}, \tag{5.3}$$

while the solid angle for a Gaussian beam (Ω_b) is calculated using the beam FWHM (θ) (Rohlfs & Wilson 2004).

$$\Omega_b = \frac{\pi \, \theta^2}{4 \, \ln 2} \tag{5.4}$$

$$= 1.133 \, \theta^2. \tag{5.5}$$

If the maps are downgraded to an N_{side} where the beam aperture is represented by more than one pixel then these pixels are correlated. The reduced χ^2 of any model fit to the data is underestimated when correlated pixels are counted as independent measurements, unless a covariance matrix is calculated. The number of pixels per 1° beam for several N_{sides} is shown in Table 5.4. The loss of small angular scale is demonstrated in Figure 5.19 which shows the Galactic plane ($25° < l < 35°$, $|b| < 5°$) as seen by C-BASS at N_{side} = 256 and 32. Therefore the chosen compromise for this T-T analysis was N_{side} = 64.

The Haslam et al. (1982) data are in mK in the Rayleigh-Jeans regime (T_{RJ}) while the *WMAP* data are in Kelvin in the thermodynamic regime (T_{CMB}). All data were converted to Kelvin within the Rayleigh-Jeans regime using the following conversion, which is derived in Appendix A.2:

$$\Delta T_{RJ} = \frac{x^2 e^2}{(e^x - 1)^2} \, \Delta T_{CMB}, \tag{5.6}$$

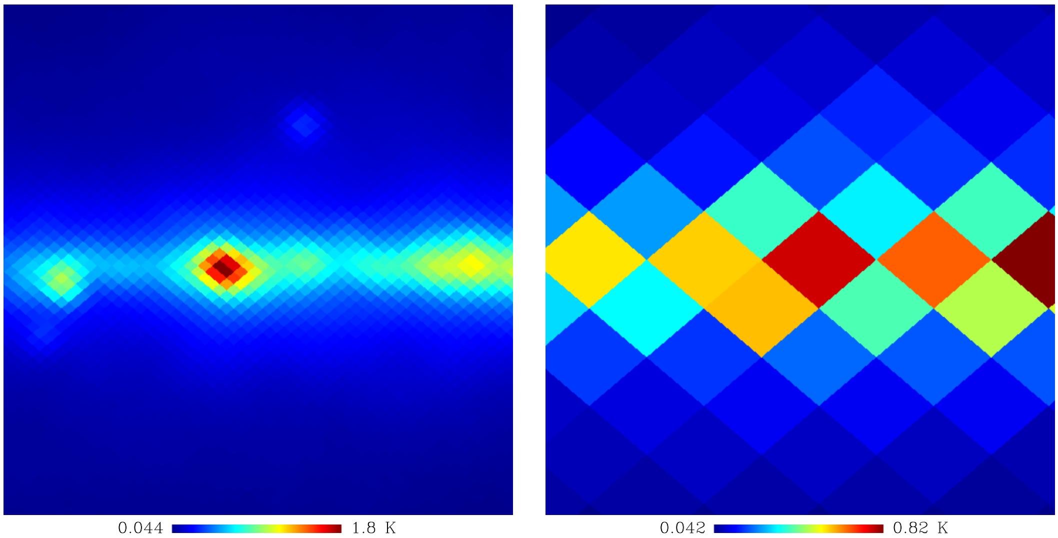

Figure 5.19: The Galactic plane ($25° < l < 35°, |b| < 5°$) as seen at 4.76 GHz and 45′ resolution by C-BASS. The image on the left is at $N_{side} = 256$ while the left image is at $N_{side} = 32$.

where

$$x = \frac{h\,\nu}{k_B\,T}. \tag{5.7}$$

The C-BASS data need an additional multiplicative factor to convert from antenna temperature to the full beam scale. This factor is 1.0881 and the term 'full beam' refers to the region within 5° degrees of the main beam peak (Holler et al. 2013).

To determine the North Polar Spur spectral indices linear plots of the data were formed and the uncertainties on the spectral indices determined were a combination of the pixel and calibration uncertainties. The pixel errors within each map have several possible contributions: the map thermal noise, the map smoothing errors, the CMB anisotropies, confusion noise and zero-level uncertainties. The CMB anisotropies are of the order $\sim 10^{-4}$ K_{CMB} and so only the *WMAP* K- band data, which are of order $\sim 10^{-3}$ K_{CMB}, feature these anisotropies as contributions to their uncertainties.

To calculate the pixel noise errors a Monte Carlo simulation was constructed, which combined the noise contributions to each pixel (p) as follows:

$$\sigma(p) = \epsilon \times (\sigma_{map}(p) + \gamma) \tag{5.8}$$

where $\sigma(p)$ is the pixel noise, ϵ is a random number, σ_{map} is the map thermal noise and γ is any additional noise contribution. For the C-BASS map 8×10^{-4} K worth of confusion noise was added, while for the Haslam et al. (1982) map a conservative 3 K of zero-level uncertainty was added and 10^{-4} K of CMB anisotropies was added for the *WMAP* map. The random number multiplicative factor is used to set up a random distribution around the pixel noise magnitude for the Monte Carlo simulation.

The map thermal noise is quoted as 0.70 K for the Haslam et al. (1982) data while the thermal noise on each *WMAP* K-band pixel is given as:

$$\sigma_{\text{intensity/polarisation}}(p) = \frac{0.001429/0.001435 \text{ K}}{\sqrt{\text{N}_{\text{obs}}}}. \tag{5.9}$$

The Haslam et al. (1982) and *WMAP* K-band (Bennett et al. 2013) noise maps formed from the pixel noise values above were then smoothed to a resolution of 1° and down-graded to HEALPix $\text{N}_{\text{side}} = 64$. The *WMAP* beams are known to be non-Gaussian (Page et al. 2003) and so the convolution beam needed was calculated by dividing a Gaussian beam of 1° FWHM by the K-band beam profile in ℓ. The noise values for each pixel were then stored in an array and the process was repeated 1000 times. The standard deviation of the 1000 noise values for one HEALPix pixel was used as the pixel noise.

The pixel noise values are used in the determination of the best fit line which was fitted using a least-squares fit which takes into account both the x- and y-axis errors. The best fit gradient (m), from which the emission spectral index is calculated from:

$$\beta = -\left(\frac{\ln(m)}{\ln(\nu_1/\nu_2)}\right), \tag{5.10}$$

has an error associated with it from the least-squares fit. The error on β is due to the error on m

$$\sigma_\beta = \left(\frac{1}{m\ f}\right) \sigma_m, \tag{5.11}$$

where

$$f = \ln\left(\frac{\nu_1}{\nu_2}\right). \tag{5.12}$$

The error on the slope parameter (m) is a quadrature combination of the fit error produced by the least-squares fitting routine and the calibration errors from both data sets:

$$\sigma_m = \sqrt{\sigma_{calib}^2 + \sigma_{fit}^2}, \tag{5.13}$$

where

$$\sigma_{calib} = \sqrt{\left(\sigma_y\right)^2 + (\sigma_x)^2}, \tag{5.14}$$

where $\sigma_{y/x}$ are the calibration errors of the two data set surveys.

This error analysis must be applied to both the intensity and the polarised intensity data. However the polarised intensity data have an additional bias related to the data noise which must be considered. Polarised intensity (PI) is constructed from Stokes Q and U:

$$\mathrm{PI} = \sqrt{(Q \pm \sigma_Q)^2 + (U \pm \sigma_U)^2}. \tag{5.15}$$

If the Stokes Q and U contributions were to be zero within a particular map pixel the measured PI would still have a value > 0 because of the Stokes Q and U uncertainties. This bias means that the measured PI is always greater than the true PI. Simmons & Stewart (1985) detail a correction for this bias which holds true under two assumptions, the signal-to-noise for both the Stokes Q and U measurements is greater than 4 and $\sigma_Q = \sigma_U = \sigma$. This bias correction is :

$$PI_{\mathrm{true}} = \sqrt{PI^2 - \sigma^2}. \tag{5.16}$$

Simmons & Stewart (1985), in fact consider three estimates of the true PI values (p_0 from the measured value (p). Using the Rice distribution:

$$F(p_0, p) = p\, e^{-\frac{\left(p^2+p_0^2\right)}{2}} J_0, \tag{5.17}$$

where J_0 is the zero order, modified Bessel function, they consider p_0 as the maximum, median and mean of this distribution. The maximum distribution estimator was first

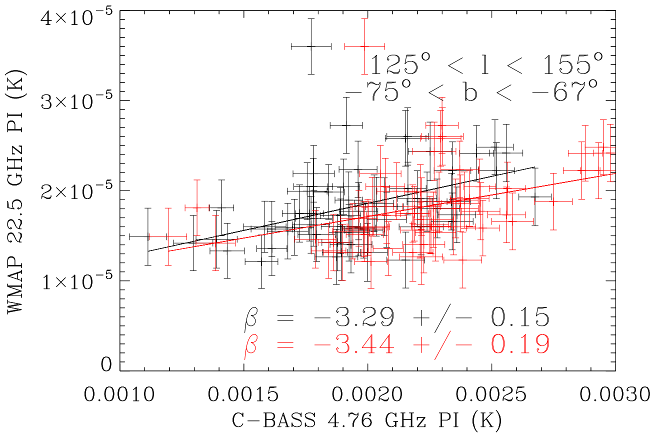

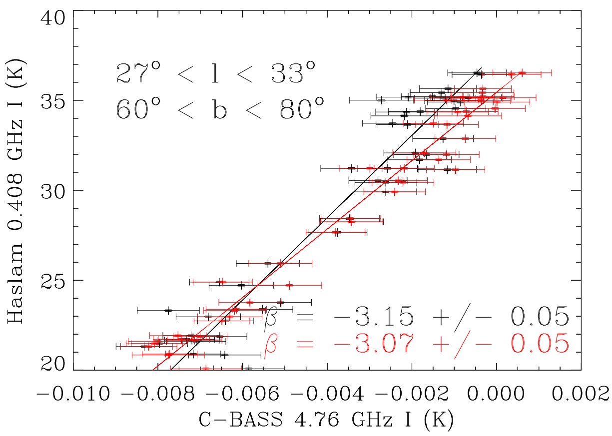

Figure 5.20: T-T plots with (black data and fit) and without (red data and fit) ground spillover removal applied. **Top:** Polarised intensity T-T plot between 4.76 and 22.5 GHz for the Cetus Arc. **Bottom:** intensity T-T plot between 0.408 and 4.76 GHz for the North Polar Spur.

used by Wardle & Kronberg (1974) and Simmons & Stewart (1985) found that all three of these estimators agree when the signal-to-noise is greater than 4. Therefore only C-BASS and *WMAP* Stokes Q and U pixels with a signal-to-noise greater than 4 were selected. The *WMAP* 22.5 GHz Stokes Q and Stokes U uncertainties are both equal to 1.435 mK (Bennett et al. 2013) and the C-BASS Stokes Q uncertainty was used for the both the Stokes Q and U uncertainties.

Figure 5.20 shows the T-T plots for the North Polar Spur intensity (0.408 – 4.76 GHz)

Measurement	β before	β after	r before	r after
NPS (intensity)	-3.07 ± 0.05	-3.15 ± 0.05	0.94 ± 0.02	0.96 ± 0.01
Cetus (PI)	-3.44 ± -0.19	-3.29 ± 0.15	0.39 ± 0.11	0.36 ± 0.11

Table 5.5: The spectral indices and correlation coefficients found using the August 2013 data in polarised intensity within the Cetus Arc and in intensity within the North Polar Spur before and after ground subtraction.

and the Cetus Arc in polarised intensity (0.408 – 22.5 GHz). The black points and fit are from the ground spillover removed C-BASS six month map while the red points and fit are from a map made using the same June to November 2013 data but, without removing the ground emission. The effect of the ground spillover can be seen to raise the measured C-BASS temperature by what seems to be a constant amount over the region examined as the spectral indices are effected but the pixel distribution around the best fit lines remain fairly constant. This is consistent with the earlier statements made about the smooth, large angular scale profile ground emission. The 0.408 – 4.76 GHz spectral indices for the North Polar Spur before and after ground subtraction are both within the expected value of ≈ -3.1 and while the ground corrected value of -3.15 is closer to the Davies et al. (2006) spectral index of $-3.18^{+0.06}_{-0.09}$ between 0.408 and 22.5 GHz all three spectral indices are consistent within their uncertainties. The ground emission removal appears to have made more of a difference within the fainter Cetus Arc in polarised intensity. The spectral index without the ground spillover correction, -3.44 ± -0.19, seems too high for the expected value of -2.90 ± 0.28 (Borka Jovanović & Urošević 2010). Removing the ground spillover brings the spectral index down to -3.29 ± 0.15 and into agreement with the expected value within the uncertainties.

The Pearson's correlation coefficients (r) show a fairly poor correlation, both before and after ground subtraction in polarised intensity within the Cetus Arc. This is due to the low signal-to-noise within this region, as confirmed by the strong correlations seen, both before and after ground subtractions in intensity within the North Polar Spur.

Table 5.5 summarises the spectral indices and correlation coefficients found within the North Polar Spur and Cetus Arc before and after ground emission subtraction.

5.3 Summary

Ground spillover is a significant systematic feature within the Northern C-BASS data. The ground emission has a maximum amplitude of $\approx$ 0.08 K in intensity $\approx$0.04 K in Stokes Q and U. This chapter has dealt with the removal of ground spillover signal from the intensity and polarisation data using ground emission templates. The templates are successful to the extent that they reduce the presence of ground spillover emission in the maps by a factor of $\approx$ 8 in intensity and $\approx$ 7 in Stokes Q and U. The level of residual ground spillover left in the maps is at a level of roughly 4 % of the sky signal in intensity 5 % in Stokes Q and 14 % in Stokes U.

The ground subtracted maps were compared to the Haslam et al. (1982) and *WMAP* data within the North Polar Spur and the Cetus Arc and it was found that the ground spillover subtraction made little difference in the high signal North Polar Spur region. Within the fainter Cetus Arc the spectral index between C-BASS and *WMAP* K-band in polarised intensity was changed from -3.44 ± 0.19 to -3.29 ± 0.15 after the ground subtraction. This implies that the ground emission was adding noticeable excess signal in polarised intensity.

Future work on the ground emission will include investigating the optimum mask to be used to filter out the Galactic plane and point source signals when forming the ground templates, applying the solar sidelobe emission removal, when completed and further testing of the effect of the destriping baseline offset used as well as the daily weather information measured. The empirical work described in this chapter will also be complimented by a theoretical model of the ground emission formed using the GRASP simulated beam convolved with the ground profile.

When the Southern telescope comes online a large portion of the Northern sky will be observed from the South, thus providing observations of the same regions of sky from sites with different ground emission. Jackknife tests between the Northern and Southern maps will further help to identify the residual ground emission left over after subtraction and if the Southern data are sufficiently free from ground emission they can be used as the model 5 GHz sky signal.

Chapter 6

Diffuse Galactic intensity emission

Once completed the C-BASS maps will represent the 5 GHz diffuse Galactic emission in both intensity and polarisation. Within the inner Galactic plane, the intensity signal is over $\sim 20\times$ greater in magnitude than the polarised intensity signal. At this stage, when the survey is incomplete and the ground removal process is yet to be thoroughly tested, analysis of a high signal-to-noise region such as the inner Galactic plane is feasible using only a few months' of data. Artefacts, such as stripes are still visible in the preliminary C-BASS maps but their effects will be negligible within the plane. In this chapter, the Northern intensity Galactic plane data from January and February 2012 will be used to verify the C-BASS calibration, act as a testbed for various free-free emission templates, separate free-free and synchrotron Galactic plane emission at 4.76 GHz and constrain the spectral form of AME emission between 4.76 and 100 GHz.

Figure 6.1 shows the Northern sky map made from the January to February 2012 survey data, calibrated but before the removal of ground signal. The colour scale has been set to minimise the appearance of ground spillover at high Galactic latitudes and to highlight the Galactic plane simply for reasons of aesthetics. Removal of the ground spillover was not crucial for the inner Galactic plane analysis as the maximum temperature that ground spillover contributes in intensity (~ 0.08 K) is roughly eight times lower than the total emission level. Figure 6.2 shows the $20^\circ < l < 40^\circ$, $-10^\circ <$

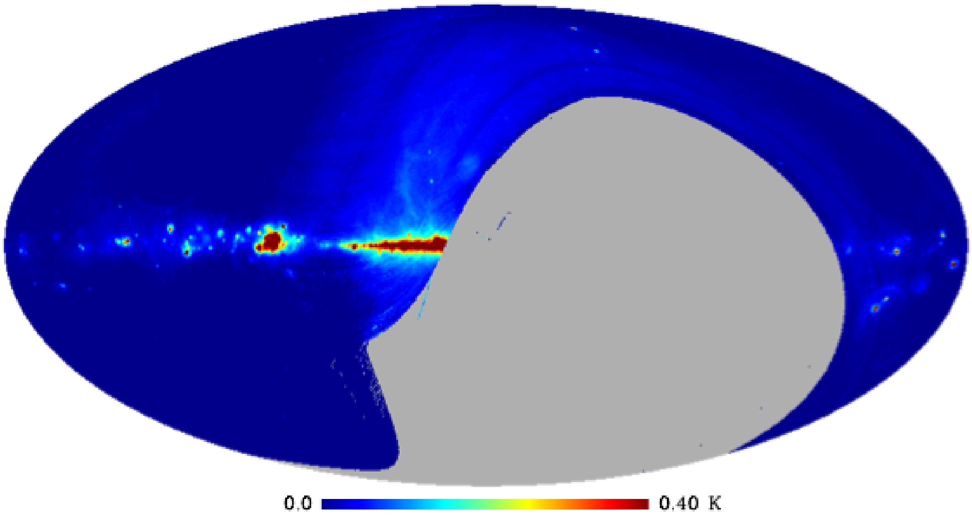

Figure 6.1: The calibrated C-BASS North two month map at HEALPix $N_{side} = 256$ and resolution $45'$ for January and February 2012. The ground spillover has not been removed and the Galactic plane $|b| < 10°$ is seen to dominate the emission.

$b < 10°$ region at 5 GHz chosen for analysis. The motivation behind the choice was the availability of a free-free emission template made using radio recombination lines within $20° < l < 44°$, $-4° < b < 4°$ (Alves et al. 2012).

6.1 Free-Free and Synchrotron emission between 0.408 and 4.76 GHz

At 4.76 GHz the C-BASS intensity map is well placed in frequency to investigate the separation of free-free and synchrotron emission within the Galactic plane using various free-free templates. This is an involved process as not only do each of the free-free templates come with their own assumptions, the spectral index of synchrotron emission is also known to vary, both spatially and spectrally. Any conclusions about the ratio of free-free and synchrotron emission within the plane and the spectral index of synchrotron emission between 0.408 and 4.76 GHz will be degenerate to some extent.

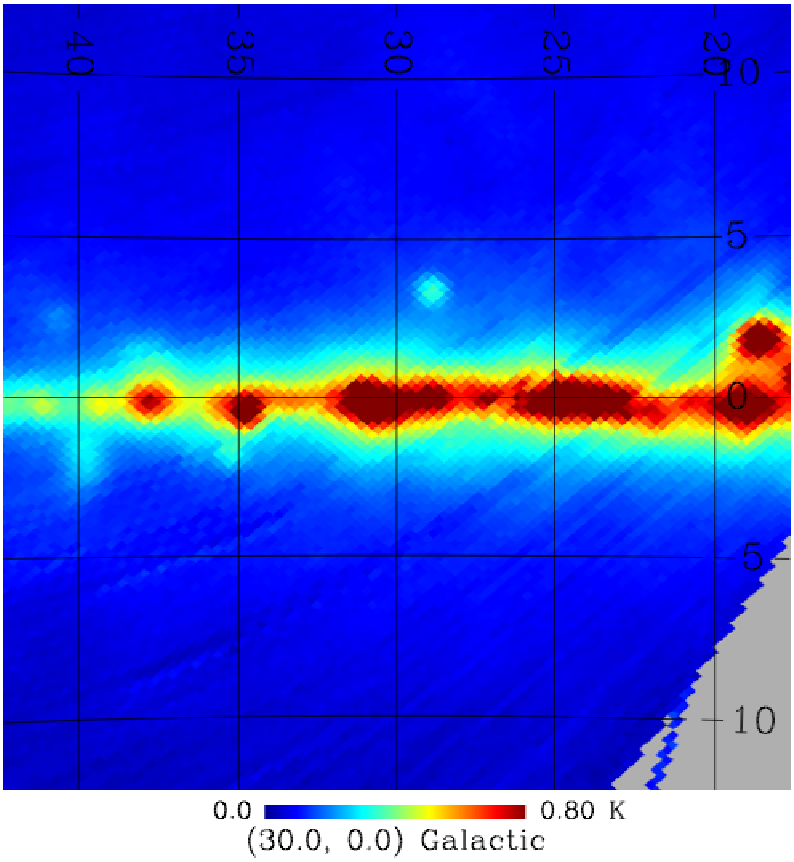

Figure 6.2: An enlarged view of the $-10° < b < 10°$, $20° < l < 40°$ region of the January to February 2012 within C-BASS North map. Resolution 45′ and HEALPix $N_{side} = 256$. Artefacts, such as stripes, are visible but much weaker than the Galactic plane signal.

This is because any comparison of free-free/synchrotron emission templates has to be done at the same frequency. In an attempt to see through this degeneracy several free-free templates will be used and both the Haslam et al. (1982) and Reich & Reich (1986) data will provide the ancillary data.

6.1.1 Free-Free Templates

Currently, there are several free-free templates available for use, some cover the full sky while others are only available or reliable within certain regions. The templates used in the Chapter have been made using Hα emission, radio recombination lines, maximum entropy methods, and Monte Carlo Markov Chain simulations.

Hα recombination line

The Hα free-free map generated from the method described in Section 1.7.2 can be produced at any frequency. A version was produced at 30 GHz, HEALPix N_{side} = 256 by Dr Clive Dickinson using an electron temperature of 7,000 K, which this work makes use of. A map of dust extinction corrected Hα data is also publicly available for those who wish to produce their own Hα free-free map. This Hα map (Finkbeiner 2003) uses an additional Hα data set on top of the WHAM and SHASSA data used by Dickinson, Davies & Davis (2003): the Virginia Tech Spectra line Survey (VTSS). The VTSS survey used cryogenically cooled CCDs to image the Northern sky at a $1'\!.6$ resolution (Dennison et al. 1998).

Radio Recombination Lines

The radio recombination line (RRL) free-free template used in this analysis is that of Alves et al. (2012) and was made using data from the HI Parkes All Sky Survey (HIPASS). HIPASS used the Parkes 21-cm multi-beam receiver to cover the $\delta < +2^\circ$ sky (Barnes et al. 2001). The RRLs measured using HIPASS were H168α (1.37 GHz), H167α (1.40 GHz) and H166α (1.42 GHz).

The free-free template produced assumed an electron temperature of 6,000 ± 1,000 K for the region it covered, $-4^\circ < b < 4^\circ, 20^\circ < l < 44^\circ$ and is at a resolution of $14'\!.8$ and with a calibration error of 15 %. The calibration error mainly comes from the uncertainty associated with the electron temperature. Figure 6.3 shows the RRL free-free template at its original resolution of $14'\!.8$ arcmin; where several compact HII regions can be seen.

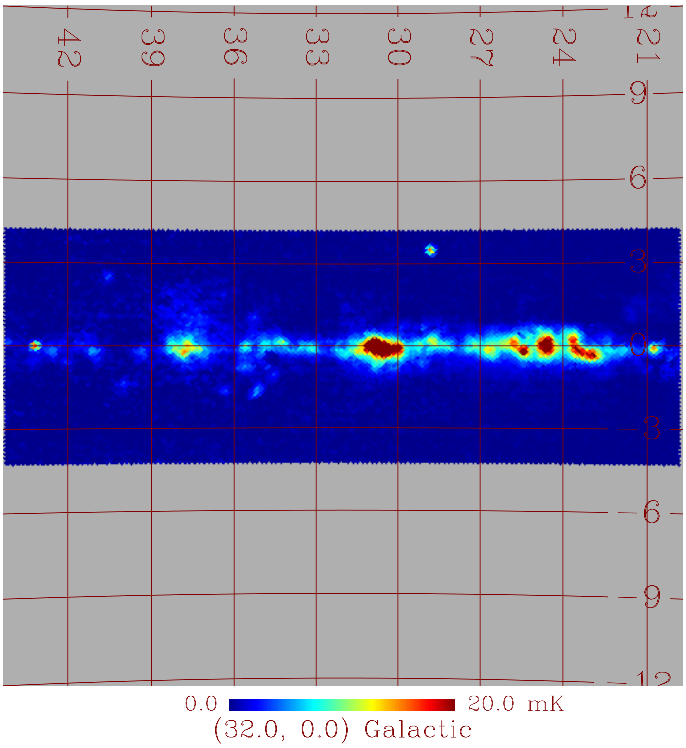

Figure 6.3: The RRL free-free templates at resolution 14$'\!.$8 arcmin and HEALPix $N_{side} = 512$.

WMAP Maximum Entropy Method

The maximum entropy method (MEM) is a Bayesian extension of the least-squares approach to fitting a model to data. Generally when you have empirical data which you are trying to fit a model to, the best fitting model is one which minimises the χ^2. MEM will instead try to minimise the 'entropy' of the fit (H) and so the MEM free-free model at 22.5 GHz is a spectral pixel-by-pixel (p) fit which uses Bayesian priors (Bennett et al. 2013):

$$H(p) = \chi^2(p) + \lambda(p)\, B(p), \tag{6.1}$$

where

$$B(p) = \sum_c T_c(p)\ \ln\left[\frac{T_c(p)}{e\ P_c(p)}\right]. \tag{6.2}$$

The T_c term is the model brightness of emission 'c' and in the nine year model, which this analysis uses, the emissions considered are synchrotron, free-free, thermal and spinning dust. This differs to the seven year model where the synchrotron and spinning dust contributions were modelled together as one component. For synchrotron/free-free/thermal dust emission, c = sync/ff/dust:

$$T_{\mathrm{sync/ff/dust}} \propto \nu^{-3.0/-2.15/+1.8}. \tag{6.3}$$

For spinning dust, the emissivity per hydrogen atom is taken from the model of Ali-Haïmoud, Hirata & Dickinson (2009), see Section 1.7.3. The spinning dust medium is assumed to be cold ($\sim$ 100 K) and neutral. The frequency of the peak brightness temperature is fixed at 14.4 GHz ($\sim$ 28 GHz in flux density) for all pixels except those brighter than 0.1 mK, these pixels have their peak temperature frequency fixed to fall between 10 and 30 GHz.

The prior used for the synchrotron emission is the 0.408 GHz Haslam et al. (1982) map. These data are used in their unfiltered form, point source included and have a zero-level offset of 3.9 K added, the 2.725 K CMB monopole subtracted and a 12.96 K extragalactic radio background added. The extragalactic contribution comes from the excess emission observed by the ARCADE 2 radiometer (Fixsen et al. 2011) which measured the absolute sky temperature at 3 GHz, 8 GHz, 10 GHz, 30 GHz and 90 GHz and identified background emission additional to the CMB which could be modelled as a power law:

$$T = \left(\frac{24.1 \pm 2.1}{\mathrm{K}}\right)\left(\frac{\nu}{310\ \mathrm{MHz}}\right)^{-2.599\pm0.036}. \tag{6.4}$$

The Haslam et al. (1982) map was scaled to the K-band frequency (22.5 GHz) using a spectral index of -2.9.

The Hα template of Finkbeiner (2003), in its dust extinction corrected form was used to form the free-free emission prior at 22.5 GHz using an electron temperature of 8,000 K. For the thermal dust prior, the 100 μm dust map extrapolated to 94 GHz, from Finkbeiner, Davis & Schlegel (1999) was used. The spinning dust prior was the dust map presented in Schlegel, Finkbeiner & Davis (1998), scaled to 22.5 GHz using 9.5 μK MJy^{-1}sr, which is the correlation slope between this dust map and a spinning dust map. This spinning dust map was formed from a least-squares fit within the Galactic plane between the five CMB subtracted *WMAP* maps (Bennett et al. 2013), the 0.408 GHz Haslam et al. (1982) map and the 2.4 GHz Duncan et al. (1995) data.

All the priors are smoothed to 1° resolution and downgraded to HEALPix $N_{\rm side}$ = 128. The 22.5 GHz MEM free-free model, which is used in this analysis, is available at HEALPix $N_{\rm side}$ = 128 and FWHM 1° [2].

WMAP Markov Chain Monte Carlo

A Markov chain is a sequence of events where the probability of the transition from one event to the next is only dependent on the probability information (the 'immanent past' information) of the previous step while Monte Carlo simulations are a way of compute the probability distribution of an event through multiple simulations. Markov Chain Monte Carlo (MCMC) numerical algorithms combine the two stochastic techniques to find the maximum likelihood ratio between a model governed by a set of parameters (γ_b) and a set of empirical data (D):

$$\text{likelihood ratio} = \frac{P(D|\gamma_b)}{P(D|\gamma_a)}, \tag{6.5}$$

where γ_a is an initial guess at the parameter set which changes to γ_b with each step of the chain.

The *WMAP* MCMC algorithm fits the following total Stokes I, Q and U emission models for each pixel (Bennett et al. 2013):

$$\begin{aligned} T(\nu, p) &= T_{\rm s}\left(\frac{\nu}{\nu_K}\right)^{\beta_{\rm s}(\nu)} + T_{\rm ff}\left(\frac{\nu}{\nu_K}\right)^{\beta_{\rm ff}} + a(\nu)\, T_{\rm CMB} \\ &+ T_{\rm d}\left(\frac{\nu}{\nu_W}\right)^{\beta_{\rm d}} + T_{\rm sd}(\nu_K)\, S_{\rm sd}(\nu) \end{aligned} \tag{6.6}$$

and

$$Q(\nu) = Q_{\rm s}\left(\frac{\nu}{\nu_K}\right)^{\beta_{\rm s}(\nu)} + Q_{\rm d}\left(\frac{\nu}{\nu_W}\right)^{\beta_{\rm d}} + a(\nu)\, T_{\rm CMB} \tag{6.7}$$

[2] http://lambda.gsfc.nasa.gov/product/map/dr5

and

$$U(\nu) = U_{\rm s}\left(\frac{\nu}{\nu_K}\right)^{\beta_{\rm s}(\nu)} + U_{\rm d}\left(\frac{\nu}{\nu_W}\right)^{\beta_{\rm d}} + \ a(\nu)\ T_{\rm CMB}, \tag{6.8}$$

where the subscripts s, ff and CMB, d and sd denote the synchrotron, free-free, CMB, thermal dust and spinning dust contributions, $S_{\rm sd}$ is the spinning dust spectrum and ν_K and ν_W are the K-band and W-band frequencies of 22.5 GHz and 93.5 GHz.

There are four sets of MCMC foreground models: models c, e, f and g. These models differ with regards to their handling of synchrotron and spinning dust emission. All the models have a fixed $a(\nu)$ parameter which converts the CMB thermodynamic temperature into the Rayleigh-Jeans regime and a free-free spectral index, which is fixed at $\beta_{\rm ff} = -2.16$. Model c leaves the thermal dust and spectral indices as free parameters and does not includ a spinning dust contribution within the fit. Model e leaves the thermal dust spectral index as a free parameter, fixes the synchrotron spectral index to -3.0 and includes a spinning dust contribution using the cold neutral medium spectral form (Ali-Haïmoud, Hirata & Dickinson 2009; Silsbee, Ali-Haïmoud & Hirata 2011) normalised to equate to one at K-band with the peak frequency rescaled, to match existing radio data, by 0.7 across the full sky. Model f is similar to model e except that the spinning dust peak rescaling/shift parameter is 0.84 and the synchrotron spectral index is allowed to vary spatially assuming a power-law form for the synchrotron emission temperature. Model g is the same as model f but instead of being modelled as a power-law the synchrotron emission is modelled as (Strong, Orlando & Jaffe 2011):

$$\frac{T(\nu)}{\rm K} \propto \left(\frac{c}{\rm m\ s^{-1}}\right)^2 \frac{1}{2}\left(\frac{I(\nu)}{\rm ergs\ cm^{-2}\ s^{-1}\ Hz^{-1}\ sr^{-1}}\right)\left(\frac{\nu}{\rm Hz}\right)^{-2}, \tag{6.9}$$

where

$$\frac{I(\nu)}{\rm ergs\ cm^{-2}\ s^{-1}\ Hz^{-1}\ sr^{-1}} = \int\left(\frac{\epsilon(\nu)}{\rm erg\ s^{-1}\ Hz^{-1}}\right)\ ds, \tag{6.10}$$

where ϵ is the combined synchrotron emissivity from both a uniform and randomly orientated magnetic field and $\int ds$ is the integral along the line-of-sight.

Figure 6.4 shows the latitude distributions of the model c, e, f and g MCMC free-free templates. The $20^\circ < l < 40^\circ$ emission was averaged every $0.^\circ8$ in latitude. Model c, which does not include the spinning dust contribution, seems to underestimate the

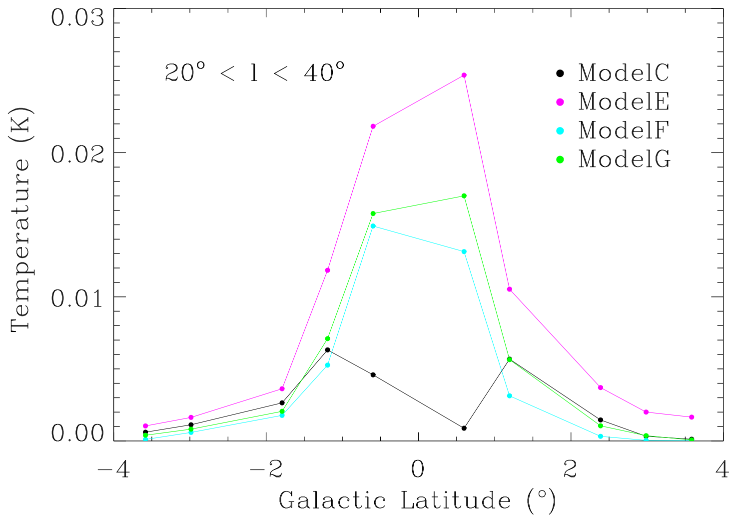

Figure 6.4: The Galactic latitude distributions of the four MCMC free-free templates at resolution 1° and HEALPix $N_{\rm side} = 64$. The $20° < l < 40°$ emission was averaged every 0.°8 in latitude.

Galactic free-free emission as a dip in the latitude distribution can be seen. Model e, which fixes the synchrotron spectral index produces a free-free emission profile of greater magnitude than the profiles produced using model f and g. Model f is the one chosen for analysis in this chapter as this model, with its spinning dust contribution and power-law model of synchrotron emission with a variable spectral index, reflects the current and widely accepted understanding of total emission contributions.

However, before the analysis on the Galactic plane, it would be useful to take our free-free templates, the ancillary and the C-BASS data to a 'test region' with a well documented spectral index to confirm that the data are all consistent.

6.1.2 Data consistency checks using Barnard's Loop

HII, ionised hydrogen, regions provide the ideal environment to test our data and free-free templates as they are free-free emission dominated and so should have a spectral index of ≈ -2.1. Barnard's Loop is an example of such a region; it is a HII shell within the Orion complex (Heiles et al. 2000). Figure 6.5 shows Barnard's Loop in Hα emission and at 4.76 GHz, as seen by Northern C-BASS. The compact sources Orion A (M42), Orion B and J060746-062303 have been masked out of the C-BASS image using an aperture 3.5$\times$ the C-BASS aperture for Orion A and B and 2$\times$ the C-BASS aperture for J060746-062303. A smaller mask size was required for J060746-062303 as the source is not as bright as Orion A or Orion B. A strong correlation of 0.88 ± 0.014 exists between the Hα emission and total 4.76 GHz emission plotted in the Figure 6.5 correlation plot. This reaffirms the statement that Barnard's Loop is dominated by free-free emission.

The Haslam et al. (1982), Reich & Reich (1986) and *WMAP* K-Band data were used to calculate the Barnard's Loop spectral index between the C-BASS data and free-free templates. The RRL template does not extend to this region and therefore this analysis could not extend to those data. The maps were all smoothed to 1° resolution, downgraded to HEALPix $N_{\rm side} = 64$ and converted into Kelvin in the Rayleigh-Jeans regime and on the full beam scale. For the Reich & Reich (1986) data the full beam scale factor is 1.55 where in this case the term 'full beam' refers to the region within 7° of the main beam peak, while for C-BASS, it is 1.0881 and full beam refers to within 5° of the main beam peak. Investigation into the correct scale factor to apply to Reich & Reich (1986) data is ongoing (see Appendix B) and so these data will be used with a calibration uncertainty of 10 % as opposed to the 5 % documented in the literature.

Figure 6.6 displays T-T plots using the C-BASS data alongside the Haslam et al. (1982), Reich & Reich (1986) and *WMAP* K-band data. A description of the pixel error calculation is given in Section 5.2.2 and, as with the T-T plots shown in that section, the errors on the derived spectral indices are a quadrature addition of the pixels noise errors and the calibration errors associated with the data sets. The 0.408 – 4.76 GHz and 4.76 –22.5 GHz T-T plots presents data with some scatter from the best fit line. This is because at 0.408 GHz/22.5 GHz, the presence of synchrotron emission/AME will lower the goodness-of-fit as a linear fit can only fully describe one emission at a time. The spectral indices of -2.16 ± 0.05, -2.15 ± 0.12 and -2.13 ± 0.05 between

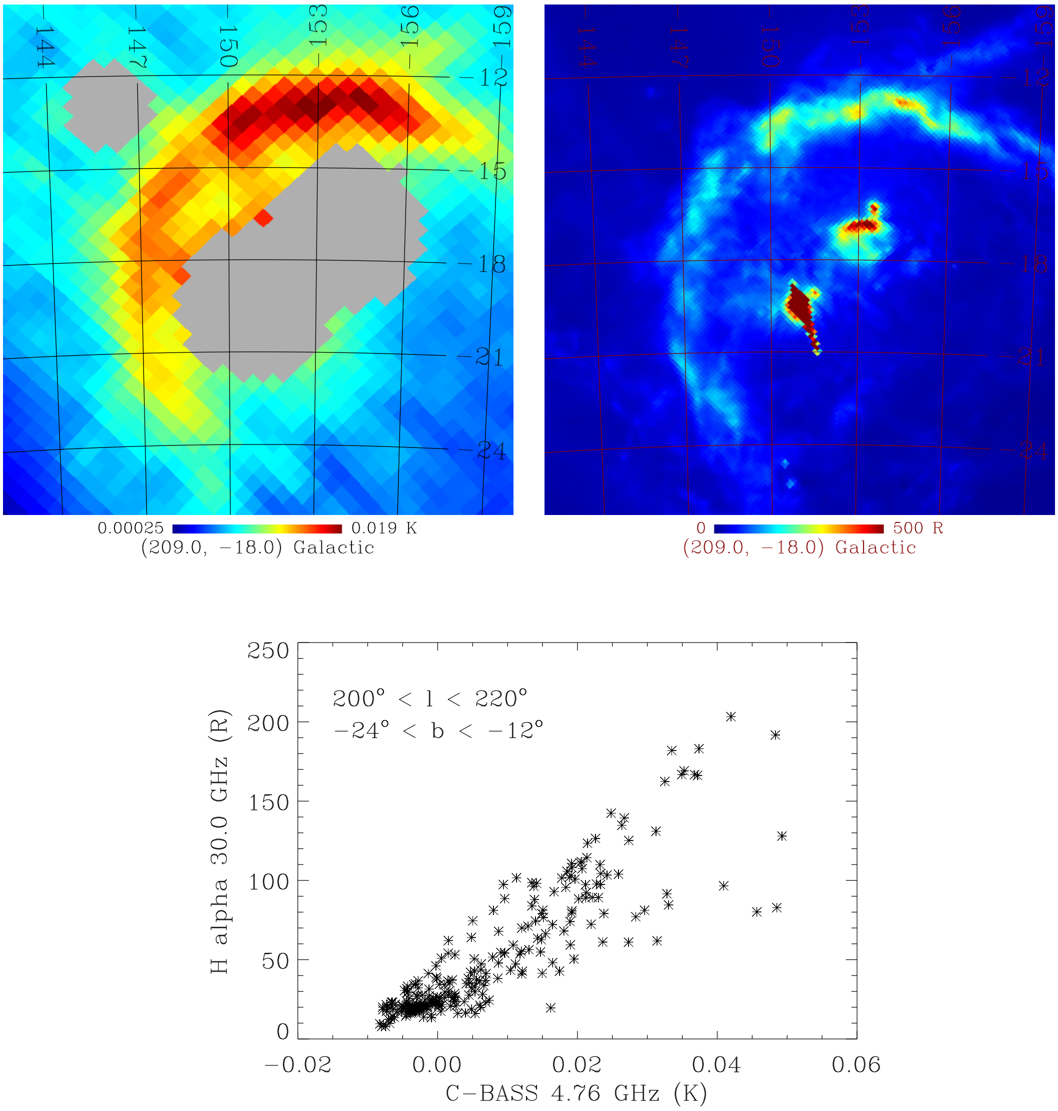

Figure 6.5: Barnard's Loop as seen **top left:** at 4.76 GHz by Northern C-BASS. N_{side} = 256 and FWHM resolution of $0^{\circ}.73$. Orion A, Orion B and J060746-062303 are masked out and **top right:** in Hα emission at HEALPix N_{side} = 512 (Finkbeiner 2003). **Bottom:** Correlation plot between the Northern C-BASS and Hα data over the Barnard's Loop region.

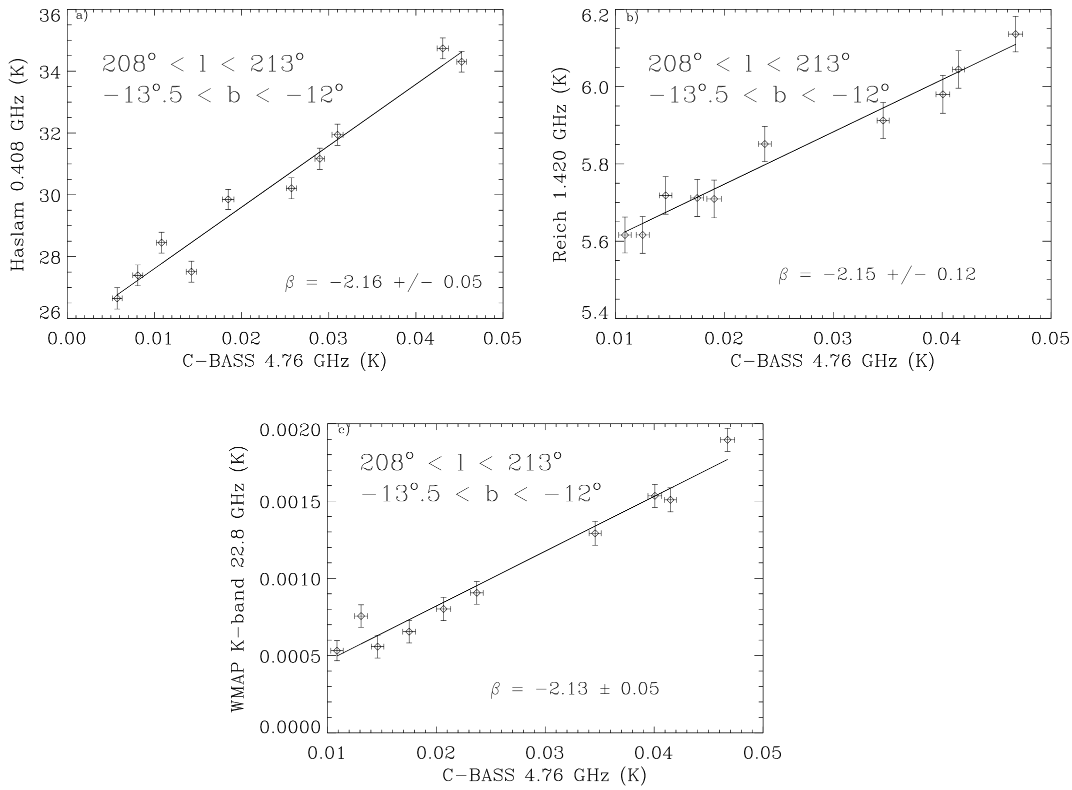

Figure 6.6: T-T plots of the Barnard's Loop region between 0.408, 1.4, 22.5 GHz and 4.76 GHz. The data have been smoothed to 1° resolution and downgraded to HEALPix $N_{side} = 64$. The derived spectral indices are consistent with a free-free spectral index of $\beta \approx 2.1$.

0.408 GHz, 1.420 GHz, 22.5 GHz and 4.76 GHz confirm, to within 1σ, a free-free dominated spectral index for Barnard's Loop.

Figure 6.7 shows Barnard's Loop TT-plots taken between the Haslam et al. (1982) and Reich & Reich (1986) data sets and the MEM and MCMC free-free templates at resolution 1°, HEALPix $N_{side} = 64$. As before, the MEM plot that includes the Haslam et al. (1982) data has some scatter around the best fit line because synchrotron emission is included. Nevertheless both the MEM plots have spectral indices within 1σ of the *WMAP* MEM free-free spectral index estimate of -2.15. Between 0.408/1.42 GHz and the MEM 22.5 GHz the spectral indices are -2.17 ± 0.03 and -2.14 ± 0.05, respectively.

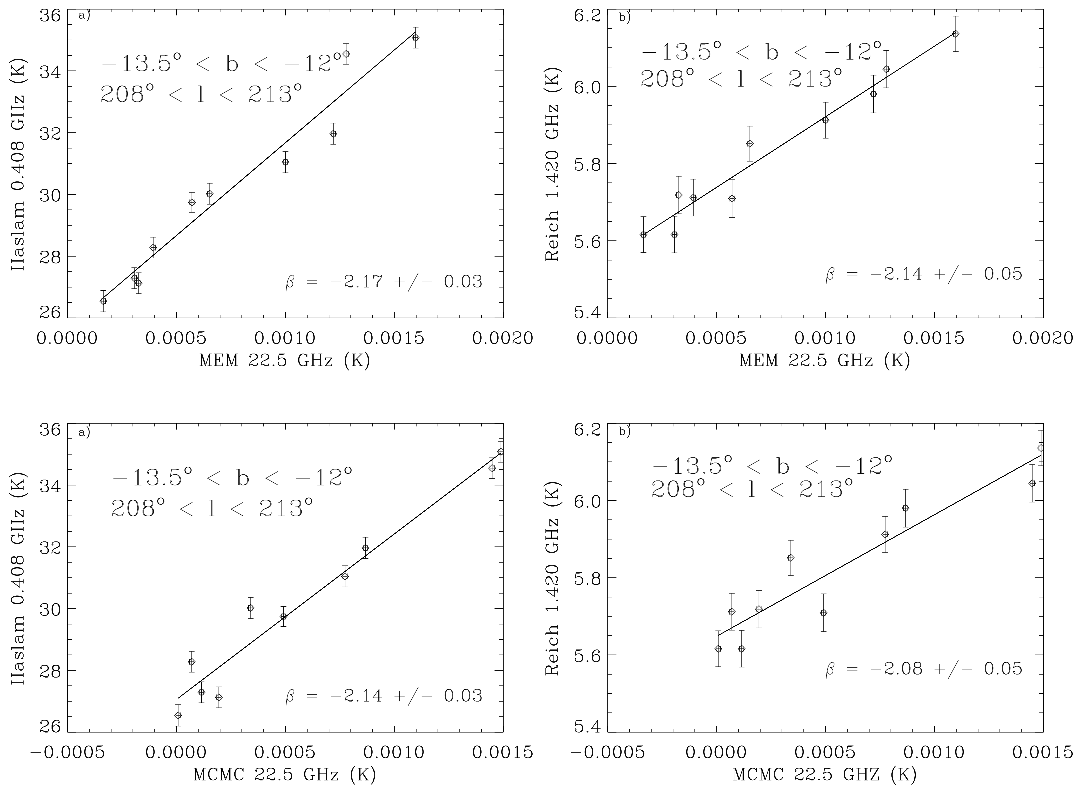

Figure 6.7: T-T plots of the Barnard's Loop region between 0.408, 1.420 and the MEM (top row) and MCMC (bottom row) 22.5 GHz free-free templates. The data have been smoothed to 1° resolution and downgraded to HEALPix N_{side} = 128. The derived spectral indices are consistent with a free-free spectral index of $\beta \approx 2.1$.

The equivalent MCMC plots are shown on the bottom row of Figure 6.7 at 1° resolution and HEALPix N_{side} = 64. The spectral indices of -2.14 ± 0.03 (for 0.408 – 22.5 GHz) and -2.08 ± 0.05 (for 1.420 – 22.5 GHz) are within a 1σ agreement of the expected free-free thermal index of ≈ 2.1. From this T-T analysis, it can be seen that both the *WMAP* MEM and MCMC 22.5 GHz free-free templates successfully reproduce the free-free dominated total emission expected within the Barnard's loop region.

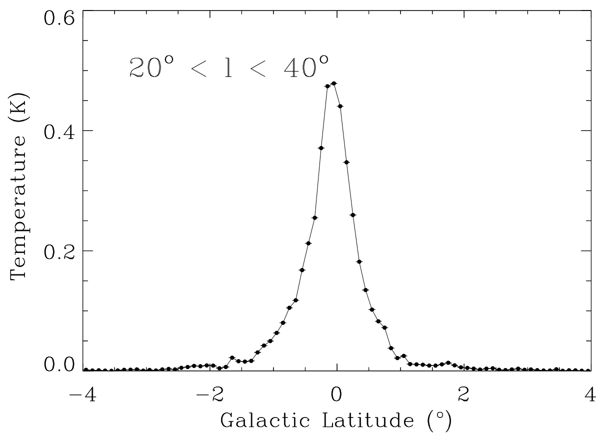

Figure 6.8: Latitude cut of the RRL free-free template with average longitudinal values, taken every 0.°1 in latitude, between 20° and 40°. The RRL free-free template are shown at their original FWHM of 14.′8 and $N_{side} = 512$. The narrow (≈ 1°) distribution of free-free emission is evident.

6.1.3 Off-Plane Synchrotron emission

The total diffuse Galactic plane emission seen at 5 GHz is a mixture of free-free and synchrotron emission. These two emissions display very different latitude distributions across the Galactic plane. Free-free emission is known to have quite a narrow latitude distribution while synchrotron emission is broader (Broadbent, Osborne & Haslam 1989). Figure 6.8 shows a latitude cut of the RRL free-free template across its full latitude range but averaged (at every 0.°1) between 20° and 40° in longitude. The narrow shape of the free-free distribution is clear; this indicates the free-free contribution is less than the synchrotron contribution beyond two degrees in latitude from $b = 0°$. This hypothesis can be tested by looking at the off-plane ($4° < |b| < 10°$) emission spectral indices.

T-T plots were made within the off-plane latitude range of $4° < |b| < 10°$, based on the belief that this region is dominated by synchrotron emission between 0.408/1.420 and 5 GHz. The latitude range was spilt between positive and negative latitudes to take into account the presence of the North Polar Spur and the Gould Belt.

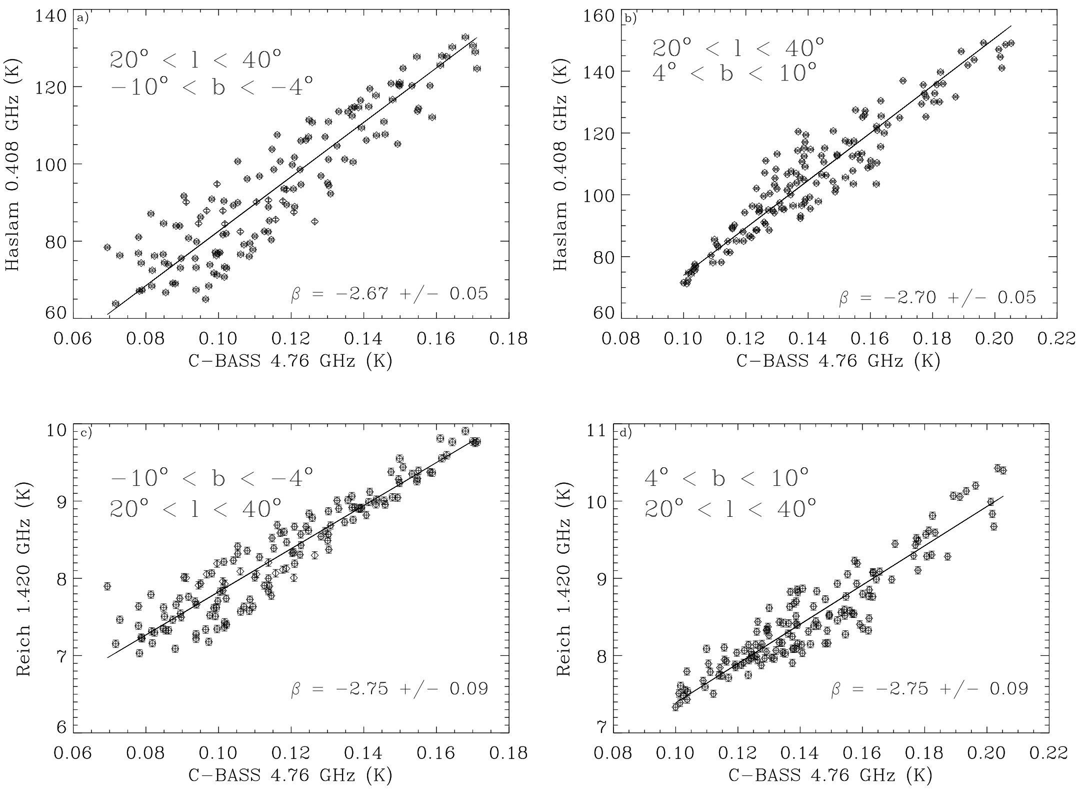

Figure 6.9: T-T plot between 0.408 and 4.76 GHz for **a)** $-10° < b < -4°$ and **b)** $10° > b > 4°$. T-T plot for 1.420 and 4.76 GHz for **c)** $-10° < b < -4°$ and **d)** $10° > b > 4°$.

The Gould Belt is a star forming disc, tilted at $\sim$ 17° to the Galactic plane first observed by naked eye, because of its bright OB stars by Herschel and Gould. Davies (1960) characterised it as a $\sim$ 500 pc radius 'sub system' within the Milky Way containing the Sun as well as numerous HI clouds. Using the HIPPARCOS catalogue (Perryman et al. 1997), which contains parallax measurements of the positions and distance for $> 100,000$ stars within $\sim$ 200 pc of Earth, Perrot & Grenier (2003) modelled the Gould Belt in 3D to locate the Belt centre at (104 ± 4) pc from the Sun with a thickness of 60 pc. They also note the high supernova rate inside the Belt which they estimate to be between three and five times higher than in the Galactic plane.

Figure 6.9 shows the T-T plots between 0.408/1.420 GHz and 4.76 GHz for the

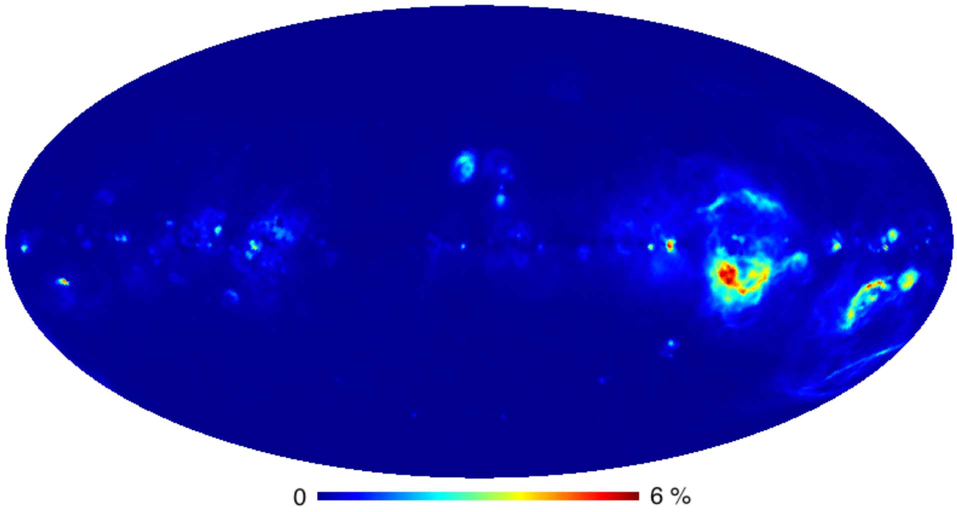

Figure 6.10: The ratio between the Hα free-free map scaled to 0.408 GHz and the Haslam et al. (1982) 0.408 GHz map. The Hα map was scaled using $\beta = -2.1$ and both maps were smoothed to 1° resolution and downgraded to HEALPix $N_{side} = 128$.

positive and negative off-plane latitudes within the $20° < l < 40°$ longitude range. Figures 6.9b) and 6.9d) feature the beginning of the Gould Belt region in their latitude range as well as the base of the North Polar Spur and each can be seen to each display what would appear to be the combination of two different linear forms. These combinations originate from the inclusion of synchrotron emission of a different spectral index to the Galactic synchrotron emission. The 0.408 to 4.76 GHz spectral indices of -2.67 ± 0.05 and -2.70 ± 0.05 are on average flatter than the spectral indices of -2.75 ± -0.09 and -2.67 ± 0.09 between 1.420 and 4.76 GHz and this is consistent with the literature as discussed in Section 1.2.1.

The spectral indices shown in Figure 6.9 range from -2.67 ± 0.06 to -2.75 ± 0.09, which implies the presence of either a relatively flat spectrum synchrotron emission or a combination of steep spectrum synchrotron emission and free-free emission. The Dickinson, Davies & Davis (2003) Hα free-free emission all-sky template can be used as an off-plane free-free template to gauge the contribution of free-free emission to these spectral indices.

The scaling from 30 GHz to 0.408/1.420/4.76 GHz required for the Hα free-free

Lon. (°)	**Lat.** (°)	ν **GHz**	β	β_{corr}
20 – 40	$-10 \rightarrow -4$	0.408 – 4.76	-2.67 ± 0.05	-2.65
20 – 40	$4 \rightarrow 10$	0.408 – 4.76	-2.70 ± 0.05	-2.72
20 – 40	$-10 \rightarrow -4$	1.420 – 4.76	-2.75 ± 0.09	-2.77
20 – 40	$4 \rightarrow 10$	1.420 – 4.76	-2.67 ± 0.09	-2.74

Table 6.1: The off-plane ($4^\circ < |b| < 10^\circ$) spectral indices between 0.408/1.420 GHz and 4.76 GHz with and without free-free emission subtraction using the Hα free-free template.

map was achieved using a spectral index of $\beta = -2.1$. These scaled free-free templates at 0.408/1.420/4.76 GHz were then subtracted pixel-by-pixel from the Haslam et al. (1982), Reich & Reich (1986) and C-BASS maps after all the data were smoothed to 1° resolution and downgraded to HEALPix $N_{side} = 64$. The spectral analysis shown in Figure 6.9 was then repeated on the free-free subtracted maps. Table 6.1 shows the spectral indices obtained with and without the Hα free-free correction and it can be seen that the off-plane free-free contribution is within the spectral index uncertainties between 0.408 GHz and 4.76 GHz. The Hα-corrected indices are quoted without uncertainties as the uncertainties associated with the Hα free-free template are largely dependent on the fraction of dust along the line-of-sight. As the corrected spectral indices are simply shown to emphasise the insignificant contribution of the off-plane free-free emission at these frequencies, the Hα template uncertainties are not a major concern.

The insignificant contribution of the free-free emission at 0.408 GHz within $4^\circ < |b| < 10^\circ$ is illustrated by Figure 6.10 which compares the ratio between the Hα free-free map, scaled to 0.408 GHz using $\beta = -2.1$ and the Haslam et al. (1982) 0.408 GHz map. It can be seen that, at maximum, the free-free contribution is roughly 6 % of the total emission at 0.408 GHz map. The maximum contributions of ~ 6 % are seen within the Gum nebula and Barnard's Loop while the off-plane contributions are $<$ 1 %.

6.1.4 In-Plane Synchrotron emission

Within the Galactic plane, the contribution of free-free emission to the total emission between 0.408 GHz and 5 GHz emission is far from negligible. The region covered by the RRL free-free template, $-4^\circ < b < 4^\circ$, $20^\circ < l < 40^\circ$, is deep within what is referred to as the 'Zone of Avoidance' because of the high proportion of dust which can obscure galaxies at optical wavelengths (Lucas et al. 2008).

The success of the RRL free-free template is primarily dependent on the accuracy of the electron temperature used to convert from the RRL temperature integral to the free-free brightness temperature. The electron temperature dictates the magnitude of the free-free template produced and Alves et al. (2012) use a constant, average electron temperature of 6,000 K across their region after having identified 15 HII regions within $20^\circ < l < 44^\circ, |b| < 4^\circ$ which vary in electron temperature from 5,300 to 8,800 K. Figure 6.11 uses latitude cuts to explore the different magnitudes of the the various free-free templates across the full RRL longitude range and a smaller subset of that range. As the MCMC template is only available at $N_{side} = 64$, the data presented in Figure 6.11 must be downgraded to this N_{side}. The N_{side} dictates the latitude range over which to average the data, for $N_{side} = 64$ $0.^\circ8$ is the minimum latitude step for at least one pixel per longitude value. The data are also all smoothed to 1° resolution. The first cut averages over $21^\circ < l < 26^\circ$, the second over the full RRL longitude range $20^\circ < l < 40^\circ$ and both span the full RRL latitude range $-4^\circ < b < 4^\circ$. The 21° to 26° longitude range was selected to be a typical diffuse region as it contained the least bright, compact areas in the C-BASS map.

In addition to the MCMC, MEM and RRL free-free templates plotted in Figure 6.11, there is also the profile of the total C-BASS emission distribution as well as three 4.76 GHz free-free maps. These maps were created by subtracting a 4.76 GHz synchrotron model away from the C-BASS data. For this synchrotron model, the Haslam et al. (1982) 0.408 GHz data were cleaned of their small amount of free-free emission using a pixel-by-pixel subtraction of the RRL data, scaled to 0.408 GHz using a spectral index of −2.13. The 0.408 GHz synchrotron map produced could then be scaled to 4.76 GHz and subtracted from the C-BASS data to form a 4.76 GHz free-free map. This process is illustrated schematically in Figure 6.12. As the spectral index required to scale synchrotron emission from 0.408 GHz to 4.76 GHz within the Galactic plane is not known, three possible values within the expected range were tested: −2.6, −2.7 and −2.8. These spectral indices were chosen with the Bennett et al. (2003b) synchrotron spectral index of −2.7 between 0.408 – 22.5 GHz for the Galactic plane in mind. It is possible to subtract the 0.408 GHz synchrotron data from the C-BASS data within the Galactic plane despite the different survey zero-levels between C-BASS and Haslam et al. (1982) because the large signal within this region prevents the zero-level offsets from dominating the variation in signal between the two maps.

The data shown in Figure 6.11 are all scaled to 4.76 GHz. For the RRL template this involved a spectral index of −2.13 while the MEM and MCMC templates use a slightly steeper free-free spectral index of $\beta = -2.15$ appropriate for their higher 22.5 GHz original frequency. All the profiles have their baseline levels subtracted so that just the in-plane emissions could be compared. The baseline level was established using a cosecant fit to each of the curves out to $|b| < 10°$:

$$y = A + \frac{B}{\sin\left(|b| + C\right)}, \tag{6.11}$$

where A is the baseline level. Figure 6.11a) indicates that the MCMC templates overestimate the amount of free-free emission present within $21° < l < 26°$, as the MCMC free-free intensity at 4.76 GHz is larger than the total C-BASS intensity at $0\overset{\circ}{.}4$. For both latitude ranges shown in Figure 6.11 the RRL free-free template is the lowest in magnitude. Currently, the view is that an electron temperature of 7,000 K is a more accurate average value for this region of the Galactic plane (private communication with R. Davies) and so the Alves et al. (2012) electron temperature of 6,000 K would result in the RRLs being $\sim$ 10 % too low in temperature. The plots in Figure 6.11 would be consistent with either this statement or the the idea that a 6,000 K electron temperature is accurate but the synchrotron spectral index between 0.408 GHz and 4.76 GHz is in

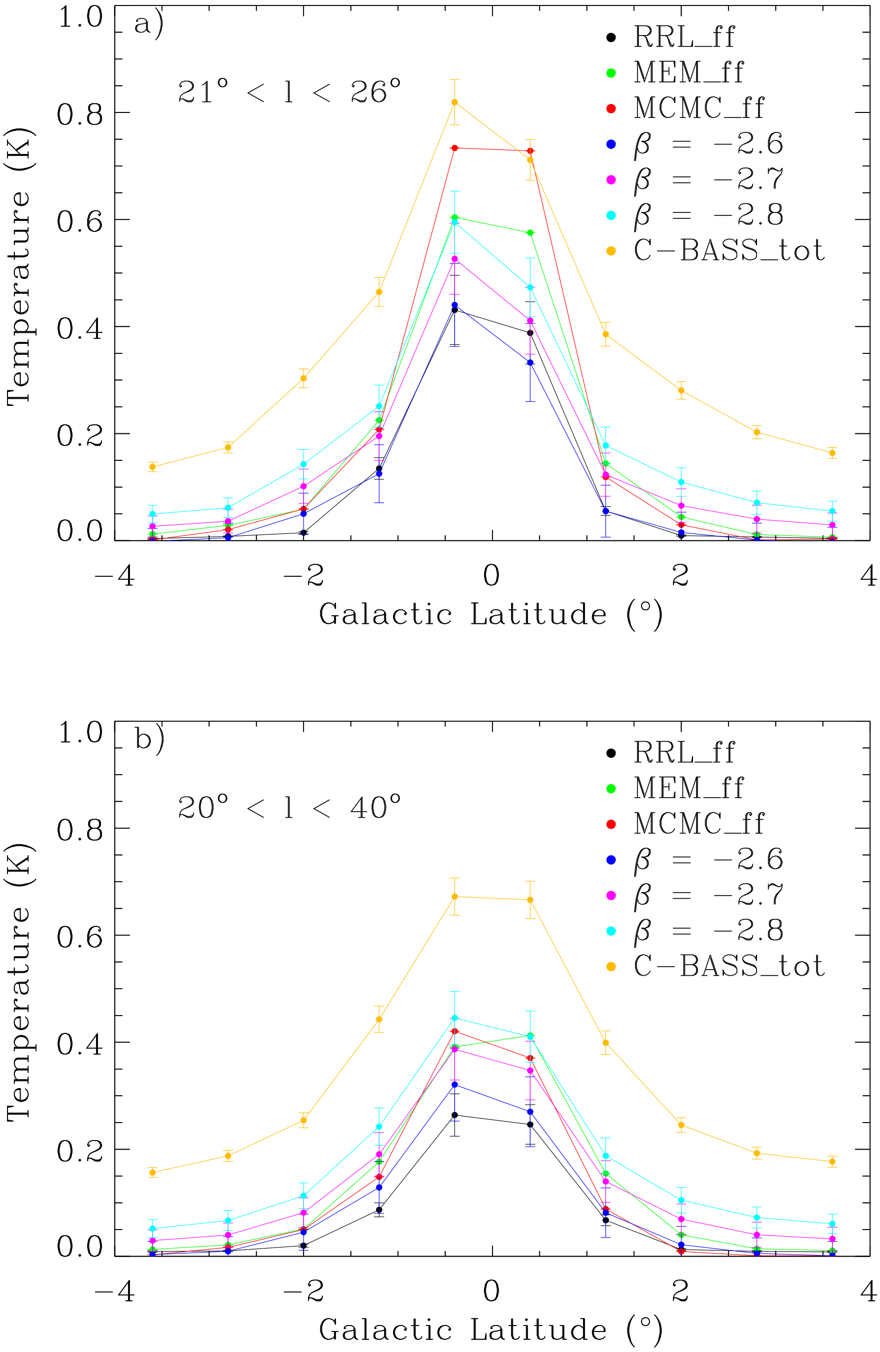

Figure 6.11: Free-free latitude distribution for $|b| < 4°$ using averaged longitude data from the RRL, MCMC, MEM free-free templates and the 4.76 GHz free-free maps all scaled to 4.76 GHz for the longitude range of **a)** 21° – 26° and **b)** 20° – 40°. The maps have been smoothed to 1° resolution and downgraded to HEALPix $N_{\rm side} = 64$.

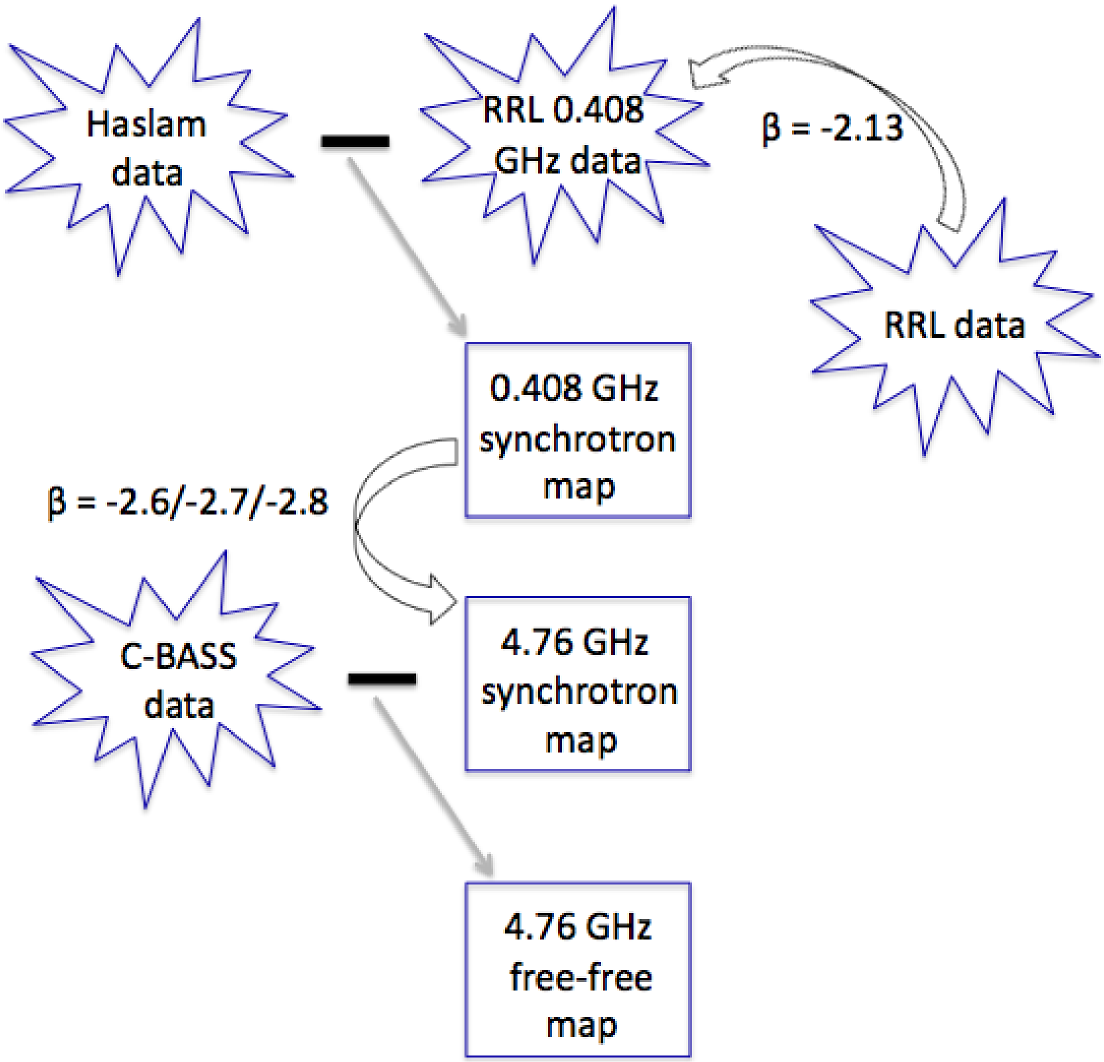

Figure 6.12: An illustration of the 4.76 GHz free-free map making process which uses the C-BASS, Haslam et al. (1982) and RRL free-free template data.

fact closer to -2.5 than -2.6.

The MEM free-free template is consistent with a 0.408/4.76 GHz synchrotron spectral index of -2.8 for both latitude ranges and with the MCMC free-free template for the full RRL latitude range. In their analysis, Alves et al. (2012) compare their free-free template with the MEM 7-year free-free template and find the MEM free-free template to ~ 30 % larger than theirs. Here the MEM 9-year free-free template is considered, which differs to the 7-year template as it takes the spinning dust contribution into account. Despite the difference between the 7- and 9-year versions, this analysis also sees a difference in the RRL and MEM templates of 30 – 40 %.

Synchrotron models at 0.408 GHz, 1.42 GHz and 4.76 GHz were made using the RRL template and the Haslam et al. (1982), Reich & Reich (1986) and C-BASS data. Figure 6.13 shows synchrotron, $N_{side} = 256$, resolution 1° maps in the form of latitude cuts over the same regions shown in Figure 6.11. Both plots display the broad peaks typically associated with synchrotron emission. A free-free spectral index of −2.13 was used to scale the RRL free-free template to the different frequencies required. The spectral indices required to scale the 0.408/1.42 GHz to 4.76 GHz ($\beta_{0.408/1.420-4.76}$) were calculated as:

$$\beta_{0.408/1.420-4.76} = \frac{\ln \overline{S}}{\ln\left(\frac{4.76}{0.408/1.420}\right)}, \tag{6.12}$$

where $\overline{S}$ is the mean of the ratio between the 4.76 GHz and the 0.408/1.42 GHz synchrotron curve values which lie $|b| < 2°$. Only the peak values were used, instead of the whole curves because of the asymmetry between the the negative and positive $|b| > 3°$ latitude points. The reason for this asymmetry is most likely to be an increase in synchrotron signal resulting from the increased supernova activity within the Gould Belt. If this were the case, one would expect to see a large asymmetry in the 0.408 GHz curve, the curve most dominated by synchrotron emission before subtracting the RRL template and this is what is seen.

The uncertainties associated with the spectral indices were calculated as:

$$\sigma_\beta = \left(\frac{1}{\ln\left(\frac{5}{\nu}\right)}\right) \sigma_c \left(\frac{S_\nu}{S_5}\right), \tag{6.13}$$

where

$$\sigma_c = \sqrt{\left(\frac{\sigma\left(\frac{S_5}{S_\nu}\right)}{\sqrt{N}}\right)^2 + \sigma_d^2}, \tag{6.14}$$

where

$$\sigma_d = \sqrt{\left(\frac{S_{5Err}}{S_5}\right)^2 + \left(\frac{S_{\nu Err}}{S_\nu}\right)^2} \times \overline{S} \tag{6.15}$$

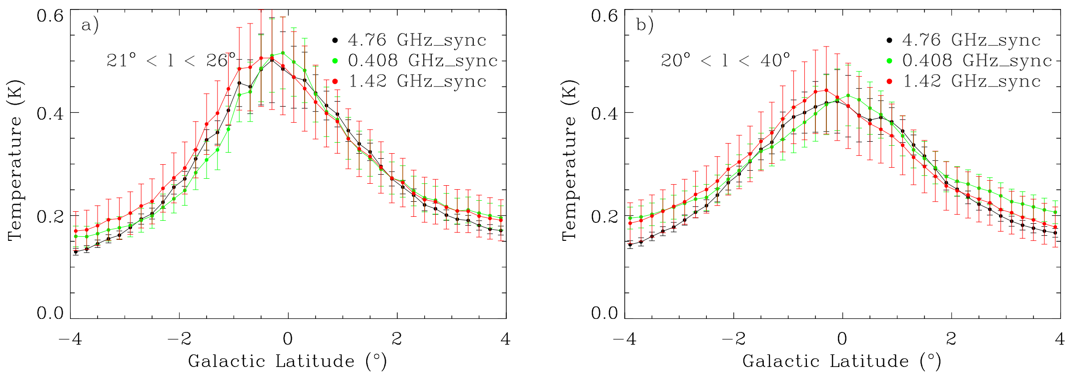

Figure 6.13: Synchrotron latitude distribution for $|b| < 4°$ using averaged longitude data from the RRL free-free subtracted Haslam et al. (1982), Reich & Reich (1986) and C-BASS data all scaled to 4.76 GHz for the longitude range of **a)** 21° – 26° and **b)** 20° – 40°. The maps have been downgraded to HEALPix $N_{\rm side} = 256$ and are smoothed to 1° resolution.

Template	**Long.** (°)	ν **range**	$\beta_{\rm sync}$
RRL	21 – 26	0.408 – 4.76	-2.65 ± 0.08
RRL	21 – 26	1.420 – 4.76	-2.73 ± 0.14
RRL	20 – 40	0.408 – 4.76	-2.63 ± 0.07
RRL	20 – 40	1.420 – 4.76	-2.71 ± 0.14

Table 6.2: The Galactic plane synchrotron spectral indices as determined using synchrotron maps formed from the C-BASS data and the RRL free-free templates.

and ν is 0.408 or 1.42 GHz and N is the number of data points. The β uncertainties are taken into account alongside the data calibration uncertainty errors in Figure 6.13, which is why the 0.408 GHz and 1.42 GHz synchrotron curves have larger error bars than the 4.76 GHz curve.

Table 6.2 shows the synchrotron spectral indices calculated using Equation 6.12 between 0.408/1.420 GHz and 4.76 GHz within $-4° < b < 4°$ and the two latitude ranges of $21° < l < 26°$ and $20° < l < 40°$. The spectral indices of -2.63 ± 0.07 and -2.71 ± 0.14 between 0.408/1.420 GHz and 4.76 GHz for $20° < l < 40°$ may suggest

Template	Long. (°)	Synchrotron / total emission (%)
RRL	21 – 26	42 ± 11
RRL	20 – 40	53 ± 8

Table 6.3: The percentage of total emission at 4.76 GHz made up by synchrotron emission as calculated using the RRL free-free template.

a slight steepening in the synchrotron spectral index between 0.408 and 1.420 GHz, however the effect is within the measurement uncertainties. Using the full C-BASS survey in this analysis will reduce the uncertainties and help to determine whether or not this slight steepening is a real effect.

Ratio of in-plane free-free and synchrotron emission

At 1.5 GHz, diffuse Galactic emission is roughly 30 % free-free and 70 % synchrotron emission (Platania et al. 1998). The ratio between free-free and synchrotron emission at 4.76 GHz can be investigated using the latitude curves of the 4.76 GHz pure synchrotron map that was created. Figure 6.14 shows latitude cuts across $-4° < b < 4°$ for the total 4.76 GHz emission as measured by C-BASS, 4.76 GHz pure synchrotron map and the RRL free-free templates scaled to 4.76 GHz using a spectral index of $\beta = -2.13$. The sum of the free-free and synchrotron contributions are plotted as a visual aid. The uncertainties on the curves shown in Figure 6.14 include the map calibration errors and it can be seen that the total emission curves are consistent with their free-free + synchrotron contributions.

The ratio between free-free and synchrotron emission at 4.76 GHz was found to be 47± 8 %: 53± 8 % in the Galactic plane ($20° < l < 40°, -4° < b < 4°$). This result is consistent with the Platania et al. (1998) result of 30 %:70 % at 1.5 GHz as a synchrotron contribution of 70 % at 1.5 GHz scales down to 54 % at 4.76 GHz, assuming a synchrotron spectral index of $\beta = -2.7$.

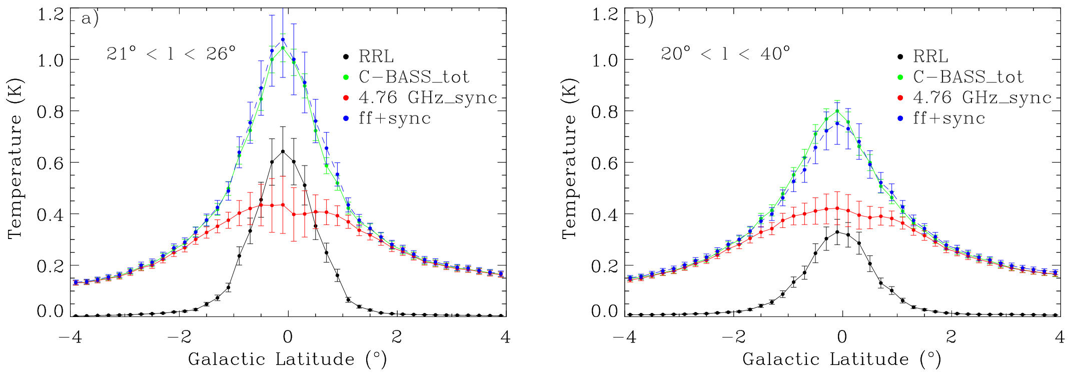

Figure 6.14: Total emission latitude distribution for $|b| < 4°$ using RRL and C-BASS data all at 4.76 GHz with the longitude data averaged between **a)** 21° and 26° and **b)** 20° and 40°. The maps have been downgraded to HEALPix $N_{\rm side} = 256$ and are smoothed to 1° resolution. The sum of the free-free and synchrotron components is also shown to aid the comparison.

6.2 Anomalous microwave emission between 5 GHz and 60 GHz

Although it is unlikely that C-BASS will be able to detect AME directly for most of the sky (see Section 1.7.3 for a discussion of the ρ Ophiuchi West molecular cloud), the 4.76 GHz data can be used alongside higher frequency data to constrain the AME spectral form. The Galactic plane within $-5° < b < 5°$ and $20° < l < 30°$ has been noted to contain AME which could make up anything between 30 % and 60 % of the total 30 GHz emission depending on the region (Planck Collaboration et al. 2011a). This result was achieved though a method known as 'Galactic Inversion' which involves modelling the total emission in any map at frequency ν by fitting to the sum of the spatially varying ISM in its various phases:

$$\begin{aligned} I_\nu(x,y) &= \sum_{i=1}^{n}\left(\epsilon^i_{\rm H_I}(\nu)\, N^i_{\rm H_I}(x,y) + \epsilon^i_{\rm H_2}(\nu)\, N^i_{\rm H_2}(x,y)\right) \\ &+ \epsilon_{\rm H_{II}}(\nu)\, N_{\rm H_{II}}(x,y) + \epsilon_{\rm s}(\nu)\, N_{\rm s}(x,y) + \epsilon_{\rm d}(\nu)\, N_{\rm d}(x,y) + C_\nu, \end{aligned} \tag{6.16}$$

where the sum is over n Galactocentric rings. N and ϵ are the column densities and emissivities for the different ISM phases considered. The phases that have been considered are: atomic (HI), molecular (H_2), ionised (HII), synchrotron emission (s) and dark gas emission (d) which is the emission that cannot be traced using CO and HI (Planck Collaboration et al. 2011b). In principle, the ionised, synchrotron and dark gas contributions should also be summed over their different ring contributions however, the information required to do this is unknown. The frequency dependent constant C_ν sets the background level of the map.

For this analysis areas within the $20^\circ < l < 40^\circ$ longitude range that showed the largest percentage (up to 60 %) of AME at 30 GHz (Planck Collaboration et al. 2011d) were chosen. These areas were $30^\circ < l < 33^\circ$, $33^\circ < l < 36^\circ$ and $36^\circ < l < 40^\circ$, all within $-0.^\circ75 < b < 0.^\circ75$. T-T plots of these regions between 4.76 GHz and 22.5 GHz will reveal whether or not diffuse AME is present.

Given that the chosen strip is deep within a star forming region, synchrotron emission should only not dominate the total Galactic emission at 4.76 GHz. At 22.5 GHz the synchrotron contribution is essentially negligible. This is shown in Figure 6.15 which presents the ratio between the 0.408 GHz map, scaled to 22.5 GHz using a spectral index of −3.1, and the 22.5 GHz K-band *WMAP* map. From Figure 6.15 it can be seen that the average synchrotron contribution to the total emission at 22.5 GHz within $|b| < 0.^\circ75$ is ≈ 3 %, assuming a synchrotron spectral index of $\beta = -3.1$ between 0.408 and 22.5 GHz. This average synchrotron contribution only increases to ≈ 11 % when a synchrotron spectral index of $\beta = -2.7$ is used.

Figure 6.16 shows the 4.76 – 22.5 GHz T-T plots within this $1.^\circ5$. Spectral indices of -1.80 ± 0.03, -2.05 ± -0.03 and -1.81 ± 0.03 can be seen within $30^\circ < l < 33^\circ$, $33^\circ < l < 36^\circ$ and $36^\circ < l < 40^\circ$. These indices are flatter than the expected free-free index of −2.1. Assuming a negligible synchrotron emission contribution and a free-free spectral index of −2.13, the percentage of the measured spectral indices that can

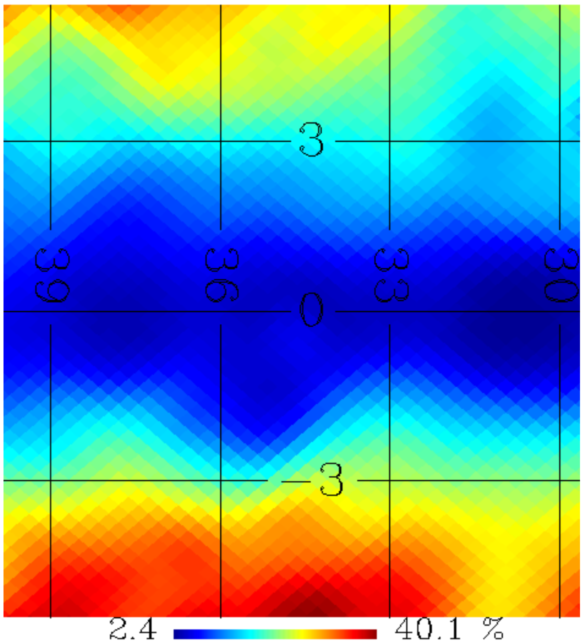

Figure 6.15: The synchrotron to total emission ratio at 22.5 GHz within the Galactic plane. The 0.408 GHz signal, scaled to 22.5 GHz using $\beta = -3.1$ was used as the synchrotron signal and the *WMAP* K-band map provided the 22.5 GHz total emission data. The maps have both been smoothed to 1° resolution and downgraded to HEALPix $\mathrm{N_{side}} = 256$.

be explained by AME emission can be calculated as follows:

$$\frac{\mathrm{AME}}{\mathrm{Total}} = \frac{\mathrm{Total} - \mathrm{FreeFree}}{\mathrm{Total}} = 1 - \frac{(22.5/4.76)^{-2.13}}{(22.5/4.76)^{\beta_{tot}}}, \tag{6.17}$$

where β_{tot} is the total emission spectral index between 4.76 GHz and 22.5 GHz. For the regions shown in Figures 6.16a) to c) the percentage of the total emission which can be explained as AME is calculated to be 40 ± 3 %, 12 ± 5 % and 39 ± 4 %, respectively. This calculation provides a 13σ, 2σ and 9 σ detection of AME within the three $-0.^\circ75 < b < 0.^\circ75$ and $30^\circ < l < 40^\circ$ subregions. These results are summarised in Table 6.4.

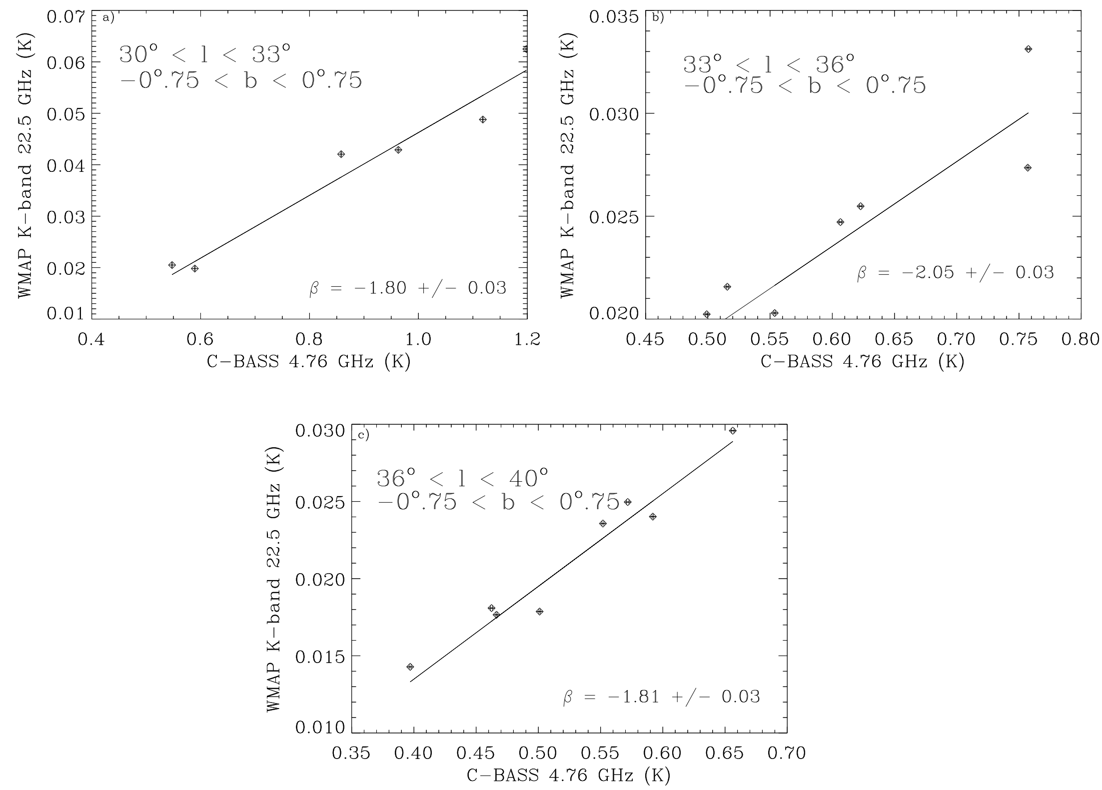

Figure 6.16: T-T plot between 4.76 and 22.5 GHz for $-0.75^\circ < b < 0.75^\circ$ and **a)** $30^\circ < l < 33^\circ$, **b)** $33^\circ < l < 36^\circ$ and **c)** $36^\circ < l < 40^\circ$. All maps have been downgraded to N_{side} 64 and smoothed to 1° resolution.

Long. (°)	β_{tot}	**AME/total emission (%)**
30 – 33	−1.80 ± 0.03	40 ± 3
33 – 36	−2.05 ± 0.03	12 ± 5
36 – 40	−1.81 ± 0.03	39 ± 4

Table 6.4: The total emission spectral indices and AME to total emission ratios between 4.76 and 22.5 GHz for $-0^\circ\!.75 < b < 0^\circ\!.75$.

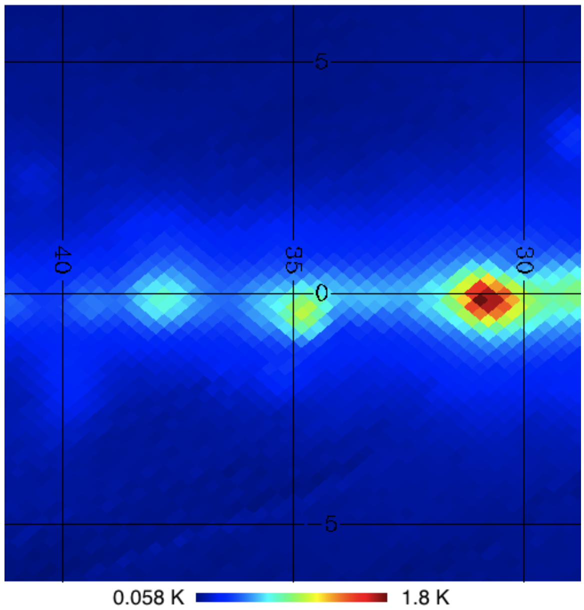

Figure 6.17: The C-BASS 4.76 GHz map within $30^\circ < l < 40^\circ$, $-5^\circ < b < 5^\circ$. The three brightest compact regions seen are, from left to right, W47, W44 and W43.

6.2.1 SEDs of compact regions

Figure 6.17 shows the region under investigation in Figure 6.16 as seen at 4.76 GHz using C-BASS. Three bright extended regions at (l, b) = ($30^\circ\!.8$,-$0^\circ\!.3$), ($34^\circ\!.8$,-$0^\circ\!.5$), ($37^\circ\!.8$,-$0^\circ\!.2$) can be seen. These are W43 (a complex HII region), W44 (a SNR dominated region) and W47 (a complex HII region), respectively.

Both W43 and W47 are discussed in the context of AME within Planck Collaboration et al. (2013a). For their analysis, Planck Collaboration et al. (2013a) use aperture photometry to determine the flux densities of 98 compact (< 1° FWHM) sources within the Galactic plane using survey data between 0.408 and 25,000 GHz. Aperture photometry involves forming an inner aperture centred on the source centre and an outer annulus to represent the source background. With the flux densities acquired through aperture photometry Planck Collaboration et al. (2013a) formed spectral energy distributions (SEDs), plots of flux density against frequency, for their 98 sources and noted that over half of their sources showed excess emission between 20 and 60 GHz. W43 and W47 were highlighted in their analysis as two potential AME candidate regions with AME detections of 8.6σ and 2.9σ.

Similar SEDs for W43, W44 and W47 can be formed by including the C-BASS data to see if the diffuse AME detections noted in Table 6.4 can be associated with more compact regions. The flux densities were also measured using aperture photometry because within the Galactic plane the complex morphology of the source background results in inaccurate Gaussian fits between the source's peak and its baseline.

The inner aperture size for this analysis was chosen to be 60′ in radius with the outer annulus spanning from 80′ to 100′ to match the radii used by Planck Collaboration et al. (2013a) as their analysis included determining the optimum aperture photometry radii using Monte Carlo simulations of injected sources. The ancillary data used alongside the C-BASS data to make the SEDs are summarised in Table 6.5. All the maps were smoothed to 1° resolution and downgraded to HEALPix $\mathrm{N_{side}} = 256$.

For the aperture photometry the maps were converted into units of Jy per pixel:

$$\frac{\mathrm{Map}}{\mathrm{Jy/pixel}} = \left(\frac{\mathrm{Map}}{\mathrm{K_{RJ}}}\right)\left(\frac{2\ k_B\ 10^{26} c^{-2}}{\mathrm{Kg\ K^{-1}}}\right)\left(\frac{\nu}{\mathrm{Hz}}\right)^2 \Omega_{\mathrm{pix}} \tag{6.18}$$

or

$$\frac{\mathrm{Map}}{\mathrm{Jy/pixel}} = \left(\frac{\mathrm{Map}}{\mathrm{MJy/Str}}\right)\left(\frac{4\ \pi}{\mathrm{N_{pix}}}\right) 10^6, \tag{6.19}$$

where Ω_{pix} is the pixel solid angle and ν is the survey frequency. The flux densities determined through aperture photometry for W43, W44 and W47 are listed in Table 6.6. The uncertainties on the flux density values were determined using the formalism laid out by Laher et al. (2012) which assume that the noise is white, uncorrelated noise:

$$\sigma_{\mathrm{apPhot}} = \sqrt{\left(n_{\mathrm{in}} + \left(\frac{\pi}{2}\right)\left(\frac{n_{\mathrm{in}}^2}{n_{\mathrm{out}}}\right)\right) \times \sigma_{\mathrm{out}}^2}, \tag{6.20}$$

where $n_{\mathrm{in/out}}$ is the number of pixels within the inner/outer aperture/annulus and σ_{out} is the standard deviation of the pixels within the outer aperture. As the outer annuli for W43, W44 and W47 overlap with other compact regions, the robust sigma routine from the IDL astronomy library was used. This routine uses the median absolute deviation

Survey	ν **(GHz)**	**Res. (′)**	$\mathbf{N_{side}}$	**Calibration (%)**	σ_t
Haslam	0.408	51	512	10	700
Reich	1.420	35	512	10	140
Jonas	2.3	20.0	256	5	30
C-BASS	4.76	45	256	5	21
WMAP	22.5	49	512	2	0.04
WMAP	33	40	512	2	0.04
WMAP	41	31	512	2	0.04
WMAP	61	21	512	2	0.04
WMAP	94	13	512	2	0.03
Planck LFI	28.4	32.65	1024	2	0.15*
Planck	44.1	27.92	1024	2	0.16*
Planck	70.3	13.01	1024	2	0.13*
Planck HFI	143	7.04	2048	2	0.01*
Planck	353	4.43	2048	2	0.005*
Planck	545	3.80	2048	10	0.003*
Planck	857	3.67	2048	10	0.001*
COBE-DIRBE	1249	37.1	1024	13.5	0.5**
COBE-DIRBE	2141	38.0	1024	10.6	32.8**
COBE-DIRBE	2997	38.6	1024	11.6	10.7**

Table 6.5: The data used in the SEDs alongside their frequency, resolution, HEALPix N_{side}, calibration uncertainty, average thermal noise (in mK, $mK_{RJ}s^{1/2}$ (*) and in MJy/sr (**)).

from the standard mean (MAD) and Tukey's biweight to exclude outlier values from the standard deviation calculation.

SEDs of W43, W44 and W47 are shown in Figure 6.18. Magnified plots of the AME bump are included within each SED to highlight the region of interest. The flux density values were fit to the following total emission model:

$$S = S_{\rm ff} + S_{\rm sync} + S_{\rm td} + S_{\rm AME}, \tag{6.21}$$

where the subscript ff denotes the free-free contribution, sync the synchrotron contribution, td the thermal dust contributions and AME the AME contributions. The small CMB contribution was considered to be negligible. The synchrotron spectral index

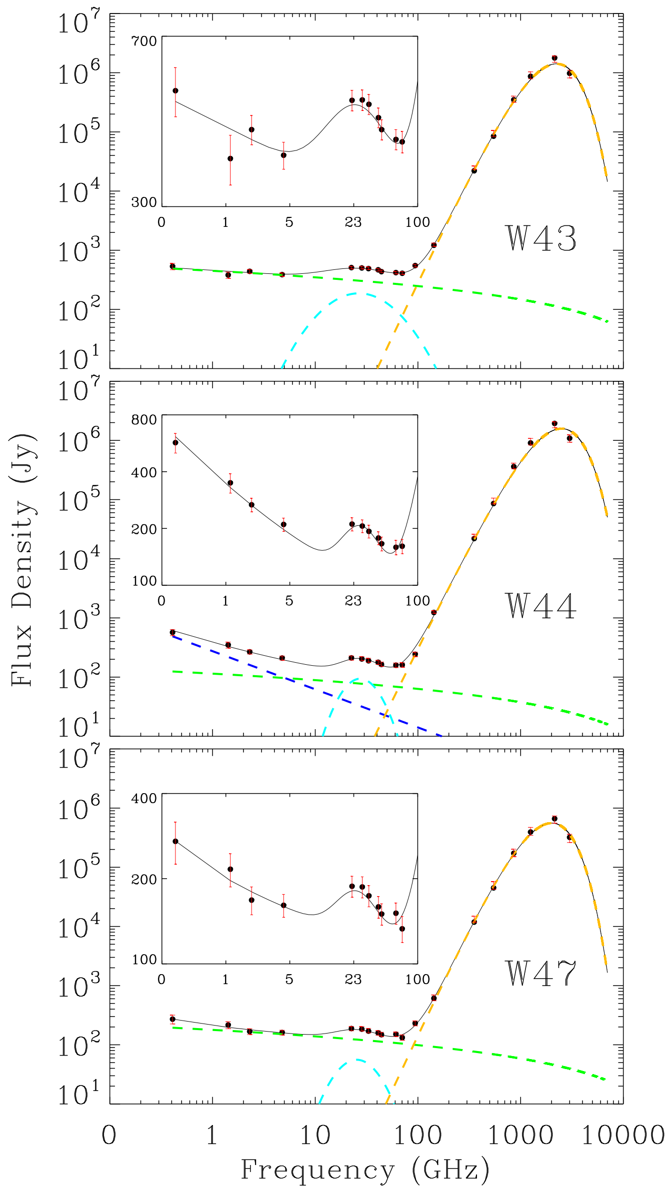

Figure 6.18: SEDs for W43, W44 and W47. Flux densities were determined via aperture photometry using the Haslam et al. (1982), Reich & Reich (1986), Jonas, Baart & Nicolson (1998), C-BASS, *WMAP*, *Planck* and *COBE*-DIRBE data. All the maps were smoothed to 1° resolution and downgraded to HEALPix N_{side} = 256. The solid black line represents the total emission model while the yellow dashed line represents the thermal dust emission model, the light blue dashed line represents AME, the dark blue dashed line represent synchrotron and the dashed green line represents free-free emission. The AME region of interest is shown as a zoomed in plot within each SED.

Frequency (GHz)	**Flux Density (Jy)**		
	W43	**W44**	**W47**
0.408	534 ± 65	570 ± 68	271 ± 46
1.420	381 ± 33	349 ± 27	216 ± 22
2.3	440 ± 32	267 ± 22	168 ± 19
4.76	387 ± 26	210 ± 17	161 ± 15
22.5	509 ± 26	211 ± 17	188 ± 16
28.4	555 ± 29	223 ± 18	199 ± 17
33	490 ± 25	189 ± 15	170 ± 15
41	467 ± 23	178 ± 14	159 ± 14
44.1	435 ± 22	164 ± 14	147 ± 13
61	419 ± 21	159 ± 14	151 ± 13
70.3	407 ± 22	160 ± 14	131 ± 14
94	551 ± 30	234 ± 21	231 ± 22
143	1210 ± 80	1233 ± 61	608 ± 71
353	22000 ± 1700	21900 ± 1300	11800 ± 1500
545	84500 ± 11000	85600 ± 11000	44700 ± 7400
857	349000 ± 43000	361000 ± 41000	172000 ± 26000
1249	867000 ± 120000	907000 ± 120000	394000 ± 63000
2141	1770000 ± 210000	1930000 ± 210000	656000 ± 91000
2997	978000 ± 140000	1090000 ± 150000	320000 ± 50000

Table 6.6: The flux densities for the W43, W44 and W37.

was allowed to vary between −2.6 and −3.1, while the thermal dust spectral index was allowed to vary between 1.1 and 2.3. The synchrotron spectral behaviour was modelled as a power-law:

$$S_{\rm sync} \propto \nu^{\beta_{\rm sync}+2}. \tag{6.22}$$

The free-free emission was modelled from the brightness temperature ($T_{\rm ff}$):

$$S_{\rm ff} = \frac{2\, k_B\, T_{\rm ff}\, \Omega \nu^2}{c^2}, \tag{6.23}$$

where c is the speed of light, k_B is the Boltzmann constant, Ω is the solid angle, ν is the frequency and the calculation for $T_{\rm ff}$ is detailed in Section 1.7.2 . An electron temperature of 7,000 K was used.

The thermal dust was assumed to behave as a grey body and normalised using the

250 μm optical depth (τ_{250}):

$$S_{\rm td} = 2\,\frac{h\,\nu^3}{c^2}\frac{1}{e^x - 1}\,\tau_{250}\,(\nu/1.2\ \mathrm{THz})^{\beta}\,\Omega, \tag{6.24}$$

where

$$x = \frac{h\,\nu}{k_B\,T_{\rm d}}, \tag{6.25}$$

where $T_{\rm d}$ is the thermal dust temperature and Ω is the solid angle of the inner aperture.

The AME component was fit as a parabola in $\log S - \log \nu$ (Bonaldi et al. 2007):

$$S_{\rm AME} \propto 10^{A\ \log_{10}\nu + B} \times \nu^2, \tag{6.26}$$

where

$$A = -\left(\frac{m_{60}\log_{10}\nu_{max}}{\log\frac{\nu_{max}}{60}} + 2\right), \tag{6.27}$$

and

$$B = \left(\frac{m_{60}}{2\ \log_{10}\frac{\nu_{max}}{60}}\right)\ \log_{10}\nu^2, \tag{6.28}$$

where m_{60} is a free parameter which represents the slope of the parabola at 60 GHz and ν_{max} is the AME peak frequency. This method of AME fitting was chosen as it requires no prior information on the physical properties of dust grains responsible for the emission. The `SpDust` code (Ali-Haïmoud, Hirata & Dickinson 2009; Silsbee, Ali-Haïmoud & Hirata 2011) is also available for the modelling of spinning dust emission but it requires many input parameters, such as the hydrogen number density, the gas temperature, the intensity of the radiation field responsible for the spinning, the fraction of ionised hydrogen and carbon, the Helium formation efficiency, the r.m.s. dust dipole moment and the grain size distribution. Therefore, the simpler, parabola model for AME was chosen for use in this analysis.

Colour corrections (see Section 4.6.2) are applied to the *WMAP*, *Planck* and *COBE*-DIRBE data within the least squares fitting routine so that the model fitted spectrum can be used as the source spectrum, which is required for colour correction. The *WMAP* colour corrections are calculated by weighting the bandpass at a lower, central and upper limit, these limits and their weights are given in Bennett et al. (2013). The IDL code used to compute the *Planck* LFI and HFI colour corrections is readily available[3]. The *COBE* colour corrections values are given by a quadratic fit to the colour correction coefficients provided on the LAMBDA website. The colour correction code used in this work was not written by this author but by Dr. Mike Peel and Dr. Clive Dickinson. The model is fitted to the data which have not been colour corrected and so the model needs to be subjected to the inverse colour corrections first, then the data are colour corrected so that the data points plotted represent the true source flux densities at the desired frequencies.

Table 6.7 shows the difference between the flux densities measured for W43, W44 and W47 and those predicted by the combined free-free, synchrotron and thermal dust emission models. The significance levels of these deviations are also listed within the table and the maximum deviation between 20 GHz and 60 GHz is taken as the significance of the AME detection.

The W43 data are fairly well fitted by the total emission model with a reduced χ^2 of 1.89. The fitted parameter values are 26.3± 0.3 K for the thermal dust temperature, 1.57 ± 0.04 for the thermal dust spectral index, 4 ± 2 for the m_{60} parameter, 27± 3 GHz for the spinning dust peak frequency, 25 ± 5 cm^{-6} pc for the EM and 0.009 ± 0.0009 for τ_{250}. The AME peak is identified at the 4.9σ level and the large uncertainty on the m_{60} parameter comes from the fact that this parameter is characterised by very few data points.

The W44 data are the least well fit by the total emission model with a reduced χ^2 of 2.49. This is due to a slightly poorer fit to the grey body model of thermal dust. The fitted parameter values are -2.57 ± 0.08 for the synchrotron spectral index, 24.8± 0.4 K for the thermal dust temperature, 1.72 ± 0.05 for the thermal dust spectral index, 5 ± 2 for the m_{60} parameter, 27± 3 GHz for the spinning dust peak frequency, 25 ± 5 cm^{-6} pc for the EM and 0.009 ± 0.0009 for τ_{250}. The AME peak is identified at the 6.0σ level.

The W47 data are well fitted by the total emission model with a reduced χ^2 of 0.80. The fitted parameter values are 20± 1 K for the thermal dust temperature, 1.89 ± 0.10

[3]http://externaltools.planck.fr/

ν	**W43 excess (Jy)**	**W44 excess (Jy)**	**W47 excess (Jy)**
0.408	19 ± 88 (0.22)	−81 ± 83 (−0.98)	81± 53 (1.52)
1.420	−76 ± 63 (−1.21)	17 ± 36 (0.47)	47 ± 33 (1.45)
2.3	5 ± 60 (0.08)	3 ± 29 (0.11)	7 ± 30 (0.25)
4.76	−14 ± 54 (−0.26)	17 ± 21 (0.78)	13 ± 26 (0.49)
22.5	178 ± 47 (3.82)	96 ± 18 (5.21)	66 ± 24 (2.79)
28.4	**233 ± 47 (4.93)**	**114 ± 19 (5.95)**	**81 ± 24 (3.39)**
33	173 ± 44 (3.90)	82 ± 16 (5.01)	53 ± 22 (2.38)
41	155 ± 43 (3.63)	70 ± 15 (4.61)	43 ± 21 (2.03)
44.1	123 ± 42 (2.93)	54 ± 15 (3.56)	32 ± 20 (1.55)
61	92 ± 43 (2.17)	24 ± 16 (1.52)	26 ± 20 (1.28)
70.3	58 ± 45 (1.27)	−5 ± 16 (−0.29)	−5 ± 22 (−0.24)
94	75 ± 65 (1.15)	−65 ± 26 (−2.51)	31 ± 32 (0.96)
143	−9 ± 212 (−0.04)	149 ± 93 (1.60)	26 ± 112 (0.23)
353	−1332 ± 6798 (−0.20)	−194 ± 2770 (−0.07)	−574 ± 3992 (−0.14)
545	−9467 ± 34969 (−0.27)	−1539 ± 16036 (−0.10)	−5414 ± 20985 (−0.26)
857	7972 ± 158308 (0.05)	44988 ± 67949 (0.66)	−4158 ± 95497 (−0.04)
1249	66552 ± 462503 (0.14)	144002 ± 201264 (0.72)	9661 ± 267512 (0.04)
2141	322810 ± 1198425 (0.27)	360653 ± 506685 (0.71)	103997 ± 582581 (0.18)
2997	−155123 ± 1238395 (−0.13)	−350196 ± 559867 (−0.63)	−14133 ± 482465 (−0.03)

Table 6.7: The W43, W44 and W47 flux density deviations from the combined free-free, synchrotron and thermal dust emission model expressed in terms of Jy. The significance levels of the excesses are shown in parentheses and the peak excess values or each source, due to AME emission, are in bold.

for the thermal dust spectral index, 5 ± 4 for the m_{60} parameter, 25 ± 5 GHz for the spinning dust peak frequency, 49 ± 4 cm^{-6} pc for the EM and 0.008 ± 0.003 for τ_{250}. The AME peak is identified at the 3.4σ level. It should be noted that the EM fitted values are lower than the literature values of ≈ 140 cm^{-6} pc but this is to be expected as the fitted EM values are only an effective EM for the 1° inner aperture.

The analysis was repeated with the 4.76 GHz C-BASS point excluded from the fits to quantify the value of this additional data point. Table 6.8 shows the fitted parameters for W43, W44 and W47 with and and without the C-BASS data point included in the fit. It can be seen that the lack of 4.76 GHz data increases the reduced χ^2 values for W44 and W47, significantly increases the uncertainty on the synchrotron spectral index for W44 and the uncertainty associated with the free-free EM of W43. The AME peak frequency for W43 and W44 are seemingly unaffected by the C-BASS data point but for W47 the uncertainty doubles. Although the W43 AME peak frequency is not affected by the 4.76 GHz data point, from Figure 6.18 it can be seen that the W43 AME model parabola is much wider than the W44 or W47 parabola. This suggests the W43 data are still not well enough constrained and that data between 4.76 and 22.5 GHz would be of great use for this spectral fit.

As mentioned, the Planck Collaboration et al. (2013a) analysis highlighted W43 and W47 as two potential AME candidate regions. However a 0.36 and 0.37 portion of the excess emission seen for W43 and W47 respectively was attributed to emission from ultra compact H_{II} regions. Ultra compact H_{II} (UCHII) regions are densely packed areas of ionised hydrogen, within which massive star formation occurs. They are defined as possessing an $EM > 10^6$ cm^{-6} pc and an electron temperature (T_b) of $\sim 10^4$ K (Draine 2011). At low frequencies, typically under 15 GHz (Hoare et al. 2007), some UCHII regions may be optically thick, moving into the optically thin regime at frequencies higher than 15 GHz:

$$T_b = T_e\,(1 - \exp^{-\tau})\,, \tag{6.29}$$

where τ (the optical depth) $\ll 1$ indicates the optically thin regime and $\tau \gg 1$ indicates

Parameter	W43 With	W43 Without	W44 With	W44 Without	W47 With	W47 Without
Reduced χ^2	1.89	1.83	2.49	4.09	0.80	1.10
β_{sync}	–	–	-2.57 ± 0.08	-2.71 ± 0.15	–	–
T_{D}	26.3 ± 0.3	24.5 ± 0.6	24.8 ± 0.4	26.6 ± 0.9	20 ± 1	21 ± 2
β_{thermal}	1.57 ± 0.04	1.67 ± 0.04	1.72 ± 0.05	1.64 ± 0.04	1.89 ± 0.10	1.81 ± 0.12
m_{60}	2 ± 1	2 ± 1	4 ± 2	7 ± 4	5 ± 4	2 ± 1
ν_{peak}	27 ± 4	26 ± 4	27 ± 3	28 ± 2	25 ± 5	21 ± 10
EM	109 ± 9	117 ± 15	25 ± 5	38 ± 6	49 ± 4	30 ± 4
τ_{250}	0.007 ± 0.0004	0.008 ± 0.0009	0.009 ± 0.0009	0.007 ± 0.0009	0.008 ± 0.003	0.008 ± 0.003

Table 6.8: The W43, W44 and W47 fitted total emission parameters with and without the C-BASS data point.

the optically thick regime. If a source were to be positioned within a region containing an optically thick UCHII source at low frequencies this would result in what would appear to be excess emission at higher frequencies where the UCHII region becomes optically thin. In the light of the Planck Collaboration et al. (2013a) analysis, the contribution from UCHII regions must now be considered to help determine whether or not the excess emission is entirely due to AME.

6.2.2 Contribution to excess emission from UCHII regions

In Planck Collaboration et al. (2013a), the method of Dickinson (2013) and Wood & Churchwell (1989) was employed to identify possible UCHII regions. This method uses the fact that UCHII regions generally possess IRAS colours (brightness ratios) of $\log_{10}\left(\frac{S_{60}}{S_{12}}\right) \geq 1.30$ and $\log_{10}\left(\frac{S_{25}}{S_{12}}\right) \geq 0.57$. Since then, however, a new catalogue of UCHII regions at 5 GHz has become available via the CORNISH VLA survey.

The Co-Ordinated Radio 'N' Infrared Survey for High mass star formation (CORNISH) survey covers the $10° > l < 65°, |b| < 1°$ region of the Galactic plane at a resolution of 1.5 arcsec and r.m.s noise of 0.4 mJy per beam (Purcell et al. 2013). Using the online catalogue 30, 20 and 16 possible UCHII regions were found within a 2° radius of W43, W44 and W47, respectively. Their flux densities, FWHM values, brightness temperatures and optical depth values calculated using Equation 6.29 and an assumed electron temperature of 10,000 K are shown in Table 6.9. None of the 66 UCHII regions found are optically thick at 5 GHz

Source	S **(mJy)**	**FWHM (″)**	T_b **(K)**	τ
W43	969.33	4.59	2250.12	0.25
	301.66	3.29	1362.97	0.15
	466.99	10.81	195.44	0.02
	87.53	3.26	402.79	0.04
	92.37	1.79	1409.89	0.15
	710.36	6.30	875.30	0.09
	85.45	5.54	136.16	0.01
	25.79	3.20	123.17	0.01
	325.47	3.09	1667.07	0.20
	11.70	2.01	141.63	0.01

Continued on next page

Table 6.9 – continued from previous page

Source	S (mJy)	FWHM (″)	T_b (K)	τ
	296.24	7.81	237.33	0.02
	37.39	3.14	183.53	0.02
	353.06	2.69	2385.77	0.27
	23.83	1.69	407.53	0.04
	7.04	2.02	84.38	0.01
	26.23	4.15	74.48	0.01
	80.96	10.03	39.36	0.01
	268.86	9.33	151.05	0.02
	96.79	5.81	140.23	0.01
	4.54	1.62	84.60	0.01
	13.64	1.79	208.19	0.02
	954.80	9.38	530.72	0.05
	14.48	2.41	12.19	0.01
	3116.20	9.62	1647.77	0.18
	49.98	6.57	56.53	0.01
	26.68	4.27	71.56	0.01
	533.63	12.38	170.28	0.02
	309.28	9.83	156.53	0.02
	97.38	2.26	932.42	0.10
	13.12	2.14	140.11	0.01
W44	67.75	3.67	246.00	0.02
	10.54	3.26	48.50	0.01
	7.52	1.68	130.30	0.01
	20.23	2.72	133.73	0.01
	8.92	1.74	144.09	0.01
	47.80	2.43	395.89	0.04
	352.37	5.88	498.43	0.05
	50.41	1.50	1095.70	0.12
	35.87	1.50	779.67	0.08
	1762.63	5.75	2607.26	0.3
	11.44	1.55	232.87	0.02
	187.75	2.53	1434.49	0.15
	317.60	5.12	592.52	0.06
	107.63	2.19	109.75	0.01
	842.22	10.14	400.60	0.04
	9.62	2.14	102.73	0.01
	75.16	8.78	47.68	0.01
	22.34	1.86	315.80	0.03
	9.31	1.62	173.49	0.02
	378.59	4.02	1145.71	0.12
W47	16.02	1.76	252.93	0.03
	20.89	2.45	170.20	0.02
	2561.21	8.92	1574.25	0.17
	406.46	8.18	297.08	0.03
	210.28	5.18	383.26	0.04

Continued on next page

Table 6.9 – continued from previous page

Source	S (mJy)	FWHM ($''$)	T_b (K)	τ
	20.24	2.22	200.85	0.02
	25.99	4.26	70.04	0.01
	35.68	7.02	35.41	0.01
	88.30	8.28	62.99	0.01
	11.52	2.51	8.21	0.01
	7.84	1.60	5.59	0.01
	19.88	2.69	14.18	0.01
	311.31	3.57	222.07	0.02
	9.31	1.62	6.64	0.01
	22.34	1.86	15.94	0.01
	62.27	1.95	44.42	0.01

Table 6.9: The flux density, FWHM, and optical depth values of the UCHII regions found within 2° of W43, W44 and W47 using the CORNISH 5 GHz catalogue.

The combined 5 GHz fluxes of the sources within 2° of W43, W44 and W47 are 9.4 Jy, 4.3 Jy and 3.8 Jy, respectively. Assuming a free-free spectral index of −2.15 these contributions would scale to 0.2 Jy, 0.09 Jy and 0.08 Jy at 30 GHz. Therefore, the excess emission associated with W43, W44 and W47 cannot be accounted for by UCHII regions and can be attributed to AME.

6.3 Summary

It has been possible to validate the C-BASS data calibration within the 5 % uncertainty level through T-T analysis of Barnard's Loop using the January to February 2012 Northern preliminary intensity data. T-T analysis was also used to ascertain the off-plane ($|b| > 4°$) synchrotron spectral index between 0.408 and 4.76 GHz. This was found to be ≈ -2.70 and a slight steepening between the 0.408 – 4.76 GHz and 1.420 – 4.76 GHz spectral indices was seen, although this was within the uncertainties.

Latitude profiles within the Galactic plane ($|b| < 4°$) showed that the MCMC template was overestimating the free-free emission at 4.76 GHz within $21^\circ < l < 26^\circ$ because the predicted free-free emission was as large as the total intensity measured by C-BASS. Synchrotron emission latitude profiles were made at 0.408, 1.420 and 4.76 GHz within the Galactic plane and the synchrotron spectral index was found to be -2.63 ± 0.07 between 0.408 and 4.67 GHz and -2.71 ± 0.14 between 1.420 and 4.76 GHz. The ratio of synchrotron to total emission at 4.76 GHz within the Galactic plane was determined to be 53 ± 8 %.

Finally the C-BASS data were used alongside higher frequency data to constrain the spectrum of AME. T-T analysis between C-BASS and *WMAP* K-band revealed an AME to total emission ratio of 10 – 40 % within the $30^\circ < l < 40^\circ, -0\overset{\circ}{.}75 < b < 0\overset{\circ}{.}75$ strip. SED analysis of the compact regions W43, W44 and W47 revealed AME detections at the 4.9σ, 6.0σ and 3.4σ significance levels with shapes consistent with the spinning dust model of AME. The analysis of W47 in particular revealed that C-BASS data, as well as further 5 – 23 GHz data, are in fact vital for the characterisation of the AME spectral bump of certain regions.

Chapter 7

Conclusions

7.1 Summary

Upon completion C-BASS will provide the CMB community with polarisation maps of synchrotron emission for use in the accurate measurement of primordial B-modes. Additionally, both the intensity and polarisation maps will be used to constrain the spectral index of synchrotron emission and AME and act as a testbed for free-free emission templates. The maps will be at a FWHM of $45'$ and a sensitivity of 0.1 mK per beam in polarisation.

The work carried out for this thesis took the form of technical work, commissioning, data reduction and data analysis. The majority of the technical work was within the Northern cryostat and had the aim of mitigating the microphonics problem. The success of the work carried out in the Northern cryostat enabled the 1.2 Hz oscillations within the TOD to take a form stable enough to be removed post-processing. The commissioning work for the Northern receiver identified two sources of permanent, in-band RFI, which resulted in notch filters being added to the passband, as well as Hot/Cold Load tests which characterised the receiver noise. The Northern system was measured to have a system temperature of ≈ 40 K, a noise level of ≈ 2 mK $\sqrt{\mathrm{s}}$ and a polarisation knee frequency of 10 mK. The Southern receiver commissioning also involved Hot/Cold Load tests, which put the receiver temperature at ≈ 20 K as well as the identification of a misalignment within part of the horn which was resolved through re-machining.

Within the C-BASS data reduction pipeline the data are calibrated relative to an internal noise diode. The vital next step is the calibration of this noise diode "unit" into Kelvin using astronomical sources. The work within this thesis details a method of calibration which uses 2D Gaussian fitting to determine the measured C-BASS antenna temperature of Cas A, Tau A and Cyg A in noise diode units. These values are then compared to the antenna temperature which C-BASS should measure in Kelvin, as calculated from flux density values documented within the literature. This method successfully produces conversion factors between noise diode units and Kelvin which display no correlation with parallactic angle and are stable to within 1 % over periods of several months. Atmospheric opacity, although only a 1 % effect for Northern C-BASS, had also to be calculated and accounted for within this calibration. This was successfully done through both the empirical SkyDip method as well as a theoretical calculation based on the atmospheric slab model of the atmosphere and pressure, temperature and relative humidity measurements. The colour corrections needed for the calibrator sources Tau A and Cyg A, relative to Cas A, were found to be less than 1 %. The C-BASS calibration scheme, taking into account colour corrections, opacity corrections, the noise diode stability and the aperture efficiency uncertainty, was found to be accurate to better than 5 %.

The presence of ground spillover emission within the C-BASS maps has long obscured the high latitude Galactic features within the intensity maps and the Galactic plane signal within the polarised intensity maps. A method for removing this contaminant signal from the TOD has been developed and is based around the creation and removal of ground emission templates. These templates are one dimensional functions of azimuth and were made in Stokes I, Q and U for both survey elevations (37° and 47°). Although still under investigation this method has significantly limited the presence of ground emission within the C-BASS six month maps; the ground emission has been reduced by a factor of ≈ 8 in intensity and ≈ 7 in Stokes Q and U. The residual ground emission remaining in the maps is roughly 4 % of the sky signal in intensity, 5 % of the sky signal in Stokes Q and 14 % of the sky signal in Stokes U.

The good quality C-BASS intensity data available during this thesis enabled the investigation of free-free and synchrotron emission within and just off of the Galactic plane. Within the off-plane region of $20^\circ < l < 40^\circ, -10^\circ < b < -4^\circ$ the synchrotron spectral index was determined to be $\beta = -2.65 \pm 0.05$ between 0.408 and 4.76 GHz and $\beta = -2.75 \pm 0.09$ between 1.420 and 4.76 GHz. Various free-free templates, *WMAP* MEM, *WMAP* MCMC and RRLs, were trialled in the in-plane $20^\circ < l < 40^\circ, |b| < 4^\circ$ region and it was found that the *WMAP* MCMC template overestimates the free-free emission present at 4.76 GHz. The synchrotron spectral index within the plane, using the RRL free-free template was found to be -2.63 ± 0.07 between 0.408 and 4.76 GHz and -2.71 ± 0.14 between 1.420 and 4.76 GHz and the ratio of synchrotron to free-free emission at 4.76 GHz is 53 ± 8 %:47 ± 8 %. The ability of C-BASS data to constrain AME was also explored through SEDs of the compact regions W43, W44 and W47. Aperture photometry was used to detect AME at a 4.9σ, 6.0σ and 3.4σ level within W43, W44 and W47. The C-BASS data point was needed to constrain the synchrotron component of W44 and the peak AME frequency of W47.

7.2 Future work

From the perspective of the CMB community the most exciting aspect of the C-BASS data release will be the all-sky Stokes Q and U maps. These maps will provide all-sky information on synchrotron emission at 5 GHz for use in component separation. The C-BASS central frequency is high enough for the data at high latitudes to not be seriously effected by Faraday rotation, unlike the 1.420 GHz Wolleben et al. (2006) DRAO survey of the Northern hemisphere. The next stage of data reduction for Northern C-BASS will include the calibration of the Stokes Q and Stokes U polarisation data, using Tau A.

The data reduction pipeline is being expanded and improved upon and forthcoming features will include solar sidelobe removal and the optimisation of the 1.2 Hz removal, so as to produce maps limited by thermal noise in polarisation and confusion noise in intensity. To verify the removal of systematic noise, the jackknife tests which were explored in this thesis will be automated and increased to included the full suite of possible data selections.

While the Northern survey data collection is drawing to a finish, the commissioning of the Southern telescope is in process and the receiver is being prepared for relocation to its final site in the Karoo. Southern C-BASS data will open up opportunities to study the Galactic Haze, to improve the ground emission removal using the regions of sky observed by both Northern and Southern C-BASS and to observe the prominent AME region ρ Ophiucus.

Part I

Appendices

Appendix A

Fundamental Astrophysics

A.1 Reddening

Stars will appear fainter with increasing observational distance because of the attenuation of their electromagnetic radiation. The inverse square law states that the intensity measured after attenuation will be inversely proportional to distance squared. Attenuation, however is not the only effect capable of dimming measured intensity; interstellar extinction is the dimming of starlight by interstellar dust. The extinction (A_λ) at a wavelength λ is calculated in magnitudes using the observed flux (F^0_λ) and the expected flux (F_λ) (Draine 2011):

$$\frac{A_\lambda}{\text{mag}} = 2.5\ \log_{10}\left[\frac{F^0_\lambda}{F_\lambda}\right] \tag{A.1}$$

$$= 2.5\ \log_{10}\left[e^{\tau_\lambda}\right]. \tag{A.2}$$

Interstellar extinction increases towards the blue end of the electromagnetic spectrum thus making the light that eventually reaches Earth appear redder. The term 'reddening' itself is normally reserved to describe the difference between the extinctions at 4405 Å (B band) and 5470 Å (V band):

$$\text{Reddening} = E(B - V) \tag{A.3}$$

$$= A_B - A_V \tag{A.4}$$

and the extinction slope across wavelength is

$$R_V = \frac{A_V}{E(B-V)}. \tag{A.5}$$

A.2 Rayleigh-Jeans Vs Thermodynamic temperature

The brightness/intensity of a blackbody at a temperature T in thermodynamic equilibrium is given by the Planck function:

$$B_\nu(T) = \frac{2\,h\,\nu^3}{c^2}\frac{1}{e^{\frac{h\,\nu}{k_B\,T}}-1}, \tag{A.6}$$

where h is Planck's constant, k_B is the Boltzmann constant and ν is the measurement frequency (Rohlfs & Wilson 2004). Figure A.1 shows various measurements of the CMB temperature alongside the intensity spectrum of a blackbody in thermal equilibrium at 2.73 K. At low frequencies/long wavelengths the relationship between frequency and brightness temperature is clearly different from that at $\nu > 30$ GHz, the low frequency regime is known as the Rayleigh-Jeans regime. Within this Rayleigh-Jeans limit $h\,\nu \ll k_B\,T$ and so:

$$e^x \sim 1 + x, \tag{A.7}$$

where

$$x = \frac{h\,\nu}{k_B\,T}, \tag{A.8}$$

therefore

$$B_{RJ}(T) = \frac{2\,\nu^2\,k_B\,T}{c^2}. \tag{A.9}$$

The Rayleigh-Jeans temperature can be expressed as

$$T_{RJ} = \frac{c^2}{2\,k_B\nu^2}\,B \tag{A.10}$$

$$, = \frac{h\,\nu}{k_B}\frac{1}{e^x-1}, \tag{A.11}$$

and the conversion between Rayleigh-Jeans temperature and thermodynamic temperature can be obtained by calculating the change in Rayleigh-Jeans temperature caused

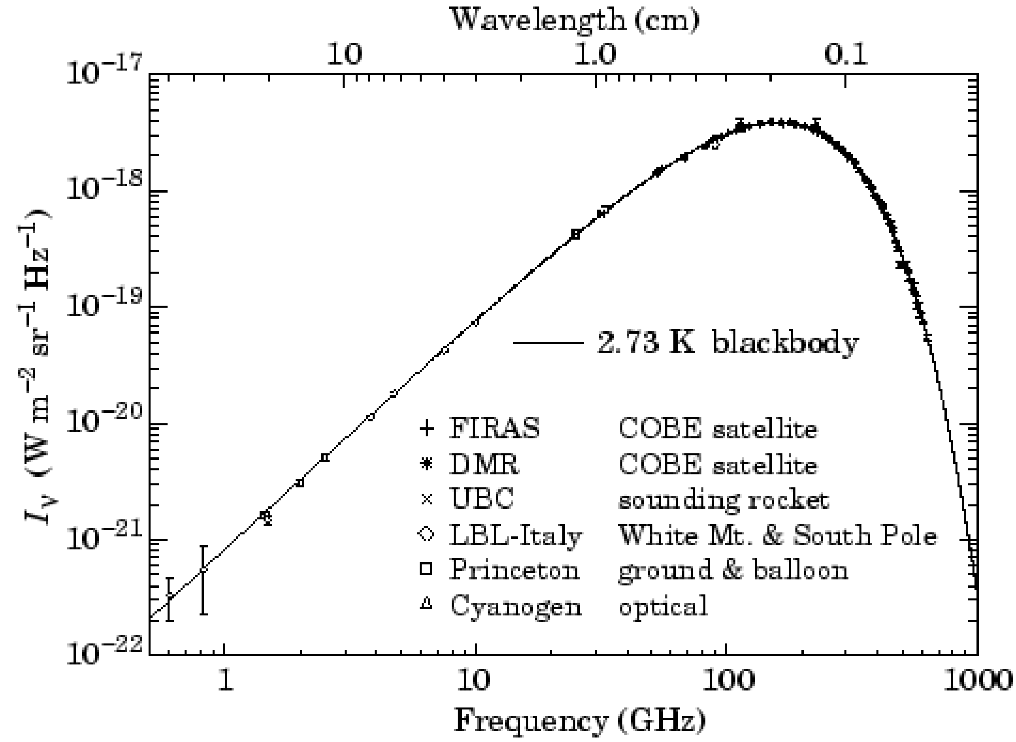

Figure A.1: Various measurements of the CMB fit using the intensity spectrum of a blackbody at 2.73 K. Image from Charles (2001).

by the change in the thermodynamic temperature (T):

$$\frac{d\,T_{RJ}}{d\,T} = \frac{x^2\,e^x}{(e^x - 1)^2}. \tag{A.12}$$

Appendix B

The Reich full beam scaling factor

Throughout this thesis the Reich & Reich (1986) data set are used after having been multiplied by a factor of 1.55 to put them on the same brightness scale as the data they will be used alongside. This factor comes from the 1.55 ± 0.08 conversion factor between the Stockert full beam and the Effelsberg main beam temperatures at 1.420 GHz, which (Reich & Reich 1988) find through T-T analysis. This factor is still under investigation as not all the analyses conducted using the Reich & Reich (1986) data agree on this 1.55 multiplication (private communication with Dr Clive Dickinson and Professor Hans-Kristian Eriksen). Additionally, there is not a well defined definition of what is considered to be the full beam scale; different surveys use different definitions. Reich & Reich (1986) define the full beam as within 7° of the main beam. The main beam and full beam efficiencies of the Stockert telescope are 55 % and 69 %, respectively (Reich & Reich 1986), which would imply correction factors of 1.82 to convert the data to the main beam scale and 1.45 to convert the data to the full beam scale. The 1.55 scaling is between these two factors implying that is a correction onto a temperature scale between the main and full beam temperature scale.

Figure B.1 shows a selection of T-T plots for the Barnard's Loop region of $208^\circ < l < 213^\circ, -13\overset{\circ}{.}5 < b < -12^\circ$ all using Reich & Reich (1986) data. As this region is known to be free-free emission dominated the Reich & Reich (1986) data were multiplied by the factor that was required to result in a spectral index of -2.1. The

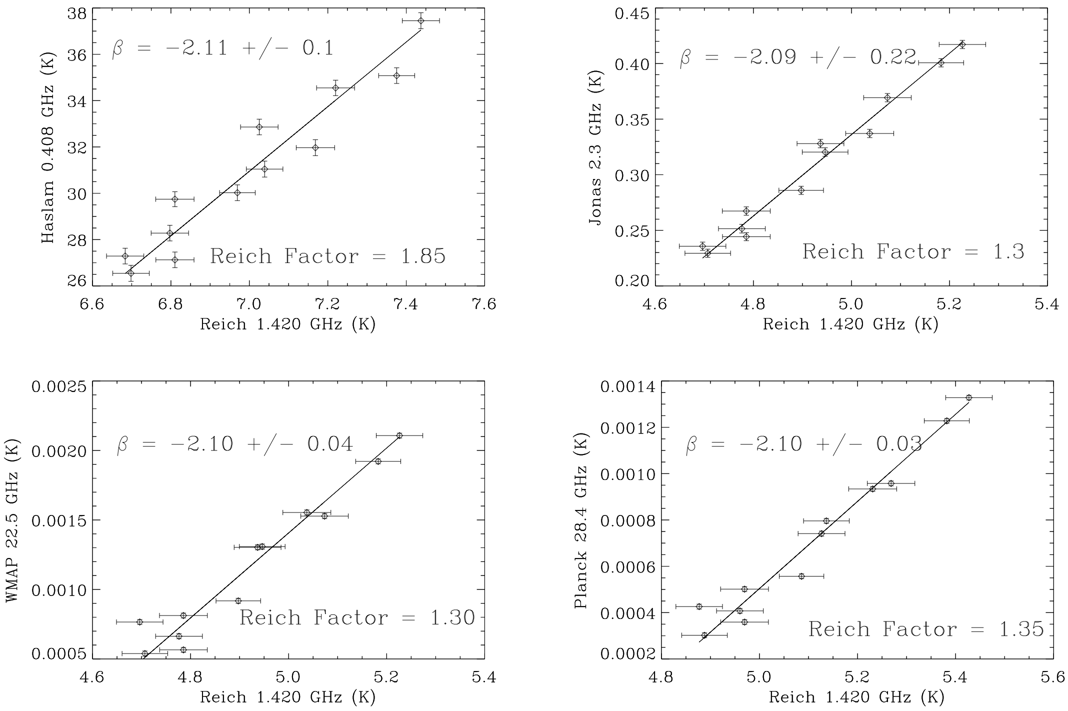

Figure B.1: T-T plots within $208^{\circ} < l < 213^{\circ}, -13^{\circ}\!.5 < b < -12.0^{\circ}$ between, **clockwise from top left:** 0.408 and 1.420 GHz, 2.3 and 1.420 GHz, 1.420 GHz and 22.5 GHz and 1.420 and 28.4 GHz. The *Planck* 28.4 GHz data are used with the SMICA CMB map subtracted from it.

Planck 28.4 GHz data have had the CMB anisotropies subtracted using the *Planck* SMICA (Spectral Matching Independence Component Analysis) CMB map, which fits for the CMB within the harmonic domain.

It can been be seen that the factor required is between 1.3 and 1.85, with the 0.408 –1.420 GHz T-T plot result responsible for the upper limit of 1.85. Ignoring the 0.408 – 1.420 GHz result would seem to place the correct factor at ≈1.30, which may imply that the 0.408 GHz Haslam et al. (1982) data are not on the full beam scale themselves. Figure B.2 shows a T-T plot for the same Barnard's Loop region shown in Figure B.1 between 0.408 and 22.5 GHz. It can be seen that the expected free-free spectral index of $\beta = -2.1$ is obtained when the Haslam et al. (1982) data are used at 70 %

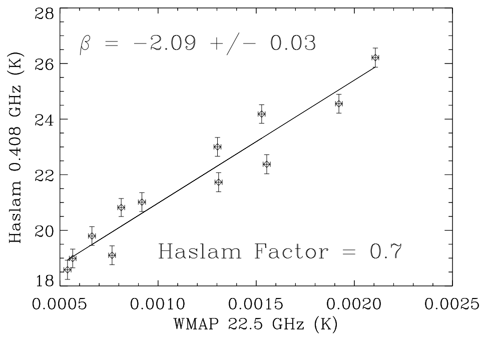

Figure B.2: T-T plot within $208^\circ < l < 213^\circ, -13\overset{\circ}{.}5 < b < -12.0^\circ$ between 0.408 and 22.5 GHz.

of their intensity, thus implying that the Haslam et al. (1982) data are too high. The C-BASS data with their better defined beam and calibration will be a critical factor in determining the calibration factors required for these older, lower frequency surveys.

The Reich & Reich (1986) data are used after multiplication of 1.55 throughout this thesis as this value is currently the standard value used and is within the 1.3 –1.85 range found. However, the T-T plots shown in Figure B.1 and B.2 have been included to illustrate that work determining the exact factor is ongoing and that determining a single, well defined temperature scale for all the low frequency data sets to be presented on is a necessary and important task.

References

Abdo A. A. et al., 2009, ApJ, 707, 55

Ali-Haïmoud Y., Hirata C. M., Dickinson C., 2009, MNRAS, 395, 1055

Altenhoff W. J. et al., 1960, Technical Report 59, Veroff. Univ. Sternwart Bonn, 59

Alves M. I. R. et al., 2012, MNRAS, 422, 2429

Barkats D. et al., 2005, ApJL, 619, L127

Barnes D. G. et al., 2001, MNRAS, 322, 486

Bartlett J. G., 2006, Journal of Physics Conference Series, 39, 1

Battye R. A. et al., 2011, MNRAS, 413, 132

Baumann D. et al., 2009, in American Institute of Physics Conference Series, Vol. 1141, American Institute of Physics Conference Series, Dodelson S., Baumann D., Cooray A., Dunkley J., Fraisse A., Jackson M. G., Kogut A., Krauss L., Zaldarriaga M., Smith K., eds., pp. 10–120

Bennett C. L. et al., 2003a, ApJS, 148, 1

Bennett C. L. et al., 2003b, ApJS, 148, 97

Bennett C. L. et al., 2013, ApJS, 208, 20

Bersanelli M. et al., 1995, ApJ, 448, 8

Bersanelli M. et al., 1994, ApJ, 424, 517

BICEP2 Collaboration et al., 2014, ArXiv e-prints:1403.3985

Bock D., 1999, BIMA Memo No. 74.

Bonaldi A. et al., 2007, MNRAS, 382, 1791

Borka Jovanović V., Urošević D., 2010, Journal of Physics Conference Series, 257, 012030

Bowden M. et al., 2004, in Society of Photo-Optical Instrumentation Engineers (SPIE)

Conference Series, Vol. 5489, Ground-based Telescopes, Oschmann Jr. J. M., ed., pp. 84–94

Broadbent A., Osborne J. L., Haslam C. G. T., 1989, MNRAS, 237, 381

Brutsaert W., 1975, Water Resources Research, 11, 742

Buder I., 2010, in Society of Photo-Optical Instrumentation Engineers (SPIE) Conference Series, Vol. 7741, Society of Photo-Optical Instrumentation Engineers (SPIE) Conference Series

Carretti E. et al., 2013, Nature, 493, 66

Carretti E. et al., 2010, MNRAS, 405, 1670

Casassus S. et al., 2008, MNRAS, 391, 1075

Charles P., 2001, http://www.astro.soton.ac.uk/ pac/ph112/notes/notes/node182.html

Condon J. J. et al., 1998, AJ, 115, 1693

Copley C. J., 2013, PhD thesis, University of Oxford

Davies R. D., 1960, MNRAS, 120, 483

Davies R. D. et al., 2006, MNRAS, 370, 1125

Davis R. J. et al., 2009, Journal of Instrumentation, 4, 2002

de Oliveira-Costa A. et al., 2008, MNRAS, 388, 247

Dennison B. et al., 1998, in IAU Symposium, Vol. 179, New Horizons from Multi-Wavelength Sky Surveys, McLean B. J., Golombek D. A., Hayes J. J. E., Payne H. E., eds., p. 182

Dickinson C., 2013, Advances in Astronomy, 2013

Dickinson C. et al., 2004, MNRAS, 353, 732

Dickinson C. et al., 2009, ApJ, 690, 1585

Dickinson C., Davies R. D., Davis R. J., 2003, MNRAS, 341, 369

Dickinson C., Peel M., Vidal M., 2011, MNRAS, 418, L35

Dobler G., 2012, ApJ, 750, 17

Dobler G. et al., 2010, ApJ, 717, 825

Draine B. T., 2011, Physics of the Interstellar and Intergalactic Medium, Princeton University Press

Draine B. T., Hensley B., 2012, ApJ, 757, 103

Draine B. T., Lazarian A., 1998, ApJL, 494, L19

Draine B. T., Lazarian A., 1999, ApJ, 512, 740

Duncan A. R. et al., 1995, MNRAS, 277, 36

Dunkley J. et al., 2009, ApJ, 701, 1804

Eisenstein D. J. et al., 2005, ApJ, 633, 560

Finkbeiner D. P., 2003, ApJS, 146, 407

Finkbeiner D. P., 2004, ApJ, 614, 186

Finkbeiner D. P., Davis M., Schlegel D. J., 1999, ApJ, 524, 867

Fixsen D. J., 2009, ApJ, 707, 916

Fixsen D. J. et al., 2011, ApJ, 734, 5

Frey T., 1999, Applied Microwave and Wireless, 76

Gao X. Y. et al., 2010, A&A, 515, A64

Gaustad J. E. et al., 2001, PASP, 113, 1326

Górski K. M. et al., 2005, ApJ, 622, 759

Gregory P. C. et al., 1996, ApJS, 103, 427

Grimes P. K. et al., 2007, ArXiv e-prints:0709.1777

Hafez Y. A. et al., 2008, MNRAS, 388, 1775

Halverson N. W. et al., 2002, ApJ, 568, 38

Haslam C. G. T. et al., 1982, A&AS, 47, 1

Haverkorn M., Katgert P., de Bruyn A. G., 2004, A&A, 427, 549

Heiles C. et al., 2000, ApJ, 536, 335

Hincks A. D. et al., 2010, ApJS, 191, 423

Hoang T., Lazarian A., Martin P. G., 2013, ApJ, 779, 152

Hoare M. G. et al., 2007, Protostars and Planets V, 181

Holler C. M. et al., 2013, IEEE Transactions on Antennas and Propagation, 61, 117

Hu W., Dodelson S., 2002, ARA&A, 40, 171

Jonas J. L., Baart E. E., Nicolson G. D., 1998, MNRAS, 297, 977

Kaplan J., 2003, Comptes Rendus Physique, 4, 917

Keating B. G. et al., 2003, in Society of Photo-Optical Instrumentation Engineers (SPIE) Conference Series, Vol. 4843, Polarimetry in Astronomy, Fineschi S., ed., pp. 284–295

Kermish Z. D. et al., 2012, in Society of Photo-Optical Instrumentation Engineers (SPIE) Conference Series, Vol. 8452, Society of Photo-Optical Instrumentation Engineers (SPIE) Conference Series

King O. G., 2009, PhD thesis, University of Oxford

King O. G. et al., 2010, in Society of Photo-Optical Instrumentation Engineers (SPIE) Conference Series, Vol. 7741, Society of Photo-Optical Instrumentation Engineers (SPIE) Conference Series

King O. G. et al., 2014, MNRAS, 438, 2426

Kogut A., 2012, ApJ, 753, 110

Komatsu E. et al., 2011, ApJS, 192, 18

Kopp C., Wallace C., 2004, School of Computer Science and Software Engineering, Monash University, Melbourne, 21

Kovac J. M. et al., 2002, Nature, 420, 772

Kraus J. D., 1966, Radio astronomy, McGraw-Hill

Laher R. R. et al., 2012, PASP, 124, 737

Lange A. E. et al., 2001, Phys. Rev. D, 63, 042001

Lawson K. D. et al., 1987, MNRAS, 225, 307

Leitch E. M. et al., 1997, ApJL, 486, L23

López-Caraballo C. H., Génova-Santos R., 2013, in Highlights of Spanish Astrophysics VII, pp. 256–257

Lucas P. W. et al., 2008, MNRAS, 391, 136

Martin J., Vennin V., Peter P., 2012, Phys. Rev. D, 86, 103524

Mather J. C., 1982, Optical Engineering, 21, 769

Meinhold P. et al., 2009, Journal of Instrumentation, 4, 2009

Mennella A. et al., 2003, A&A, 410, 1089

Mezger P. G., Henderson A. P., 1967, ApJ, 147, 471

Milogradov-Turin J., Nikolić S., 1995, Bulletin Astronomique de Belgrade, 151, 7

Murphy T. et al., 2010, MNRAS, 402, 2403

Myers S. T. et al., 2003, MNRAS, 341, 1

Oster L., 1961, Reviews of Modern Physics, 33, 525

Padin S. et al., 2002, PASP, 114, 83

Page L. et al., 2003, ApJS, 148, 39

Page L. et al., 2007, ApJS, 170, 335

Peel M. W. et al., 2012, MNRAS, 424, 2676

Penzias A. A., Wilson R. W., 1965, ApJ, 142, 419

Perrot C. A., Grenier I. A., 2003, A&A, 404, 519

Perryman M. A. C. et al., 1997, A&A, 323, L49

Pietranera L. et al., 2007, MNRAS, 376, 645

Pietrobon D. et al., 2012, ApJ, 755, 69

Planck Collaboration et al., 2011a, A&A, 536, A21

Planck Collaboration et al., 2013a, ArXiv e-prints:1309.1357

Planck Collaboration et al., 2013b, ArXiv e-prints:1303.5062

Planck Collaboration et al., 2013c, ArXiv e-prints:1303.5062

Planck Collaboration et al., 2012, ArXiv e-prints:1208.5483

Planck Collaboration et al., 2011b, A&A, 536, A19

Planck Collaboration et al., 2011c, A&A, 536, A20

Planck Collaboration et al., 2011d, A&A, 536, A20

Planck Collaboration et al., 2014, ArXiv e-prints

Platania P. et al., 1998, ApJ, 505, 473

Purcell C. R. et al., 2013, ApJS, 205, 1

QUIET Collaboration et al., 2012, ApJ, 760, 145

QUIET Collaboration et al., 2011, ApJ, 741, 111

Reich P., Reich W., 1986, A&AS, 63, 205

Reich P., Reich W., 1988, A&AS, 74, 7

Reichborn-Kjennerud B. et al., 2010, in Society of Photo-Optical Instrumentation Engineers (SPIE) Conference Series, Vol. 7741, Society of Photo-Optical Instrumentation Engineers (SPIE) Conference Series

Reynolds R. J. et al., 1998, PASA, 15, 14

Richards P. L. et al., 2002, in American Institute of Physics Conference Series, Vol. 616, Experimental Cosmology at Millimetre Wavelengths, de Petris M., Gervasi M., eds., pp. 12–17

Rohlfs K., Wilson T. L., 2004, Tools of radio astronomy, Springer

Ruhl J. et al., 2004, in Society of Photo-Optical Instrumentation Engineers (SPIE) Conference Series, Vol. 5498, Z-Spec: a broadband millimeter-wave grating spectrometer: design, construction, and first cryogenic measurements, Bradford C. M., Ade P. A. R., Aguirre J. E., Bock J. J., Dragovan M., Duband L., Earle L., Glenn J., Matsuhara H., Naylor B. J., Nguyen H. T., Yun M., Zmuidzinas J., eds., pp. 11–29

Runyan M. C. et al., 2003, ApJS, 149, 265

Schlegel D. J., Finkbeiner D. P., Davis M., 1998, ApJ, 500, 525

Silk J., 1967, Nature, 215, 1155

Silsbee K., Ali-Haïmoud Y., Hirata C. M., 2011, MNRAS, 411, 2750

Simmons J. F. L., Stewart B. G., 1985, A&A, 142, 100

Sissenwine N., Dubin M., Wexler H., 1962, J. Geophys. Res., 67, 3627

Smith E. K., 1982, Radio Science, 17, 1455

Stanimirovic S., Altschuler D., Goldsmith P., Salter C., eds., 2002, Astronomical Society of the Pacific Conference Series, Vol. 278, Single-Dish Radio Astronomy: Techniques and Applications

Story K. T. et al., 2013, ApJ, 779, 86

Strong A. W., Orlando E., Jaffe T. R., 2011, A&A, 534, A54

Sun X. H. et al., 2008, A&A, 477, 573

Sutton D. et al., 2010, MNRAS, 407, 1387

Tasker N. J. et al., 1994, AJ, 107, 2115

Tegmark M., 1995, Proc. Enrico Fermi, Course CXXX11, Varenna, 1995, 1

Tello C. et al., 2013, A&A, 556, A1

The LSPE collaboration et al., 2012, ArXiv e-prints:1208.0281

Turtle A. J. et al., 1962, MNRAS, 124, 297

Vinyaikin E. N., 2007, Astronomy Reports, 51, 570

Wagner W., Pruss A., 1993, Journal of Physical and Chemical Reference Data, 22, 783

Wardle J. F. C., Kronberg P. P., 1974, ApJ, 194, 249

Waters J. W., 1976, Methods of Experimental Physics, 12, 142

Weiland J. L. et al., 2011, ApJS, 192, 19

Wolleben M. et al., 2006, A&A, 448, 411

Wood D. O. S., Churchwell E., 1989, ApJS, 69, 831

Wright E. L. et al., 1992, ApJL, 396, L13

Zacchei A. et al., 2011, A&A, 536, A5

Zaldarriaga M., Seljak U., 1997, Phys. Rev. D, 55, 1830